Electronic and Magnetic Properties of Topological Quantum Materials

Thesis submitted for the degree of

Doctor of Philosophy (Science)

in

Physics (Experimental)

by

Susanta Ghosh

Department of Physics

University of Calcutta

2025

Dedicated to my maa and baba

Declaration

I hereby declare that the work presented in this thesis is entirely my own. Neither this thesis nor any part of it has been submitted elsewhere for any degree/diploma or academic award. I have duly cited all original sources and references used throughout the document. Furthermore, I affirm that I have upheld the highest standards of academic integrity and honesty. I have not misrepresented, fabricated, or manipulated any data, facts, ideas, or sources in the preparation of this thesis.

Susanta Ghosh
Kolkata, India
Date:

Acknowledgement

I am truly honored to have completed my Ph.D. at the S. N. Bose National Centre for Basic Sciences. The excellent academic environment and advanced research facilities have greatly contributed to my growth both intellectually and personally. During this journey, I have been lucky to learn from and receive guidance from many people whose support and encouragement have shaped my approach to education and research. I sincerely thank all of them for their valuable help and inspiration.

I would like to express my sincere gratitude to my Ph.D. supervisor, Professor Kalyan Mandal, for his unwavering academic support and guidance throughout the course of my doctoral studies. His valuable advice, generous assistance, and approachable nature played a significant role in helping me successfully complete my Ph.D.

I am deeply grateful to Dr. Thirupathaiah Setti, my Ph.D. guide and supervisor, for his invaluable support throughout my research journey. His profound knowledge, clear vision, and dedicated guidance have been instrumental at every stage of this work. I sincerely appreciate his enthusiastic involvement and continuous encouragement, which were crucial to the successful completion of this work. I am especially thankful for his careful review and thorough refinement of my manuscripts, which significantly improved the quality of this research.

I would like to express my sincere gratitude to Dr. Awadhesh Narayan and Dr. Nayana Devaraj from IISc Bangalore for their valuable collaboration.

I sincerely acknowledge all the members of my Thesis Advisory Committee for their time, guidance, and for critically evaluating the progress of my research throughout the course of my doctoral work.

I sincerely thank the S. N. Bose National Centre for Basic Sciences for providing a supportive research environment. The excellent facilities, peaceful campus, and comfortable living conditions greatly helped my academic work. I am especially grateful to the Technical Research Centre (TRC) for their important support, as much of my research

used their advanced instruments funded by the Department of Science and Technology (DST), Government of India. I gratefully acknowledge the financial support provided by SNBNCBS and also extend my sincere appreciation to the University Grants Commission (UGC), India, for the award of the Ph.D. fellowship, which significantly contributed to the completion of this work.

I am truly thankful to the members of the Quantum-Materials Lab (QML) for creating a collaborative and intellectually stimulating environment that greatly enriched my research experience. The camaraderie and support that I received from Indrani Kar, Susmita Changdar, Achintya Low, Sayan Routh, Shubham Purwar, Soumya Ghorai, Anupam Barik, and Ankita Das played a vital role in both my academic and personal journey. I am especially grateful to Achintya Low for his consistent support, valuable guidance, and insightful scientific discussions throughout my research journey. I also sincerely thank my junior, Soumya Ghorai, for his constant encouragement and warm friendship. I sincerely thank the postdoctoral researchers in our group, Dr. Tushar Kanti Bhowmik, Dr. Reena Goyal, Dr. Pankaj Maheshwari, Dr. Tusita Sau, and Dr. Ayana Mukhopadhyay, for generously sharing their knowledge and guidance throughout my research. Their support has greatly contributed to my academic growth.

I would like to express my sincere appreciation to the administrative staff of SNBNCBS, particularly Ms. Nibedita Konar, Ms. Chandrakana Chatterjee, Mr. Rupam Porel, Mr. Jaydeep Kar, and Mr. Swarup Dutta, for their efficient administrative support, which contributed significantly to the smooth progress of my academic and research activities. I also sincerely thank the technical staff at S. N. Bose National Center for Basic Sciences, Rishikesh Nandi, Shakti Nath Das, Urmi Chakrabarty, Joy Bandopadhyay, Sourabh Sinha, and Debarghya Ghosh, for their consistent assistance during experimental measurements. Their expertise and dedication were essential to the smooth progress of my research work.

Words cannot fully express my deep gratitude to my parents, Renuka Ghosh and Sanjit Kumar Ghosh. Their boundless love, sacrifices, and unwavering faith have been the foundation of my strength. Being their son is my greatest blessing. I also thank my elder sister, Sonali Ghosh, for her selfless care of our parents and steady support, which has given me the confidence to pursue my goals. I am deeply grateful to my cousin Dr. Chandan Ghosh for his unwavering support and inspiring journey, which has been a constant motivation.

Susanta Ghosh

Abstract

Topological materials offer a versatile platform for the realization of novel quantum states with potential applications in future electronics and quantum technologies. Among them, kagome lattice systems are of particular interest due to their unique geometry, which gives rise to a rich interplay of geometrical frustration, magnetism, and topological electronic states. These features can host exotic phenomena such as Dirac and Weyl fermions, flat bands, quantum spin liquids, skyrmion lattices, and anomalous and topological Hall effect (AHE and THE). The primary goal of this thesis is to synthesize high-quality single crystals of various kagome compounds and systematically investigate their structural, electronic, magnetic, and magnetotransport properties.

We synthesized single crystals of Mn-rich and Ge-rich Mn_3Ge, a noncollinear kagome antiferromagnet that hosts Weyl fermions. Unlike Mn-rich $Mn_{3+x}Ge$, Ge-rich $Mn_{2.94}Ge$ exhibits multiple magnetic transitions below the Néel temperature, including a spin reorientation (T_{SR}) and a low temperature ferromagnetic-like phase. Also, the anomalous Hall conductivity peaks at T_{SR} and decreases with temperature. Together, these findings demonstrate how strongly the magnetic and topological characteristics of Mn_3Ge depend on its chemical composition. We further studied the effect of Fe doping in $Mn_{(3+x)-\delta}Fe_\delta Ge$ (δ = 0, 0.30, 0.62). Doping induces a transition from metallic to semiconducting behavior at $\delta = 0.30$ and a metal-insulator transition near 100 K at $\delta = 0.62$. Fe substitution enhances in-plane ferromagnetism, increases magnetocrystalline anisotropy, introduces a spin-glass-like state, and reduces the spontaneous AHE. Interestingly, a THE signal emerges uniquely at $\delta = 0.30$ due to the formation of noncoplaner spin texture. Furthermore, we synthesized single crystals of Fe_3Ge, a ferromagnetic topological kagome metal. We observed strong anisotropy in Hall conductivity and a rare temperature-driven evolution of the intrinsic AHE, associated with a reorientation of the magnetic easy axis from out-of-plane to in-plane. Additionally, a pronounced in-plane THE emerges below the spin reorientation transition. Subsequently, we synthesized rare-earth-based kagome Dirac semimetals RFe_6Sn_6 (R = Ho, Dy), which exhibit extremely large magnetoresistance (XMR) up to $3 \times 10^3\%$. Hall measurements reveal near-perfect electron-hole compensation and high carrier mobility, accounting for the XMR behavior. The angle-dependent magnetoresistance (ADMR) pattern varies significantly with temperature, reflecting Fermi surface modulation.

রূপরেখা

টপোলজিক্যাল উপাদানসমূহ নতুন কোয়ান্টাম অবস্থার বাস্তবায়নের জন্য একটি বহুমুখী প্ল্যাটফর্ম প্রদান করে, যার ভবিষ্যতের ইলেকট্রনিক্স ও কোয়ান্টাম প্রযুক্তিতে সম্ভাব্য প্রয়োগ রয়েছে। এর মধ্যে কাগোমে ল্যাটিসযুক্ত যৌগগুলি তাদের অনন্য জ্যামিতির কারণে বিশেষভাবে আগ্রহের কেন্দ্রবিন্দুতে রয়েছে। এই কাঠামো জ্যামিতিক ফ্রাস্ট্রেশন, চৌম্বকীয় কার্যকলাপ এবং টপোলজিক্যাল ইলেকট্রনিক অবস্থা, এই তিনটির অনন্য সংমিশ্রণে ডিরাক ও ওয়েইল ফার্মিয়ন, ফ্ল্যাট ব্যান্ড, কোয়ান্টাম স্পিন লিকুইড, স্কাইর্মিয়ন ল্যাটিস এবং অ্যানোমালাস ও টপোলজিক্যাল হল প্রভাব (AHE ও THE)-এর মতো এক্সোটিক কোয়ান্টাম ঘটনা সৃষ্টি করে। এই থিসিসের প্রাথমিক লক্ষ্য হল বিভিন্ন কাগোমে যৌগের উচ্চমানের একক ক্রিস্টাল প্রস্তুত করা এবং তাদের গাঠনিক, ইলেকট্রনিক, চৌম্বকীয় ও পরিবাহী ধর্মাবলম্বী বৈশিষ্ট্য পদ্ধতিগতভাবে বিশ্লেষণ করা।

আমরা, Mn-সমৃদ্ধ ও Ge-সমৃদ্ধ Mn_3Ge একক ক্রিস্টাল প্রস্তুত করেছি, যা একটি ননকোলিনিয়ার কাগোমে অ্যান্টিফেরোম্যাগনেট এবং ওয়েইল ফার্মিয়নের বাহক। Ge-সমৃদ্ধ $Mn_{2.94}Ge$ যৌগে Néel তাপমাত্রার নিচে একাধিক চৌম্বক রূপান্তর যেমন স্পিন রি-ওরিয়েন্টেশন এবং একটি নিম্ন তাপমাত্রার ফেরোম্যাগনেটিক সদৃশ দশা দেখা যায়। অ্যানোমালাস হল পরিবাহিতা স্পিন রি-ওরিয়েন্টেশন বিন্দুতে সর্বোচ্চ হয় এবং পরবর্তীতে হ্রাস পায়। একসাথে, এই অনুসন্ধানগুলি দেখায় যে Mn_3Ge এর চৌম্বকীয় এবং টপোলজিক্যাল বৈশিষ্ট্যগুলি এর রাসায়নিক গঠনের উপর কতটা নির্ভরশীল। পরবর্তী পর্যায়ে, $Mn_{(3+x)-\delta}Fe_\delta Ge$ ($\delta = 0, 0.30, 0.62$) যৌগগুলিতে Fe ডোপিং-এর প্রভাব বিশ্লেষণ করা হয়েছে। $\delta = 0.30$-এ ধাতব থেকে সেমিকন্ডাক্টিং রূপান্তর এবং $\delta = 0.62$ -এ প্রায় 100 K তে ধাতব-অন্তরক রূপান্তর পরিলক্ষিত হয়েছে। Fe প্রতিস্থাপন ইন-প্লেন ফেরোম্যাগনেটিজম বৃদ্ধি করে, ম্যাগনেটোক্রিস্টালাইন অ্যানিসোট্রপি বাড়ায়, স্পিন-গ্লাস সদৃশ দশা সৃষ্টি করে এবং AHE হ্রাস করে। লক্ষণীয়ভাবে, $\delta = 0.30$ -এ একটি টপোলজিক্যাল হল সিগন্যাল (THE) দেখা যায়, যা নন-কোপ্লানার স্পিন টেক্সচারের ফলে উদ্ভূত। এরপর, Fe_3Ge একক ক্রিস্টাল প্রস্তুত করা হয়েছে, যা একটি ফেরোম্যাগনেটিক কাগোমে ধাতু। এতে হল পরিবাহিতার শক্তিশালী অ্যানিসোট্রপি এবং অভ্যন্তরীণ AHE-এর একটি বিরল তাপমাত্রা-চালিত বিবর্তন লক্ষ্য করা যায়, যা চৌম্বকীয় অক্ষের আউট-অফ-প্লেন থেকে ইন-প্লেন রি-ওরিয়েন্টেশনের সাথে সম্পর্কিত। এই রূপান্তরের নিচে একটি সুস্পষ্ট ইন-প্লেন THE আবির্ভূত হয়। সবশেষে, বিরল-মুলধাতু ভিত্তিক কাগোমে ডিরাক সেমিমেটাল RFe_6Sn_6 (R = Ho, Dy) একক ক্রিস্টাল সফলভাবে প্রস্তুত করা হয়েছে, যা 3×10^3 % পর্যন্ত চরম মাত্রার ম্যাগনেটোরেজিস্ট্যান্স (XMR) প্রদর্শন করে। হল ইফেক্ট পরিমাপের মাধ্যমে প্রায় নিখুঁত ইলেকট্রন-হোল সাম্যাবস্থা ও উচ্চ চার্জ ক্যারিয়ার গতিশীলতা নিশ্চিত করা হয়, যা XMR-এর উৎস হিসেবে কাজ করে। তাপমাত্রা অনুযায়ী ADMR প্যাটার্নে উল্লেখযোগ্য পরিবর্তন ফার্মি সারফেস মড্যুলেশনের ইঙ্গিত বহন করে।

Contents

Chapter 1

Introduction

Topology is a mathematical concept, exploring the spatial features that remain intact under smooth physical transformations, such as twisting or flexing, without involving any breaks or separations [1]. In simpler terms, the topology classifies the objects based on their fundamental connectivity rather than on their precise geometric shape. Since both a sphere and a flat disc can be smoothly transformed from one to another and have no holes, they are regarded as topologically similar. In contrast, a torus and a coffee cup, each with a single hole, share a topological classification distinct from that of the sphere and flat disc. This classification is quantified using a topological invariant known as the genus number g, which counts the number of holes in a surface, here $g = 0$ for spheres and discs, $g = 1$ for tori and cups (see Fig. 1.1).

Topology in condensed matter physics offers a fundamental way to understand and predict the stable, quantized properties of quantum systems. Topological properties help classifying different phases of matter beyond conventional symmetries. In conventional systems, the normal state arises from symmetry-breaking mechanisms described by Landau's theory of phase transitions [2, 3]. In this framework, the free energy of the system is represented by an order parameter, and variations in this order parameter cause phase transitions. These transitions are associated with the spontaneous symmetry breaking, where the macroscopic state of the system changes with external conditions, such as temperature or pressure. In contrast, topological phases are characterized by global invariants of the band structure, such as the Chern number or the $\mathbb{Z}_2$ index. They are protected by robust edge or surface states. Topological phase transitions require a change in these topological invariants, making them stable against local perturbations, in contrast to conventional phases, which follow the Landau theory of phase transitions.

The discovery of the quantum Hall effect (QHE) in 1980 [4] marked a significant advancement in condensed matter physics, revealing the existence of topological phases of matter. In this effect, a two-dimensional electron gas subjected to a strong magnetic field exhibits quantized Hall conductance, which is remarkably robust against disorder. This quantization arises from the presence of chiral edge states, which are topologically

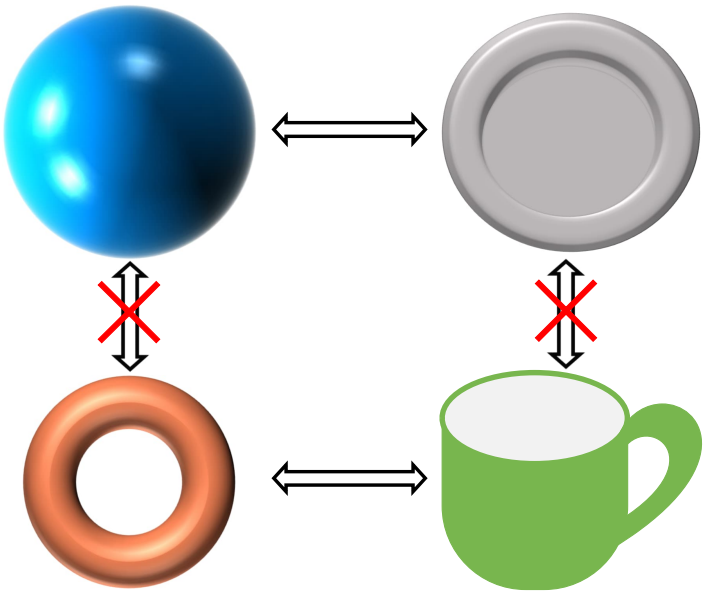

Figure 1.1: A sphere can be continuously deformed into a disc, demonstrating their topological equivalence. Similarly, a coffee cup can be deformed into a torus. However, a sphere or a disk cannot be transformed into a torus or a coffee cup, revealing a fundamental topological difference.

protected and do not rely on spontaneous symmetry breaking. Instead, these phases are characterized by topological invariants, reflecting the global properties of the electronic band structure. Building on the discovery of the QHE, the exploration of topological phases accelerated, unveiling a variety of novel quantum states of matter. Notable milestones include the identification of the two-dimensional topological insulator (2005) [5], the three-dimensional topological insulator (2007) [6, 7], the Dirac semimetal (2014) [8, 9], and the Weyl semimetal (2015) [10, 11], illustrating the wide range of phenomena within this domain. The emergence of these topological phases has reshaped our understanding of matter, leading to deeper explorations into phases that defy traditional symmetry-breaking mechanisms.

On the other hand, the kagome lattice, with its geometrically frustrated network of corner-sharing triangles, is a platform for hosting exotic topological phases of matter. Coupling frustration with magnetism leads to quantum spin liquids [12, 13], massive Dirac fermions [14], Weyl fermions [15, 16], and skyrmions [17], with potential implications in quantum technologies. Weyl fermions appear in kagome magnets like $Co_3Sn_2S_2$ [16], Mn_3Sn [15], Mn_3Ge [18], and Fe_3Sn_2 [19]. Quantum spin liquids emerge in frustrated systems such as $KCu_6AlBiO_4(SO_4)_5Cl$ [20] and $YCu_3(OH)_6Br_2[Br_x(OH)_{1-x}]$ [21]. Skyrmionic textures, observed in Fe_3Sn_2[17], $Gd_3Ru_4Al_{12}$[22], and Mn_4Ga_2Sn[23], highlight the deep connection between topology and magnetism.
A microscopic understanding of these novel topological quantum materials is crucial for

unlocking their potential applications in future quantum computing and spintronics technologies. Kagome lattice materials, with their unique magnetic structures and topological properties, are prime candidates for hosting exotic quantum phenomena. Exploring the intrinsic microscopic properties is crucial for assessing their potential applications in quantum technology. To unravel the macroscopic and microscopic intricacies of these exotic magnetic topological materials, their synthesis is a crucial first step. Therefore, the primary objective of my thesis is to synthesize high-quality single crystals of diverse topological quantum materials, specifically kagome compounds, and systematically explore their structural, electronic, magnetic, and magneto-transport properties.

Chapter 1 provides an overview of topological materials, beginning with the quantum Hall effect and its role in establishing topological phases. It introduces key theoretical concepts, including the Chern number and Berry curvature, and explores various topological systems, such as topological insulators, Weyl semimetals, and Dirac semimetals. The chapter discusses kagome lattice systems and their unique properties. It concludes with an overview of key physical phenomena, including magnetic behavior, anomalous and topological Hall effects, and magnetoresistance.

Chapter 2 presents the experimental methodologies employed in this work. It begins with a detailed account of single-crystal growth techniques, followed by the characterization methods used to assess structural and compositional quality, including X-ray diffraction (XRD), energy-dispersive X-ray spectroscopy (EDXS), scanning electron microscopy (SEM), and transmission electron microscopy (TEM). The chapter also provides an overview of the Quantum Design PPMS DynaCool system, detailing its operating principles and modules like the vibrating sample magnetometer (VSM), electrical transport option (ETO), and heat capacity option, used for measuring magnetic, electrical transport, Hall effect, magnetoresistance, and specific heat properties of the crystals.

Chapters 3 to 6 present the experimental findings on various kagome materials synthesized during my Ph.D. research. Chapter 3 examines $Mn_{2.94}Ge$, where multiple anomalous magnetic transitions occur at low temperatures. A significant change in the anomalous Hall effect behavior is observed near the spin reorientation transition, a feature absent in Mn-excess Mn_3Ge. Chapter 4 extends this study to $Mn_{(3+x)-\delta}Fe_\delta Ge$, exploring how Fe substitution at the Mn site affects the electronic, magnetic, and topological properties. Chapter 5 presents a comprehensive study on the directional dependence of magnetism and the Hall effect in single-crystalline Fe_3Ge. We observed a temperature-dependent intrinsic anomalous Hall effect in this material, an unusual behavior that is rarely reported. Chapter 6 focuses on the synthesis of RFe_6Sn_6 (R = Ho, Dy) single crystals and their magnetic, magnetoresistance, and Hall-effect properties. In addition, it explores the

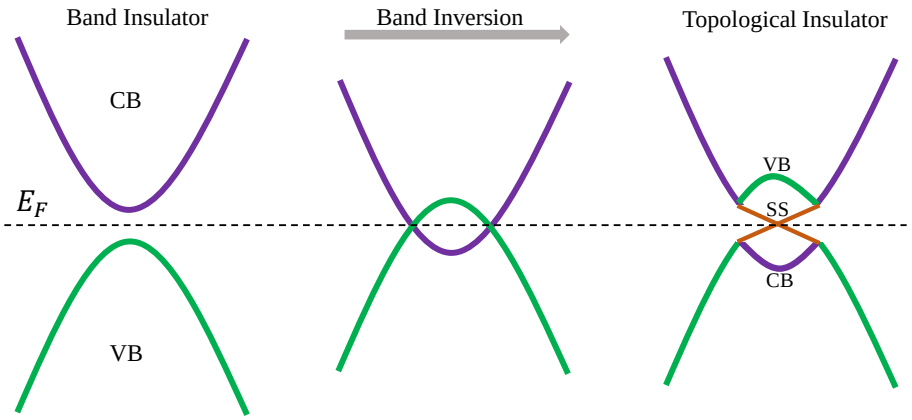

Figure 1.2: In a normal insulator, a distinct band gap separates the conduction and valence bands. However, conductive surface states appear within the insulating bulk gap in a topological insulator due to band inversion caused by strong spin-orbit coupling (SOC).

angle-dependent magnetoresistance behavior in these systems.

1.1 Topological Insulator

Insulators are characterized by their inability to conduct electricity due to a significant energy gap existing between their valence and conduction bands. Traditionally, distinctions between different insulating materials have been made based on quantitative factors, such as the band structure and the magnitude of the energy gap. Recent advancements have revealed that insulators can be categorized based on the topological properties of their band structures [1, 24–26]. In conventional insulators, the conduction and valence bands follow a typical band ordering. However, when strong spin-orbit coupling (SOC) is introduced, this band ordering gets inverted, giving rise to a distinct class of materials known as topological insulators (TIs) (see Fig. 1.2). The inversion of the bulk band structure in a topological insulator results in emergence of metallic surface states. Therefore, TIs are uniquely characterized by the presence of surface states that are gapless and energetically situated within the bulk energy gap. The surface states generally display Dirac cone-like dispersion, characterized by spin-momentum locking, where the electron's spin is oriented perpendicular to its momentum direction. Numerous materials have been revealed to be topological insulator [27, 28], including HgTe [29, 30], Bi_2Se_3, Bi_2Te_3, Sb_2Te_3 etc[31, 32].

1.1.1 Quantum Hall Effect

Condensed matter physics has turned its attention to topological materials since K.V. Klitzing discovered the quantum Hall effect (QHE) in 1980, a breakthrough recognized with the Nobel Prize in 1985. QHE is observed in two-dimensional electron systems at

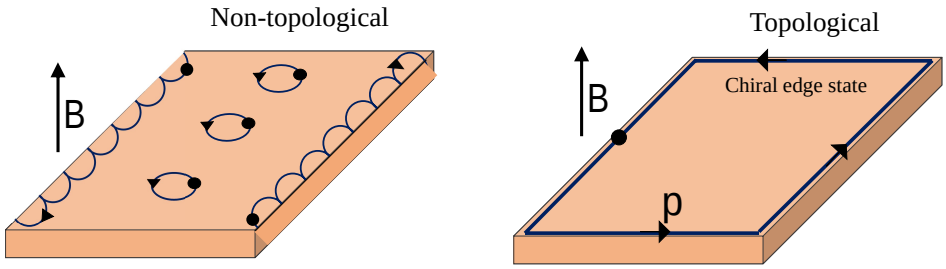

Figure 1.3: A two-dimensional electron system exposed to a magnetic field **B** applied perpendicular to its plane giving rise to chiral edge states, a hallmark of broken time-reversal symmetry. The schematic is reproduced from Ref. [33].

very low temperatures in the presence of perpendicular magnetic fields. QHE manifests as a stepwise quantization of the Hall resistance $R_{xy} = h/Ne^2$. This quantization arises from topologically protected edge states, laying the groundwork for the concept of topological phases of matter.

Figure 1.3 depicts a scenario where a two-dimensional electron system is exposed to an external magnetic field **B** oriented perpendicularly to its plane. In the classical framework, electrons follow curved paths due to the Lorentz force. These trajectories can be categorized into two types: closed orbits in the bulk region, away from the sample boundaries, and open orbits near the edges. The latter repeatedly interacts with the sample boundary, giving rise to skipping orbits. Under the influence of a magnetic field, these skipping trajectories establish the emergence of propagating edge states that travel along the sample boundary.

The quantization of periodic carrier motion in a strong magnetic field converts a skipping trajectory into quasi-one-dimensional edge channels that go along the edges of the sample [34, 35]. The momentum direction of the edge states **P** is intrinsically linked to the orientation of the magnetic field. This inherent directionality of the edge state provides protection against disorder, which is always present to some extent in real materials. Random electrostatic potential fluctuations, which typically result in elastic momentum scattering processes of the form $P \rightarrow -P$, are the main source of disorder at low temperatures. However, because there are no counter-propagating modes in chiral edge states, such backscattering is strictly inhibited. This unidirectional transport, a direct result of broken time-reversal symmetry, underlies the dissipationless conduction observed in the quantum Hall effect [36].

This precise quantization of R_{xy} was initially explained using quantum mechanical principles, specifically through the formation of Landau levels [37]. Landau levels arise from the motion of two-dimensional electron gas in the presence of an external magnetic field **B**. The dynamics of an electron with charge $-e$, mass m, and velocity $\dot{\mathbf{x}}$ can be described using the Lagrangian formalism. The corresponding Lagrangian expression for

such a system is given by:

$$L = \frac{1}{2}m\dot{\mathbf{x}}^2 - e\dot{\mathbf{x}}.\mathbf{A} \tag{1.1}$$

In this formulation, the electromagnetic vector potential is symbolized by $\mathbf{A}$, which is linked to the magnetic field by $\mathbf{B} = \nabla \times \mathbf{A}$. When a gauge transformation is applied to $\mathbf{A}$, it introduces an additional term, $\nabla\alpha$, where α is a scalar function. However, this transformation does not affect the equations of motion, ensuring that the Lagrangian remains invariant under gauge transformations.
Next, we calculate the Hamiltonian from the Lagrangian:

$$H = \dot{\mathbf{x}}.\mathbf{p} - L = \dot{\mathbf{x}}.\frac{\partial L}{\partial \dot{\mathbf{x}}} - L = \frac{1}{2m}\left(\mathbf{p} + e\mathbf{A}\right)^2 \tag{1.2}$$

In this context, $\mathbf{p}$ represents the canonical momentum. For a magnetic field pointing along the z-axis ($\mathbf{B} = B\hat{\mathbf{z}}$), a convenient form of the vector potential in the Landau gauge is $\mathbf{A} = Bx\hat{\mathbf{y}}$. With this choice of gauge, the Hamiltonian in Eqn. 1.2 can be rewritten as follows:

$$H = \frac{p_x^2}{2m} + \frac{1}{2m}\left(p_y + eBx\right)^2 \tag{1.3}$$

With the chosen Landau gauge, translational symmetry is preserved along the y-direction, making p_y and H commute. Consequently, the momentum operator p_y can be expressed as $\hbar k_y$:

$$H = \frac{p_x^2}{2m} + \frac{(\hbar k_y + eBx)^2}{2m} \tag{1.4}$$

The given Hamiltonian closely resembles that of a harmonic oscillator confined along the x-axis. By rewriting Eqn. 1.4 in a comparable form, we obtain:

$$H = \frac{p_x^2}{2m} + \frac{m\omega_c^2}{2}\left(x + k_y l_B^2\right)^2 \tag{1.5}$$

Here, $\omega_c = \frac{eB}{m}$ represents the cyclotron frequency, which defines the circular motion of electrons in the presence of a magnetic field $B\hat{\mathbf{z}}$ (see Fig. 1.3. The parameter $l_B = \sqrt{\frac{\hbar}{eB}}$ is known as the magnetic length. The Hamiltonian in Eqn. 1.5 resembles that of a harmonic oscillator but with a displacement of $k_y l_B^2$ along the x-axis. The corresponding energy eigenvalues are given by:

$$E_N = \hbar\omega_c\left(N + \frac{1}{2}\right) \tag{1.6}$$

Figure 1.3(b) illustrates the energy levels in relation to the density of states (DOS). In summary, the application of a magnetic field $B\hat{\mathbf{z}}$ to a free electron gas quantizes the electronic states into discrete, equally spaced energy levels known as Landau levels. The

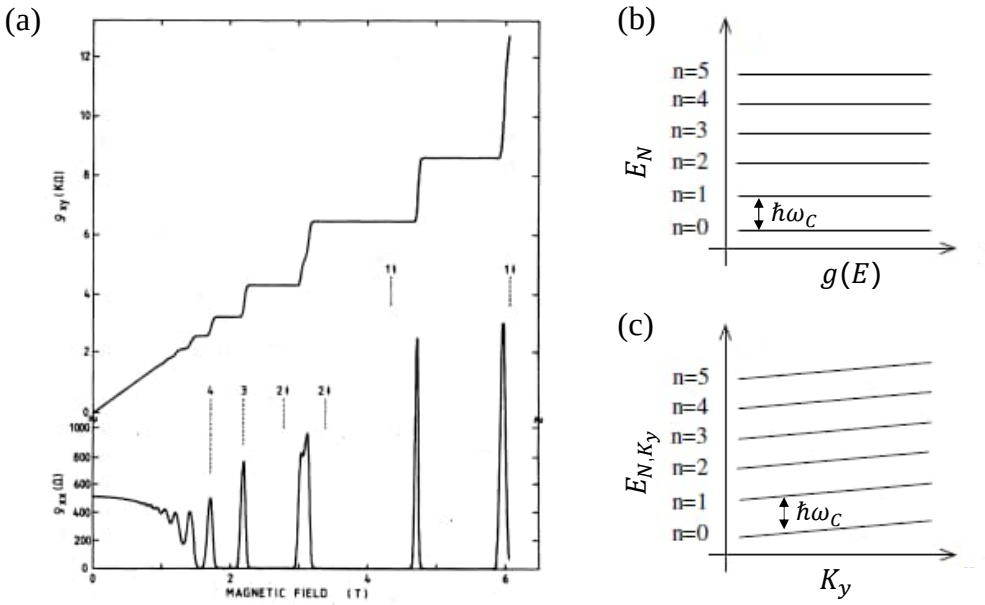

Figure 1.4: (a) Quantum Hall Effect (QHE) as first observed by K. V. Klitzing. The image is taken from Ref.[38]. (b) Landau level formation in the presence of a magnetic field. (c) Modification of Landau levels under combined magnetic and electric fields.

number of available quantum states in each Landau level is given by BA/Φ_0, where A represents the sample area, and $\Phi_0 = 2\pi\hbar/e$ is the magnetic flux quantum. For electrons, considering spin degeneracy ($S = 2$), the total number of occupied states in a single Landau level doubles to $2BA/\Phi_0$. When N Landau levels are completely filled, the Hall resistance in the QHE displays quantized plateaus at $R_{xy} = h/(Ne^2)$. It is important to note that Landau levels exhibit an energy gap of $\hbar\omega_c$ between occupied and unoccupied states, similar to an insulator. However, a finite Hall resistance is still observed in the QHE. The applied electric field $E\hat{\mathbf{x}}$ during Hall measurements is to be considered to address this seeming contradiction. Incorporating the electric potential $V = -Ex$, Eqn. 1.3 modifies accordingly:

$$H = \frac{p_x^2}{2m} + \frac{1}{2m}\left(p_y + eBx\right)^2 + eEx \tag{1.7}$$

and the corresponding energy eigenstates become

$$E_{N,k_y} = \hbar\omega_c\left(N + \frac{1}{2}\right) - eE\left(k_y l_B^2 + \frac{eE}{m\omega_c^2}\right) + \frac{mE^2}{2B^2} \tag{1.8}$$

In the presence of an applied electric field, the eigenstates become dependent on k_y. A graphical representation of Landau levels under this condition is shown in Fig. 1.4(b). The electron group velocity is given by $v_y = \frac{1}{\hbar}\frac{dE_{N,k_y}}{dk_y} = -E/B$, indicating that electrons undergo drift motion along the y-direction. Consequently, instead of exhibiting insulating behavior, the system displays quantized Hall resistance.

1.1.2 TKNN invariant

The quantized Hall conductance observed in 2D electron systems exhibiting the QHE is topologically characterized by the TKNN invariant. Chiral edge channels in the QHE carry current without dissipation and are immune to impurities. Their robustness and exact current quantization highlight a deep topological foundation. Furthermore, the observation of quantized Hall resistance in certain materials (quantum anomalous Hall insulators), even in the absence of an external magnetic field, cannot be fully accounted for by Landau level theory alone. This is where the groundbreaking work of D.J. Thouless, M. Kohmoto, M.P. Nightingale, and M. Den Nijs (TKNN) in 1982 [36] becomes crucial. The TKNN theory establishes that the Hall conductivity denoted as σ_{xy}, can be expressed through the integrated Berry curvature $[\Omega(\mathbf{k})]$ of the Bloch wave functions $[u_m(\mathbf{k})]$ across the entire Brillouin zone (BZ) of a two-dimensional crystal exhibiting the QHE:

$$\sigma_{xy} = \frac{Ne^2}{h} = \frac{e^2}{h}\frac{1}{2\pi}\oint_{BZ}\Omega(\mathbf{k})d^2\mathbf{k} \tag{1.9}$$

The integral expression $\frac{1}{2\pi}\oint_{BZ}\Omega(\mathbf{k})\,d^2\mathbf{k}$ defines a topological quantity known as the TKNN invariant. This invariant plays a central role in characterizing the topological nature of electronic bands. To better understand its significance, the following section will introduce the concept of Berry curvature $\Omega(\mathbf{k})$, which underlies this formulation.

1.1.3 Berry Curvature

Berry curvature is a fundamental quantity describing the geometric properties of Bloch electrons in crystals. It arises from the Berry phase, a geometric phase accumulated by a quantum state as the Hamiltonian adiabatically evolves along a closed loop in momentum space (the Brillouin zone). Consider an electron in a crystal, characterized by a Bloch state $|\psi_n(\mathbf{k})\rangle$, where $\mathbf{k}$ is the crystal momentum inside the Brillouin zone and n is the band index. When $\mathbf{k}$ adiabatically traces a closed loop C in momentum space and returns to its initial point, the electron's wavefunction accumulates not only a dynamical phase associated with its energy but also an additional geometric phase known as the Berry phase, denoted by $\gamma_n(C)$.

$$\gamma_n(C) = i\oint_C\langle\psi_n(\mathbf{k})|\nabla_{\mathbf{k}}\psi_n(\mathbf{k})\rangle\cdot d\mathbf{k} = \oint_C\mathbf{A}_n(\mathbf{k})\cdot d\mathbf{k} \tag{1.10}$$

Here, $\mathbf{A}_n(\mathbf{k}) = i\langle\psi_n(\mathbf{k})|\nabla_{\mathbf{k}}\psi_n(\mathbf{k})\rangle$ is the Berry connection (or Berry potential) for the n-th band. It acts as a vector potential in momentum space.
Similarly to how a magnetic field is defined as the curl of the vector potential in real space, the Berry curvature ($\mathbf{\Omega}_n(\mathbf{k})$) is defined as the curl of the Berry connection in momentum space:

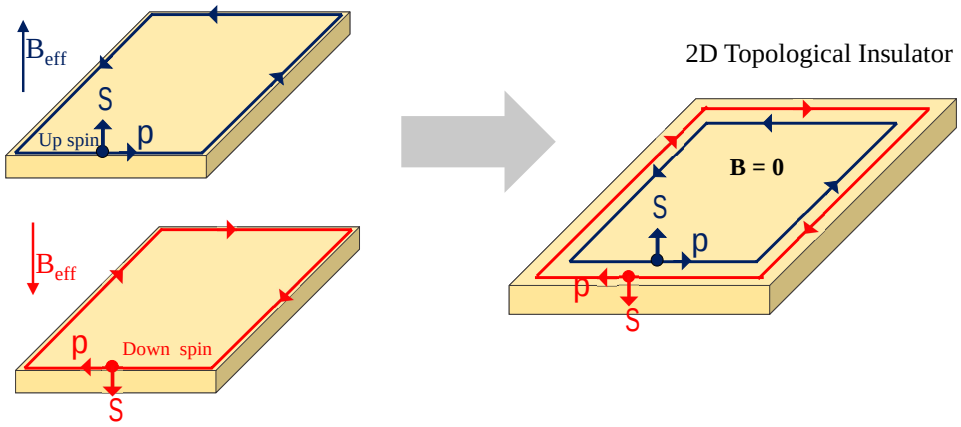

Figure 1.5: Diagrammatic representation of 2DTIs with helical edge states. The schematic is reproduced from Ref. [33].

$$\mathbf{\Omega}_n(\mathbf{k}) = \nabla_{\mathbf{k}} \times \mathbf{A}_n(\mathbf{k}) \tag{1.11}$$

In three dimensions, the Berry curvature is a vector field in momentum space. In Cartesian coordinates, its components are given by:

$$(\mathbf{\Omega}_n(\mathbf{k}))_i = \epsilon_{ijk} \frac{\partial}{\partial k_j} (\mathbf{A}_n(\mathbf{k}))_k \tag{1.12}$$

where ϵ_{ijk} is the Levi-Civita symbol.

Unlike the Berry connection, which depends on the choice of the phase of the wavefunction (it is gauge-dependent), the Berry curvature is gauge-invariant. This makes it a physically meaningful local quantity that characterizes the geometric properties of the Bloch bands in momentum space.

In condensed matter physics, two primary types of Berry phases are considered: one defined in momentum space ($\mathbf{k}$-space) and the other in real space ($\mathbf{r}$-space). Analogous to classical electromagnetism, Berry curvature acts like an effective magnetic field, while the Berry phase corresponds to the associated magnetic flux. In momentum space, Berry phases typically arise from nontrivial band topology in the electronic structure, whereas in real space, they are generally linked to complex magnetic textures. A key property of Berry phases in the Brillouin zone (BZ) is their quantization: the integral of the Berry curvature over a closed surface in the BZ yields an integer multiple of 2π,

$$\int_{\mathcal{BZ}} \Omega(\mathbf{k})\, d^2\mathbf{k} = 2\pi C, \tag{1.13}$$

where C is the Chern number, a topological invariant that plays a crucial role in distinguishing topological phases of matter.

1.1.4 Two-Dimensional Topological Insulator

In addition, the physics of the recently found two-dimensional topological insulators (2DTIs), also known as the quantum spin Hall (QSH) state, relies on the resilient edge states [5, 39, 29, 40]. Unlike the QHE, which requires an external magnetic field and breaks time-reversal symmetry, 2DTIs have edge states that are topologically protected even when no magnetic field is applied. In 2DTIs, strong intrinsic spin–orbit coupling acts as an effective magnetic field that points in opposite directions for spin-up and spin-down electrons (see Fig.1.5). This results in two time-reversed copies of quantum Hall states, each supporting a gapless edge mode. Consequently, 2DTIs host helical edge states, characterized by spin-momentum locking, where electrons with opposite spins propagate in opposite directions. Unlike the chiral edge states of quantum Hall systems, which emerge in TRS-broken conditions, these helical edge states are shielded by TRS. Helical edge states in 2DTIs appear as pairs of time-reversed states, known as Kramers doublets. These edge states exhibit linear energy-momentum dispersion that crosses within the bulk band gap, as illustrated in Fig. 1.6, reflecting their topologically protected nature. The 2DTI state was first identified in a semiconductor quantum well structure, where a layer of HgTe was embedded between two CdTe layers [29].

1.1.5 $\mathbb{Z}_2$ Invarient

In the quantum spin Hall (QSH) state, the total electric charge flow along the conducting edge channels cancels out. Consequently, this integer TKKN invariant is insufficient to define the QSH phase since it leads to a zero Chern number (C=0). The $\mathbb{Z}_2$ topological invariant enters the picture at this point and provides the fundamental tool for describing this topologically distinct state. Time-reversal symmetry ($\mathcal{T}$) plays a key role in defining the $\mathbb{Z}_2$ invariant. This symmetry imposes a constraint on the Hamiltonian, expressed as $\mathcal{T}H(k)\mathcal{T}^{-1} = H(-k)$, where k is the crystal momentum. In fermionic systems with spin-1/2, the nature of time-reversal symmetry, where $\mathcal{T}^2 = -\mathbf{1}$ (Kramers theorem), results in Kramers degeneracy. Consequently, all energy levels become at least two-fold degenerate at the time-reversal invariant momenta (TRIM) in the Brillouin zone. The topological invariant $\mathbb{Z}_2$ serves to differentiate between two types of time-reversal symmetric insulators. When $\mathbb{Z}_2 = 0$ (a trivial insulator), the material can be smoothly transformed into a standard band insulator without closing its bulk energy gap, and it lacks topologically protected surface states. In contrast, when $\mathbb{Z}_2 = 1$ (a topological insulator), the material hosts topologically protected surface states [39].

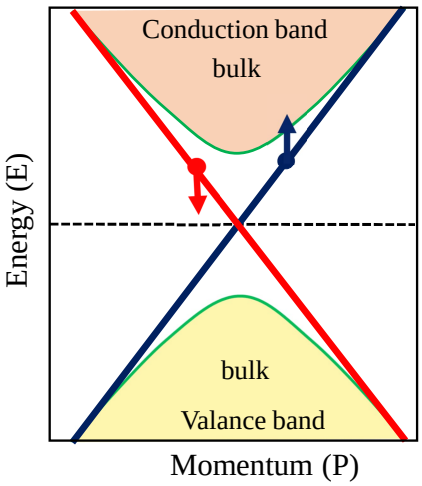

Figure 1.6: A schematic representation of the band structure of a two-dimensional topological insulator (2DTI), where helical edge states emerge within the bulk gap, connecting the conduction and valence bands. The schematic is reproduced from Ref. [33].

1.1.6 Three-Dimensional Topological Insulator

In a two-dimensional topological insulator (2DTI), the bulk remains insulating, while one-dimensional helical edge states form at the boundaries. In contrast, a three-dimensional (3D) topological insulator features an insulating bulk but supports two-dimensional conducting surface states. These surface states host massless Dirac fermions, exhibiting spin-momentum locking where the electron spin is locked perpendicular to its momentum. The surface Dirac cones are protected against gapping as long as TRS is preserved. Although 2D TIs feature robust helical edge states, their realization typically requires precisely engineered quantum wells and clean samples at low temperatures. In contrast, 3D TIs present naturally occurring materials with intrinsic topological properties, enabling observation under more practical conditions, even at room temperature.

The classification of three-dimensional topological insulators (3D TIs) is determined by four $\mathbb{Z}_2$ topological invariants: ν_0, ν_1, ν_2, and ν_3 [6, 31, 1]. Among the four $\mathbb{Z}_2$ invariants, ν_0 distinguishes between strong ($\nu_0 = 1$) and weak ($\nu_0 = 0$) topological insulators. The remaining invariants (ν_1, ν_2, ν_3) specify the Miller indices of the reciprocal lattice planes where topologically protected $\mathbf{k}$-points arise. In strong TIs, surface states are protected by time-reversal symmetry and encircle an odd number of time-reversal invariant momenta (TRIM) in the Brillouin zone. When $\nu_0 = 0$, the system behaves as a weak topological insulator, where nontrivial topology appears along certain crystallographic directions. Such materials can be viewed as stacks of two-dimensional quantum spin Hall (QSH) layers, with their chiral edge states combining to form surface states along the stacking axis. However, unlike strong TIs, where surface states are protected by time-reversal symmetry against disorder, the surface states in weak TIs are more fragile and can be

easily disrupted by defects or weak interlayer interactions.
Experimentally, several 3DTIs have been identified, including $Bi_{1-x}Sb_x$ [41], Bi_2Se_3 [42, 32], Bi_2Te_3 [42], and Sb_2Te_3 [31]. These materials exhibit robust topological surface states protected by time-reversal symmetry.

1.2 Topological Semimetals

The valence and conduction bands in semimetals do not overlap like in ordinary metals; rather, they intersect at particular points (nodes) or lines close to the Fermi level [43]. A semi-metal becomes classified as a topological semimetal when its band crossings point to be robust and protected by the intrinsic topological characteristics of the material. These topological semimetals are characterized by linearly dispersive electronic bands located at several high-symmetry points within the Brillouin zone (BZ). The stability of these band-crossing points (BCPs) is guaranteed by the presence of fundamental symmetries, such as time-reversal symmetry (TRS) and/or inversion symmetry (IS). Based on the specific symmetry mechanism that safeguards these BCPs, topological semimetals are classified primarily as Dirac semimetals[9, 44, 45] or Weyl semimetals [46, 11, 47].

1.2.1 Dirac Semimetal

Paul Dirac presented a groundbreaking equation in 1928 that brought together Einstein's special theory of relativity with single-particle quantum mechanics to create the first relativistic framework for explaining spin-1/2 particles, such as electrons [48, 49]. The covariant formulation of the Dirac equation, which governs the dynamics of relativistic fermions, is given by:

$$(i\hbar\gamma^{\mu}\partial_{\mu} - mc)\psi = 0 \tag{1.14}$$

In this expression, $\mu = 0, 1, 2, 3....$ represents dimensionality of the space, c denotes the speed of light, m is the rest mass of the particle, and γ^{μ} are the Dirac gamma matrices. Dirac originally formulated his equation to describe free fermions in vacuum under high-energy conditions, where the particle's energy and momentum are related by Einstein's relation $E^2 = (pc)^2 + (m_0c^2)^2$. However, in condensed matter systems, electrons experience various interactions within the material and are not isolated. Instead, their collective excitations behave like emergent particles known as quasiparticles. When these quasiparticles obey the Dirac equation with a non-zero mass term ($m \neq 0$), they are referred to as Dirac fermions. Materials in which such Dirac fermions appear are known as Dirac semimetals. The electronic band structure of a Dirac semimetal is characterized by the presence of four-fold degenerate points in the momentum space, which are termed Dirac points. This fourfold degeneracy arises from the crossing of two doubly degenerate

bands (due to spin degeneracy), protected by the combined action of time-reversal and inversion symmetries.

The first experimental observation of Dirac fermions occurred in graphene [50], a two-dimensional Dirac semimetal where electrons behave as massless relativistic particles. Extending this concept to three dimensions is more complex. In three-dimensional systems, spin–orbit coupling (SOC) generally introduces a mass term m, leading to the opening of an energy gap at the Dirac point. Consequently, additional crystalline symmetries, such as rotational symmetry or specific space group symmetries, are essential to stabilize gapless Dirac nodes [51, 52].
Several materials, including Cd_3As_2 [45, 9], $ZrTe_5$, $Bi_{1-x}Sb_x$ [53], Na_3Bi [44, 54], $HoMn_6Sn_6$ [55], and TiBiSSe [56] have been experimentally confirmed to exhibit Dirac semimetal behavior. Dirac semimetals demonstrate extraordinary transport phenomena, including the chiral magnetic effect [53, 46, 57], exceptionally high charge carrier mobility [58, 59], and large nonsaturating magnetoresistance [58, 59], making them promising platforms for investigating topological quantum states.

1.2.2 Weyl semimetal

Shortly after Dirac formulated his relativistic wave equation, Hermann Weyl in 1929 derived an alternative equation that describes massless fermions [60, 61]. This equation takes the form:

$$i\hbar\partial_t\psi_\pm = \pm c\,\mathbf{p}\cdot\sigma\,\psi_\pm \tag{1.15}$$

where $\psi_\pm$ denotes the wave function associated with particles of positive or negative chirality, and the corresponding Hamiltonian is $\mathcal{H}_\pm = \pm c\,\mathbf{p}\cdot\sigma$, with σ representing the Pauli matrices. Weyl fermions, which were previously believed to exist only in high-energy physics, are now found in condensed matter systems, emerging as low-energy quasiparticles in a class of materials known as Weyl semimetals. In Weyl semimetals, the conduction and valence bands exhibit a linear crossing at isolated points within the Brillouin zone, termed Weyl nodes. These special points, which give the material its unique topological features, always come in pairs with opposing chirality. The energy of these Weyl points follows the relationship $E = \pm pc$, and they are located at distinct positions in momentum space, separated by a specific momentum vector $\mathbf{k}$. When these oppositely charged Weyl nodes converge at the same $\mathbf{k}$-point, their topological charges annihilate and give rise to a Dirac node, resulting in massless Dirac fermions. Conversely, the splitting of a Dirac point due to symmetry breaking leads to the emergence of a pair of Weyl nodes.

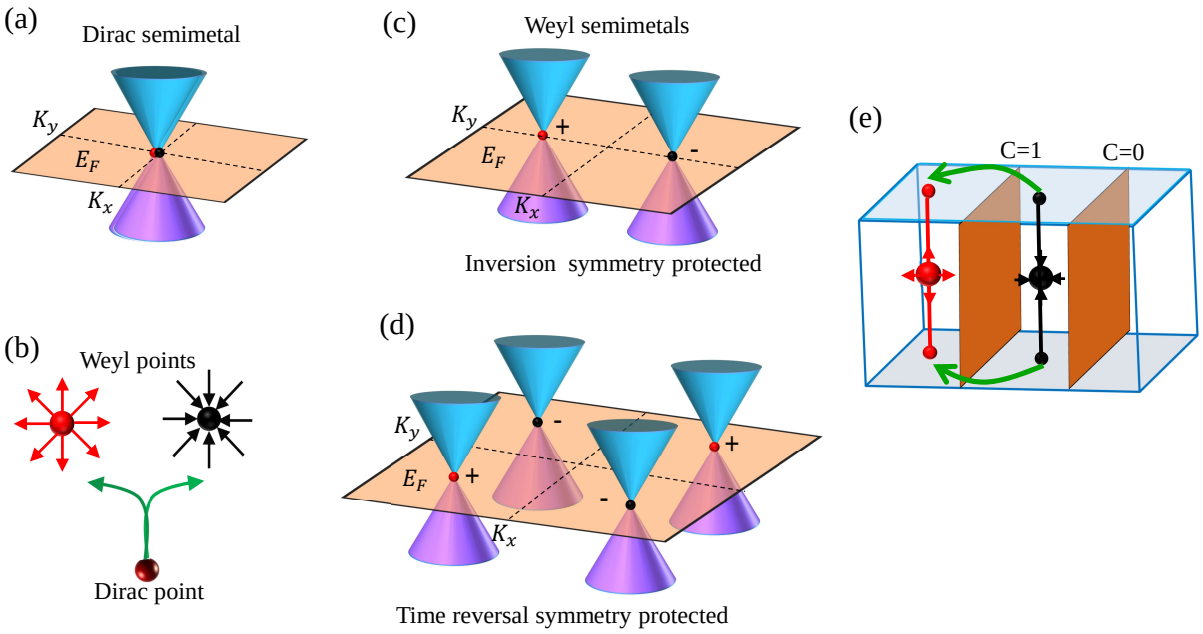

Figure 1.7: (a) Linear band dispersion near the Dirac point in a Dirac semimetal (DSM), stabilized by the coexistence of time-reversal symmetry (TRS) and inversion symmetry (IS). (b) A Dirac point can split into minimum two oppositely chiral Weyl points. (c) Band dispersion of a Weyl semimetal (WSM) where IS is preserved and TRS is broken, resulting in the emergence of a minimum of two Weyl nodes at the same energy. (d) Band dispersion of a WSM protected by TRS with broken IS, leading to a minimal 4 Weyl nodes. (e) Diagrammatic representation of a WSM in 3-D momentum space. The red and black points represent Weyl nodes of opposite chirality. Their surface projections are linked by topologically protected Fermi arcs, shown as green arrows. The finite Berry flux enclosed between the Weyl nodes results in a non-zero Chern number $C = 1$ for intermediate momentum planes, while planes outside this region exhibit $C = 0$. The figures are reproduced from Ref. [62].

Figure 1.7(a) schematically depicts a Dirac cone arising from the linear crossing of conduction and valence bands at a Dirac point, stabilized by the concurrent presence of inversion symmetry (IS) and time-reversal symmetry (TRS). Breaking either IS or TRS lifts the four-fold degeneracy at the Dirac point, leading to the emergence of multiple Weyl points. Specifically, breaking TRS while preserving IS results in the formation of at least two Weyl points with opposite chirality, which remain at the same energy due to the protection afforded by inversion symmetry [Fig. 1.7(c)]. In contrast, breaking inversion symmetry (IS) while preserving time-reversal symmetry (TRS) leads to the formation of a minimum of four Weyl points [Fig. 1.7(d)]. Under preserved TRS, Weyl nodes at momenta $\mathbf{k}$ and $-\mathbf{k}$ must carry the same chirality. To satisfy the requirement of zero net topological charge across the Brillouin zone, additional Weyl nodes with opposite chirality must emerge at different momenta. As a result, TRS-protected Weyl semimetals necessarily host at least four Weyl points.

Materials such as the TaAs [47] and $MoTe_2$ [63] families exhibit Weyl semimetallic phases

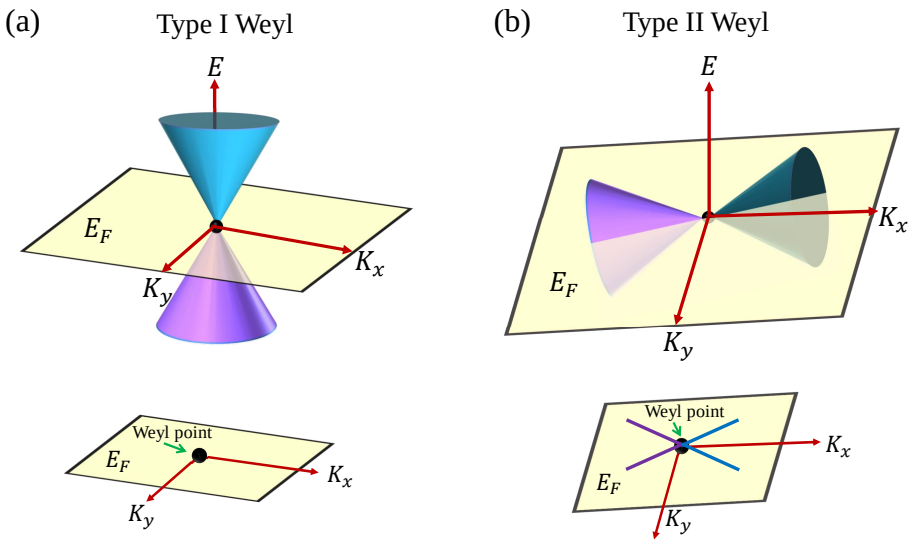

Figure 1.8: Schematic representations of (a) type-I and (b) type-II Weyl semimetals, showing constant energy contours intersecting the Weyl nodes. The diagrams are reproduced from Ref. [62].

(WSM) that arise through broken inversion symmetry (IS). TRS-breaking Weyl semimetals are of considerable interest due to their ability to exhibit a significant anomalous Hall effect (AHE), arising from the nonzero Berry curvature. TRS broken Weyl fermions appear in kagome magnets like $Co_3Sn_2S_2$ [16], Mn_3X (X = Sn, Ge, Ga) series [15, 64–66], and Fe_3Sn_2 [19].

Weyl fermions are uniquely characterized by their behavior as effective magnetic monopoles in momentum space. This phenomenon arises from the Berry curvature, a fundamental geometric property of the electronic band structure that acts like a magnetic field in **k**-space. At a Weyl node, the Berry curvature either diverges outward (acting as a source) or converges inward (acting as a sink), depending on the node's chirality. The topological charge associated with each Weyl point, its chirality, can be calculated by integrating the Berry curvature over a closed surface surrounding the node. This concept is schematically illustrated in Fig.1.7(e).

A further characteristic of Weyl semimetals is the appearance of Fermi arcs, which are unusual surface states that link the oppositely chiral projections of Weyl nodes on the material's boundary. These arcs are a direct consequence of the topological nature of the bulk Weyl nodes and are guaranteed to exist by their monopole character. Interestingly, Fermi arcs from opposite surfaces are topologically connected through the bulk, forming a unique fingerprint of Weyl physics in these materials [52], as seen in Fig.1.7(e).

The topological Fermi arcs were first realized in WSM TaAs by ARPES measurements [47]. Subsequently, $MoTe_2$ [67] and other transition metal dichalcogenides [68, 69] were also found to exhibit topological Fermi arcs and WSM phase.

Weyl semimetals are broadly classified into two types based on the geometry of their energy dispersion near the Weyl nodes. Type I Weyl semimetals feature upright, conical band crossings resulting in point-like Fermi surfaces. In contrast, Type-II Weyl semimetals exhibit strongly tilted Weyl cones in energy–momentum space, leading to an overlap of electron and hole pockets near the Weyl points. In both cases, the Weyl point itself appears at the touching point of conduction and valence bands, as illustrated in Fig.1.8(a) and (b).

1.3 Kagome Lattice Systems

The kagome lattice is a two-dimensional periodic structure characterized by a network of corner-sharing triangles, forming a pattern that resembles traditional Japanese woven baskets, where the name kagome originates (kago meaning basket and me referring to eye or mesh). Due to its unique geometry, the kagome lattice inherently exhibits geometrical frustration. This makes it a prime candidate for studying exotic magnetic ground states like quantum spin liquids. This distinctive lattice structure supports a range of intriguing phenomena, including flat bands, Dirac points, and non-trivial band topology, making it a promising platform for exploring correlated electronic phases and topological effects. Moreover, the kagome lattice's distinctive electronic, magnetic, and geometric structure enables it to host a range of exotic physical phenomena. This makes the kagome lattice an ideal platform for investigating topological quantum materials, particularly in the context of their electronic and magnetic properties.

1.3.1 Geometrical Frustration

In a triangular lattice with antiferromagnetic (AFM) exchange interactions, spins prefer to align antiparallel to their neighbors. However, due to the triangular geometry, it is impossible for all three spins in a triangle to simultaneously satisfy this condition. If two spins are antiparallel, the third cannot be antiparallel to both. This inherent conflict leads to geometrical frustration, resulting in six degenerate spin configurations that prevent long-range ordering (see Fig. 1.9). The ground state becomes a quantum superposition of these configurations, resulting in long-range spin entanglement. This entangled state can support fractionalized spin excitations, characteristic of a quantum spin liquid (QSL) phase [12, 70, 13]. Kagome lattices, composed of corner-sharing triangles forming a hexagonal network, naturally host such geometric frustration and are prime candidates for realizing QSLs. Notable examples include $KCu_6AlBiO_4(SO_4)_5Cl$ [20] and $YCu_3(OH)_6Br_2[Br_x(OH)_{1-x}]$ [21].

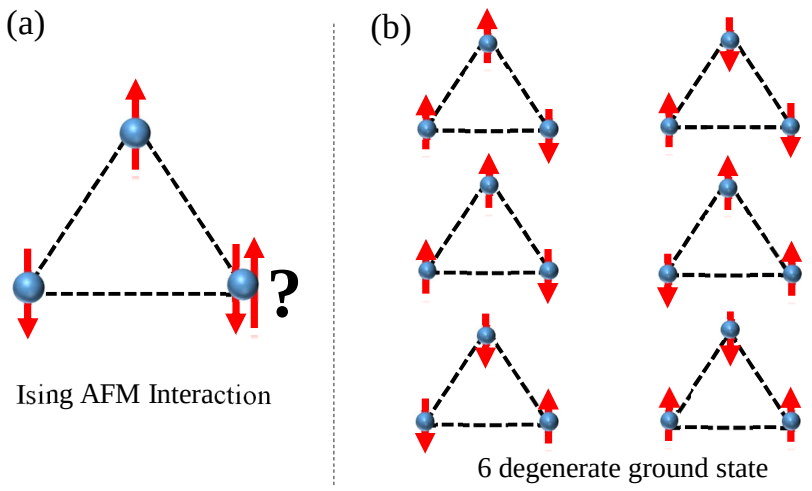

Figure 1.9: (a) Geometric frustration within a triangular Ising antiferromagnet. (b) Possibility of diverse ground state configurations.

1.3.2 Electronic Properties

The tight-binding model for electrons on a kagome lattice is represented by the Hamiltonian,

$$\mathcal{H} = -t \sum_{\langle ij \rangle, \sigma} (c^{\dagger}_{i,\sigma} c_{j,\sigma} + \text{h.c.}), \tag{1.16}$$

where t is the nearest-neighbor hopping amplitude and h.c. refers to the Hermitian conjugate. Here, $c^{\dagger}_{i,\sigma}$ and $c_{i,\sigma}$ are the creation and annihilation operators for electrons with spin σ at site i. This model produces an electronic band structure characteristic of the kagome lattice, as shown in Fig. 1.10(c), comprising Dirac points, van Hove singularities, and a flat band arising from the destructive interference inherent to the lattice geometry [71, 72].

At the energy level $E_3 = 2t$, the kagome lattice exhibits an ideal flat band that extends uniformly throughout the Brillouin zone [Fig. 1.10(f)]. This unusual band originates from localized eigenstates whose wavefunctions are confined due to the kagome geometry. Specifically, the lattice arrangement leads to precise destructive interference of electronic hopping amplitudes, effectively quenching the kinetic motion. This cancellation mechanism, illustrated in Fig. 1.10(b), is responsible for the emergence of the non-dispersive, flat electronic band. Also Dirac cones would emerge at the corners of the hexagonal BZ [Fig.1.10(d)]. In addition two van Hove singularities also appear at the boundary of the BZ [Fig.1.10(e)].

A wide range of Kagome-lattice-based materials have been intensively investigated in recent years, revealing diverse and intriguing physical properties [73–77]. One notable example is $Co_3Sn_2S_2$, which is a kagome ferromagnet where Co atoms form a Kagome net-

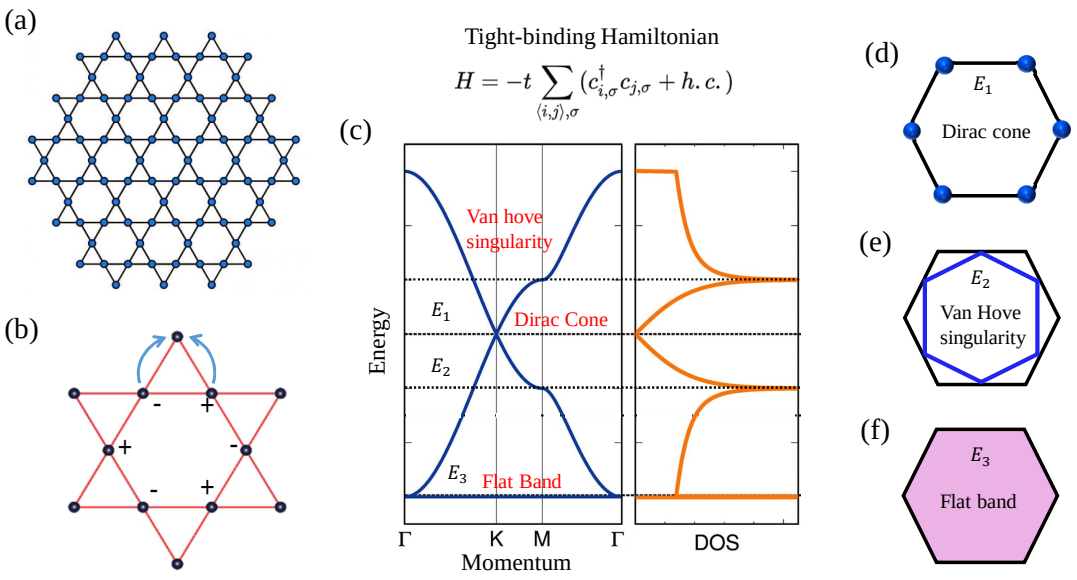

Figure 1.10: (a) 2D kagome network. (b) Kagome lattice electron confinement with nearest-neighbor hopping exhibits flat band eigenstates with alternating phase (±) on adjacent sublattices. (c) Tight-binding Hamiltonian and electron band structure. The presence of (d) Dirac cones, (e) van Hove singularities, and a (f) flat band within the hexagonal Brillouin zone. The figures are reproduced from Ref. [71]

work. This compound exhibits a pronounced intrinsic anomalous Hall effect, attributed to momentum-space Berry curvature arising from broken time-reversal symmetry [16]. Furthermore, it hosts Weyl fermions that contribute to a chiral anomaly in electronic transport [73, 16]. Another important class of materials, Mn_3X (X = Sn, Ge), is non-collinear antiferromagnets that challenged the traditional understanding of anomalous Hall effect phenomena, previously believed to occur only in ferromagnets. Nakatsuji et al. [74] reported anomalous Hall conductivity in Mn_3Sn, marking a paradigm shift. In Mn_3X systems, the anomalous Hall effect (AHE) originates from the non-zero Berry curvature in momentum space, which is a consequence of the specific non-collinear magnetic order locally breaking time-reversal symmetry ($\mathcal{T}$) in the presence of type-II Weyl nodes in the electronic band structure [18, 78, 15, 79].

Other Kagome metals such as FeSn and CoSn have attracted attention due to the emergence of flat bands near the Fermi level, which may lead to correlated electronic states [75, 80, 81]. Additionally, the AV_3Sb_5 (A = alkali metals) family has drawn considerable interest for hosting superconductivity alongside charge density wave (CDW) ordering [76, 82]. These features make them potential candidates for realizing topological superconductivity and hosting exotic quasiparticles like Majorana fermions [83]. Recently, rare-earth-based Kagome compounds such as RMn_6Sn_6 [77] have emerged as a clean platform for studying Mn-based Kagome networks. Notably, $TbMn_6Sn_6$ has been reported to exhibit characteristics of a quantum-limit Chern magnet [84], highlighting the richness of magnetic topological phases in kagome materials. Near room temperature, the anti-

ferromagnetic YMn_6Sn_6 exhibits a huge topological Hall effect [85]. Compounds such as $HoMn_6Sn_6$ [55] and $LiMn_6Sn_6$ [86] exhibit a pronounced anomalous Hall effect along with unconventional magnetic behavior and host Dirac points at the high-symmetry K point.

1.4 Magnetism

Magnetism, a cornerstone of physics, emerges from the intrinsic motion of electric charges at the atomic level. Specifically, the intrinsic spin and the orbital motion of electrons are the primary quantum mechanical origins of magnetic moments. Each electron behaves as a microscopic magnet, possessing its own magnetic dipole moment. The collective alignment and interaction of these individual electronic magnetic moments across all the atoms within a material dictate the material's macroscopic magnetic properties.

1.4.1 Spin Magnetic moment

Electrons inherently carry a fundamental type of angular momentum called spin (S). This spin is characterized by a fixed quantum number $s = \frac{1}{2}$, indicating that electrons exist in two possible spin states, commonly called spin-up and spin-down, Fig.1.11. Electron spin is essential for producing magnetic moments and is the basis for many quantum and magnetic events in condensed matter systems. The magnitude of the spin angular moment is $|S| = \hbar\sqrt{s(s+1)}$.
The corresponding spin magnetic moment is

$$\vec{\mu_S} = -g_s \frac{e}{2m_e}\vec{S} \tag{1.17}$$

Here, $g_s \approx 2$ denotes the Landé g-factor for the electron, while e and m_e represent the electron's charge and mass, respectively.

1.4.2 Orbital Magnetic Moment

Electrons orbiting the nucleus possess orbital angular momentum L, arising from their quantized motion in atomic orbitals. In quantum mechanics, this angular momentum is described by the quantum number l, where $|L| = \hbar\sqrt{l(l+1)}$. The motion of the charge particle creates a magnetic moment μ_L, given by

$$\vec{\mu_L} = -\frac{e}{2m_e}\vec{L} \tag{1.18}$$

The orbital magnetic moment μ_L and the orbital angular momentum L of an electron are opposite in direction because of the negative charge of the electron.

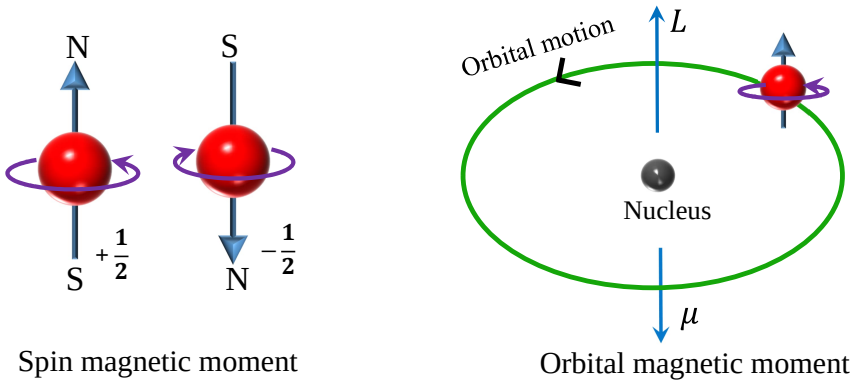

Figure 1.11: Spin and orbital magnetic moment of electron

1.4.3 Total Magnetic Moment

An electron's total angular momentum is the vector sum of its spin and orbital components: $\vec{J} = \vec{L} + \vec{S}$. This leads to total magnetic moment $\vec{\mu_J} = \vec{\mu_L} + \vec{\mu_S}$. The corresponding total magnetic moment can be written as,

$$\vec{\mu_J} = -g_J \frac{e}{2m_e} \vec{J}. \tag{1.19}$$

The Landé g-factor, g_J is determined by the following formula:

$$g_J = 1 + \frac{J(J+1) + S(S+1) - L(L+1)}{2J(J+1)} \tag{1.20}$$

1.4.4 Magnetic Ordering

Magnetic ordering in a material arises from a complex combination of factors, including its crystal structure, the electronic configuration of its constituent atoms, and the nature of interactions between magnetic moments (e.g., exchange interactions). These elements collectively determine how atomic or ionic magnetic moments arrange themselves within a solid, giving rise to various types of magnetic order. The main categories include

Ferromagnetism: Ferromagnetic materials are characterized by the parallel alignment of neighboring atomic magnetic moments, leading to spontaneous net magnetization even without an external magnetic field. A key feature of ferromagnets is hysteresis, where the magnetization depends on the material's prior exposure to magnetic fields. However, above the Curie temperature (T_C), thermal agitation overcomes the exchange interactions, and the material transitions to a paramagnetic state, losing its spontaneous magnetization.

Antiferromagnetism: Antiferromagnetic materials exhibit a magnetic ordering in which adjacent atomic magnetic moments align antiparallel, resulting in a complete cancellation

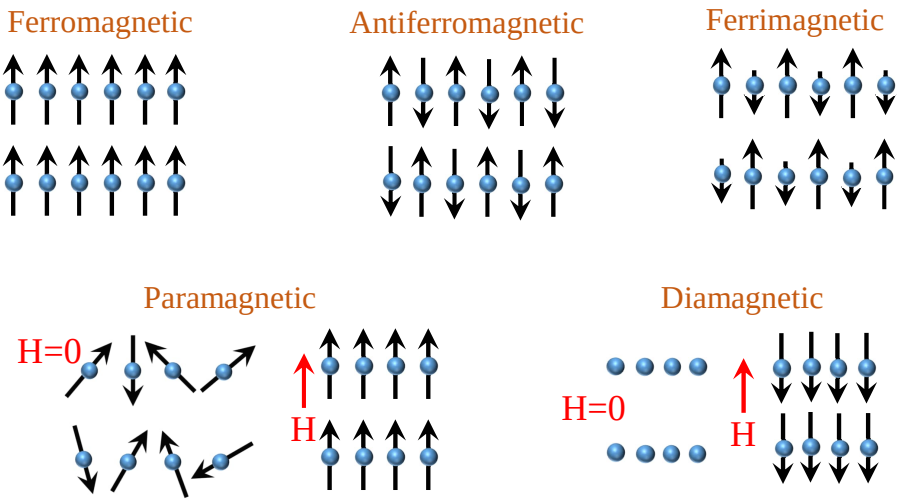

Figure 1.12: Spin configuration of various types of magnetic ordering.

of the net magnetization. This ordered state is stable below a characteristic temperature known as the Néel temperature (T_N).

Ferrimagnetism: Ferrimagnetism is a magnetic ordering phenomenon characterized by antiparallel alignment of magnetic moments on distinct sublattices within a material, similar to antiferromagnetism. However, unlike in antiferromagnets, the opposing magnetic moments in ferrimagnets are unequal in magnitude, resulting in a net spontaneous magnetization. Although this net moment is typically smaller than that observed in ferromagnets, ferrimagnetic materials still exhibit key ferromagnetic properties such as hysteresis.

Paramagnetism: Paramagnetic materials possess randomly oriented atomic magnetic moments in the absence of an external magnetic field, resulting in zero net magnetization. Upon application of an external magnetic field, these moments partially align with the field, producing a weak induced magnetization that disappears once the field is removed.

Diamagnetism: Diamagnetism is a universal but weak magnetic response observed in all materials, arising from induced changes in the orbital motion of electrons when subjected to an external magnetic field. This effect generates a magnetization opposite to the applied field, resulting in a small, negative magnetic moment that is largely temperature-independent.

Complex Magnetic Ordering: In addition to conventional magnetic orders, materials can exhibit more intricate magnetic behaviors. Helimagnetism involves a spiral arrangement of magnetic moments across layers, while canted antiferromagnetism features slightly misaligned antiparallel spins, yielding a weak net magnetization. Spin glasses are characterized by randomly frozen magnetic moments due to competing interactions, resulting in a disordered magnetic state below a specific freezing temperature. Superparamagnetism occurs in nanoscale ferromagnetic or ferrimagnetic particles, where

thermal fluctuations can randomly reorient the magnetization, eliminating remanence despite strong individual moments.

1.5 Hall Effect

The Hall effect, a fundamental phenomenon in solid-state physics, results from the action of the Lorentz force on charge carriers moving through a conductor under a perpendicular magnetic field. It has found widespread utility in a variety of technological applications, from precise magnetic field sensing for the characterization of materials' electronic properties. Typically, in the standard Hall effect, the Hall resistivity exhibits a direct proportional relationship with the strength of the applied magnetic field. The rate at which this resistivity changes with the field is uniquely determined by the concentration of charge carriers within the material. However, in certain magnetic materials, the Hall resistivity does not follow this linear behavior. Instead, it shows a direct correlation with the magnetization of the material. This behavior is referred to as the anomalous Hall effect (AHE). Beyond the conventional and anomalous Hall effects, certain materials exhibit additional contributions to Hall resistivity that cannot be solely attributed to magnetization. These extra contributions may originate from the topological Hall effect (THE), which arises from non-coplaner spin textures within the material.

1.5.1 Anomalous Hall Effect

The behavior of Hall resistivity (ρ_{xy}) in ferromagnetic vs nonmagnetic conductors under a perpendicular magnetic field (H_z) was shown to differ significantly in early experimental studies. In conductors lacking intrinsic magnetism, the Hall resistivity (ρ_{xy}) exhibits a linear increase with the magnitude of the applied magnetic field (H_z) oriented perpendicularly to the current. In contrast, ferromagnetic materials exhibit a sharp initial rise in ρ_{xy} at low H_z, which eventually levels off, reaching a saturation value that remains almost unchanged even as H_z increases further (Fig. 1.13). Kundt observed that, for materials like Fe, Co, and Ni, the saturated Hall resistivity is about in line with the magnetizationM_z [87]. Subsequent experiments by Pugh [88] and Pugh and Lippert [89] demonstrated an empirical relationship between the Hall resistivity ρ_{xy}, the applied magnetic field H_z, and the spontaneous magnetization M_z, expressed as:

$$\rho_{xy} = R_0 H_z + R_s M_z \tag{1.21}$$

In this case, the ordinary Hall effect is represented by the first term $R_0 H_z$, and the AHE, which is the contribution from spontaneous magnetization, is represented by the second term $R_s M_z$. Unlike R_0, which is predominantly influenced by carrier density, R_s

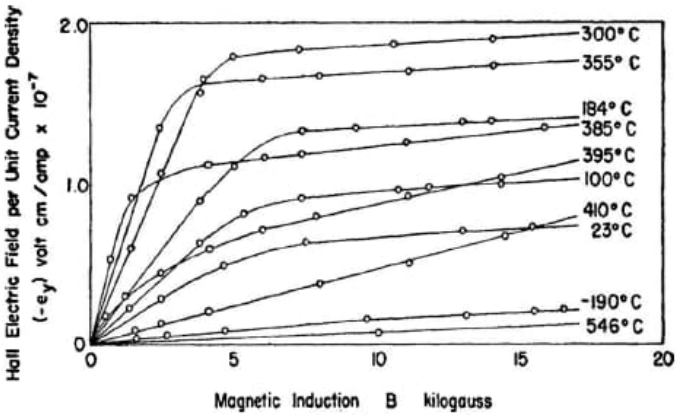

Figure 1.13: The anomalous Hall resistivity of Ni is presented as a function of the external magnetic field, taken from [90].

was found to exhibit a more complex dependence on various material-specific parameters, particularly longitudinal resistivity ρ_{xx}. Early studies on the relationship between Hall resistivity (ρ_{xy}) and resistivity (ρ_{xx}) often used a power-law formula, $\rho_{xy} \propto \rho_{xx}^{\alpha}$, where α was usually 1 or 2. There has been a long-standing debate about the origin of the anomalous Hall effect (AHE).

The semiclassical theories of the anomalous Hall effect (AHE), developed by Smit and Berger, emphasized the role of impurity-induced disorder in non-ideal crystals. Smit proposed that the primary origin of AHE lies in skew scattering, an asymmetric deflection of charge carriers resulting from spin-orbit coupling with impurities (see Fig. 1.14 (c)). This mechanism leads to a linear scaling of the anomalous Hall resistivity with longitudinal resistivity ($\rho_{xy} \propto \rho_{xx}$). In contrast, Berger suggested that AHE arises from a side-jump process, where electrons undergo a lateral displacement during scattering from spin-orbit-coupled defects, contributing to the Hall current through a different physical mechanism (see Fig. 1.14 (c)). This mechanism results in the anomalous Hall resistivity scaling quadratically with the longitudinal resistivity, expressed as $\rho_{xy} \propto \rho_{xx}^2$.

In 1954, Karplus and Luttinger (KL) proposed a theory for the anomalous Hall effect (AHE), offering valuable insights into its underlying mechanism. They demonstrate that when a material is subjected to perpendicular electric and magnetic fields, the electrons acquire an additional velocity component, referred to as anomalous velocity, that is perpendicular to the applied fields. In ferromagnetic conductors, the net anomalous velocity from all occupied electronic states does not cancel out, resulting in a finite AHE. This contribution, originating intrinsically from the material's electronic band structure and largely independent of scattering processes, demonstrates a proportionality where the Hall resistivity (ρ_{xy}) scales quadratically with the longitudinal resistivity (ρ_{xx}), i.e., $\rho_{xy} \propto \rho_{xx}^2$. The Karplus-Luttinger (KL) theory faced criticism for neglecting disorder scattering. In contrast, semiclassical AHE theories by Smit and Berger introduced the

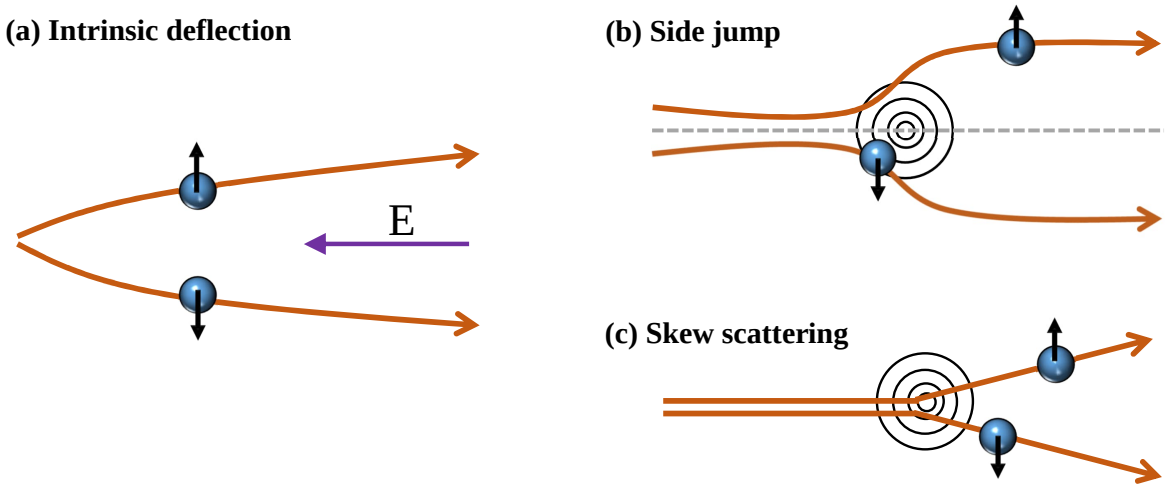

Figure 1.14: This figure illustrates the three primary mechanisms (a) intrinsic, (b) side jump, and (c) skew scattering mechanism that contribute to the anomalous Hall effect (AHE). (a) **Intrinsic deflection:** Electrons acquire an anomalous velocity component perpendicular to the applied electric field, which arises from the Berry curvature in momentum space. $\frac{d\langle \mathbf{r} \rangle}{dt} = \frac{1}{\hbar}\frac{dE}{d\mathbf{k}} + \frac{e}{\hbar}\mathbf{E} \times \mathbf{b}_n$, second term in this equation governs the anomalous velocity. (b) **Side jump:** When an electron approaches or moves away from an impurity, it undergoes a transverse displacement, known as a side jump, which occurs perpendicular to both its initial velocity and the applied electric field. (c) **Skew scattering:** Asymmetric electron scattering caused by the spin-orbit interaction, either originating from the electron itself or from the impurity. In any real material, the motion of electrons is influenced by a combination of these mechanisms. Images are remade from [90]

role of disorder. The anomalous Hall effect (AHE) remained an unresolved phenomenon for a long time. The breakthrough came with the recognition that the intrinsic component of the AHE could be understood through the concept of Berry curvature in momentum space, offering profound insight into this longstanding puzzle [91, 90]. It was later established that the Karplus-Luttinger (KL) mechanism for the intrinsic AHE is fundamentally linked to the Berry phase associated with the occupied Bloch states [91, 92, 90].

Despite ongoing debates, it is now generally accepted that the total anomalous Hall conductivity (AHC) consists of three distinct contributions:

$$\sigma_{AH} = \sigma_{int} + \sigma_{sk} + \sigma_{sj}, \tag{1.22}$$

where σ_{int} represents the intrinsic Karplus-Luttinger (KL) term, while σ_{sk} and σ_{sj} correspond to the extrinsic contributions from skew scattering and side jump mechanisms, respectively.

Differentiating between intrinsic and extrinsic contributions has proven to be a significant experimental problem in many materials where both coexist. Tian et al.[92] later introduced a new scaling law for the AHE, offering a unified and more complete

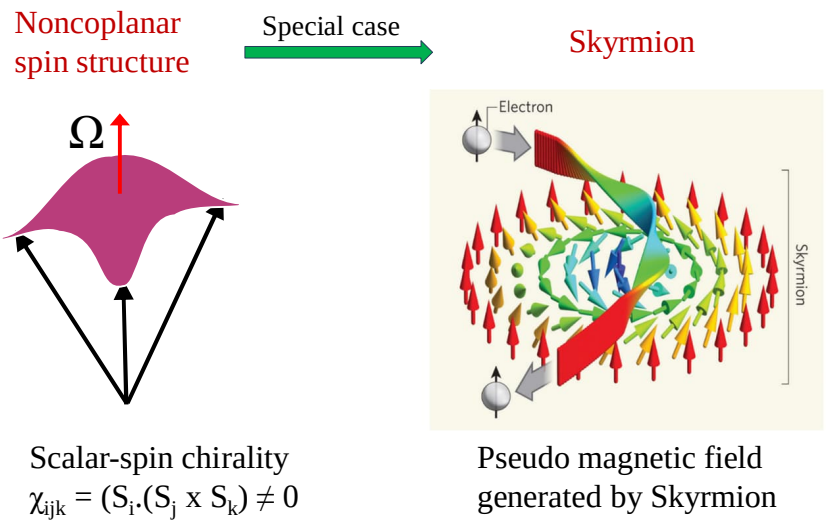

Figure 1.15: A non-coplanar spin structure with non-zero scalar-spin chirality can give rise to skyrmions. When electrons traverse such a skyrmion structure, their paths can be deflected. Image taken from Ref. [96]

framework to describe the interplay between various AHE contributions. Incorporating the residual resistivity, this TYJ scaling law is written as $\rho_{xy}^{A} = f(\rho_{xx0}, \rho_{xx})$. The empirical form of this TYJ [92, 93] scaling for AHE is,

$$\rho_{xy}^{A} = (\alpha\rho_{xx0} + \beta\rho_{xx0}^{2}) + b\rho_{xx}^{2} \tag{1.23}$$

$$\sigma_{xy}^{A} = (\alpha\sigma_{xx0}^{-1} + \beta\sigma_{xx0}^{-2})\sigma_{xx}^{2} + b = \rho_{xy0}^{ext}\sigma_{xx}^{2} + b, \tag{1.24}$$

where $\sigma_{xx0} = 1/\rho_{xx0}$ is the residual conductivity, α and β are constants, and b represents the intrinsic contribution to the conductivity originating from the Berry curvature, typically considered temperature-independent.

1.5.2 Topological Hall Effect

The topological Hall effect (THE) arises from non-coplanar spin structures, where the scalar spin chirality $[\chi_{ijk} = S_i.(S_j \times S_k)]$ becomes nonzero. This results in the creation of a real-space Berry curvature, which gives rise to the THE [94, 95]. When conduction electrons move through non-coplanar spin textures like skyrmion lattices, they adiabatically align their spins with the local magnetic moments. This creates a non-zero Berry curvature in real space, deflecting charge carriers transversely and generating a topological Hall voltage (see Fig. 1.15).

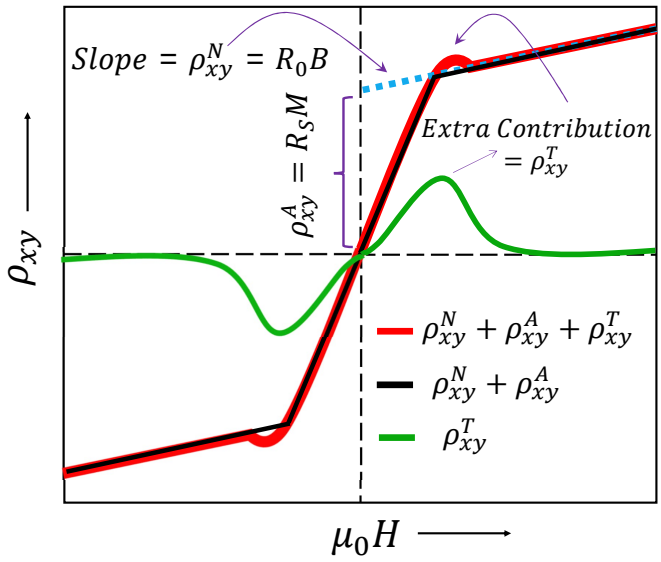

Figure 1.16: Various contributions to the total Hall resistivity. Here, ρ_{xy}^N is the normal Hall resistivity, ρ_{xy}^A denotes the anomalous Hall resistivity and ρ_{xy}^T corresponds to the topological Hall resistivity.

In Hall effect measurement, the total Hall resistivity can be represented as,

$$\begin{aligned} \rho_{xy}(H) &= \rho_{xy}^N(H) + \rho_{xy}^A(H) + \rho_{xy}^T(H) \\ &= \mu_0 R_0 H + \mu_0 R_S M + \rho_{xy}^T(H) \end{aligned} \tag{1.25}$$

Since the topological Hall effect (THE) originates from non-coplanar chiral spin textures, applying a strong external magnetic field can disrupt these configurations by aligning the spins along the field direction. As a result, the topological Hall resistivity (ρ_{xy}^T), which arises from the real-space Berry curvature generated by the non-coplanar spin structure can become negligible. So, in the high magnetic fields region $\rho_{xy}^T \to 0$ and we can rewrite the Eqn. 1.25 as,

$$\frac{\rho_{xy}^T}{\mu_0 H} = R_0 + R_S \frac{M}{H} \tag{1.26}$$

To isolate the topological Hall resistivity component from the total Hall response, we first fit the high-field Hall resistivity data using Eqn. 1.26 to determine the normal (R_0) and anomalous (R_S) Hall coefficients. These extracted coefficients are then substituted into Eqn. 1.25, allowing us to subtract the conventional contributions and obtain the topological Hall resistivity (see Fig. 1.16).

Non-coplanar spin textures in magnetic systems can emerge from a variety of intriguing origins, such as Dzyaloshinskii-Moriya interaction (DMI) in noncentrosymmetric systems, the interplay between uniaxial anisotropy and dipole-dipole interactions, and the emergence of skyrmion lattices induced by chiral domain walls [97–100]. These

mechanisms underscore the intricate relationship between lattice symmetry, magnetic anisotropy, and topologically nontrivial spin textures in governing the origin of THE. Beyond the well-established mechanisms, recent theoretical models and experimental investigations have uncovered that skyrmions, typically associated with systems lacking inversion symmetry, can also be stabilized in centrosymmetric materials. This unexpected stabilization challenges conventional perspectives and implies that nontrivial spin textures can also arise in materials with centrosymmetric crystal structures [101, 102, 95], such as Gd_2PdSi_3 [103] and $Gd_3Ru_4Al_{12}$ [22], primarily driven by magnetic frustration. Additionally, recent investigations have shown that Fe doping in Mn_3Sn enhances magnetocrystalline anisotropy and induces a non-coplanar spin structure, leading to the emergence of a topological Hall effect (THE) at low temperatures [104]. Similarly, Fe_3Sn_2, another centrosymmetric system, exhibits THE and skyrmion bubbles, driven by the formation of a non-coplanar spin structure and large magnetocrystalline anisotropy [17].

1.6 Magnetoresistance

Large magnetoresistance (MR) in magnetic materials is an uncommon phenomenon [105–107], yet its potential for technological applications is significant [108, 100, 109]. For this reason, a crucial area of study for physicists and materials scientists is the hunt for systems with extraordinarily high magnetoresistance. When an external magnetic field is applied to a material, the trajectories of free charge carriers of a current-carrying conductor are altered due to the Lorentz force. This modification in carrier motion influences the scattering processes within the material, leading to a change in its electrical resistivity. This phenomenon is known as magnetoresistance (MR), which quantifies the relative resistivity variation with the applied magnetic field. It is mathematically expressed as

$$MR = \frac{\rho(H) - \rho(0)}{\rho(0)}, \tag{1.27}$$

where $\rho(H)$ is the resistivity in the presence of a magnetic field H, and $\rho(0)$ is the resistivity in zero field. Lord Kelvin (then William Thomson) first noticed the effect in 1856 when analyzing the resistance of an iron sample. Within a material, charge carriers such as electrons preferentially navigate paths that minimize scattering events. This tendency allows electrons to travel along routes of least resistance and energy dissipation as they move across the sample. When an external magnetic field is applied to a material, electrons are deflected from their low-scattering paths due to the Lorentz force. This deviation increases the overall resistance of the sample, leading to a rise in resistivity. Therefore, a positive magnetoresistance (MR) is generally expected. It is sometimes plausible to observe negative MR in thin samples (thickness $<$ mean free path) at low temperatures. Applying a magnetic field perpendicular to the surface causes electrons

to follow circular orbits, which can reduce surface scattering. As a result, the overall resistance of the sample decreases [110]. Furthermore, ferromagnetic materials often exhibit negative magnetoresistance (MR) [105, 110, 107]. This occurs because the applied magnetic field aligns the spins along its direction, thereby reducing spin-dependent scattering. As a result, electrons can move more freely through the material, leading to a decrease in resistance.

1.6.1 Different Types of MR

MR phenomena can be categorized based on their magnitude and underlying mechanisms into various types, including ordinary MR (OMR), giant MR (GMR), colossal MR (CMR), and tunneling MR (TMR). In most of the systems, these MR (OMR) changes are relatively small, typically below 5 % [105, 111, 110]. Giant magnetoresistance (GMR) is an effect observed in reduced-dimensional systems, specifically within thin films or layered heterostructures [112, 107]. In addition, colossal magnetoresistance (CMR) is mostly observed in manganese-based perovskite oxides [108, 107]. On the other hand, tunneling magnetoresistance (TMR) is a phenomenon exhibited by magnetic tunnel junctions (MTJs), which are fabricated by inserting a thin insulating layer between two ferromagnetic films [113]. Beyond these established magnetoresistive effects, the recent discovery of extremely large magnetoresistance (XMR) in a variety of materials has generated significant scientific interest.

1.6.2 Extremely Large Magnetoresistance (XMR)

The magnetoresistance (MR) of certain metals or semimetals can show a remarkable and quick increase at low temperatures, reaching values as high as $10^3\% - 10^8\%$ or even higher. Most importantly, the MR does not attain saturation even at extremely high magnetic fields. This distinctive type of magnetoresistive behavior is classified as Extremely Large Magnetoresistance (XMR).

The origin of extremely large magnetoresistance has been widely studied, and several mechanisms have been proposed to explain this intriguing behavior. One key factor is high charge carrier mobility, which allows electrons to respond strongly to applied magnetic fields, leading to large changes in resistance [114]. Another widely accepted explanation is electron-hole compensation, where nearly equal numbers of electrons and holes contribute to electrical transport [115, 107, 116]. In systems with nearly equal densities of electrons and holes, the transverse currents induced by the Lorentz force tend to cancel, effectively suppressing the Hall electric field. This suppression allows the Lorentz force to more strongly influence carrier trajectories, enhancing their curvature. The resulting increase in carrier scattering and reduction in longitudinal mobility lead to a pronounced rise in electrical resistivity under an applied magnetic field. Additionally,

the presence of topological fermions, such as Dirac or Weyl fermions, has been linked to XMR in certain materials, where non-trivial band topology plays a significant role in enhancing magnetoresistive effects [117]. Moreover, the geometry of the Fermi surface, especially when characterized by open orbital paths, has been found to strongly influence charge transport in magnetic fields. In such cases, carriers follow extended trajectories across the Fermi surface, amplifying the MR response [118].

1.6.3 Angle Dependent Magnetoresistance (ADMR)

In many materials, the magnetoresistance exhibits strong directional dependence, meaning its magnitude varies with the orientation of the applied magnetic field relative to specific crystallographic axes. This phenomenon is known as angular-dependent magnetoresistance (ADMR). The magnetoresistance of a material is strongly linked to its Fermi surface topology [119]. The shape of the Fermi surface dictates the paths that charge carriers take under a magnetic field, consequently influencing the material's electrical conductivity [120, 119]. In many materials, the Fermi surface is highly complex and can be significantly altered by external parameters such as pressure, temperature, or doping, making its experimental characterization a challenging task. A practical and effective approach to probe the Fermi surface is through angle-dependent magnetoresistance (ADMR) measurements, which provide valuable insights into its geometry and anisotropy by analyzing how MR varies with the orientation of the applied magnetic field [119, 121].

The angle-dependent magnetoresistance (ADMR) patterns observed in various materials exhibit distinct symmetries, including twofold, fourfold, sixfold, and even higher-order symmetries. Several mechanisms have been proposed to explain the emergence of symmetric patterns in angular-dependent magnetoresistance (ADMR), each reflecting the complex interplay between structural, magnetic, and electronic factors in a material. Here are the mechanisms associated with ADMR: (i) Magnetocrystalline anisotropy, in which resistance varies due to the dependency of magnetic characteristics on crystallographic orientations, is one significant contribution. [122–124]. (ii) Spin scattering near antiphase boundaries (APBs), which disrupt spin alignment and introduce direction-dependent scattering effects, particularly in complex oxide materials [125–127]. (iii) Exchange bias, often present in systems with ferromagnetic/antiferromagnetic interfaces, can further induce anisotropic magnetic behavior that affects transport properties. (iv) Relaxation time anisotropy, arising from direction-dependent carrier scattering and Fermi surface topology, also plays a significant role in shaping ADMR symmetries [128, 129]. (v) The intrinsic lattice symmetry, which governs the overall electronic structure and often determines the rotational symmetry observed in ADMR, such as two-fold, four-fold, or six-fold patterns [130, 129]. (vi) Modulation of the density of states (DOS) near the

Fermi level, influenced by the orientation of the magnetic field, can induce angular variations in charge carrier availability and electrical conductivity, thereby contributing to the angular-dependent magnetoresistance (ADMR) [128, 131]. Collectively, these mechanisms demonstrate the involved physics behind anisotropic magnetotransport and the diverse origin of ADMR.

References

[1] M. Z. Hasan, C. L. Kane, Colloquium: Topological insulators, Rev. Mod. Phys. 82 (2010) 3045–3067.

[2] Y. Nambu, Nobel Lecture: Spontaneous symmetry breaking in particle physics: A case of cross fertilization, Rev. Mod. Phys. 81 (2009) 1015–1018.

[3] A. Trenkwalder, G. Spagnolli, G. Semeghini, S. Coop, M. Landini, P. Castilho, L. Pezzè, G. Modugno, M. Inguscio, A. Smerzi, M. Fattori, Quantum phase transitions with parity-symmetry breaking and hysteresis, Nature Physics 12 (2016) 826–829.

[4] K. v. Klitzing, G. Dorda, M. Pepper, New Method for High-Accuracy Determination of the Fine-Structure Constant Based on Quantized Hall Resistance, Phys. Rev. Lett. 45 (1980) 494–497.

[5] C. L. Kane, E. J. Mele, Quantum Spin Hall Effect in Graphene, Phys. Rev. Lett. 95 (2005) 226801.

[6] L. Fu, C. L. Kane, E. J. Mele, Topological Insulators in Three Dimensions, Phys. Rev. Lett. 98 (2007) 106803.

[7] J. E. Moore, L. Balents, Topological invariants of time-reversal-invariant band structures, Phys. Rev. B 75 (2007) 121306.

[8] S. M. Young, S. Zaheer, J. C. Y. Teo, C. L. Kane, E. J. Mele, A. M. Rappe, Dirac semimetal in three dimensions., Physical review letters 108 14 (2011) 140405.

[9] M. Neupane, S.-Y. Xu, R. Sankar, N. Alidoust, G. Bian, C. Liu, I. Belopolski, T.-R. Chang, H.-T. Jeng, H. Lin, A. Bansil, F. Chou, M. Z. Hasan, Observation of a three-dimensional topological Dirac semimetal phase in high-mobility Cd_3As_2, Nature Communications 5 (2014).

[10] L. Lu, Z. Wang, D. Ye, L. Ran, L. Fu, J. D. Joannopoulos, M. Soljačić, Experimental observation of Weyl points, Science 349 (2015) 622–624.

[11] S.-Y. Xu, I. Belopolski, N. Alidoust, M. Neupane, G. Bian, C. Zhang, R. Sankar, G. Chang, Z. Yuan, C.-C. Lee, S.-M. Huang, H. Zheng, J. Ma, D. S. Sanchez, B. Wang, A. Bansil, F. Chou, P. P. Shibayev, H. Lin, S. Jia, M. Z. Hasan, Discovery of a Weyl fermion semimetal and topological Fermi arcs, Science 349 (2015) 613–617.

[12] L. Savary, L. Balents, Quantum spin liquids: a review, Rep Progr Phys 80 (2016) 016502.

[13] C. Broholm, R. J. Cava, S. A. Kivelson, D. G. Nocera, M. R. Norman, T. Senthil, Quantum spin liquids, Science 367 (2020).

[14] L. Ye, M. Kang, J. Liu, F. von Cube, C. R. Wicker, T. Suzuki, C. Jozwiak, A. Bostwick, E. Rotenberg, D. C. Bell, L. Fu, R. Comin, J. G. Checkelsky, Massive Dirac fermions in a ferromagnetic kagome metal, Nature 555 (2018) 638–642.

[15] K. Kuroda, T. Tomita, M.-T. Suzuki, C. Bareille, A. Nugroho, P. Goswami, M. Ochi, M. Ikhlas, M. Nakayama, S. Akebi, S. Nakatsuji, Evidence for magnetic Weyl fermions in a correlated metal, Nature Materials 16 (2017) 1090–1095.

[16] N. Morali, R. Batabyal, P. K. Nag, E. Liu, Q. Xu, Y. Sun, B. Yan, C. Felser, N. Avraham, H. Beidenkopf, Fermi-arc diversity on surface terminations of the magnetic Weyl semimetal $Co_3Sn_2S_2$, Science 365 (2019) 1286–1291.

[17] Z. Hou, W. Ren, B. Ding, G. Xu, Y. Wang, B. Yang, Q. Zhang, Y. Zhang, E. Liu, F. Xu, W. Wang, G. Wu, X. Zhang, B. Shen, Z. Zhang, Observation of Various and Spontaneous Magnetic Skyrmionic Bubbles at Room Temperature in a Frustrated Kagome Magnet with Uniaxial Magnetic Anisotropy, Advanced Materials 29 (2017).

[18] A. K. Nayak, J. E. Fischer, Y. Sun, B. Yan, J. Karel, A. C. Komarek, C. Shekhar, N. Kumar, W. Schnelle, J. Kübler, et al., Large anomalous Hall effect driven by a nonvanishing Berry curvature in the noncolinear antiferromagnet Mn_3Ge, Science advances 2 (2016) e1501870.

[19] Z. Ren, H. Li, S. Sharma, D. Bhattarai, H. Zhao, B. Rachmilowitz, F. Bahrami, F. Tafti, S. Fang, M. P. Ghimire, Z. Wang, I. Zeljkovic, Plethora of tunable Weyl fermions in kagome magnet Fe3Sn2 thin films, npj Quantum Materials 7 (2022).

[20] M. Fujihala, K. Morita, R. Mole, S. Mitsuda, T. Tohyama, S.-I. Yano, D. Yu, S. Sota, T. Kuwai, A. Koda, H. Okabe, H. Lee, S. Itoh, T. Hawai, T. Masuda, H. Sagayama, A. Matsuo, K. Kindo, S. Ohira-Kawamura, K. Nakajima, Gapless spin liquid in a square-kagome lattice antiferromagnet, Nat. Commun. 11 (2020).

[21] Z. Zeng, X. Ma, S. Wu, H.-F. Li, Z. Tao, X. Lu, X.-h. Chen, J.-X. Mi, S.-J. Song, G.-H. Cao, G. Che, K. Li, G. Li, H. Luo, Z. Y. Meng, S. Li, Possible Dirac quantum spin liquid in the kagome quantum antiferromagnet $YCu_3(OH)_6Br_2[Br_x(OH)_{1-x}]$, Phys. Rev. B 105 (2022) L121109.

[22] M. Hirschberger, T. Nakajima, S. Gao, L. Peng, A. Kikkawa, T. Kurumaji, M. Kriener, Y. Yamasaki, H. Sagayama, H. Nakao, K. Ohishi, K. Kakurai, Y. Taguchi, X. Yu, T.-h. Arima, Y. Tokura, Skyrmion phase and competing magnetic orders on a breathing kagomé lattice, Nature Communications 10 (2019).

[23] D. Chakrabartty, S. Jamaluddin, S. K. Manna, A. K. Nayak, Tunable room temperature magnetic skyrmions in centrosymmetric kagome magnet mn4ga2sn, Communications Physics 5 (2022).

[24] X.-L. Qi, S.-C. Zhang, Topological insulators and superconductors, Rev. Mod. Phys. 83 (2011) 1057–1110.

[25] J. Maciejko, T. L. Hughes, S.-C. Zhang, The Quantum Spin Hall Effect, Annual Review of Condensed Matter Physics 2 (2011) 31–53.

[26] M. Z. Hasan, J. E. Moore, Three-Dimensional Topological Insulators, Annual Review of Condensed Matter Physics 2 (2011) 55–78.

[27] B. Yan, S.-C. Zhang, Topological materials, Reports on Progress in Physics 75 (2012) 096501.

[28] Y. Ando, Topological Insulator Materials, Journal of the Physical Society of Japan 82 (2013) 102001.

[29] B. A. Bernevig, T. L. Hughes, S.-C. Zhang, Quantum Spin Hall Effect and Topological Phase Transition in HgTe Quantum Wells, Science 314 (2006) 1757–1761.

[30] M. Konig, S. Wiedmann, C. Brune, A. Roth, H. Buhmann, L. W. Molenkamp, X.-L. Qi, S.-C. Zhang, Quantum Spin Hall Insulator State in HgTe Quantum Wells, Science 318 (2007) 766–770.

[31] H. Zhang, C.-X. Liu, X.-L. Qi, X. Dai, Z. Fang, S.-C. Zhang, Topological insulators in Bi_2Se_3, Bi_2Te_3 and Sb_2Te_3 with a single Dirac cone on the surface, Nature Physics 5 (2009) 438–442.

[32] Y. Xia, D. Qian, D. Hsieh, L. Wray, A. Pal, H. Lin, A. Bansil, D. Grauer, Y. S. Hor, R. J. Cava, M. Z. Hasan, Observation of a large-gap topological-insulator class with a single Dirac cone on the surface, Nature Physics 5 (2009) 398–402.

[33] G. Tkachov, Topological Insulators The Physics of Spin Helicity in Quantum Transport, Taylor Francis Group, 2015.

[34] B. I. Halperin, Quantized Hall conductance, current-carrying edge states, and the existence of extended states in a two-dimensional disordered potential, Phys. Rev. B 25 (1982) 2185–2190.

[35] A. H. MacDonald, P. Středa, Quantized Hall effect and edge currents, Phys. Rev. B 29 (1984) 1616–1619.

[36] D. J. Thouless, M. Kohmoto, M. P. Nightingale, M. den Nijs, Quantized Hall Conductance in a Two-Dimensional Periodic Potential, Physical Review Letters 49 (1982) 405–408.

[37] L. Landau, Diamagnetismus der Metalle, Zeitschrift fr Physik 64 (1930) 629–637.

[38] K. von Klitzing, The quantized Hall effect, Rev. Mod. Phys. 58 (1986) 519–531.

[39] C. L. Kane, E. J. Mele, Z_2 Topological Order and the Quantum Spin Hall Effect, Phys. Rev. Lett. 95 (2005) 146802.

[40] B. A. Bernevig, S.-C. Zhang, Quantum Spin Hall Effect, Phys. Rev. Lett. 96 (2006) 106802.

[41] D. Hsieh, D. Qian, L. Wray, Y. Xia, Y. S. Hor, R. J. Cava, M. Z. Hasan, A topological Dirac insulator in a quantum spin Hall phase, Nature 452 (2008) 970–974.

[42] Y. L. Chen, J. G. Analytis, J.-H. Chu, Z. K. Liu, S.-K. Mo, X. L. Qi, H. J. Zhang, D. H. Lu, X. Dai, Z. Fang, S. C. Zhang, I. R. Fisher, Z. Hussain, Z.-X. Shen, Experimental Realization of a Three-Dimensional Topological Insulator, Bi_2Te_3, Science 325 (2009) 178–181.

[43] A. A. Burkov, M. D. Hook, L. Balents, Topological nodal semimetals, Phys. Rev. B 84 (2011) 235126.

[44] Z. Liu, B. Zhou, Y. Zhang, Z. Wang, H. Weng, D. Prabhakaran, S.-K. Mo, Z. Shen, Z. Fang, X. Dai, et al., Discovery of a three-dimensional topological Dirac semimetal, Na_3Bi, Science 343 (2014) 864–867.

[45] S. Borisenko, Q. Gibson, D. Evtushinsky, V. Zabolotnyy, B. Büchner, R. J. Cava, Experimental Realization of a Three-Dimensional Dirac Semimetal, Phys. Rev. Lett. 113 (2014) 027603.

[46] X. Huang, L. Zhao, Y. Long, P. Wang, D. Chen, Z. Yang, H. Liang, M. Xue, H. Weng, Z. Fang, X. Dai, G. Chen, Observation of the Chiral-Anomaly-Induced Negative Magnetoresistance in 3D Weyl Semimetal TaAs, Phys. Rev. X 5 (2015) 031023.

[47] B. Q. Lv, H. M. Weng, B. B. Fu, X. P. Wang, H. Miao, J. Ma, P. Richard, X. C. Huang, L. X. Zhao, G. F. Chen, Z. Fang, X. Dai, T. Qian, H. Ding, Experimental Discovery of Weyl Semimetal TaAs, Phys. Rev. X 5 (2015) 031013.

[48] Dirac, P., The quantum theory of the electron, Proceedings of the Royal Society of London. Series A, Containing Papers of a Mathematical and Physical Character 117 (1928) 610–624.

[49] L. M. Brown, Paul A.M. Dirac's The Principles of Quantum Mechanics, Physics in Perspective 8 (2006) 381–407.

[50] K. S. Novoselov, A. K. Geim, S. V. Morozov, D. Jiang, M. I. Katsnelson, I. V. Grigorieva, S. V. Dubonos, A. A. Firsov, Two-dimensional gas of massless Dirac fermions in graphene, Nature 438 (2005) 197–200.

[51] S. M. Young, S. Zaheer, J. C. Y. Teo, C. L. Kane, E. J. Mele, A. M. Rappe, Dirac Semimetal in Three Dimensions, Phys. Rev. Lett. 108 (2012) 140405.

[52] N. P. Armitage, E. J. Mele, A. Vishwanath, Weyl and Dirac semimetals in three-dimensional solids, Rev. Mod. Phys. 90 (2018) 015001.

[53] H.-J. Kim, K.-S. Kim, J.-F. Wang, M. Sasaki, N. Satoh, A. Ohnishi, M. Kitaura, M. Yang, L. Li, Dirac versus Weyl Fermions in Topological Insulators: Adler-Bell-Jackiw Anomaly in Transport Phenomena, Phys. Rev. Lett. 111 (2013) 246603.

[54] S.-Y. Xu, C. Liu, S. K. Kushwaha, R. Sankar, J. W. Krizan, I. Belopolski, M. Neupane, G. Bian, N. Alidoust, T.-R. Chang, H.-T. Jeng, C.-Y. Huang, W.-F. Tsai, H. Lin, P. P. Shibayev, F.-C. Chou, R. J. Cava, M. Z. Hasan, Observation of Fermi arc surface states in a topological metal, Science 347 (2015) 294–298.

[55] F. Kabir, R. Filippone, G. Dhakal, Y. Lee, N. Poudel, J. Casey, A. P. Sakhya, S. Regmi, R. Smith, P. Manfrinetti, L. Ke, K. Gofryk, M. Neupane, A. K. Pathak, Unusual magnetic and transport properties in $homn_6sn_6$ kagome magnet, Phys. Rev. Mater. 6 (2022) 064404.

[56] M. Novak, S. Sasaki, K. Segawa, Y. Ando, Large linear magnetoresistance in the Dirac semimetal TlBiSSe, Phys. Rev. B 91 (2015) 041203.

[57] Q. Li, D. E. Kharzeev, C. Zhang, Y. Huang, I. Pletikosić, A. Fedorov, R. Zhong, J. Schneeloch, G. Gu, T. Valla, Chiral magnetic effect in $ZrTe_5$, Nature Physics 12 (2016) 550–554.

[58] C. Shekhar, A. K. Nayak, Y. Sun, M. Schmidt, M. Nicklas, I. Leermakers, U. Zeitler, Y. Skourski, J. Wosnitza, Z. Liu, Y. Chen, W. Schnelle, H. Borrmann, Y. Grin, C. Felser, B. Yan, Extremely large magnetoresistance and ultrahigh mobility in the topological Weyl semimetal candidate NbP, Nature Physics 11 (2015) 645–649.

[59] A. Narayanan, M. D. Watson, S. F. Blake, N. Bruyant, L. Drigo, Y. L. Chen, D. Prabhakaran, B. Yan, C. Felser, T. Kong, P. C. Canfield, A. I. Coldea, Linear Magnetoresistance Caused by Mobility Fluctuations in n-Doped Cd_3As_2, Phys. Rev. Lett. 114 (2015) 117201.

[60] H. Weyl, Elektron und Gravitation. I, Zeitschrift fr Physik 56 (1929) 330–352.

[61] P. B. Pal, Dirac, Majorana, and Weyl fermions, American Journal of Physics 79 (2011) 485–498.

[62] M. M. H. Polash, S. Yalameha, H. Zhou, K. Ahadi, Z. Nourbakhsh, D. Vashaee, Topological quantum matter to topological phase conversion: Fundamentals, materials, physical systems for phase conversions, and device applications, Materials Science and Engineering: R: Reports 145 (2021) 100620.

[63] K. Deng, G. Wan, P. Deng, K. Zhang, S. Ding, E. Wang, M. Yan, H. Huang, H. Zhang, Z. Xu, J. Denlinger, A. Fedorov, H. Yang, W. Duan, H. Yao, Y. Wu, S. Fan, H. Zhang, X. Chen, S. Zhou, Experimental observation of topological Fermi arcs in type-II Weyl semimetal $MoTe_2$, Nature Physics 12 (2016) 1105–1110.

[64] H. Yang, Y. Sun, Y. Zhang, W.-J. Shi, S. S. Parkin, B. Yan, Topological Weyl semimetals in the chiral antiferromagnetic materials Mn_3Ge and Mn_3Sn, New Journal of Physics 19 (2017) 015008.

[65] C.-Y. Huang, H. Aramberri, H. Lin, N. Kioussis, Noncollinear magnetic modulation of Weyl nodes in ferrimagnetic Mn_3Ga, Phys. Rev. B 102 (2020) 094403.

[66] T. Yu, R. Liu, Y. Peng, P. Zheng, G. Wang, X. Ma, Z. Yuan, Z. Yin, Correlated electronic structure of the kagome metal mn_3Sn, Phys. Rev. B 106 (2022) 205103.

[67] J. Jiang, Z. Liu, Y. Sun, H. Yang, C. Rajamathi, Y. Qi, L. Yang, C. Chen, H. Peng, C.-C. Hwang, S. Sun, S.-K. Mo, I. Vobornik, J. Fujii, S. Parkin, C. Felser, B. Yan, Y. Chen, Signature of type-II Weyl semimetal phase in $MoTe_2$, Nature Communications 8 (2017).

[68] S. Thirupathaiah, R. Jha, B. Pal, J. S. Matias, P. K. Das, P. K. Sivakumar, I. Vobornik, N. C. Plumb, M. Shi, R. A. Ribeiro, D. D. Sarma, mote$_2$: An uncompensated semimetal with extremely large magnetoresistance, Phys. Rev. B 95 (2017) 241105.

[69] S. Thirupathaiah, R. Jha, B. Pal, J. S. Matias, P. K. Das, I. Vobornik, R. A. Ribeiro, D. D. Sarma, Temperature-independent band structure of wte$_2$ as observed from angle-resolved photoemission spectroscopy, Phys. Rev. B 96 (2017) 165149.

[70] Y. Zhou, K. Kanoda, T.-K. Ng, Quantum spin liquid states, Rev. Mod. Phys. 89 (2017) 025003.

[71] J.-X. Yin, B. Lian, M. Z. Hasan, Topological kagome magnets and superconductors, Nature 612 (2022) 647–657.

[72] Z. Wang, W. Zhang, L. Wang, T. F. Poon, C. W. Tsang, W. Wang, J. Xie, S. T. Lam, X. Zhou, Y. Zhao, S. Wang, M.-Z. Ai, K. T. Lai, S. K. Goh, Similarities and differences in the fermiology of kagome metals AV3Sb5 (A=K, Rb, Cs) revealed by Shubnikov–de Haas oscillations, Appl. Phys. Lett. 123 (2023).

[73] E. Liu, Y. Sun, N. Kumar, L. Muechler, A. Sun, L. Jiao, S.-Y. Yang, D. Liu, A. Liang, Q. Xu, et al., Giant anomalous Hall effect in a ferromagnetic kagome-lattice semimetal, Nature physics 14 (2018) 1125–1131.

[74] S. Nakatsuji, N. Kiyohara, T. Higo, Large anomalous Hall effect in a non-collinear antiferromagnet at room temperature, Nature 527 (2015) 212–215.

[75] M. Kang, L. Ye, S. Fang, J.-S. You, A. Levitan, M. Han, J. I. Facio, C. Jozwiak, A. Bostwick, E. Rotenberg, M. K. Chan, R. D. McDonald, D. Graf, K. Kaznatcheev, E. Vescovo, D. C. Bell, E. Kaxiras, J. van den Brink, M. Richter, M. Prasad Ghimire, J. G. Checkelsky, R. Comin, Dirac fermions and flat bands in the ideal kagome metal FeSn, Nature Materials 19 (2019) 163–169.

[76] L. Nie, K. Sun, W. Ma, D. Song, L. Zheng, Z. Liang, P. Wu, F. Yu, J. Li, M. Shan, D. Zhao, S. Li, B. Kang, Z. Wu, Y. Zhou, K. Liu, Z. Xiang, J. Ying, Z. Wang, T. Wu, X. Chen, Charge-density-wave-driven electronic nematicity in a kagome superconductor, Nature 604 (2022) 59–64.

[77] W. Ma, X. Xu, J.-X. Yin, H. Yang, H. Zhou, Z.-J. Cheng, Y. Huang, Z. Qu, F. Wang, M. Z. Hasan, S. Jia, Rare Earth Engineering in $R\mathrm{Mn}_6\mathrm{Sn}_6$ (R = Gd−Tm, Lu) Topological Kagome Magnets, Phys. Rev. Lett. 126 (2021) 246602.

[78] H. Yang, Y. Sun, Y. Zhang, W.-J. Shi, S. S. P. Parkin, B. Yan, Topological Weyl semimetals in the chiral antiferromagnetic materials Mn3Ge and Mn3Sn, New Journal of Physics 19 (2016) 015008.

[79] T. Chen, T. Tomita, S. Minami, M. Fu, T. Koretsune, M. Kitatani, I. Muhammad, D. Nishio-Hamane, R. Ishii, F. Ishii, R. Arita, S. Nakatsuji, Anomalous transport due to Weyl fermions in the chiral antiferromagnets Mn3X, X=Sn, Ge, Nat Commun 12 (2021).

[80] M. Kang, S. Fang, L. Ye, H. C. Po, J. Denlinger, C. Jozwiak, A. Bostwick, E. Rotenberg, E. Kaxiras, J. G. Checkelsky, R. Comin, Topological flat bands in frustrated kagome lattice CoSn, Nature Communications 11 (2020).

[81] M. Han, H. Inoue, S. Fang, C. John, L. Ye, M. K. Chan, D. Graf, T. Suzuki, M. P. Ghimire, W. J. Cho, E. Kaxiras, J. G. Checkelsky, Evidence of two-dimensional flat band at the surface of antiferromagnetic kagome metal FeSn, Nature Communications 12 (2021).

[82] K. Jiang, T. Wu, J.-X. Yin, Z. Wang, M. Z. Hasan, S. D. Wilson, X. Chen, J. Hu, Kagome superconductors AV_3Sb_5 (A = K, Rb, Cs), National Science Review 10 (2022).

[83] Z. Liang, X. Hou, F. Zhang, W. Ma, P. Wu, Z. Zhang, F. Yu, J.-J. Ying, K. Jiang, L. Shan, Z. Wang, X.-H. Chen, Three-Dimensional Charge Density Wave and Surface-Dependent Vortex-Core States in a Kagome Superconductor CsV_3Sb_5, Phys. Rev. X 11 (2021) 031026.

[84] J.-X. Yin, W. Ma, T. A. Cochran, X. Xu, S. S. Zhang, H.-J. Tien, N. Shumiya, G. Cheng, K. Jiang, B. Lian, Z. Song, G. Chang, I. Belopolski, D. Multer, M. Litskevich, Z.-J. Cheng, X. P. Yang, B. Swidler, H. Zhou, H. Lin, T. Neupert, Z. Wang, N. Yao, T.-R. Chang, S. Jia, M. Zahid Hasan, Quantum-limit Chern topological magnetism in $TbMn_6Sn_6$, Nature 583 (2020) 533–536.

[85] Q. Wang, K. J. Neubauer, C. Duan, Q. Yin, S. Fujitsu, H. Hosono, F. Ye, R. Zhang, S. Chi, K. Krycka, H. Lei, P. Dai, Field-induced topological Hall effect and double-fan spin structure with a *c*-axis component in the metallic kagome antiferromagnetic compound YMn_6Sn_6, Phys. Rev. B 103 (2021) 014416.

[86] D. Chen, C. Le, C. Fu, H. Lin, W. Schnelle, Y. Sun, C. Felser, Large anomalous Hall effect in the kagome ferromagnet $LiMn_6Sn_6$, Phys. Rev. B 103 (2021) 144410.

[87] W. L. Webster, The Hall effect in Single Crystals of Iron, Mathematical Proceedings of the Cambridge Philosophical Society 23 (1927) 800–803.

[88] E. M. Pugh, Hall Effect and the Magnetic Properties of Some Ferromagnetic Materials, Phys. Rev. 36 (1930) 1503–1511.

[89] E. M. Pugh, T. W. Lippert, Hall e.m.f. and Intensity of Magnetization, Phys. Rev. 42 (1932) 709–713.

[90] N. Nagaosa, J. Sinova, S. Onoda, A. H. MacDonald, N. P. Ong, Anomalous Hall effect, Rev. Mod. Phys. 82 (2010) 1539–1592.

[91] T. Jungwirth, Q. Niu, A. H. MacDonald, Anomalous Hall Effect in Ferromagnetic Semiconductors, Phys. Rev. Lett. 88 (2002) 207208.

[92] Y. Tian, L. Ye, X. Jin, Proper Scaling of the Anomalous Hall Effect, Phys Rev Lett 103 (2009) 087206.

[93] D. Hou, G. Su, Y. Tian, X. Jin, S. A. Yang, Q. Niu, Multivariable Scaling for the Anomalous Hall Effect, Phys. Rev. Lett. 114 (2015) 217203.

[94] Y. Shiomi, M. Mochizuki, Y. Kaneko, Y. Tokura, Hall Effect of Spin-Chirality Origin in a Triangular-Lattice Helimagnet $Fe_{1.3}Sb$, Phys. Rev. Lett. 108 (2012) 056601.

[95] P. K. Rout, P. V. P. Madduri, S. K. Manna, A. K. Nayak, Field-induced topological Hall effect in the noncoplanar triangular antiferromagnetic geometry of Mn_3Sn, Phys. Rev. B 99 (2019) 094430.

[96] J. Zang, Topological spin textures in chiral magnets: from 2D to 3D, Bulletin of the American Physical Society 67 (2022).

[97] S. B. Gudnason, M. Nitta, Domain wall Skyrmions, Phys. Rev. D 89 (2014) 085022.

[98] R. Cheng, M. Li, A. Sapkota, A. Rai, A. Pokhrel, T. Mewes, C. Mewes, D. Xiao, M. De Graef, V. Sokalski, Magnetic domain wall skyrmions, Phys. Rev. B 99 (2019) 184412.

[99] T. Nagase, Y.-G. So, H. Yasui, T. Ishida, H. K. Yoshida, Y. Tanaka, K. Saitoh, N. Ikarashi, Y. Kawaguchi, M. Kuwahara, M. Nagao, Observation of domain wall bimerons in chiral magnets, Nat. Commun. 12 (2021).

[100] K. Yang, K. Nagase, Y. Hirayama, T. D. Mishima, M. B. Santos, H. Liu, Wigner solids of domain wall skyrmions, Nat. Commun. 12 (2021).

[101] T. Okubo, S. Chung, H. Kawamura, Multiple-q States and the Skyrmion Lattice of the Triangular-Lattice Heisenberg Antiferromagnet under Magnetic Fields, Phys. Rev. Lett. 108 (2012) 017206.

[102] S. Hayami, R. Ozawa, Y. Motome, Effective bilinear-biquadratic model for noncoplanar ordering in itinerant magnets, Phys. Rev. B 95 (2017) 224424.

[103] T. Kurumaji, T. Nakajima, M. Hirschberger, A. Kikkawa, Y. Yamasaki, H. Sagayama, H. Nakao, Y. Taguchi, T. hisa Arima, Y. Tokura, Skyrmion lattice with a giant topological Hall effect in a frustrated triangular-lattice magnet, Science 365 (2019) 914–918.

[104] A. Low, S. Ghosh, S. Changdar, S. Routh, S. Purwar, S. Thirupathaiah, Tuning of topological properties in the strongly correlated antiferromagnet Mn_3Sn via Fe doping, Phys. Rev. B 106 (2022) 144429.

[105] C. W. Heaps, The Magnetoresistance of Nickel in Large Fields, Physical Review 55 (1939) 1069–1071.

[106] S. S. P. Parkin, N. More, K. P. Roche, Oscillations in exchange coupling and magnetoresistance in metallic superlattice structures: Co/Ru, Co/Cr, and Fe/Cr, Phys. Rev. Lett. 64 (1990) 2304–2307.

[107] R. Niu, W. Zhu, Materials and possible mechanisms of extremely large magnetoresistance: a review, Journal of physics. Condensed matter 34 (2021) 113001.

[108] A. P. Ramirez, Colossal magnetoresistance, Journal of physics. Condensed matter 9 (1997) 8171–8199.

[109] O. Vitayaya, P. Z. Z. Nehan, D. R. Munazat, M. T. E. Manawan, B. Kurniawan, Magnetoresistance (MR) properties of magnetic materials, RSC Advances 14 (2024) 18617–18645.

[110] S. Blundell, Magnetism in condensed matter, OUP Oxford, 2001.

[111] J. Nickel, Magnetoresistance overview, Hewlett-Packard Laboratories, Technical Publications Department Palo Alto ..., 1995.

[112] E. Tsymbal, D. Pettifor, Perspectives of giant magnetoresistance, 2001.

[113] J. Inoue, S. Maekawa, Theory of tunneling magnetoresistance in granular magnetic films, Physical review. B, Condensed matter 53 (1996) R11927–R11929.

[114] F. Han, J. Xu, A. S. Botana, Z. L. Xiao, Y. L. Wang, W. G. Yang, D. Y. Chung, M. G. Kanatzidis, M. R. Norman, G. W. Crabtree, W. K. Kwok, Separation of electron and hole dynamics in the semimetal LaSb, Phys. Rev. B 96 (2017) 125112.

[115] W. Gao, N. Hao, F.-W. Zheng, W. Ning, M. Wu, X. Zhu, G. Zheng, J. Zhang, J. Lu, H. Zhang, C. Xi, J. Yang, H. Du, P. Zhang, Y. Zhang, M. Tian, Extremely Large Magnetoresistance in a Topological Semimetal Candidate Pyrite $PtBi_2$, Phys. Rev. Lett. 118 (2017) 256601.

[116] J. Bannies, E. Razzoli, M. Michiardi, H.-H. Kung, I. S. Elfimov, M. Yao, A. Fedorov, J. Fink, C. Jozwiak, A. Bostwick, E. Rotenberg, A. Damascelli, C. Felser, Extremely large magnetoresistance from electron-hole compensation in the nodal-loop semimetal zrp_2, Phys. Rev. B 103 (2021) 155144.

[117] K. Okawa, M. Kanou, H. Namiki, T. Sasagawa, Extremely large magnetoresistance induced by hidden three-dimensional Dirac bands in nonmagnetic semimetal InBi, Phys. Rev. Mater. 2 (2018) 124201.

[118] R. Lou, Y. F. Xu, L.-X. Zhao, Z.-Q. Han, P.-J. Guo, M. Li, J.-C. Wang, B.-B. Fu, Z.-H. Liu, Y.-B. Huang, P. Richard, T. Qian, K. Liu, G.-F. Chen, H. M. Weng, H. Ding, S.-C. Wang, Observation of open-orbit Fermi surface topology in the extremely large magnetoresistance semimetal $MoAs_2$, Phys. Rev. B 96 (2017) 241106.

[119] S. Zhang, Q. Wu, Y. Liu, O. V. Yazyev, Magnetoresistance from Fermi surface topology, Phys. Rev. B 99 (2019) 035142.

[120] N. P. Ong, Geometric interpretation of the weak-field Hall conductivity in two-dimensional metals with arbitrary Fermi surface, Phys. Rev. B 43 (1991) 193–201.

[121] J. Wang, H. Yang, L. Ding, W. You, C. Xi, J. Cheng, Z. Shi, C. Cao, Y. Luo, Z. Zhu, J. Dai, M. Tian, Y. Li, Angle-dependent magnetoresistance and its implications for Lifshitz transition in W2As3, npj quantum materials 4 (2019).

[122] C. Jin, P. Li, W. B. Mi, H. L. Bai, Magnetocrystalline anisotropy-dependent six-fold symmetric anisotropic magnetoresistance in epitaxial Co x Fe 3x O 4 films, Europhys. Lett. 100 (2012) 27006.

[123] Y. Miao, D. Yang, L. Jia, X. Li, S. Yang, C. Gao, D. Xue, Magnetocrystalline anisotropy correlated negative anisotropic magnetoresistance in epitaxial Fe30Co70 thin films, Applied Physics Letters 118 (2021).

[124] J. Zhang, X. Chen, M. Wang, Q. Zhang, W. Shi, X. Zhan, M. Zhao, Z. Li, J. Zheng, H. Zhang, F. Han, H. Yang, T. Zhu, B. Liu, F. Hu, B. Shen, Y. Chen, Y. Zhang, Y. Chen, W. Zhao, J. Sun, Proximity-Induced Fully Ferromagnetic Order with Eightfold Magnetic Anisotropy in Heavy Transition Metal Oxide CaRuO3, Advanced Functional Materials 33 (2023).

[125] R. Ramos, S. K. Arora, I. V. Shvets, Anomalous anisotropic magnetoresistance in epitaxial Fe_3O_4 thin films on MgO(001), Phys. Rev. B 78 (2008) 214402.

[126] P. Li, E. Y. Jiang, H. L. Bai, Fourfold symmetric anisotropic magnetoresistance based on magnetocrystalline anisotropy and antiphase boundaries in reactive sputtered epitaxial Fe3O4 films, Appl. Phys. Lett. 96 (2010).

[127] P. Li, C. Jin, E. Y. Jiang, H. L. Bai, Origin of the twofold and fourfold symmetric anisotropic magnetoresistance in epitaxial Fe3O4 films, J Appl Phys 108 (2010).

[128] Y. Dai, Y. W. Zhao, L. Ma, M. Tang, X. P. Qiu, Y. Liu, Z. Yuan, S. M. Zhou, Fourfold Anisotropic Magnetoresistance of $L1_0$ FePt Due to Relaxation Time Anisotropy, Physical Review Letters 128 (2022) 247202.

[129] S. Lv, H. Guo, Q. Qi, Y. Li, G. Hu, Q. Zheng, R. Wang, N. Si, K. Zhu, Z. Zhao, Y. Han, W. Yu, G. Xian, L. Huang, L. Bao, X. Lin, J. Pan, S. Du, J. He, H. Yang, H. Gao, Field-Induced Butterfly-Like anisotropic magnetoresistance in a Kagome semimetal CO3IN2S2, Advanced Functional Materials (2024).

[130] C. Hu, J. Zhu, G. Chen, J. Li, Y. Wu, Direct comparison of anisotropic magnetoresistance and planar Hall effect in epitaxial Fe3O4 thin films, Phys. Lett. A 376 (2012) 3317–3321.

[131] J. Chen, H. Li, T. Guo, P. Chen, D. Zheng, G. Yu, Y.-C. Lau, X. Xi, W. Wang, Anomalous anisotropic magnetoresistance in the topological semimetal HoPtBi, NPG Asia Materials 15 (2023).

Chapter 2

Methodology

The exotic topological and physical properties of quantum materials are typically investigated through both theoretical modeling and experimental studies. This thesis adopts an experimental approach, focusing on the synthesis of high-quality single crystals and the comprehensive study of their physical properties.

This chapter outlines the experimental methodologies employed for all the studies in this thesis. It begins with the synthesis of high-quality single crystals, followed by the structural and compositional characterization using techniques such as X-ray diffraction (XRD), energy-dispersive X-ray spectroscopy (EDXS), scanning electron microscopy (SEM), and transmission electron microscopy (TEM). The chapter also introduces the Quantum Design PPMS DynaCool system, describing its core modules, including the vibrating sample magnetometer (VSM), electrical transport option (ETO), and heat capacity option, used to investigate the magnetic, electrical, and thermal properties of the grown crystals.

2.1 Single Crystal Growth

Solids can be classified as crystalline or amorphous according to the arrangement of their constituent atoms, molecules, or ions. Crystalline solids exhibit a well-ordered, repeating three-dimensional lattice structure that extends over long ranges. In contrast, the amorphous state lacks this periodicity, resulting in a disordered atomic or molecular structure. Crystalline solids can be further categorized into polycrystalline and single-crystal materials. A polycrystal consists of numerous small crystallites or grains, each with its own orientation, separated by grain boundaries. In contrast, a single crystal is characterized by a continuous and uninterrupted lattice structure that extends throughout the entire material without grain boundaries. This uniformity imparts superior mechanical, optical, and electronic properties, making single crystals essential for advanced technological applications. From a research perspective, high-quality single crystals are vital

for accurately measuring a material's fundamental physical properties. In polycrystalline materials, grain boundaries act as scattering centers, distorting charge carrier behavior and causing deviations in electrical transport measurements. Additionally, studying anisotropic properties, such as direction-dependent electrical and magnetic behavior, requires single crystals. Therefore, high-quality single crystals are essential for obtaining reliable and precise data.

Single crystals can be grown using a variety of methods, each optimized for different materials and desired crystal qualities. Frequently used techniques include chemical vapor transport (CVT), melt and control cooling method, the Bridgman-Stockbarger technique, the Czochralski pulling method, flux growth, and solid-state synthesis. The choice of method depends on the specific characteristics and growth needs of the material. In this thesis, the melt and controlled cooling method was primarily employed to grow Mn_3Ge, Fe-doped Mn_3Ge, and Fe_3Ge single crystals. Additionally, the flux growth technique was used for the synthesis of RFe_6Sn_6 (R = Ho, Dy) single crystals.

2.1.1 Nucleation Phenomena

The initial stage of single crystal growth is nucleation, where a small number of atoms, ions, or molecules in a supersaturated solution, melt, or vapor self-assemble into a stable, ordered arrangement that mimics the crystal's structure. This tiny, ordered aggregate is called a nucleus. In single crystal growth, it's important to control nucleation so that only one nucleus forms and grows into a large well-ordered crystal. If more than one nucleus forms, the crystal grows in multiple directions, resulting in a polycrystalline structure rather than a single continuous crystal. Numerous natural phenomena are driven by nucleation. A well-known example is the formation of raindrops, where water vapor condenses around tiny particles in the atmosphere. Similarly, when a carbonated beverage is opened, the sudden drop in pressure causes carbon dioxide bubbles to nucleate and rise to the surface.

Types of Nucleation

- **Homogeneous nucleation:** Homogeneous nucleation occurs uniformly throughout the parent phase without any preferential sites. This process typically requires a high degree of supersaturation or undercooling because it involves overcoming a substantial energy barrier. It's rare in practical crystal growth since it is energetically less favorable.

- **Heterogeneous nucleation:** Heterogeneous nucleation takes place at specific sites such as container walls, impurities, or seed crystals. It has a lower energy barrier compared to homogeneous nucleation and is the dominant mechanism in most prac-

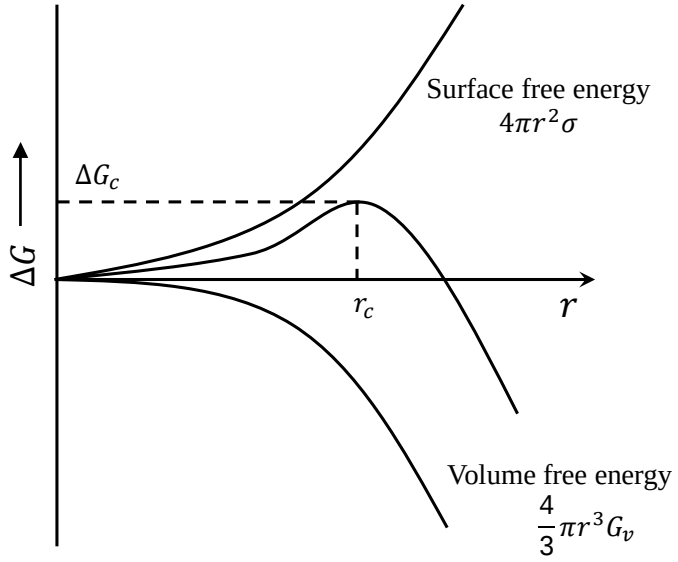

Figure 2.1: Change in free energy during the formation of a nucleus. The diagram is remade from Ref. [1].

tical crystal growth methods. In single crystal growth, controlled heterogeneous nucleation is often initiated using a seed crystal to guide the growth direction and orientation.

The formation of a liquid droplet or solid nucleus in a uniform medium requires energy to create a new surface. This total work W combines the positive surface energy W_s and the negative bulk energy W_ν, expressed as:

$$W = W_s - W_\nu \tag{2.1}$$

For a spherical droplet in a supersaturated solutions, this becomes:

$$W = a\sigma - \nu G_\nu \tag{2.2}$$

Where σ is the surface tension, and G_ν is the energy released per unit volume from the phase transformation.
For a droplet of radius r, the Gibbs free energy change is:

$$\Delta G = 4\pi r^2\sigma - \frac{4}{3}\pi r^3 G_\nu \tag{2.3}$$

To find the critical nucleus size, set the derivative $d(\Delta G)/dr = 0$, yielding the critical radius:

$$r_c = \frac{2\sigma}{G_\nu} \quad \text{and} \quad \Delta G_c = \frac{16\pi\sigma^3}{3G_\nu^2} \tag{2.4}$$

This defines the size and energy barrier a nucleus must overcome to grow spontaneously.

Figure 2.1 illustrates how the energy change during nucleation depends on cluster radius: the surface energy increases with r^2, while the volume energy decreases with r^3, creating an energy barrier with a maximum at the critical radius r_c. Clusters smaller than this r_c are unstable and tend to dissolve, as the surface energy cost outweighs the bulk energy gain. Only clusters reaching r_c, the critical nucleus, can grow further by lowering total energy through bulk phase transformation, overcoming the surface energy barrier.

The nucleation rate depends not only on thermodynamic factors but also on kinetic parameters such as diffusion rate and temperature. While high undercooling or supersaturation boosts the nucleation rate, it can lead to multiple nuclei and hinder single-crystal formation. To obtain a single crystal, nucleation must be carefully controlled by suppressing random nucleation and initiating growth at a defined site using a seed crystal to ensure orderly and directed crystal development.

2.1.2 Melt Growth Method

Single crystal growth can be achieved through phase transitions from (i) liquid to solid, (ii) vapor to solid, and (iii) solid to solid. Melt growth uses a controlled liquid-to-solid transformation to form single crystals. Materials that melt congruently or nearly congruently can be grown using melt growth techniques. In this process, the material is first melted and then solidified under controlled conditions, often using a seed crystal to guide the growth orientation. Because atoms in the melt are already mobile, the growth is not limited by diffusion, allowing for relatively fast crystal formation. This technique avoids the use of solvents or flux, minimizing contamination and enabling the production of high-purity crystals. Several well-established methods fall under melt growth, including the Bridgman–Stockbarger method, where a crucible is moved through a temperature gradient; the Czochralski method, where a seed is pulled from the melt; and the floating zone technique, which uses localized melting and solidification without a crucible to eliminate contamination.

Beyond these directional solidification techniques, a simpler variant involves melt growth via controlled cooling in a box furnace without imposing a spatial temperature gradient. This method is less complex and effective for growing single crystals of materials that do not require stringent growth conditions, making it a practical choice for compounds with congruent or near-congruent melting behavior. In this method, constituent elements are weighed in stoichiometric ratios and thoroughly ground to obtain a homogeneous mixture. This mixture may first be synthesized into a polycrystalline precursor through a solid-state reaction or directly loaded into a crucible for melting. The material is then completely melted at a temperature well above its melting point.

After the melt is held (soaking) for a sufficient time to ensure homogeneity, the furnace temperature is slowly lowered at a controlled rate. Unlike directional solidification techniques, this method does not rely on a spatial temperature gradient; instead, the entire melt is cooled uniformly.

Although this method lacks directional control, it supports natural crystal growth through spontaneous nucleation, increasing the likelihood of multiple nucleation events and consequently polycrystalline formation. However, under well-optimized conditions, such as slow cooling and minimal thermal gradients, spontaneous nucleation can be limited to one or a few dominant sites, allowing the growth of large and high-quality single crystals. This approach offers significant advantages due to its simplicity, low cost, and ability to produce structurally coherent crystals without complex equipment. It is particularly well-suited for early-stage growth studies and for materials where advanced directional techniques are unnecessary.

We used this simplified melt and control cooling growth method using a conventional high-temperature box furnace. Despite the limitations of this setup, we successfully optimized the growth conditions, particularly the stoichiometry, soaking time, and controlled cooling rate, to achieve high-quality single crystals. Using this approach, we were able to grow sizable and well-formed single crystals of Mn_3Ge, Fe-doped Mn_3Ge, and Fe_3Ge.

2.1.3 Flux Growth Method

Flux growth is a widely used crystal growth technique that employs a solvent, known as a flux, to dissolve the starting materials at high temperatures and allow crystal formation during cooling. The flux can be a third-party material (such as a metal, salt, or oxide) or a component of the target compound itself, in which case the process is known as self-flux growth. Like melt growth, flux growth involves a liquid-to-solid phase transformation, but it occurs at significantly lower temperatures because the flux reduces the effective crystallization point. This makes flux growth particularly suitable for materials that decompose, oxidize, or melt incongruently at high temperatures. In this method, the crystals grow gradually as the solution becomes supersaturated during slow cooling or evaporation. Although there is some risk of flux inclusion, especially with third-party fluxes, careful control of the conditions can yield high-quality crystals. In general, both third-party and self-flux methods offer a versatile and effective approach for the growth of complex or thermally sensitive materials that are difficult to produce via conventional melt growth.

The choice of flux is critical to the success of the technique. Suitable fluxes include low melting point metals such as Sn, Bi, Pb, and In for intermetallic systems, as well as salts and oxides such as alkali halides (e.g. NaCl and KCl), carbonates, borates, and

other metal oxides for oxide materials. An ideal flux should provide sufficient solubility for the solute, remain chemically inert with respect to both the material and the crucible, and be easily separable from the grown crystals.

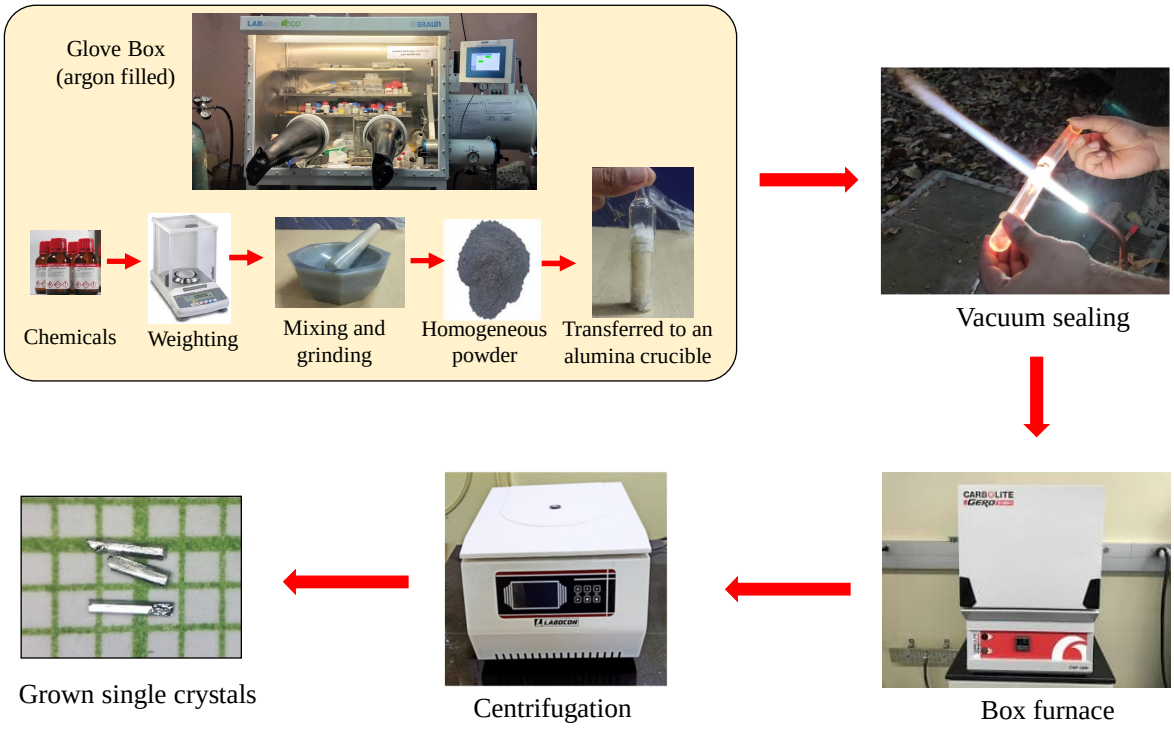

Figure 2.2: The flowchart represents the step-by-step process of single crystal growth.

Figure 2.2 illustrates the step-by-step procedure of the flux growth technique for single crystal synthesis. The process begins with accurately weighing the precursor elements in stoichiometric or flux-rich ratios, followed by thorough mixing inside an argon-filled glove box to prevent oxidation or moisture contamination. The prepared mixture is then transferred into an alumina crucible, which is loosely covered with quartz wool to act as a filter during the later flux separation step. This crucible is placed inside a quartz ampoule, which is sealed under a partial argon atmosphere to maintain an inert environment during heating. The sealed ampoule is then subjected to a controlled thermal profile inside a high-temperature box furnace. The temperature is first raised to a level sufficient to fully melt the mixture, ensuring homogenization. Following this, the melt gradually cooled, typically at a rate of about 2 °C per hour, to promote slow crystallization of the supersaturated solution. Once the desired lower temperature is reached, the ampoule is promptly removed while still hot and placed in a centrifuge. The centrifugal force helps to separate the remaining molten flux from the formed crystals, which are collected on the quartz wool filter.

This technique, when properly optimized, is effective in growing high-quality single crystals, particularly for compounds with incongruent melting behavior or sensitivity to high-

temperature decomposition.
For my thesis work, I successfully grew single crystals of $HoFe_6Sn_6$ and $DyFe_6Sn_6$ using the self-flux method, with tin (Sn) serving as the flux material.

2.2 Material Characterization Techniques

Once single crystals are grown successfully, it is essential to characterize them to confirm their quality, composition, and structural properties. Characterization helps verify whether the desired phase has been achieved and whether the crystals are suitable for further physical property measurements. Various materials characterization techniques are essential to understand the structural, compositional, and morphological properties of a sample. X-ray diffraction (XRD) is used to identify crystal structure, lattice parameters, and phase purity. Energy dispersive X-ray spectroscopy (EDXS or EDS), often coupled with scanning electron microscopy (SEM), provides elemental composition and homogeneity of the elements. SEM offers high-resolution imaging to examine surface texture, grain boundaries, and particle size. Transmission electron microscopy (TEM) provides atomic-scale imaging and detailed information about crystal defects, interfaces, and internal structures. These characterization steps are essential to verify the quality and suitability of the grown crystals for further studies.

2.2.1 X-Ray Diffraction (XRD)

When an X-ray beam strikes a solid with a periodic atomic arrangement, such as a crystalline structure, the atoms in the crystal lattice scatter the X-rays (see fig. 2.3 (a)). The regular arrangement of atomic planes causes the scattered X-rays to interfere constructively at certain angles, producing a diffraction pattern that reflects the internal structure of the material. This phenomenon forms the basis for X-ray diffraction (XRD), a powerful technique used to investigate the crystallographic arrangement, identify phases, and determine the structural parameters of crystalline materials.

Bragg's Law is a fundamental relation that describes the condition for constructive interference of X-rays scattered by the periodic atomic planes in a crystalline material. It is expressed mathematically as

$$2d \sin\theta = n\lambda \tag{2.5}$$

where n is the order of reflection (an integer), λ is the wavelength of the incident X-rays, d is the spacing between atomic planes in the crystal, θ is the angle of incidence (also known as the Bragg angle). Strong diffraction peaks are observed when the path length difference between X-rays reflected from adjacent atomic planes is an integer multiple of the incident X-ray wavelength (λ).

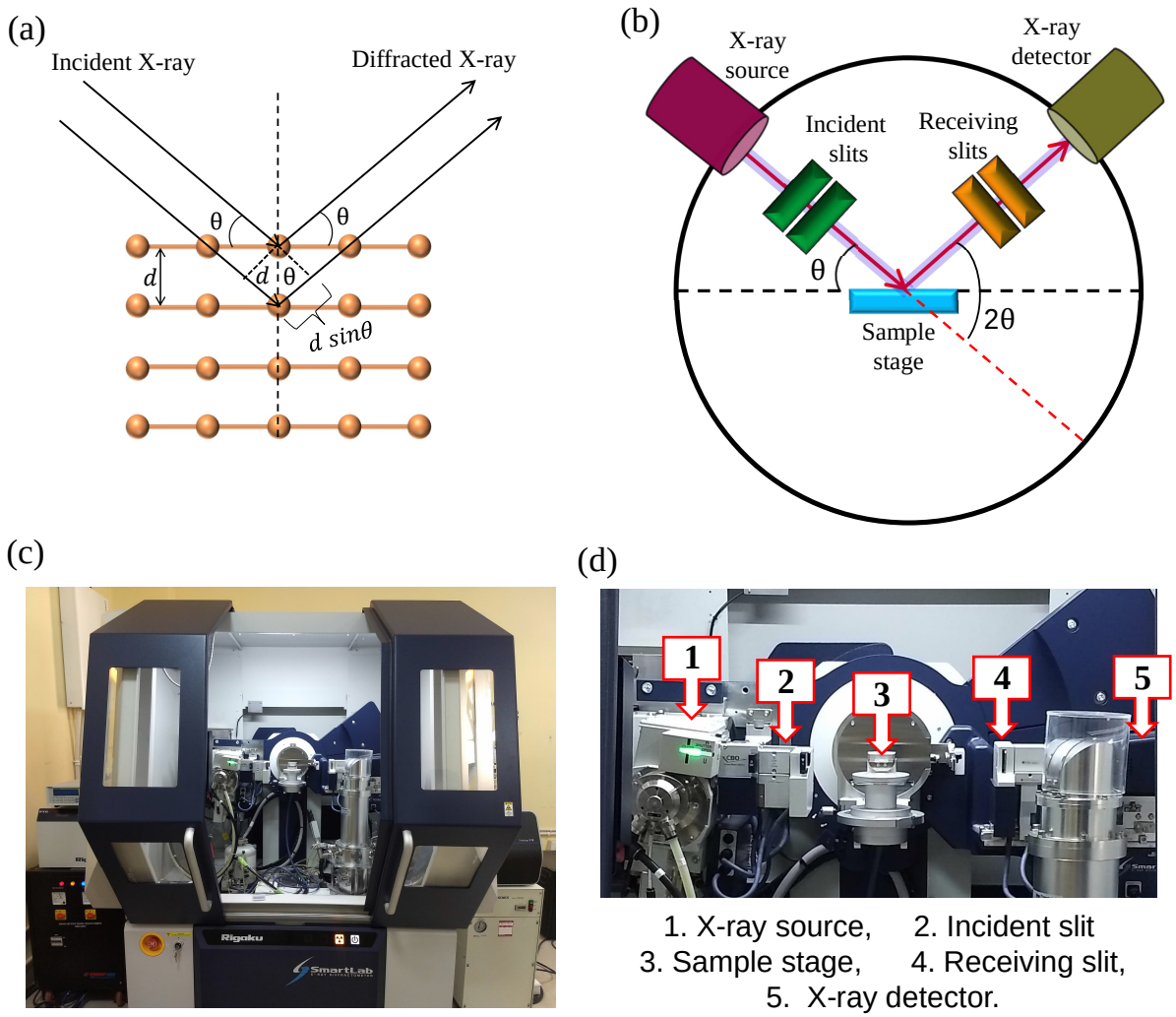

Figure 2.3: (a) Schematic representation of X-ray beams diffracting off crystal lattice planes (Bragg's planes). (b) A schematic view of the core components of an X-ray diffractometer system. (c) The 9 KW Rigaku SmartLab XRD instrument at SNBNCBS, utilized for precise structural analysis of our samples. (d) Different components of the XRD instrument. The component names that are indicated by numbers are listed at the bottom.

In XRD analysis, by precisely measuring the angles (2θ) at which these intense diffraction peaks occur for a known X-ray wavelength, we can utilize Eq. 2.5 to determine the interplanar spacings (d), characteristic of the crystal structure. The diffraction pattern, characterized by the positions and intensities of the peaks, serves as a unique signature for identifying crystalline phases. It also offers valuable information on unit cell parameters, crystallite size, and the various phases present within the material.

After obtaining the diffraction pattern, Rietveld refinement was carried out using FullProf software to accurately determine the crystal structure, lattice parameters, and other structural details. Rietveld refinement is a whole-pattern fitting method in XRD that refines a theoretical diffraction pattern against experimental data to extract detailed structural information. It starts with a crystal structure model and instrumental param-

eters, iteratively adjusting them to minimize the difference between the calculated and observed patterns using a least-squares approach. This allows for precise determination of lattice parameters, atomic positions, site occupancies, thermal parameters, and can also provide quantitative phase analysis, crystallite size, microstrain, and texture information. By analyzing the entire diffraction pattern, Rietveld refinement offers a comprehensive and accurate characterization of crystalline materials, especially complex systems and mixtures.

XRD measurements in this work were performed using a high-power Rigaku SmartLab diffractometer (9 kW) equipped with a Cu-Kα radiation source ($\lambda = 1.5406$Å), as illustrated schematically in Figures 2.3 (c) and 2.3 (d). The X-ray generation process begins inside a high-vacuum X-ray tube, where thermionic emission from a heated tungsten (W) filament produces a focused electron beam. This beam is accelerated by a high voltage, typically ranging from 20 to 45 kV, and directed towards a copper (Cu) anode. When the electron beam hits the copper anode, it generates characteristic Cu-Kα X-rays, predominantly Kα_1. These X-rays are then refined using a series of primary slits that filter and collimate the beam to produce a narrow and well-focused incident X-ray beam. The resulting X-ray beam is directed onto the surface of the sample, where it interacts with the crystal planes and is diffracted according to Bragg's Law. The diffracted rays are subsequently refined through a series of optical components, including a parallel slit analyzer, Soller slits, and a receiving slit, which enhance angular resolution and signal clarity. Detection of the diffracted X-rays is carried out using a high-sensitivity hybrid photon counting (HPC) detector that ensures accurate peak identification and intensity measurement.

The Rigaku SmartLab system operates in a $\theta - \theta$ goniometer geometry, where both the X-ray source and detector move symmetrically around a fixed sample stage. This allows precise control over the incident and detection angles, labeled as θ for the source and θ for the detector, respectively. For comparison, other systems such as the Rigaku MiniFlex II use a geometry $\theta - 2\theta$, in which the X-ray tube remains fixed while the detector rotates by 2θ to track the diffracted beams. This configuration is commonly used in conventional powder XRD setups. The combination of high beam power, advanced optics, and precise goniometer control in the SmartLab setup enables high-resolution structural analysis of crystalline materials.

2.2.2 Energy Dispersive X-ray Spectroscopy (EDXS)

Energy Dispersive X-ray Spectroscopy (EDXS or EDS) is a powerful analytical technique used to determine the elemental composition of materials at the microscale. It is commonly integrated with high-resolution imaging systems such as scanning electron

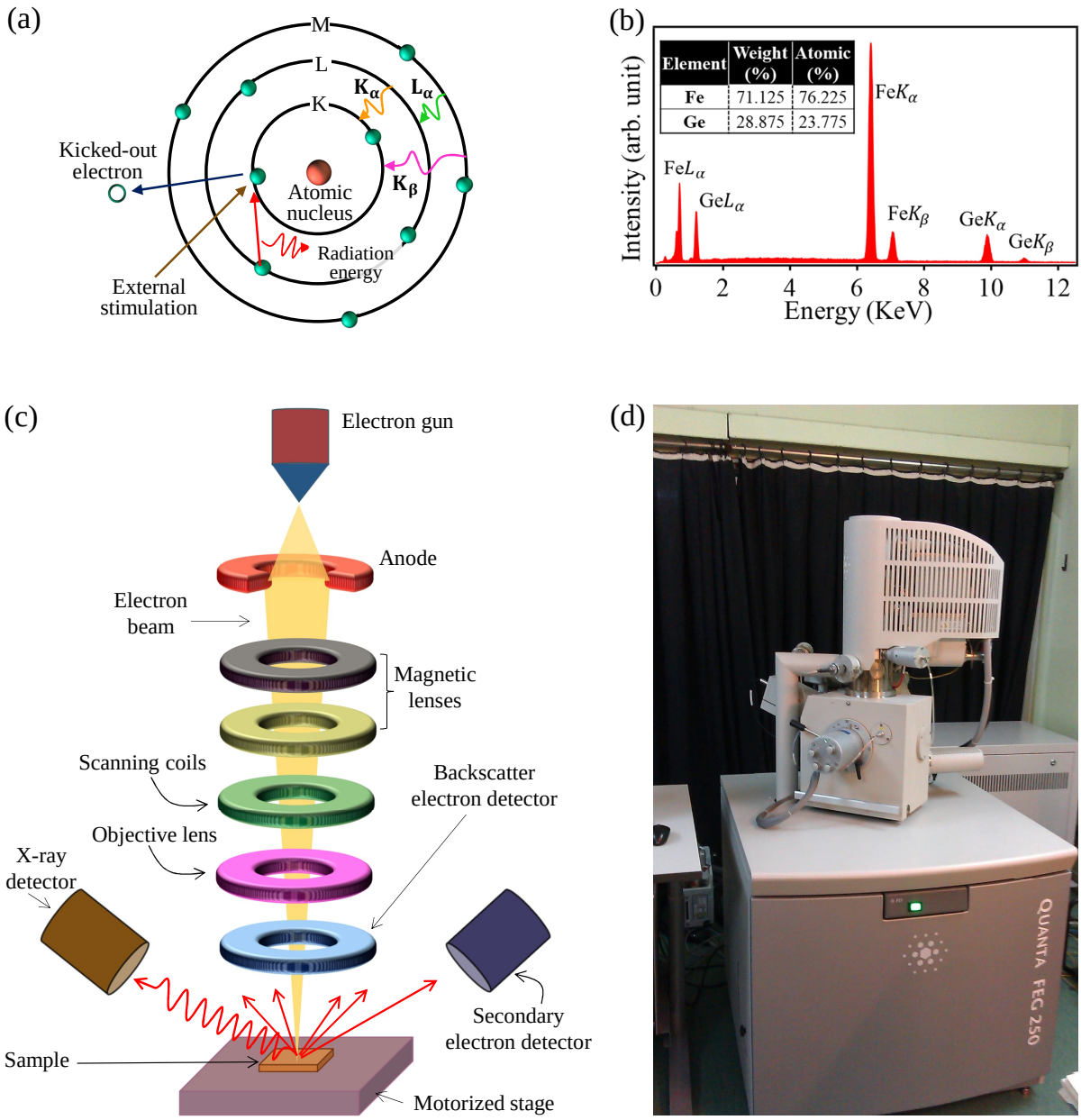

Figure 2.4: (a) Characteristic X-ray lines, such as K and L lines, arise when electrons from higher energy levels transition to lower inner shells, releasing energy as X-rays. (b) A typical EDXS spectrum displays the characteristic X-ray peaks emitted by the elements present in the Fe_3Ge sample. (c) Schematic illustration showing the key components of a scanning electron microscope (SEM). (d) A photograph of an EDXS system integrated with the FE-SEM was used for characterizing our samples at SNBNCBS.

microscopes (SEM) or transmission electron microscopes (TEM), allowing for simultaneous structural and compositional analysis. By detecting characteristic X-rays emitted from the sample upon interaction with a focused electron beam, EDS provides qualitative and quantitative information about the elements present in a localized region of the specimen.

The fundamental principle of EDXS is based on the interaction between a high-

energy electron beam and atoms in a solid specimen. When a high-energy electron beam hits the sample, it knocks out electrons from the inner parts of the atoms. This creates empty spaces, or vacancies, in those inner shells. To fill these gaps, electrons from higher shells come down, and as they do, they release energy in the form of X-rays. These X-rays have specific energies that help identify which elements are in the sample. The energy carried by the emitted X-rays corresponds to the difference between two specific energy levels within an atom, which are characterized by their principal quantum number, n. These energy levels are organized into electron shells designated as K, L, M, and N, corresponding to principal quantum numbers $n = 1, 2, 3$, and 4, respectively. Figure 2.4(a) illustrates how characteristic X-rays are produced through electron transitions between these shells. For example, when an electron moves from the L shell down to fill a vacancy in the K shell, the emitted X-ray is called K_α. Similarly, an electron moving from the M shell to the K shell results in K_β X-rays. Transitions from the M and N shells down to the L shell generate L_α and L_β X-rays, respectively. These distinct X-ray energies serve as elemental signatures in energy-dispersive X-ray spectroscopy.

Each element in the periodic table has a unique atomic structure, which results in the emission of characteristic X-rays with specific energies when the atoms are excited. By detecting these characteristic X-rays, it is possible to identify the elements present in a sample. Figure 2.4(b) shows the EDS spectrum of Fe_3Ge, highlighting the characteristic peaks such as K_α, K_β, L_α, and L_β for elements like iron (Fe) and germanium (Ge). The intensity of these peaks depends on how likely certain electron transitions are to occur. For example, transitions from the L shell to the K shell happen more frequently than those from the M shell to the K shell, which explains why K_α peaks are generally stronger than K_β peaks for both Fe and Ge. To perform quantitative analysis, the background signal is first removed from the measured spectrum. Then, the relative intensities of the element-specific peaks are used to calculate their weight percentages. Finally, atomic percentages are obtained by normalizing these values using the atomic weights of the respective elements.

Figure 2.4(d) shows the complete setup used for EDS analysis, integrated with a Field Emission Scanning Electron Microscope (FESEM). For EDS measurements, the sample is placed under a low vacuum (1 mbar), and an electron beam with an accelerating voltage of 20–25 kV is directed onto its surface. The interaction between the beam and the sample generates characteristic X-rays unique to each element. These X-rays are then detected using a Silicon Drift Detector (SDD), and the resulting spectrum is analyzed to determine the elemental composition based on the intensity of each characteristic X-ray line.

2.2.3 Field Emission Scanning Electron Microscopy (FESEM)

Field Emission Scanning Electron Microscopy (FESEM) is an advanced imaging technique widely used for characterizing the surface morphology of materials with nanometer-scale resolution. Unlike conventional SEM, which uses thermionic electron sources, FESEM employs a field emission gun that generates a highly coherent and intense electron beam. This beam, due to its reduced spot size and higher brightness, allows for significantly improved spatial resolution, often down to sub-nanometer levels.

The working principle of FESEM is based on scanning a finely focused electron beam across the sample surface. When the primary electrons interact with the atoms of the sample, various signals such as secondary electrons (SE), backscattered electrons (BSE), and characteristic X-rays are emitted. These signals are collected by detectors to form detailed images and to perform compositional analysis. SE imaging is particularly useful for studying surface topography, while BSE imaging provides contrast based on atomic number, and EDS (Energy Dispersive X-ray Spectroscopy) enables elemental identification.

The internal configuration of a typical FESEM setup, as schematically illustrated in Fig. 2.4(c), includes a field emission electron gun, a series of electromagnetic lenses for beam focusing, and scanning coils for beam deflection. The electron beam is first emitted by the gun and then passes through a series of condenser and objective lenses, which refine its focus before it strikes the sample surface. This focused interaction enables high-resolution visualization of features such as surface roughness, porosity, texture, and defects.

FESEM is employed to determine the presence of grain boundaries in the sample. In a single crystalline phase, grain boundaries are absent, whereas in a polycrystalline phase, grain boundaries are visible in the FESEM images. Therefore, FESEM analysis serves as a valuable tool for verifying the quality and crystallinity of the sample.

2.2.4 Transmission Electron Microscopy (TEM)

Transmission Electron Microscopy (TEM) is a powerful technique used to study the internal structure of materials at atomic to nanometer scales. Unlike Scanning Electron Microscopy (SEM), which provides surface information, TEM allows researchers to investigate the internal microstructure by transmitting a high-energy electron beam (typically 100–300 keV) through an ultra-thin sample, usually less than 100 nanometers thick. As the electrons pass through the specimen, they interact with the atomic potentials within the material, resulting in various scattering events. These interactions produce transmitted, diffracted, and scattered electrons that carry detailed information about the sample's crystallography, defects, grain boundaries, and phase composition.

The core components of a TEM system include an electron gun (usually a thermionic

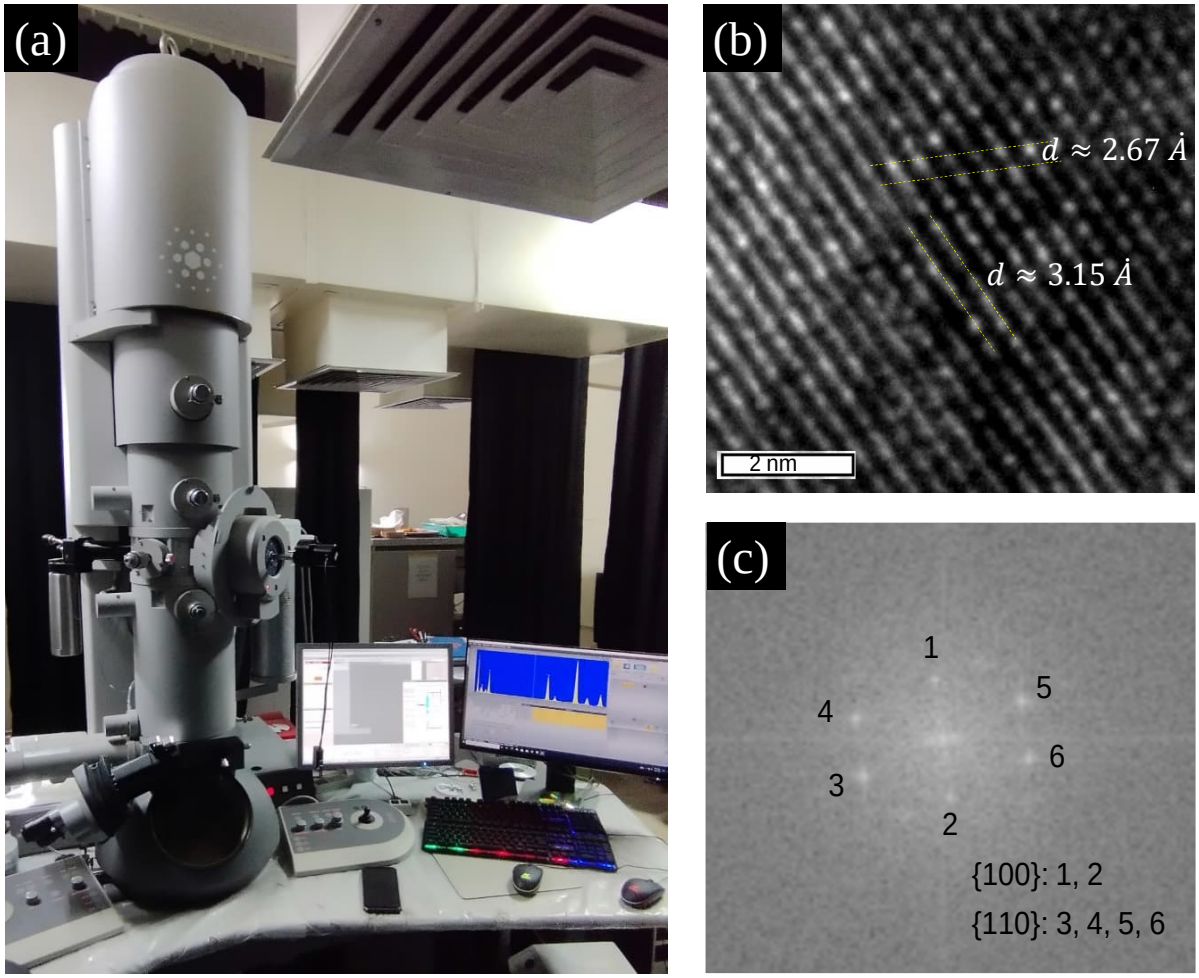

Figure 2.5: (a) Photograph of the TECNAI TEM instrument at SNBNCBS used for transmission electron microscopy analysis. (b) High-resolution TEM image of Mn_3Ge, showing real-space lattice fringes from which interplanar spacing is determined. (c) Selected Area Electron Diffraction (SAED) pattern of Mn_3Ge, representing the reciprocal space lattice structure.

or field emission source), electromagnetic condenser lenses to focus the electron beam, an objective lens to form the initial image, and intermediate and projector lenses to magnify the image onto a fluorescent screen or camera. Depending on how the electrons interact with the sample, different imaging and analytical modes can be employed, such as bright-field imaging, dark-field imaging, selected area electron diffraction (SAED), and high-resolution TEM (HRTEM). Advanced techniques like Energy dispersive X-ray spectroscopy (EDS) can also be integrated for elemental analysis. TEM provides unmatched spatial resolution, making it an essential tool in materials science, nanotechnology, and condensed matter physics for understanding structure-property relationships at the atomic scale.

Figure 2.5 (a) shows the image of the TECNAI TEM instrument at SNBNCBS used for transmission electron microscopy analysis. Figure 2.5(b) presents the high-

resolution transmission electron microscopy (HRTEM) image of Mn_3Ge, revealing well-defined lattice fringes corresponding to atomic planes in real space. These fringes arise from the periodic arrangement of atoms within the crystal structure and provide direct visual evidence of crystallinity. By measuring the spacing between adjacent fringes, the interplanar spacing (d-spacing) can be accurately determined, offering valuable structural information at the atomic scale. This analysis is essential for confirming phase purity, crystallographic orientation, and overall structural integrity of the material. Figure 2.5(c) shows the selected area electron diffraction (SAED) pattern of Mn_3Ge, which represents the reciprocal space projection of the crystal lattice. The SAED pattern consists of a series of diffraction spots arranged in a specific symmetry, corresponding to the periodic atomic arrangement within the material. The sharpness and regularity of the spots indicate a high degree of crystallinity, while the spacing and symmetry of the pattern provide information about the crystal structure, orientation, and possible presence of defects or secondary phases.

2.3 Magnetic Measurements

Magnetic characterization of the samples was carried out using the Vibrating Sample Magnetometer (VSM) module integrated into the Quantum Design Physical Property Measurement System (PPMS). This technique is based on the principle of electromagnetic induction, specifically Faraday's law, which states that a time-dependent magnetic flux through a closed loop generates an electromotive force (EMF). In practice, the sample is subjected to a uniform external magnetic field to induce magnetization and is mechanically vibrated in a sinusoidal motion perpendicular to the direction of the applied field. As the magnetized sample oscillates, the magnetic flux it produces changes with time. This dynamic flux passes through a set of fixed pickup coils positioned around the sample, resulting in an induced voltage. According to Faraday's law, the induced EMF is given by

$$\epsilon = -\frac{d\Phi_B}{dt} \tag{2.6}$$

where Φ_B is the magnetic flux and ϵ is the resulting EMF. The negative sign, as described by Lenz's law, indicates that the induced EMF opposes the change in flux.
The induced voltage in the pickup coils is directly proportional to the magnetic moment of the sample. This weak signal is amplified and extracted using a lock-in amplifier, which locks onto the vibration frequency to separate the signal from noise. By analyzing the output voltage, one can determine key magnetic parameters such as saturation magnetization, remanence, coercivity, and the shape of the hysteresis loop.

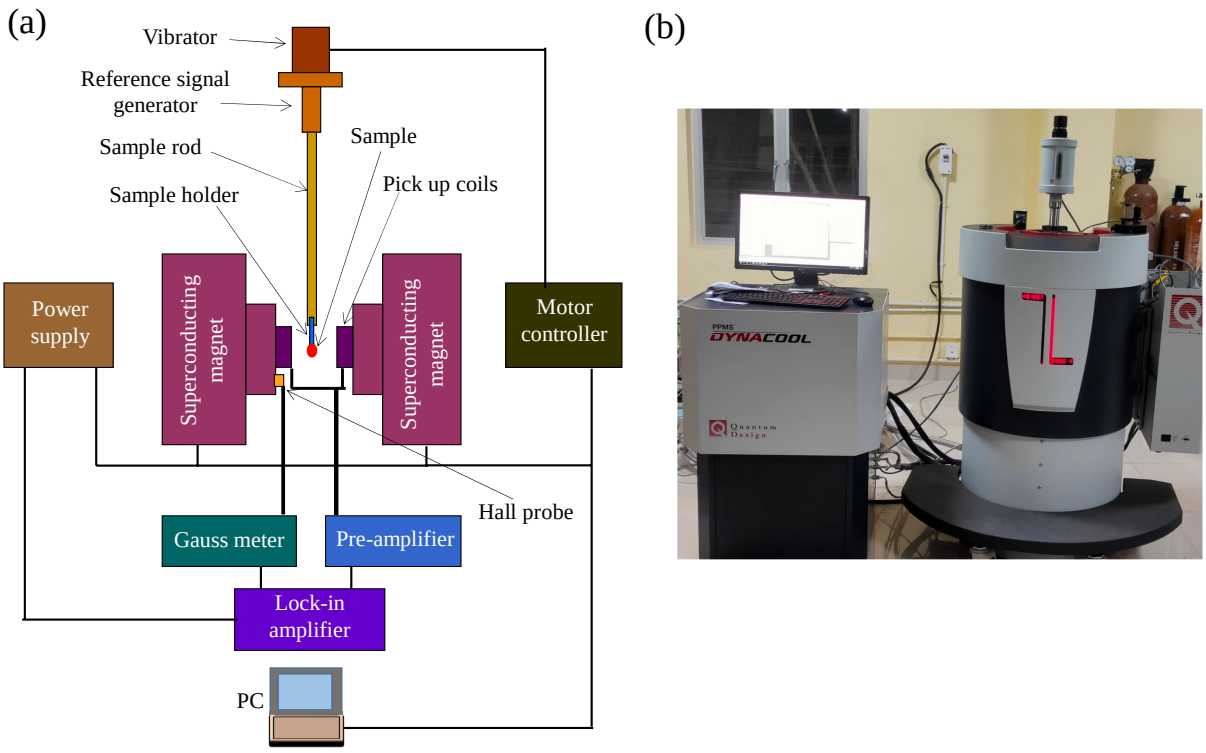

Figure 2.6: (a) Schematic illustration of the VSM device. (b) Photograph of the Quantum Design PPMS instrument with VSM attachment.

A schematic representation of the VSM setup is shown in Fig. 2.6 (a). The sample is mounted on a non-magnetic rod that is attached to a vibrating unit. This rod moves the sample up and down within a superconducting magnet that generates a highly uniform magnetic field. As the sample oscillates, it modulates the magnetic flux through nearby detection coils. For sinusoidal motion with vibration frequency f and amplitude A, the induced voltage in the pickup coils can be described as:

$$V_{\text{coil}} = 2\pi f C m A \sin(2\pi f t) \tag{2.7}$$

where C is a calibration constant determined by the system geometry, and m is the sample's magnetic moment. Measuring this voltage allows for accurate quantification of the magnetic response under various applied magnetic fields.

All measurements in this work were performed using the VSM option in the QD-PPMS system at SNBNCBS (see figure 2.6 (b)), which provides precise control over magnetic fields up to 9 T and temperatures ranging from 2 K to 400 K. The standard vibration frequency used was 40 Hz. The system offers high sensitivity, capable of detecting magnetic moments as small as 10^{-6} emu. Furthermore, the VSM module includes a high-temperature oven attachment, enabling measurements to be extended to elevated temperatures in the range of 400 K to 1000 K, thereby supporting comprehensive mag-

netic studies across a wide thermal span.

2.4 Electrical Transport Measurement

Electrical resistivity measures the inherent resistance of a material to electric current, serving as a key metric to distinguish conductors, semiconductors, and insulators on the basis of their conductive properties. An applied electric or magnetic field induces the movement of charge carriers (usually electrons) through a material. As these carriers propagate, they experience scattering from various sources, including other electrons, phonons, spins, holes, and impurities. These scattering mechanisms, specifically electron-electron, electron-phonon, electron-spin, electron-hole, and electron-impurity interactions, collectively determine carrier mobility and ultimately govern the material's electrical resistivity. By measuring resistivity, we can gain valuable insight into interactions and better understand the transport behavior and underlying physics of the material.

2.4.1 Four Probe Method

The four-probe technique is a reliable method to accurately measure electrical resistivity, especially in materials with low resistance, such as metals. Since the samples studied in this thesis exhibit metallic behavior, precise measurement is crucial. To ensure accuracy and eliminate contact resistance effects, the four-probe method was used for all resistivity measurements in this work. Two widely used methods for measuring the electrical resistivity of solid materials using the four-probe technique are (i) the linear four-probe method and (ii) the Van der Pauw method. In the linear four-probe method, four collinear contacts are placed on the sample surface, the current is applied through the two outer probes, while the voltage is measured across the two inner probes. On the other hand, in the Van der Pauw method, four small contacts are positioned at the periphery of the sample, and resistivity is determined through multiple current-voltage measurements in different configurations (see fig.2.7 (a))[2]. For all transport measurements in this work, I primarily used the linear four-probe technique because of its suitability for the sample geometry and its straightforward approach to accurately determine electrical resistivity.

A schematic representation of the standard four-probe resistivity measurement setup is shown in Fig. 2.7(a). In this measurement setup, a lock-in amplifier serves as an AC voltage source that drives current through the sample and a known reference resistor R_L, which are connected in series. As the sample resistance R_S is very small, R_L is included in the circuit to limit the voltage drop across the sample, thereby minimizing Joule heating and preventing thermal damage. Let V_S be the voltage drop across the sample and V_L the voltage drop across the reference resistor R_L. Since both components

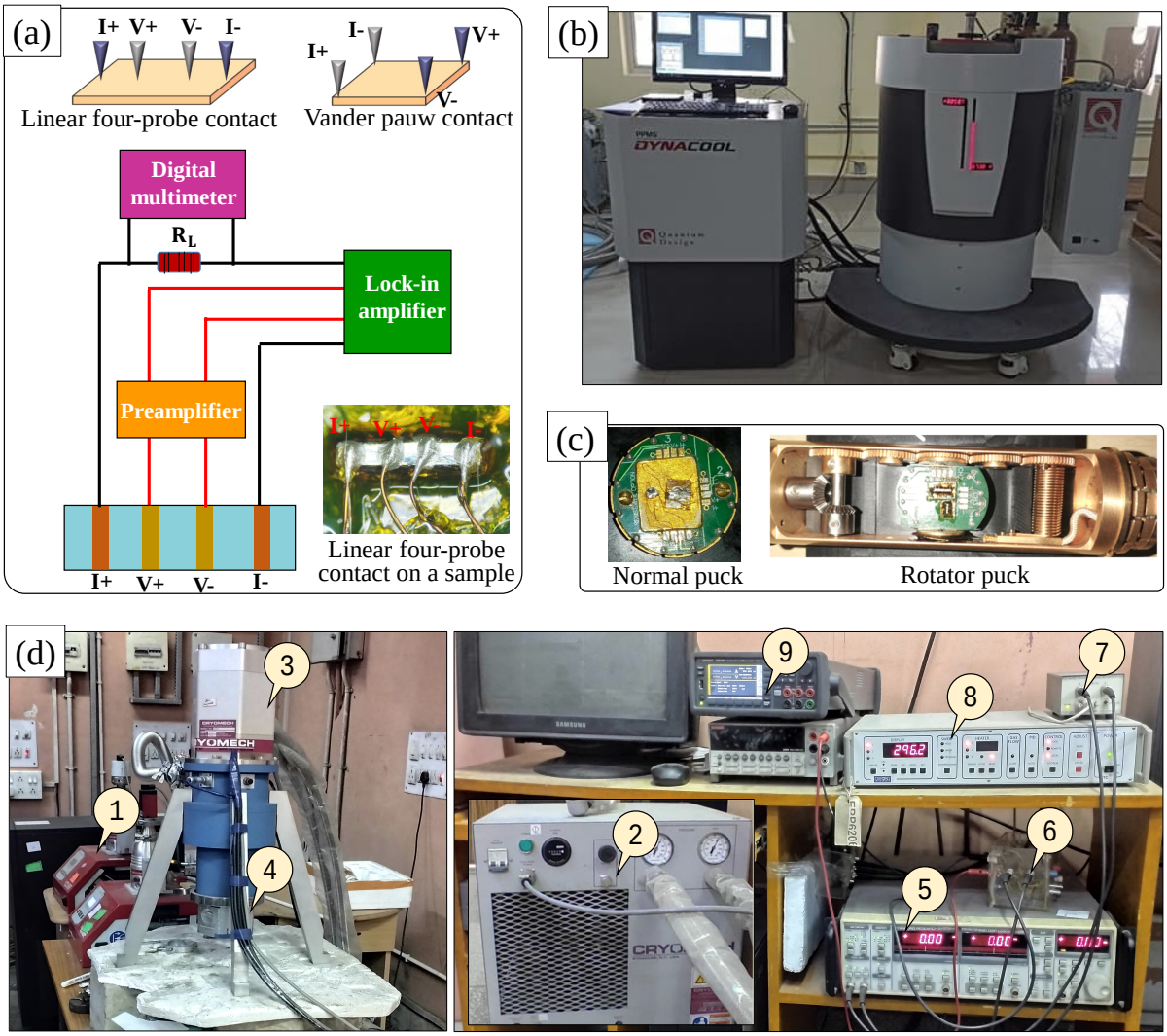

Figure 2.7: (a) Schematic illustration of the four-probe configuration used for resistivity measurements. Typical Van der Pauw and linear arrangements for four-probe resistivity measurements are shown in the top drawings. The bottom right inset shows the photograph of a linear four-probe connection on a single crystal. (b) An image of the Quantum Design PPMS system at SNBNCBS, which measures resistivity in the presence of changing magnetic fields, temperatures, and rotational angles. (c) Snapshots of normal and rotator puck. (d) Image of the in-house resistivity setup designed for temperature-dependent resistivity measurements. The component names that are indicated by numbers with off-white circles are listed at the bottom.

are in series, the same current I flows through them, and it can be expressed as:

$$I = \frac{V_L}{R_L}. \tag{2.8}$$

Using Ohm's law, the sample resistance is given by:

$$R_S = \frac{V_S}{I} = \frac{V_S}{V_L} \times R_L. \tag{2.9}$$

Therefore, the sample resistance R_S can be accurately determined by measuring the voltages V_S and V_L, along with the known resistor R_L.

Copper wires were employed to establish the four-probe connections. The wires were attached to the samples using vacuum-compatible Epo-Tek H2OE silver epoxy. A high-resolution Leica S9i microscope was utilized to accurately position the four-probe contacts on the sub-millimeter-sized samples for these measurements. Temperature-dependent resistivity measurements without an applied magnetic field were performed using our in-house resistivity setup (Fig. 2.7(d)) over the temperature range of 3.5 to 320 K. For measurements involving variations in temperature, magnetic field, and rotational angle, a Quantum Design PPMS equipped with both the ETO and rotator options (Fig.2.7(b)) was used. This system enables magnetic fields up to 9 T, temperature control from 2 to 360 K, and full 360-degree sample rotation.

2.4.2 Low-Temperature Resistivity Setup

For resistivity measurements using the low-temperature resistivity setup, the sample was mounted on the sample stage of a CRYOMECH closed-cycle refrigerator (CCR)-based cryostat, which allows cooling down to 3.5 K. The sample temperature was controlled through a multi-step process. First, the cryostat was evacuated using a Pfeiffer turbomolecular pump (TMP) to create a vacuum environment essential for efficient thermal isolation. Once the desired vacuum level was achieved, a Cryomech compressor was activated to cool the cryostat, bringing the temperature down to approximately 3.5 K. After reaching the base temperature, a temperature sweep was carried out using an Oxford Instruments ITC 503 PID controller, allowing precise and stable control of the temperature during measurements. An AC voltage in the range of 1–5 V at a frequency of 111.11 Hz was applied across the sample and a standard series resistor R_L (typically 1–2 kΩ) using a Stanford Research Systems SR830 digital signal processing (DSP) lock-in amplifier. The voltage drop across the reference resistor V_L was measured using a Keithley 2000 digital multimeter (DMM). To measure the voltage drop across the sample V_S, the differential voltage leads (V^+ and V^-) were first connected to an SR554 transformer preamplifier, which amplified the signal by a factor of 100. The amplified signal was then fed back into the lock-in amplifier for detection. Temperature control was achieved using an Oxford Instruments™ ITC-503 temperature controller, which regulated the rate of temperature change during the experiment. The sample temperature was monitored using an Rh-Fe thermocouple mounted on the sample stage. To automate and monitor the entire measurement process, all instruments were interfaced with a desktop computer via

a General Purpose Interface Bus (GPIB). A custom LabVIEW program was employed for instrument control and data acquisition.

2.4.3 ETO and Rotator Option in 9T QD-PPMS

We performed field-dependent and temperature-dependent resistivity measurements, including magnetoresistance and Hall effect studies, using the 9T Quantum Design Physical Property Measurement System (QD-PPMS) equipped with the Electrical Transport Option (ETO) at our institute's central facility (SNBNCBS). We utilized the system's rotator option for angle-dependent magnetoresistance measurements, which provides precise control over the sample orientation relative to the applied magnetic field direction. This advanced setup allowed us to thoroughly study how the transport properties of our samples change with direction, temperature, and magnetic field.

The snapshot of the 9T QD-PPMS set-up is shown in Figure 2.7(b). Superconducting electromagnets are ideal for generating high magnetic fields, as they exhibit zero electrical resistance below their critical temperature and therefore do not produce heat during operation. In the PPMS system, the magnet is constructed from a niobium-titanium (Nb-Ti) alloy, which becomes superconducting below approximately 10 K [3]. To maintain this superconducting state, the magnet is enclosed in a cryogenic chamber and cooled to 4.2 K using a Cryomech helium compressor. The magnetic field strength is regulated through a programmable current supply, which precisely controls the current flowing through the superconducting magnet. The entire measurement system is interconnected with a central control unit, enabling automated data acquisition, instrument calibration, and real-time monitoring of experimental parameters. Two types of sample pucks were used for resistivity measurements, as shown in Fig. 2.7(c). The ETO option of the PPMS was utilized to perform temperature- and field-dependent measurements using a standard puck, commonly referred to as the normal puck. In cases where angle-dependent measurements were required, the sample was mounted on a rotator puck, allowing precise angular control via the rotator option of the system. Resistivity measurements were performed using an AC excitation current applied to the sample, as detailed in the previous section. For magnetoresistance measurements, a standard linear four-probe configuration was employed. In Hall effect measurements, a transverse geometry was utilized, where the voltage leads were oriented perpendicular to the current leads, and the magnetic field was applied perpendicular to both the current and voltage directions.

2.5 Specific Heat Measurements

Specific heat measurement is an effective method to study phase transitions in materials. It often shows noticeable changes at critical temperatures, indicating variations

in electronic, phononic or magnetic behavior. The total specific heat of a solid is given by $C = C_{\text{el}} + C_{\text{ph}} + C_{\text{mag}}$, where C_{el} is the electronic part, C_{ph} is due to lattice vibrations, and C_{mag} comes from magnetic contributions. The temperature dependence of specific heat is usually analyzed using the Debye and Einstein models, which describe how atoms vibrate in a crystal.

In the Quantum Design PPMS, specific heat is measured using the thermal relaxation method. The sample is attached to a thermally isolated platform with Apiezon-N grease to ensure good heat transfer. This platform, equipped with a heater and a thermometer, is suspended by thin wires that provide both thermal isolation and electrical connections. During the measurement, a known amount of heat is applied to raise the temperature of the platform (heating phase). After heating stops, the platform cools down, and the temperature decay is recorded (relaxation phase). This cooling follows an exponential trend defined by a relaxation time constant (τ). The specific heat is then determined using the formula $C = K \cdot \tau$, where K is the thermal conductance of the system. Measurements are performed under vacuum conditions to reduce heat loss from convection, thereby improving accuracy. To isolate the specific heat of the sample, the heat capacities of the platform and Apiezon-N grease (collectively called addenda) are measured separately and subtracted from the total. This approach enables the precise and sensitive determination of specific heat over a broad range of temperatures and magnetic fields.

References

[1] H. Bhat, Introduction to Crystal Growth: Principles and practice, 2014.

[2] L. J. van der PAUW, A method of measuring specific resistivity and Hall effect of discs of arbitrary shape, World Scientific, pp. 174–182.

[3] D. Patel, S. H. Kim, W. Qiu, M. Maeda, A. Matsumoto, G. Nishijima, H. Kumakura, S. Choi, J. H. Kim, Niobium-titanium (Nb-Ti) superconducting joints for persistent-mode operation, Scientific Reports 9 (2019).

Chapter 3

Unusual Multiple Magnetic Transitions and Anomalous Hall Effect Observed in Antiferromagnetic Weyl Semimetal, $Mn_{2.94}Ge$ (Ge-rich)

3.1 Introduction

Topological materials such as the topological insulator (TI), the Dirac semimetal (DSM), and the Weyl semimetal (WSM) are some of the most widely discussed systems in recent days in the class of topological quantum materials. In Dirac semimetals, the nodal points are protected by both time-reversal and inversion symmetry [1, 2]. Breaking the time-reversal or inversion symmetry creates a Weyl semimetal [3, 4]. In this way, we can have two types of Weyl semimetals based on the broken symmetry, such as the non-magnetic Weyl semimetal created by the inversion symmetry breaking [5, 6] and the magnetic Weyl semimetal (MWSM) created by breaking the time-reversal symmetry [7]. Interestingly, in the presence of magnetism, the topological materials exhibit exotic quantum phenomena such as the quantum anomalous Hall effect (QAHE), large intrinsic AHE, topological Hall effect (THE), Chern insulating state, etc. [8–10]. Though many magnetic Weyl semimetals have been predicted theoretically, only a few have been experimentally realized, such as $Co_3Sn_2S_2$ [11, 12], Co_2MnGa [13], Mn_3Sn [14], Fe_3Sn_2 [15] and $YbMnBi_2$ [16].
Among the MWSMs, noncollinear and coplanar Mn_3X (X = Sn and Ge) antiferromagnets have recently received a great deal of attention from the research community due to their distinct magnetic and topological properties despite sharing a similar crystal structure. For instance, Mn_3Sn shows a magnetic transition within 260–275 K from a

high-temperature noncollinear AFM order to a low-temperature spin-spiral structure [17–19]. In contrast, no such magnetic transition has been observed to date in Mn_3Ge down to the lowest possible temperature [20–24]. Few other reports demonstrated the topological Hall effect (THE) in addition to the anomalous Hall effect (AHE) in $Mn_{3-x}Sn$ [25, 19], while Mn_3Ge is mainly known to show the AHE without THE. Nevertheless, the anomalous Hall effect found in both systems mainly originated from the nonzero Berry-phase in the momentum space [20, 24, 26, 27]. Further, the electronic and magnetic properties of Mn_3X (X = Sn and Ge) are sensitive to the Mn concentration and crystal growth techniques [28, 21, 22]. Mn_3Ge can have either a hexagonal or tetragonal phase depending on the synthesis procedure and annealing temperature [29, 30].

The tetragonal Mn_3Ge shows a ferrimagnetic ordering at a Curie temperature of $T_C \approx$ 710 K, and the hexagonal Mn_3Ge shows antiferromagnetic (AFM) ordering at a Néel temperature of $T_N \approx$ 365-400 K [20, 22, 31, 30]. In the hexagonal phase, the neutron diffraction studies revealed an inverse triangular spin-structure with Mn moments aligned within the kagome layers to create a 120° spin-structure of noncollinear antiferromagnetic ordering [21, 32]. Besides the noncollinear AFM ordering, a tiny ferromagnetic moment is observed in these systems due to the geometrical frustration among the Mn magnetic moments within the Kagome lattice network [21, 33]. This tiny spontaneous magnetization combined with the nonzero momentum-space Berry phase gives rise to large AHE at low temperatures [20, 22]. Generally, these systems are grown with excess Mn, such as $Mn_{3+x}X$ where x varies between 0.2 and 0.4 [34, 20–22]. However, recent studies showed that the self-flux technique can grow the $Mn_{3-x}Sn$ crystals with Sn-rich [17, 19].

In this contribution, we report on the successful growth of high-quality $Mn_{2.94}Ge$ (Ge-rich) single crystals, and a thorough study of the magnetic and Hall effect properties. The magnetic property study shows multiple magnetic transitions in this system, such as spin-reorientation (T_{SR}) and ferromagnetic-like transitions below the Néel temperature of 353 K. Also consistent with the magnetic measurements, the Hall effect data shows an unusual behavior around T_{SR}. The anomalous Hall conductivity (AHC) increases with increasing temperature up to T_{SR}, and then gradually decreases with increasing temperature. This observation is quite in contrast to the $Mn_{3+x}Ge$ (Mn-rich) system, as in $Mn_{3+x}Ge$ the AHC gradually decreases with increasing temperature, with the highest AHC obtained at the lowest temperatures [20, 22, 35]. We argue that the unusual Hall effect properties observed in the studied Ge-rich, $Mn_{2.94}Ge$, system are driven by the spin-reorientation transition similar to the Mn_3Sn. Our study suggests that the magnetic and Hall effect properties of Mn_3Ge are very sensitive to the Mn concentration present in the system.

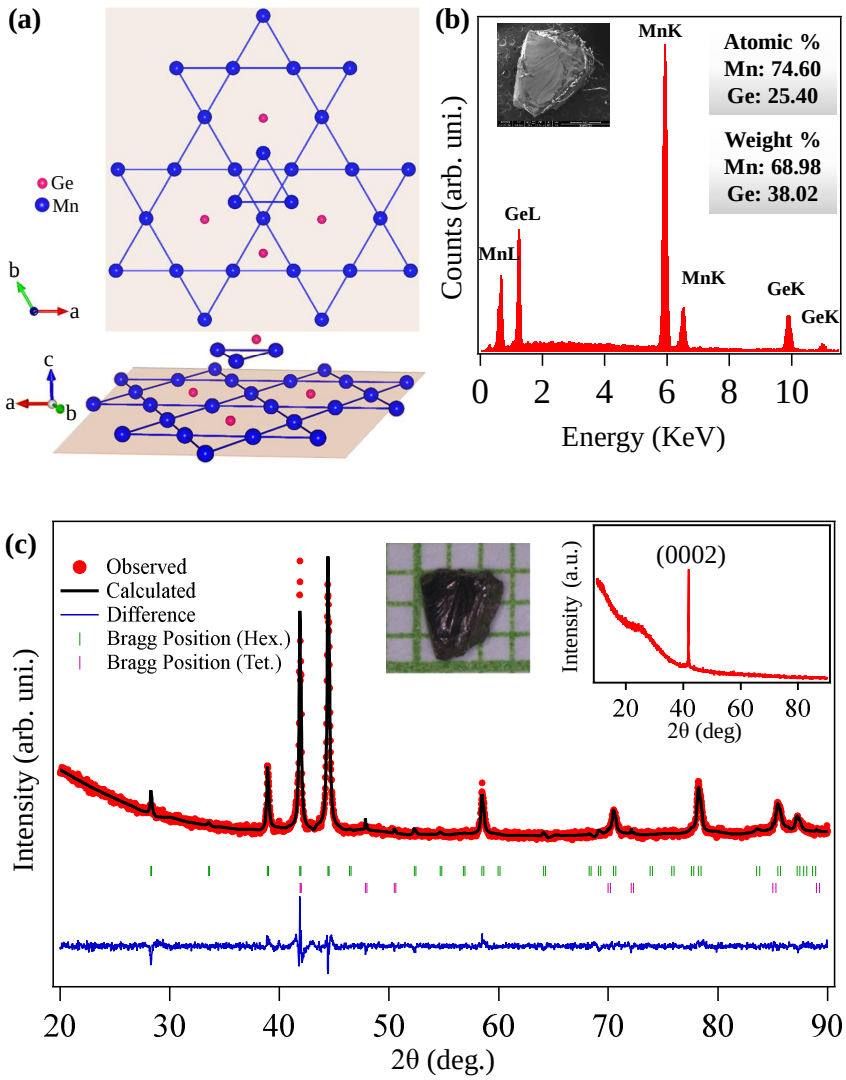

Figure 3.1: (a) Top view and side view of Mn_3Ge hexagonal crystal structure, showing the kagome lattice formed by the Mn atoms. (b) Energy dispersive X-ray spectroscopy (EDS) of $Mn_{2.94}Ge$ single crystal. (c) The powder X-ray diffraction pattern of crushed single crystals overlapped with the Rietveld refinement of $Mn_{2.94}Ge$ using hexagonal and tetragonal phases. Insets in (c) show a photographic image of $Mn_{2.94}Ge$ single crystal and an XRD pattern taken on the single crystal.

3.2 Experimental details

Single crystals of $Mn_{2.94}Ge$ were prepared by the melt-growth method using the high-temperature muffle furnace. In this method, Manganese (Alfa Aesar 99.95%) and Germanium (Alfa Aesar 99.999%) powders were taken in a ratio of 3.6:1, mixed thoroughly in the glove box under an argon environment before sealing in a preheated quartz ampoule in a vacuum of $10^{\breve{}4}$ mbar. The sealed quartz tube was then heated in the muffle furnace up to 1050^{o}C, and kept at that temperature for the next 24 hours. The tube was slowly cooled to 740^{o}C at 2 K/h. After prolonged annealing at 740^{o}C for five more days, the

ampoule was quenched in ice water to avoid low-temperature phases. In this method, the obtained Mn_3Ge single crystals were of a typical size of 2×2 mm^2 and looked shiny. Phase purity and crystal structure were checked using the powder X-ray diffraction (XRD) technique with Cu-K_α radiation in a Rigaku X-ray diffractometer (9 KW). Using energy dispersive X-ray spectroscopy (EDS), we find the actual chemical composition of as-prepared samples to be of $Mn_{2.94\pm0.03}Ge$, which is very close to the nominal composition of Mn_3Ge. Electrical transport, Hall effect, and magnetic properties studies were performed in a 9-Tesla physical property measurement system (PPMS, Dynacool, Quantum Design) within the temperature range of 2–380 K. Electrical transport and Hall effect measurements were performed using the four-probe technique. Copper leads were attached to the sample using EPO-TEK H21D silver epoxy. For a comparative study, we also grew the single crystals of $Mn_{3.20\pm0.02}Ge$ (Mn-rich).

3.3 Results and Discussions

3.3.1 Structural Properties

Mn_3Ge is known to crystalize into the Ni_3Sn-type hexagonal structure with a space group of $P6_3/mmc$ (194). The Mn atoms form the kagome lattice with triangles and hexagons in the *xy*-plane, while the Ge atom sits at the centre of the hexagon. A couple of such kagome lattice planes are stacked along the *z*-axis per unit cell, as shown in Fig. 3.1(a). Powder XRD pattern of crushed single crystals is shown in Fig. 3.1(c) overlapped with the Rietveld refinement performed using the hexagonal and tetragonal mixed phases. The Rietveld refinement confirms the majority phase of $Mn_{2.94}Ge$ to the hexagonal crystal structure with a small impurity tetragonal phase (3.5%). Earlier reports too suggested the presence of hexagonal and tetragonal mixed phases in these systems [22, 36]. Except for the small impurity tetragonal phase, we did not notice any other impurity phases such as Mn_5Ge_3, Mn_5Ge_2, $Mn_{11}Ge_8$, etc. [37–39] in our studied composition. Estimated hexagonal lattice parameters from the Rietveld refinement are a (b) = 5.3290(3) Å and c = 4.3047(6) Å, which are comparable to the previous reports on $Mn_{3+x}Ge$ [23, 24]. The XRD pattern taken on the single crystal of $Mn_{2.94}Ge$ is shown in the inset of Fig. 3.1(c), suggesting that the crystal growth plane is parallel to the *z*-axis.

3.3.2 Magnetic Properties

Magnetization as a function of temperature [$M(T)$] is measured in field-cooled (FC) and zero-field-cooled (ZFC) modes using a magnetic field (H) of 500 Oe applied parallel ($H \parallel z$) and perpendicular ($H \perp z$) to the *z*-axis as shown in Fig. 3.2(a). The $M(T)$ of $Mn_{2.94}Ge$ exhibits an anomalous hump-like structure at around 115 K, clearly visible

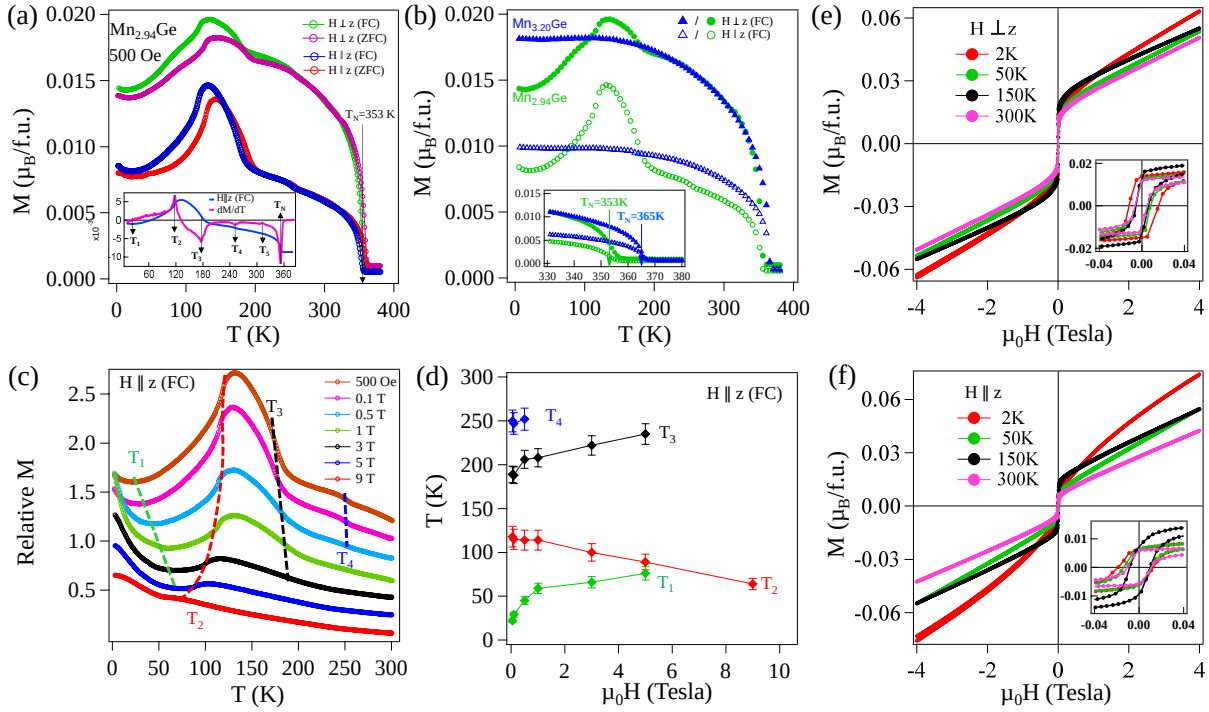

Figure 3.2: (a) Temperature-dependent magnetization, $M(T)$, measured in zero-field-cooled (ZFC) and field-cooled (FC) modes for $H \parallel z$ and $H \perp z$. Inset in (a) depicts dM/dT of FC $M(T)$ taken for $H \parallel z$, clearly showing multiple magnetic transitions $T_1 - T_5$ and a Néel temperature (T_N). (b) Overlapped $M(T)$ data of both $Mn_{2.94}Ge$ and $Mn_{3.20}Ge$ single crystals. The bottom inset in (b) demonstrates the change in Néel temperature (T_N) with Mn concentration. (c) $M(T)$ measured under various magnetic fields for $H \parallel z$ in FC mode. The dashed lines on the data are the eye-guides showing shifts in the transition temperatures with increasing applied fields, drawn with the help of dM/dT as shown in Fig.3.3). (d) Transition temperatures, T_1, T_2, T_3, and T_4, are plotted as a function of the applied field. The top-right inset in (d) shows $M(T)$ measured at different fields up to 9 T in the FC mode for $H \parallel z$. (e) and (f) Magnetization isotherms, $M(H)$, measured at different temperatures for $H \perp z$ and $H \parallel z$, respectively.

from both $H \perp z$ and H$\parallel z$ directions. In addition, several unusual magnetic transitions were also identified below the antiferromagnetic transition (T_N) of 353 K. To pinpoint the transition temperatures, we performed the first derivative of Magnetization to the temperature (dM/dT) as shown in the inset of Fig. 3.2(a). Thus, with the help of dM/dT, we could identify various unknown transition temperatures T_1 to T_5 and the AFM Néel temperature T_N. Fig. 3.2(b) shows a comparative $M(T)$ data between Mn-deficit $Mn_{2.94}Ge$ and Mn-excess $Mn_{3.20}Ge$ compounds. Foremost, we observe differing Néel temperatures between these two compounds such as T_N=365 K for $Mn_{3.20}Ge$ and 353 K for $Mn_{2.94}Ge$. Next, we do not observe the low-temperature hump-like structure in the Mn-excess $Mn_{3.20}Ge$, unlike in the Mn-deficit $Mn_{2.94}Ge$. The Néel temperature of 365 K in $Mn_{3.20}Ge$ is consistent with previous reports on similar Mn-excess $Mn_{3+x}Ge$ systems. Here, the T_N varies between 365 and 400 K depending on the amount of excess

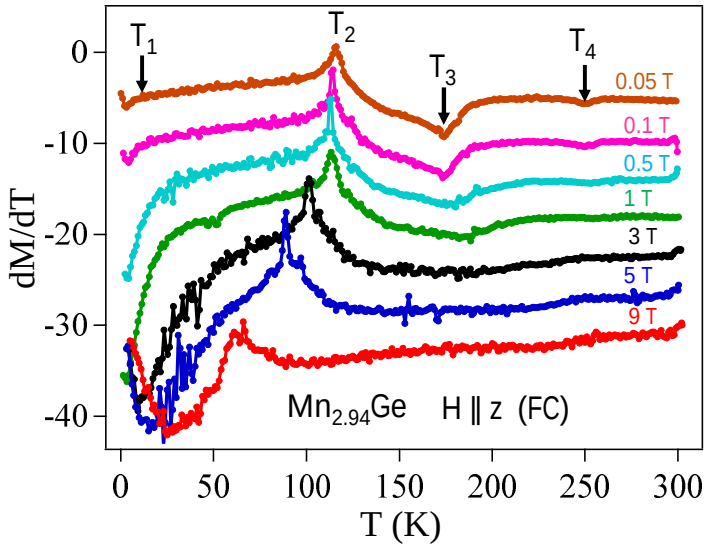

Figure 3.3: dM/dT of FC M(T) of Fig. 3.2(c) taken for $H \parallel z$ at different applied fields, clearly showing the multiple magnetic transitions T_1 – T_4.

Mn present in the system [21, 20, 22, 24, 35].

To fully explore the nature of unusual magnetic transitions, we measured $M(T)$ in the FC mode by varying the applied field from 500 Oe to 9 T as shown Fig. 3.2(c) within the temperature range of 2-300 K. From the first derivatives (dM/dT) we obtained the transition temperatures $T_1 - T_4$ and are plotted in Fig. 3.2(d) as a function of applied field. From Fig. 3.2(d), we notice that T_1 increases with increasing field (from 22 K at 500 Oe to 75 K at 5 T), T_2 decreases with increasing field (from 118 K at 500 Oe to 64 K at 9 T), and T_3 increases with increasing field (from 188 K at 500 Oe to 235 K at 5 T). These observations clearly suggest that T_1 and T_3 are ferromagnetic-like transitions, while T_2 is an AFM-like transition [40–42]. Further, we find T_4 at around 250 K, visible only at lower applied fields (<1 T) almost field-independent. Since the field-dependent $M(T)$ was taken only up to 300 K, we are unable to comment on the nature of T_5 transition, which is found at 310 K [see Fig. 3.2(a)].

Next, the field-dependent magnetization $M(H)$ at different temperatures for the in-plane ($H \perp z$) and out-of-plane ($H \parallel z$) field directions is shown in Figs. 3.2(e) and 3.2(f), respectively. In-plane and out-of-plane $M(H)$ data display spontaneous magnetization with a small hysteresis loop around the zero field. Linear and unsaturated magnetization at higher fields demonstrates a predominant AFM character, while the spontaneous magnetization and the magnetic hysteresis indicate a weak ferromagnetic component in the system. From the in-plane ($H \perp z$) $M(H)$ data, we estimate the spontaneous magnetization $M_{SP} = 0.017\mu_B$/f.u. and the coercive field H_C =62 Oe at 300 K. From out-of-plane ($H \parallel z$) $M(H)$ data, the values of M_{SP} and H_C are $0.008\mu_B$/f.u and 111 Oe, respectively, at 300 K. Consistent with the $M(T)$ data, the spontaneous magnetization is higher at 150 K for both field directions [see insets in Figs. 3.2(e) and 3.2(f)].

Further, we draw a detailed comparison among our magnetic measurements, Mn-excess $Mn_{3+x}Ge$ [34, 20–22] and Mn_3Sn [17, 19]. Mn_3Sn usually shows a sudden drop in the magnetization due to spin-reorientation (T_{SR}) transition within the temperature range of 265–275 K, depending on the chemical composition and preparation method [43, 18]. Note that the spin-reorientation transition in Mn_3Sn is from a triangular-spin structure (AFM) to a spiral-spin structure (AFM). Thus, it is an AFM-to-AFM magnetic transition. On the other hand, $Mn_{2.94}Ge$ [see Figs. 3.2(e) and 3.2(f)] has an AFM ordering throughout the measured temperature range similar to Mn_3Sn. Therefore, the gradual decrease of magnetization below T_2 in $Mn_{2.94}Ge$ is plausibly due to a gradual reorientation of Mn spins [see Fig. 3.2(c)], unlike in Mn_3Sn where it is spontaneous. Since the low-temperature multiple magnetic transitions below T_N=353 K (T_1, T_2, T_3, and T_4) are observed only in the Mn-deficit $Mn_{2.94}Ge$ but not in the Mn-excess $Mn_{3.20}Ge$, we suggest that the Mn deficiency plays a crucial role in triggering the complex magnetic structure in this system. This suggestion is qualitatively supported by previous reports made on the Mn-deficient $Mn_{3-x}Ge$ (x=0.35 and 0.4) [29, 44], where several anomalous magnetic transitions were found below the T_N. Further, the spin-reorientation transition temperature T_{SR} observed from different Mn-deficiency systems appears nearly the same. Means, in our studied system of $Mn_{2.94}Ge$ the $T_{SR} \approx 114$ K, whereas $T_{SR} \approx 120$ K in $Mn_{2.6}Ge$ [44].

3.3.3 Electrical and Magnetotransport Properties

In-plane (ρ_{xx}) and out-of-plane (ρ_{zz}) longitudinal electrical resistivity are plotted as a function of temperature in Fig. 3.4(a). Both ρ_{xx} and ρ_{zz} suggest an overall metallic nature of the sample, which is in agreement with previous reports on $Mn_{3+x}Ge$ [22, 23]. Fig. 3.4(b) depicts in-plane (ρ_{xy}) and out-of-plane (ρ_{zx}) Hall resistivity plotted as a function of temperature. Here, the Hall resistivity ρ_{xy} is obtained for the current applied along the x-direction, field applied along the z-direction, and the Hall voltage measured along the y-direction. Similarly, the Hall resistivity ρ_{zx} is obtained for the current applied along the z-direction, field applied along the y-direction, and the Hall voltage measured along the x-direction. The Hall resistivity was measured using both positive (1 T) and negative (-1 T) magnetic fields and calculated using the formula $\frac{\rho_H(H)-\rho_H(-H)}{2}$ in order to eliminate the magnetoresistance contribution. Fig. 3.4(c) depicts temperature-dependent in-pane (σ_{xy}) and out-of-plane (σ_{zx}) Hall conductivity calculated using the formulae, $\sigma_{xy} = -\frac{\rho_{xy}}{(\rho_{xx}^2+\rho_{xy}^2)}$ and $\sigma_{zx} = -\frac{\rho_{zx}}{(\rho_{zz}^2+\rho_{zx}^2)}$, respectively.

The values of out-of-plane Hall conductivity (σ_{zx}) are significantly higher than the values of in-plane Hall conductivity (σ_{xy}) at all measured temperatures, consistent with earlier reports [20, 22, 24]. As can be noticed from Fig. 3.4(c), σ_{zx} increases gradually with decreasing temperature, reaching a maximum of 362.48 $\Omega^{-1}cm^{-1}$ at around 95±5K. Below this, σ_{zx} decreases with decreasing temperature. Similarly, the Hall conductiv-

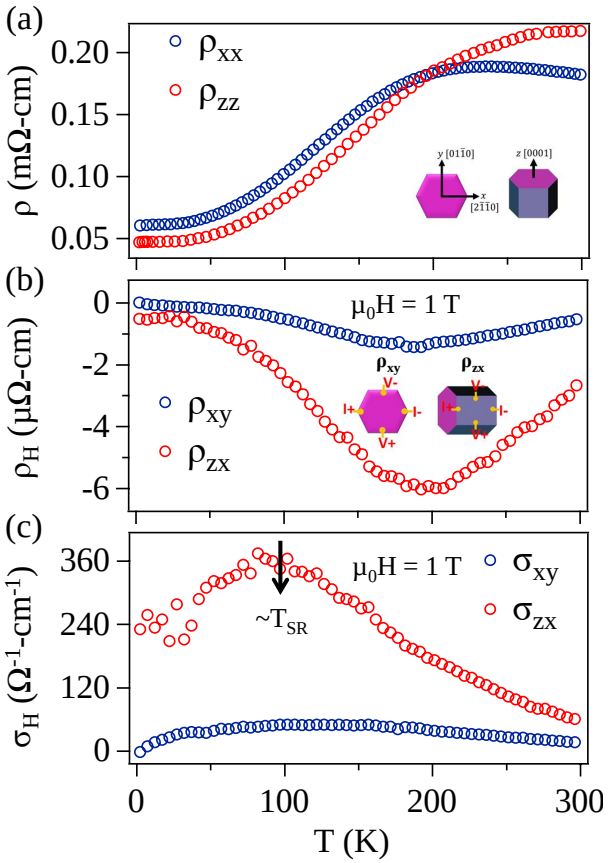

Figure 3.4: (a) Resistivity as a function of temperature plotted for two crystallographic axes directions, ρ_{xx} and ρ_{zz}. Inset in (a) shows the x,y, and z-axis directions on the hexagonal crystal. (b) In-plane (ρ_{xy}) and out-of-plane (ρ_{zx}) Hall resistivity measured as a function of temperature under a magnetic field of 1 T. Inset in (b) shows Hall resistivity ρ_{xy} and ρ_{zx} measuring geometry. (c) In-plane (σ_{xy}) and out-of-plane (σ_{zx}) Hall conductivity calculated from the Hall resistivity of (b) plotted as a function of temperature.

ity σ_{xy} increases with decreasing temperature, reaching a maximum of 50 $\Omega^{-1}cm^{-1}$ at around 110±5K, and below this σ_{xy} decreases with decreasing temperature. Notably, the maximum of σ_{xy} found at 110 K is close to the spin-reorientation transition (T_2 or T_{SR}) of 114 K. A similar sort of relation is noticed between the Hall conductivity and spin-reorientation transition of Mn_3Sn, where the Hall conductivity gradually increases with temperature down to T_{SR}=275 K and suddenly drops to zero below T_{SR} [17]. Since in the studied system $Mn_{2.94}Ge$, the Mn spins reorient gradually, we should observe a gradual decrease in AHC below the T_{SR}. Let us also emphasize here that, although non-zero magnetization (M) is necessary to realize the AHE, the large AHE observed in this system is mainly governed by the electronic band structure originated Berry curvature [24, 26, 27]. Therefore, it is unlikely that the magnetic transitions at T_1, T_3, and T_4 pose any significant impact on the AHC except for the spin-reorientation transition at T_{SR} as the Berry curvature changes at T_{SR} due to time-reversal symmetry breaking in the

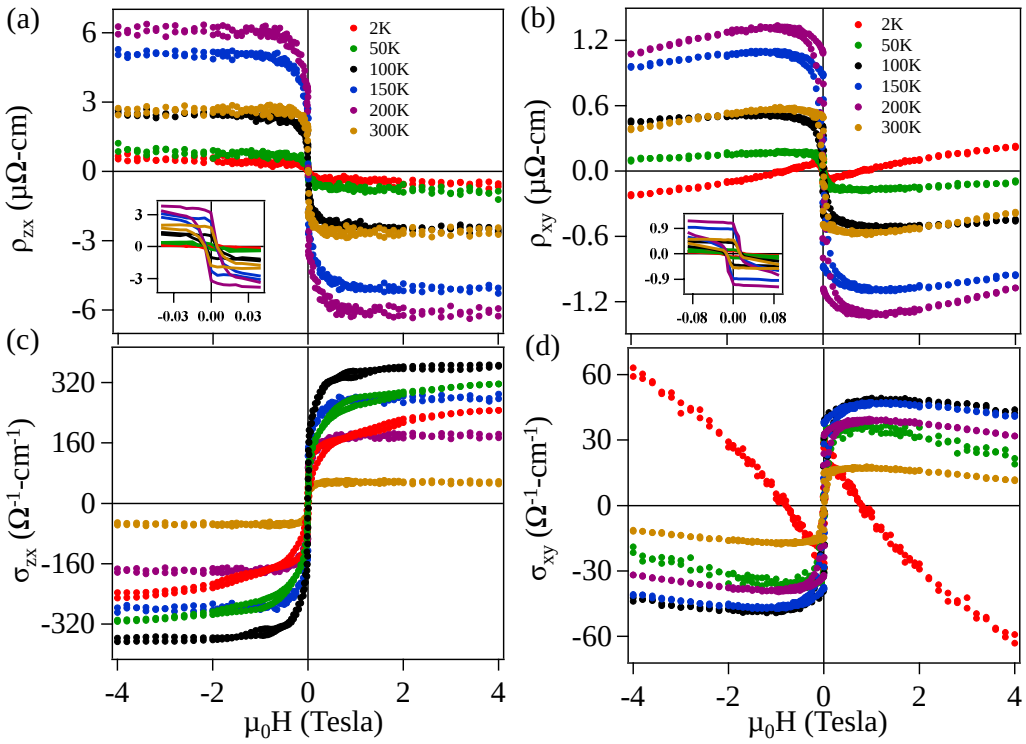

Figure 3.5: (a) and (b) Out-of-plane (ρ_{zx}) and in-plane (ρ_{xy}) Hall resistivity plotted as a function of applied field, respectively. Zoomed-in data at low magnetic fields are shown in the insets of (a) and (b). (c) and (d) Out-of-plane (σ_{zx}) and in-plane (σ_{xy}) Hall conductivity plotted as a function of field calculated from the data of (a) and (b), respectively.

presence of triangular spin-structure [7]. Nevertheless, the magnetization [$M(T)$] macroscopically affects the temperature dependence of AHC as evidenced by the similarities in the temperature-dependent σ_{xy} [see Fig. 3.4(c)] and magnetization [see Fig. 3.2(a)]. Precisely, the large AHC intrinsically originated from the Berry curvature is temperature independent, but the temperature dependence of AHC, as observed from Fig. 3.4(c), is governed by temperature-dependent magnetization.

Next, field-dependent out-of-plane Hall resistivity (ρ_{zx}) measured at various temperatures is plotted in Fig. 3.5(a). We observe a sudden jump in ρ_{zx} near the zero field, which then saturates with increasing magnetic field, the signature of an anomalous Hall effect. From the zoomed-in data of ρ_{zx} as shown in the inset of Fig. 3.5(a), we observe a hysteretic behavior near the zero fields that is consistent with the magnetization hysteresis [see Fig. 3.2(e)]. Fig. 3.5(c) shows out-of-plane Hall conductivity (σ_{zx}) plotted as a function of field. In agreement with $\sigma_{zx}(T)$ shown in Fig. 3.5(c), we observe a maximum anomalous Hall jump in $\sigma_{zx(H)}$ at around 100 K. Similarly, field-dependent in-plane Hall resistivity (ρ_{xy}) and Hall conductivity (σ_{xy}) are plotted in Figs. 3.5(b) and 3.5(d), respectively. Since the in-plane anomalous Hall jump is small, σ_{xy} is mostly dominated by the normal Hall contribution, which varies linearly with the field. Thus, unlike in ρ_{zx}, we do not find

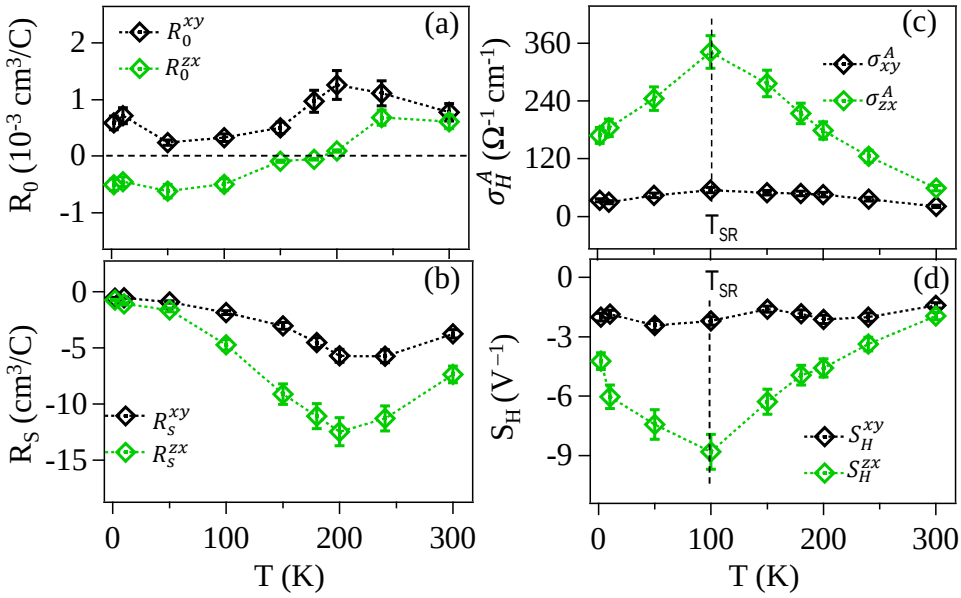

Figure 3.6: Temperature-dependent (a) normal Hall coefficient (R_0), (b) anomalous Hall coefficient (R_s), (c) anomalous Hall conductivity (σ_H^A), and (d) scaling coefficient (S_H). See the text for more details.

saturation in ρ_{xy}. Further, nonlinear Hall conductivity around zero fields is observed in σ_{xy} at 2 K, which is in agreement with the $M(H)$ data [see Fig. 3.2(f)]. Since the Hall resistivity shown in Figs. 3.5(a) and 3.5(b) is the total Hall resistivity (ρ_H), they have contributions from the normal Hall resistivity (ρ_H^N) and anomalous Hall resistivity (ρ_H^A) in such a way that $\rho_H = \rho_H^N + \rho_H^A$. Here, $\rho_H^N = \mathrm{R}_0\mu_0\mathrm{H}$ and $\rho_H^A = \mathrm{R}_S\mu_0 M$. R_0 is the normal Hall coefficient, and R_S is the anomalous one.

Figs. 3.6(a) and 3.6(b) depict temperature-dependent R_0 and R_S values, respectively, obtained by fitting ρ_{zx} and ρ_{xy} data using the relation $\rho_H = \mathrm{R}_0\mu_0\mathrm{H}+\mathrm{R}_S\mu_0\mathrm{M}$. The value of out-of-plane R_S^{zx} is about three orders higher than R_0^{zx}, indicating a clear dominance of the anomalous Hall contribution over the normal Hall contribution in the out-of-plane. Fig. 3.6(c) depicts σ_H^A plotted as a function of temperature calculated using the relation $\sigma_H^A = -\frac{M\mu_0 R_S}{\rho^2}$. At room temperature, the values of in-plane and out-of-plane anomalous Hall conductivity are of $\sigma_{zx}^A = 59.09\ \Omega^{-1}cm^{-1}$ and $\sigma_{xy}^A = 20.63\ \Omega^{-1}cm^{-1}$. We observe that the Hall conductivities are maximum, $\sigma_{zx}^A = 342.05\ \Omega^{-1}cm^{-1}$ and $\sigma_{xy}^A = 54.94\ \Omega^{-1}cm^{-1}$, at around the spin-reorientation transition temperature of 100 K. However, below 100 K, consistent with the magnetization data [see Fig. 3.2(a)], σ_{xy}^A and σ_{zx}^A decrease with temperature. Further, the anomalous Hall resistivity (AHR) is generally proportional to ρ^2 as it originates from the intrinsic Berry curvature [27, 22]. Thus, the scaling coefficient can be written as $S_H = \frac{\mu_0 R_S}{\rho^2}$. Fig. 3.6(d) depicts S_H plotted as a function of temperature. We find that S_H^{zx} strongly depends on the temperature, $S_H^{zx} \sim$ -1.95 V^{-1} (at 300K), -8.81 V^{-1} (at 100K), and -4.24 V^{-1} (at 2 K). On the other hand, S_H^{xy} is nearly constant at all measured temperatures. In general, for the intrinsic AHE, $\sigma_H^A \propto$ M, the scaling coefficient

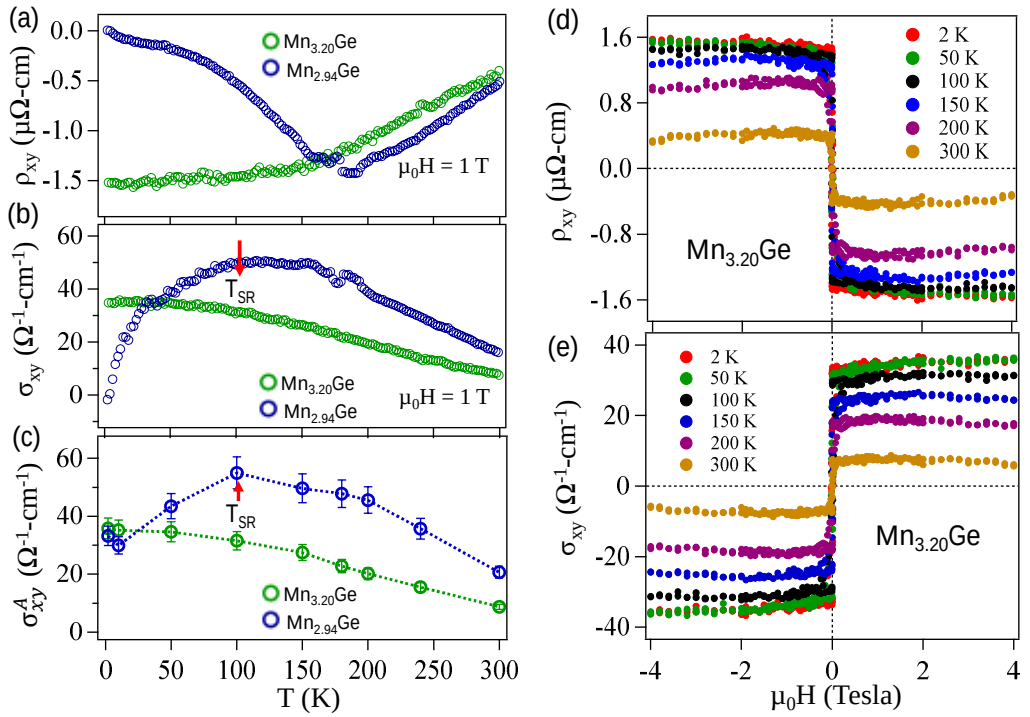

Figure 3.7: (a) In-plane (ρ_{xy}) Hall resistivity data as a function of temperature measured with a magnetic field of 1 T from both $Mn_{3.20}Ge$ and $Mn_{2.94}Ge$ samples. (b) In-plane (σ_{xy}) Hall conductivity calculated from the Hall resistivity of (a) plotted as a function of temperature. (c) Anomalous Hall conductivity (σ^A_{xy}), calculated from field dependent Hall resistivity data. (d) and (e) ρ_{xy} and σ_{xy} plotted as a function of applied field for $Mn_{3.20}Ge$.

S_H should be a temperature-independent constant [45–47].

Finally, in Fig. 3.7 we compare the Hall effect data between Mn-rich ($Mn_{3.2}Ge$) and Ge-rich ($Mn_{2.94}Ge$) compounds. Figs. 3.7(a) and 3.7(b) depict the in-plane Hall resistivity (ρ_{xy}) and Hall conductivity (σ_{xy}) of $Mn_{3.2}Ge$ plotted as a function of temperature, measured with an applied field of 1 T, and overlapped with the similar data of $Mn_{2.94}Ge$ taken from Figs. 3.4(b) and 3.4(c). ρ_{xy} and σ_{xy} of $Mn_{3.2}Ge$ are in very good agreement with previous reports on Mn-rich, $Mn_{3+x}Ge$, systems [20, 22, 35]. From a closer observation of the Hall conductivity data [see Fig. 3.7(b)], we can clearly see that the Hall conductivity of $Mn_{3.2}Ge$ monotonically increases with decreasing temperature and reaches maximum σ_{xy} as we approach the low temperatures. On the other hand, in the case of $Mn_{2.94}Ge$, the Hall conductivity gradually increases with decreasing temperature but a change in the slope is noticed at around T_{SR}. Further decreasing the sample temperature below T_{SR}, in contrast to $Mn_{3.2}Ge$, Hall conductivity decreases with temperature. Similar behaviour is noticed from the anomalous Hall conductivity (σ^A_{xy}) plotted as a function of temperature as shown in Fig. 3.7(c). Figs. 3.7(d) and 3.7(e) display ρ_{xy} and σ_{xy} of $Mn_{3.2}Ge$ plotted as a function of applied field measured at various sample temperatures. Consistent with the $\rho_{xy}(T)$ and $\sigma_{xy}(T)$ shown in Figs. 3.7(a) and 3.7(b), the saturated value of Hall con-

ductivity at higher fields gradually increases with decreasing the temperature. Whereas from the similar data of $Mn_{2.94}Ge$, shown in Figs. 3.5(b) and 3.5(d), we observe gradual decrease in the Hall conductivity above and below T_{SR} with a maximum noticed at T_{SR}.

3.4 Summary

In summary, we have grown $Mn_{2.94}Ge$ (Ge-rich) single crystals to study the electrical transport, magnetic, and magnetotransport properties. Importantly, we show that the magnetic and magnetotransport properties of $Mn_{2.94}Ge$ are different from $Mn_{3+x}Ge$ (Mn-rich), particularly at low temperatures. We identify that the magnetic and Hall properties of $Mn_{2.94}Ge$ are qualitatively similar to those of Mn_3Sn. Consistent with the magnetic properties, the Hall effect study shows unusual behavior around the spin-reorientation transition. This observation contrasts the previous studies on $Mn_{3+x}Ge$ as no such spin-reorientation transition is observed. Further, by comparing the results of $Mn_{2.94}Ge$ and $Mn_{3.20}Ge$ from this study with those of previous reports on $Mn_{3+x}Ge$ we propose that the Mn concentration plays a crucial role in shaping the magnetic and Hall properties of Mn_3Ge.

References

[1] S. M. Young, S. Zaheer, J. C. Y. Teo, C. L. Kane, E. J. Mele, A. M. Rappe, Dirac Semimetal in Three Dimensions, Phys. Rev. Lett. 108 (2012) 140405.

[2] Z. Liu, B. Zhou, Y. Zhang, Z. Wang, H. Weng, D. Prabhakaran, S.-K. Mo, Z. Shen, Z. Fang, X. Dai, et al., Discovery of a three-dimensional topological Dirac semimetal, Na_3Bi, Science 343 (2014) 864–867.

[3] B. Q. Lv, H. M. Weng, B. B. Fu, X. P. Wang, H. Miao, J. Ma, P. Richard, X. C. Huang, L. X. Zhao, G. F. Chen, Z. Fang, X. Dai, T. Qian, H. Ding, Experimental Discovery of Weyl Semimetal TaAs, Phys. Rev. X 5 (2015) 031013.

[4] L. Yang, Z. Liu, Y. Sun, H. Peng, H. Yang, T. Zhang, B. Zhou, Y. Zhang, Y. Guo, M. Rahn, et al., Weyl semimetal phase in the non-centrosymmetric compound TaAs, Nature physics 11 (2015) 728–732.

[5] M. N. Ali, J. Xiong, S. Flynn, J. Tao, Q. D. Gibson, L. M. Schoop, T. Liang, N. Haldolaarachchige, M. Hirschberger, N. P. Ong, R. J. Cava, Large, non-saturating magnetoresistance in WTe2, Nature 514 (2014) 205.

[6] X. Huang, L. Zhao, Y. Long, P. Wang, D. Chen, Z. Yang, H. Liang, M. Xue, H. Weng,

Z. Fang, X. Dai, G. Chen, Observation of the Chiral-Anomaly-Induced Negative Magnetoresistance in 3D Weyl Semimetal TaAs, Phys. Rev. X 5 (2015) 031023.

[7] B. Yan, C. Felser, Topological materials: Weyl semimetals, Annual Review of Condensed Matter Physics 8 (2017) 337–354.

[8] J. M. Taylor, A. Markou, E. Lesne, P. K. Sivakumar, C. Luo, F. Radu, P. Werner, C. Felser, S. S. P. Parkin, Anomalous and topological Hall effects in epitaxial thin films of the noncollinear antiferromagnet Mn_3Sn, Phys. Rev. B 101 (2020) 094404.

[9] W. Ning, Z. Mao, Recent advancements in the study of intrinsic magnetic topological insulators and magnetic Weyl semimetals, APL Materials 8 (2020) 090701.

[10] Y. Deng, Y. Yu, M. Z. Shi, Z. Guo, Z. Xu, J. Wang, X. H. Chen, Y. Zhang, Quantum anomalous Hall effect in intrinsic magnetic topological insulator $MnBi_2Te_4$, Science 367 (2020) 895–900.

[11] E. Liu, Y. Sun, N. Kumar, L. Muechler, A. Sun, L. Jiao, S.-Y. Yang, D. Liu, A. Liang, Q. Xu, et al., Giant anomalous Hall effect in a ferromagnetic kagome-lattice semimetal, Nature physics 14 (2018) 1125–1131.

[12] N. Morali, R. Batabyal, P. K. Nag, E. Liu, Q. Xu, Y. Sun, B. Yan, C. Felser, N. Avraham, H. Beidenkopf, Fermi-arc diversity on surface terminations of the magnetic Weyl semimetal $Co_3Sn_2S_2$, Science 365 (2019) 1286–1291.

[13] I. Belopolski, K. Manna, D. S. Sanchez, G. Chang, B. Ernst, J. Yin, S. S. Zhang, T. Cochran, N. Shumiya, H. Zheng, B. Singh, G. Bian, D. Multer, M. Litskevich, X. Zhou, S.-M. Huang, B. Wang, T.-R. Chang, S.-Y. Xu, A. Bansil, C. Felser, H. Lin, M. Z. Hasan, Discovery of topological Weyl fermion lines and drumhead surface states in a room temperature magnet, Science 365 (2019) 1278–1281.

[14] Kuroda, K. and Tomita, T. and Suzuki, Michi-To and Bareille, C. and Nugroho, A.A. and Goswami, P. and Ochi, Masayuki and Ikhlas, M. and Nakayama, Mitsuhiro and Akebi, S. and Noguchi, Ryo and Ishii, R. and Inami, Nobuhito and Ono, Kanta and Kumigashira, H. and Varykhalov, Andrei and Muro, T. and Koretsune, Takashi and Arita, Ryotaro and Nakatsuji, S., Evidence for magnetic weyl fermions in a correlated metal, Nature Materials 16 (2017) 1090.

[15] A. Biswas, O. Iakutkina, Q. Wang, H. C. Lei, M. Dressel, E. Uykur, Spin-Reorientation-Induced Band Gap in Fe_3Sn_2: Optical Signatures of Weyl Nodes, Phys. Rev. Lett. 125 (2020) 076403.

[16] S. Borisenko, D. Evtushinsky, Q. Gibson, A. Yaresko, K. Koepernik, T. Kim, M. Ali, J. van den Brink, M. Hoesch, A. Fedorov, et al., Time-reversal symmetry breaking type-II Weyl state in $YbMnBi_2$, Nature communications 10 (2019) 1–10.

[17] N. H. Sung, F. Ronning, J. D. Thompson, E. D. Bauer, Magnetic phase dependence of the anomalous Hall effect in Mn_3Sn single crystals, Appl. Phys. Lett. 112 (2018) 132406.

[18] J. Yan, X. Luo, H. Lv, Y. Sun, P. Tong, W. Lu, X. Zhu, W. Song, Y. Sun, Room-temperature angular-dependent topological Hall effect in chiral antiferromagnetic Weyl semimetal Mn_3Sn, Appl. Phys. Lett. 115 (2019) 102404.

[19] A. Low, S. Ghosh, S. Changdar, S. Routh, S. Purwar, S. Thirupathaiah, Tuning of topological properties in the strongly correlated antiferromagnet Mn_3Sn via Fe doping, Phys. Rev. B 106 (2022) 144429.

[20] A. K. Nayak, J. E. Fischer, Y. Sun, B. Yan, J. Karel, A. C. Komarek, C. Shekhar, N. Kumar, W. Schnelle, J. Kübler, et al., Large anomalous Hall effect driven by a nonvanishing Berry curvature in the noncolinear antiferromagnet Mn_3Ge, Science advances 2 (2016) e1501870.

[21] N. Yamada, H. Sakai, H. Mori, T. Ohoyama, Magnetic properties of ϵ-Mn_3Ge, Physica B+ C 149 (1988) 311–315.

[22] N. Kiyohara, T. Tomita, S. Nakatsuji, Giant Anomalous Hall Effect in the Chiral Antiferromagnet Mn_3Ge, Phys. Rev. Applied 5 (2016) 064009.

[23] L. Xu, X. Li, X. Lu, C. Collignon, H. Fu, J. Koo, B. Fauqué, B. Yan, Z. Zhu, K. Behnia, Finite-temperature violation of the anomalous transverse Wiedemann-Franz law, Science Advances 6 (2020) eaaz3522.

[24] T. Chen, T. Tomita, S. Minami, M. Fu, T. Koretsune, M. Kitatani, I. Muhammad, D. Nishio-Hamane, R. Ishii, F. Ishii, et al., Anomalous transport due to Weyl fermions in the chiral antiferromagnets Mn_3X, X= Sn, Ge, Nature communications 12 (2021) 1–14.

[25] X. Li, C. Collignon, L. Xu, H. Zuo, A. Cavanna, U. Gennser, D. Mailly, B. Fauqué, L. Balents, Z. Zhu, K. Behnia, Chiral domain walls of Mn_3Sn and their memory, Nat. Commun. 10 (2019) 3021.

[26] T. Jungwirth, Q. Niu, A. H. MacDonald, Anomalous Hall Effect in Ferromagnetic Semiconductors, Phys. Rev. Lett. 88 (2002) 207208.

[27] N. Nagaosa, J. Sinova, S. Onoda, A. H. MacDonald, N. P. Ong, Anomalous Hall effect, Rev. Mod. Phys. 82 (2010) 1539–1592.

[28] E. Krén, J. Paitz, G. Zimmer, É. Zsoldos, Study of the magnetic phase transformation in the Mn_3Sn phase, Physica B+ C 80 (1975) 226–230.

[29] T. Ohoyama, X-ray and magnetic studies of the manganese-germanium system, J. Phys. Soc. Japan 16 (1961) 1995–2002.

[30] E. Arras, D. Caliste, T. Deutsch, F. Lançon, P. Pochet, Phase diagram, structure, and magnetic properties of the Ge-Mn system: A first-principles study, Phys. Rev. B 83 (2011) 174103.

[31] N. Yamada, Atomic magnetic moment and exchange interaction between Mn atoms in intermetallic compounds in Mn-Ge system, J. Phys. Soc. Japan 59 (1990) 273–288.

[32] A. S. Sukhanov, S. Singh, L. Caron, T. Hansen, A. Hoser, V. Kumar, H. Borrmann, A. Fitch, P. Devi, K. Manna, C. Felser, D. S. Inosov, Gradual pressure-induced change in the magnetic structure of the noncollinear antiferromagnet Mn_3Ge, Phys. Rev. B 97 (2018) 214402.

[33] S. Tomiyoshi, Y. Yamaguchi, T. Nagamiya, Triangular spin configuration and weak ferromagnetism of Mn_3Ge, J. Magn. Magn. Mater. 31 (1983) 629–630.

[34] S. Tomiyoshi, Polarized neutron diffraction study of the spin structure of Mn_3Sn, J. Phys. Soc. Japan 51 (1982) 803–810.

[35] C. Wuttke, F. Caglieris, S. Sykora, F. Scaravaggi, A. U. B. Wolter, K. Manna, V. Süss, C. Shekhar, C. Felser, B. Büchner, C. Hess, Berry curvature unravelled by the anomalous Nernst effect in Mn_3Ge, Phys. Rev. B 100 (2019) 085111.

[36] V. Rai, S. Jana, M. Meven, R. Dutta, J. Perßon, S. Nandi, Unconventional magnetoresistance and electronic transition in Mn_3Ge Weyl semimetal, Phys. Rev. B 106 (2022) 195114.

[37] N. Yamada, K. Maeda, Y. Usami, T. Ohoyama, Magnetic Properties of Intermetallic Compound $Mn_{11}Ge_8$, Journal of the Physical Society of Japan 55 (1986) 3721–3724.

[38] D. Duc Dung, W. Feng, D. Van Thiet, I.-S. Park, S. Bo Lee, S. Cho, Strain modified enhanced ferromagnetism in Mn_3Ge_2 thin films on GaAs(001) and GaSb(001), J. Appl. Phys. 113 (2013) 153908.

[39] C. Zeng, S. C. Erwin, L. C. Feldman, A. P. Li, R. Jin, Y. Song, J. R. Thompson, H. H. Weitering, Epitaxial ferromagnetic Mn_5Ge_3 on Ge(111), Appl. Phys. Lett. 83 (2003) 5002–5004.

[40] I. Raičević, D. Popović, C. Panagopoulos, L. Benfatto, M. B. Silva Neto, E. S. Choi, T. Sasagawa, Skyrmions in a Doped Antiferromagnet, Phys. Rev. Lett. 106 (2011) 227206.

[41] S. Gupta, K. Suresh, A. Nigam, Observation of large positive magnetoresistance and its sign reversal in GdRhGe, Journal of alloys and compounds 586 (2014) 600–604.

[42] M. Szlawska, D. Gnida, P. Ruszała, M. J. Winiarski, M. Samsel-Czekała, M. Schmidt, Y. Grin, D. Kaczorowski, Antiferromagnetic Ordering and Transport Anomalies in Single-Crystalline $CeAgAs_2$, Materials 13 (2020) 3865.

[43] T. F. Duan, W. J. Ren, W. L. Liu, S. J. Li, W. Liu, Z. D. Zhang, Magnetic anisotropy of single-crystalline Mn_3Sn in triangular and helix-phase states, Appl. Phys. Lett. 107 (2015) 082403.

[44] N. Yamada, T. Ohashi, T. Ohoyama, Magnetic Phase Transition of ζ-$Mn_{2.6}Ge$, J. Phys. Soc. Japan 51 (1982) 2041–2042.

[45] N. Manyala, Y. Sidis, J. F. DiTusa, G. Aeppli, D. P. Young, Z. Fisk, Large anomalous Hall effect in a silicon-based magnetic semiconductor, Nat. Mater. 3 (2004) 255–262.

[46] C. Zeng, Y. Yao, Q. Niu, H. H. Weitering, Linear Magnetization Dependence of the Intrinsic Anomalous Hall Effect, Phys. Rev. Lett. 96 (2006) 037204.

[47] Q. Wang, S. Sun, X. Zhang, F. Pang, H. Lei, Anomalous Hall effect in a ferromagnetic Fe_3Sn_2 single crystal with a geometrically frustrated Fe bilayer kagome lattice, Phys. Rev. B 94 (2016) 075135.

Chapter 4

Tuning of Electrical, Magnetic, and Topological Properties of Magnetic Weyl Semimetal $Mn_{3+x}Ge$ by Fe doping

4.1 Introduction

Topological materials with kagome lattice structure offer many intriguing quantum phenomena such as the Weyl [1, 2] and Dirac fermions [3, 4] in solids, quantum spin liquid state [5], superconductivity [6], anomalous Hall effect (AHE) [7], topological Hall effect (THE) [8], and skyrmion lattice [9, 10]. Though there exist many topological kagome systems, the topological kagome magnets have gained much attention due to their potential technological applications in spintronics as well as from a fundamental science point of view due to strong electronic correlations present in these systems [11, 12]. For instance, $Co_3Sn_2S_2$ is a ferromagnetic Weyl semimetal showing giant AHE and zero-field Nernst effect [7, 13]. The noncollinear and coplanar antiferromagnetic (AFM) Weyl semimetals, Mn_3X (X = Sn and Ge), show large AHE originating from the nonzero Berry phase in momentum space [14–18]. On the other hand, ferromagnetic Weyl semimetal Fe_3Sn_2 shows both THE and AHE [19]. A nonzero Berry phase in the momentum space leads to an intrinsic anomalous Hall effect. In contrast, the nonzero total scalar-spin chirality [$\chi_{ijk} = S_i.(S_j \times S_k)$] summed over the lattice, producing the nonzero real-space Berry curvature, generates the topological Hall effect [20, 21, 17].

In noncentrosymmetric magnets such as MnSi [22, 23], FeGe [24, 25], MnGe [9], and FeCoSi [26], THE originates from the chiral-spin structure stabilized by the Dzyaloshinskii-Moriya interaction (DMI). On the other hand, in centrosymmetric magnets such as

$La_{1-x}Sr_xMnO_3$ [27], Fe_3Sn_2 [28, 29], and $Mn_{3-\delta}Fe_\delta Sn$ [30], THE originates from the chiral-spin structure stabilized by strong magnetic anisotropy. To date, many systems of various magnetic orderings have been found to show THE, including the skyrmionic crystals [22, 31, 32], the antiferromagnets (AFM) [33, 34], the spin glass systems [35, 36], the frustrated magnets [37, 38], the double-exchanged ferromagnets [39, 40], and the magnetic skyrmion arrays [41–44]. Among them, the frustrated kagome magnets such as $PdCrO_2$ [38], Gd_2PdSi_3 [45], and $Mn_{3+x}Sn$ and Fe_3Sn_2 [8, 17] are more interesting as they are rich in physics due to the triangular spin-lattice in the kagome network. Mn_3Ge, like its sister compound Mn_3Sn, is a noncollinear antiferromagnet with a hexagonal crystal structure of space group $P6_3/mmc$ [46, 14, 16, 15]. Here, the Mn atoms form the kagome network with triangles and hexagons in the *ab*-plane of the crystal, with the Ge atom sitting at the centre of hexagon [47, 48, 15, 16]. $Mn_{3+x}Sn$ shows a spin-reorientation transition at around 260–270 K, while no such spin-reorientation transition is found in $Mn_{3+x}Ge$ down to the lowest possible temperature. Further, $Mn_{3+x}Sn$ shows a low-temperature spin-glass transition at around 50 K but is not found in $Mn_{3+x}Ge$. Earlier, we found that Fe doping at the Mn site can significantly tune the electrical, magnetic, and magnetotransport properties of $Mn_{3-\delta}Fe_\delta Sn$ [30].

In this contribution, we systematically studied the electrical, magnetic, and Hall effect properties of $Mn_{(3+x)-\delta}Fe_\delta Ge$ (δ=0, 0.30, and 0.62) by varying the Fe doping concentration. Fe doping significantly changes the electrical resistivity and magnetic properties of $Mn_{3+x}Ge$. Most importantly, we observe a topological Hall state only in the compound with δ=0.30 of Fe doping but not in the parent system and the system with δ=0.62 of Fe doping. In addition, increasing the Fe doping concentration significantly reduces the spontaneous anomalous Hall effect observed in the parent system. In the manuscript, we thoroughly explain our experimental observations.

Table 4.1: Lattice parameters obtained from the single crystal XRD (SCXRD) measurements.

Composition	a (Å)	b (Å)	c (Å)	α (^{o})	β (^{o})	γ (^{o})
$Mn_{3.48}Ge$ (δ=0)	5.350(5)	5.352(5)	4.308(9)	90.06(17)	90.18(16)	120.00(2)
$Mn_{2.97}Fe_{0.30}Ge$ (δ=0.30)	5.313(2)	5.314(2)	4.302(18)	90.06(3)	89.91(3)	119.93(4)
$Mn_{2.69}Fe_{0.62}Ge$ (δ=0.62)	5.294(6)	5.282(8)	4.281(11)	90.5(2)	89.7(2)	120.00(3)

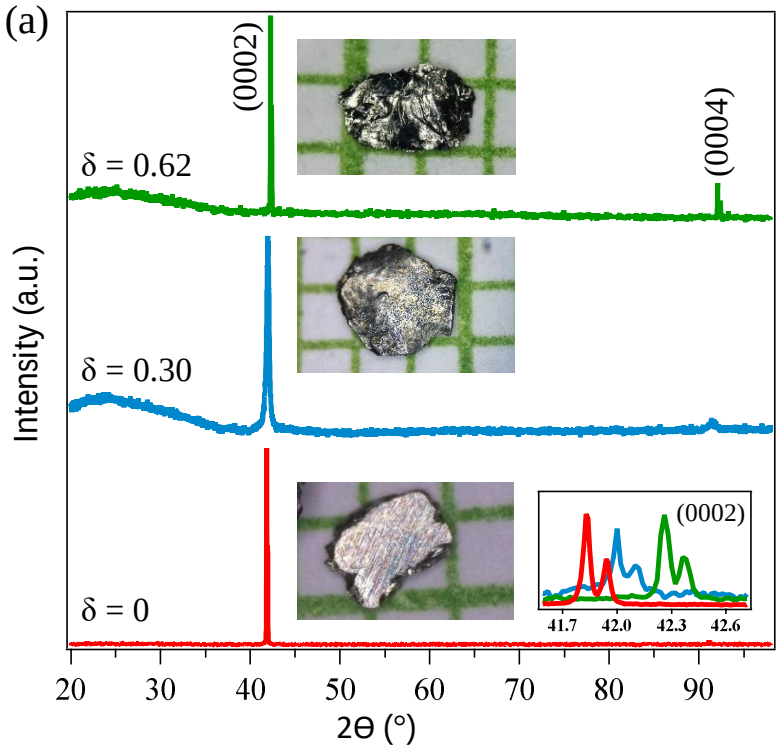

Figure 4.1: Powder XRD patterns of $Mn_{3.48}Ge$ (δ=0), $Mn_{2.97}Fe_{0.30}Ge$ (δ=0.30), and $Mn_{2.69}Fe_{0.62}Ge$ (δ=0.62) single crystals. Bottom-right inset shows zoomed-in (0002) peaks of δ=0, 0.30, and 0.62 compounds, demonstrating the shift in peak position with doping. Photographic image of the respective compositions are shown.

4.2 Experimental details

Single crystals of $Mn_{(3+x)-\delta}Fe_{\delta}Ge$ (δ=0, 0.30, and 0.62) were prepared by the melt-growth method using a high-temperature muffle furnace. In this method, Manganese (Alfa Aesar 99.95%), Iron (Alfa Aesar 99.99%), and Germanium (Alfa Aesar 99.999%) powders were taken in stoichiometric ratio, mixed thoroughly in the glove-box under an argon environment before sealing them in a preheated quartz ampoule under a vacuum of $10^{\breve{}4}$ mbar. The sealed quartz tube was then heated in a muffle furnace up to 1050^{o}C and kept at that temperature for 24 hours. The tube was slowly cooled to 760^{o}C for δ=0, 780^{o}C for δ=0.30, and 800^{o}C for δ=0.62 at a rate of 2 K/h. After prolonged annealing at the respective growth temperatures for five more days, the ampules were quenched in ice water to avoid the impurity phases. As-grown single crystals of $Mn_{(3+x)-\delta}Fe_{\delta}Ge$ were looking shiny and had a typical size of 2×1.5 mm^2.

Phase purity and crystal structure of the single crystals were examined by using single crystal X-ray diffraction (SCXRD, SuperNova, Rigaku) and powder X-ray diffraction (XRD, Rigaku SmartLab) with Cu-K_{α} radiation of wavelength λ=1.5406 Å. Using energy dispersive X-ray spectroscopy (EDS of EDAX), we find the actual chemical composition of the as-prepared samples to be $Mn_{3.48\pm0.02}Ge$, $Mn_{2.97\pm0.05}Fe_{0.30\pm0.02}Ge$, and

$Mn_{2.69\pm0.04}Fe_{0.62\pm0.02}Ge$. Usually, $Mn_{3+x}Ge$ forms with excess Mn without any control on the Mn concentration [47, 16, 49, 46]. Thus, we also got the crystals with excess Mn. For convinience, we represent the systems $Mn_{3.48}Ge$, $Mn_{2.97}Fe_{0.30}Ge$, and $Mn_{2.69}Fe_{0.62}Ge$ in the manuscript by δ=0, 0.30, and 0.62, respectively, wherever applicable. Electrical transport, Hall effect, and magnetic property studies were performed using a 9-Tesla physical property measurement system (PPMS, Dynacool, Quantum Design) within the temperature range of 2–380 K. Electrical transport and Hall measurements were performed using the four-probe technique. Copper leads were attached to the sample using EPO-TEK H20E silver epoxy.

4.3 Results

4.3.1 Structural Properties

Mn_3Ge crystalizes into the Ni_3Sn-type hexagonal structure with a space group of $P6_3/mmc$ (194), with the Mn atoms sitting on the *ab*-plane to form a breathing kagome lattice, while the Ge atoms sit at the center of the hexagons [15, 16]. A couple of kagome lattice planes are stacked along the *c*-axis per unit cell. XRD patterns taken on the single crystal of $Mn_{(3+x)-\delta}Fe_\delta Ge$ is shown in Fig. 4.1, suggesting that the crystal growth is parallel to the *c*-axis. The bottom right inset in Fig. 4.1 shows zoomed-in (0002) peaks of the parent, δ=0.30, and δ=0.62 compounds. Here we observe that with increased Fe doping, (0002) peaks are shifted to higher 2θ values. This indicates a decrease in the lattice parameter *c*. Optical images of the as-grown single crystals of different compositions are shown in the middle insets of Fig. 4.1. Lattice parameters obtained from the single crystal XRD of δ=0, 0.30, and 0.62 compounds are tabulated in Tab. 4.1.

4.3.2 Magnetic Properties

To explore the magnetic properties, magnetization as a function of temperature $[M(T)]$ was measured in the field-cooled (FC) and zero-field-cooled (ZFC) modes under a magnetic field (H) of 500 Oe applied parallel ($H \parallel z$) and perpendicular ($H \perp z$) to the *z*-axis as shown in Figs. 4.2(a), 4.2(b), and 4.2(c) from the δ=0, 0.30, and 0.62 compounds, respectively. From Fig. 4.2(a), we identify an antiferromagnetic (AFM) transition at a Néel temperature of T_N=365 K in $Mn_{3.48}Ge$, consistent with previous reports on $Mn_{3+x}Ge$ where T_N was found between 365 K and 400 K depending on the x value [47, 15, 16, 46, 50]. Below T_N, the magnetization increases with decreasing temperature and saturates at very low temperatures for both $H \parallel z$ and $H \perp z$ directions. From Fig. 4.2(b), we observe a similar behavior of magnetization from the δ=0.30 sample, except that T_N is reduced to 298 K. A down-turn in the ZFC $M(T)$ data is noticed at a very low sample temperature

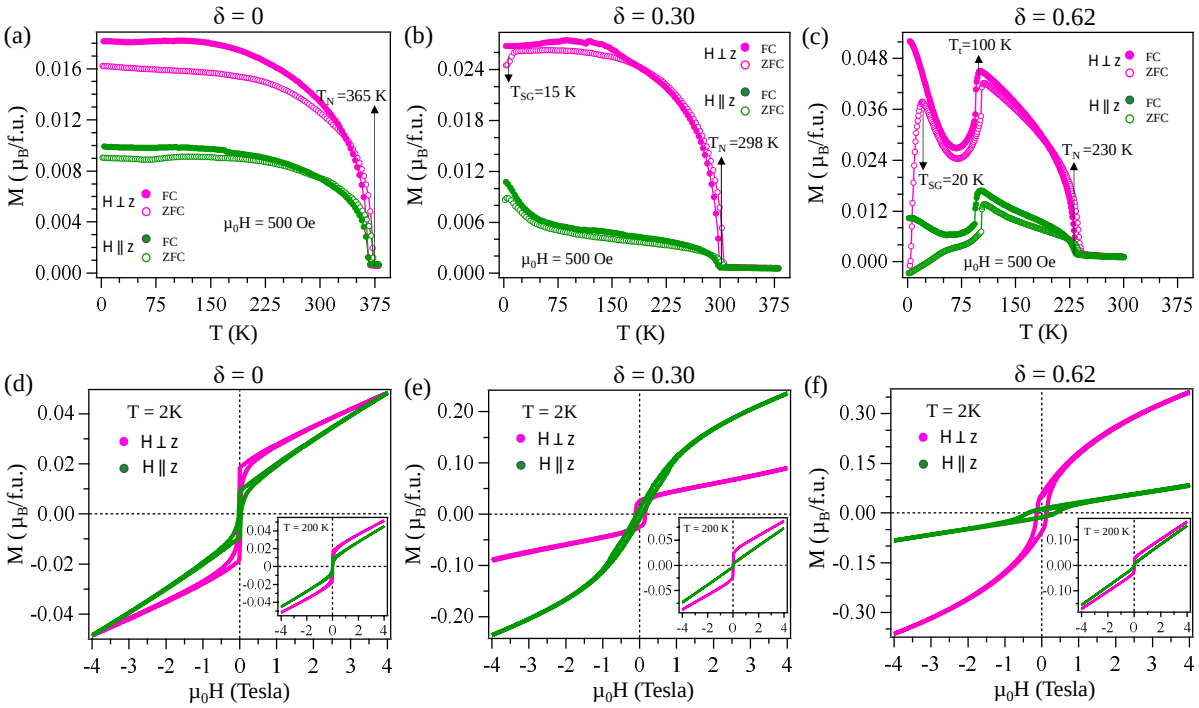

Figure 4.2: Temperature-dependent magnetization $[M(T)]$ of $Mn_{(3+x)-\delta}Fe_{\delta}Ge$ measured in zero-field-cooled (ZFC) and field-cooled (FC) modes with $H \parallel z$ and $H \perp z$ for δ=0 (a), δ=0.30 (b), and δ=0.62 (c). Similarly, magnetization isotherms $[M(H)]$ measured at 2 K with $H \parallel z$ and $H \perp z$ for δ=0 (d), δ=0.30 (e), and δ=0.62 (f). Insets of (d), (e), and (f) are $M(H)$ data measured at 200 K from δ=0, 0.30, and 0.62, respectively. See Supplemental Material for the $M(H)$ data measured at several other sample temperatures.

of 15 K, which is clearly visible with $H \perp z$. This hints at a spin-glass-like transition induced by the Fe doping [51–54]. Next, from Fig. 4.2(c), we observe a further decrease in T_N to 230 K with a Fe doping of δ=0.62 in addition to a sudden drop in magnetization at 100 K from both $H \parallel z$ and $H \perp z$ directions. This kind of magnetization drop earlier reported on Mn_3Sn was understood as an AFM-to-AFM magnetic transition [55, 56]. Moreover, at 20 K, we observe a downturn in the ZFC $M(T)$ data, clearly visible from the $H \perp z$ direction, which is sharper than δ=0.30 compound.

Interestingly, from the $M(T)$ of $Mn_{3.48}Ge$ measured in the FC mode, we notice almost two times higher in-plane magnetization ($H \perp z$) than the out-of-plane magnetization ($H \parallel z$) at 2 K, indicating a strong magnetic anisotropy in this systems. Such strong magnetic anisotropy in $Mn_{3.48}Ge$, despite being an AFM metal, mainly originates from the geometrical frustration of the Mn magnetic moments within the kagome lattice plane, producing a finite net magnetic moment [47, 57]. Further, from Figs. 4.2(b) and 4.2(c) we can notice that the in-plane magnetization increases nearly three times and four times compared to the out-of-plane magnetization for the Fe doping concentration of δ=0.30 and 0.62, respectively. Thus, the magnetic anisotropy rapidly increases with Fe doping concentration.

Figs. 4.2(d), 4.2(e), and 4.2(f) show magnetization isotherms [$M(H)$] measured at 2 K with $H \parallel z$ and $H \perp z$ directions from the δ=0, 0.30, and 0.62 compounds, respectively. From Fig. 4.2(d), we observe a spontaneous magnetization at lower fields, which then linearly increases with the field. Further, consistent with $M(T)$ data [see Fig. 4.2(a)], the in-plane spontaneous magnetization is nearly two times higher than that of out-of-plane magnetization at lower fields. Inset in Fig. 4.2(d) shows $M(H)$ data taken at 200 K. Nevertheless, we do not find any significant difference in the $M(H)$ data between 2 and 200 K. On the other hand, more interestingly, from the $M(H)$ data of the δ=0.30 compound [see Fig. 4.2(e)], we find a quite complex magnetization isotherm. That means the out-of-plane ($H \parallel z$) magnetization increases more rapidly than the in-plane ($H \perp z$) magnetization with increasing applied field and eventually dominates the in-plane magnetization beyond 0.3 T of applied field when measured at 2 K. We further notice that at 4 T of the applied field, the out-of-plane magnetization is nearly three times higher than that of the in-plane. This observation is in stark contrast to the parent system, where we observe dominating in-plane magnetization throughout the applied field up to 4 T. The inset in Fig. 4.2(e) shows the isotherm measured at 200 K, demonstrating that the in-plane magnetization dominates the out-of-plane throughout the applied field up to 4 T, which is similar to the parent system. Further, Fe doping of δ=0.62 converts the system more into an in-plane ferromagnet (with a sigmoid-like $M(H)$ loop) and an out-of-plane antiferromagnet (with a linear $M(H)$ loop), as shown in Fig. 4.2(f).

4.3.3 Electrical and Magnetotransport Properties

Fig. 4.3(a) depicts the zero-field in-plane longitudinal electrical resistivity (ρ_{xx}) of the δ=0, 0.30, and 0.62 compounds measured between 2 and 300 K. We notice from the resistivity that the parent compound, $Mn_{3.48}Ge$, exhibits overall a metallic behavior with temperature that is in agreement with earlier reports on $Mn_{3+x}Ge$ [16]. On the other hand, with the Fe doping of δ=0.30, the system exhibits a semiconducting or a bad-metallic behavior as ρ_{xx} increases with decreasing temperature. With further increasing the Fe doping to δ=0.62, we observe that the ρ_{xx} increases with decreasing temperature before a sharp drop in the resistivity takes place at 100 K [see Fig. 4.3(a)], below 100 K the system behaves like a metal. Such a sudden drop in the resistivity at 100 K is possibly due to the in-plane AFM-to-AFM magnetic transition [see Fig. 4.2(c)] leading to the metal-insulator (MI) transition as reported earlier on $Mn_{3-\delta}Fe_{\delta}Sn$ [30] and on $Mn_{2.34}Fe_{0.66}Ge$ [58].

Fig. 4.3(b) depicts the Hall resistivity [$\rho_{xy}(T)$] δ=0, 0.30, and 0.62 compounds measured as a function of temperature. Here, ρ_{xy} stands for the in-plane Hall resistivity (ab-plane) measured with the current applied parallel to the x-axis and field applied parallel to the z-axis, while the Hall voltage is measured along the y-axis. Hall resistivity was measured

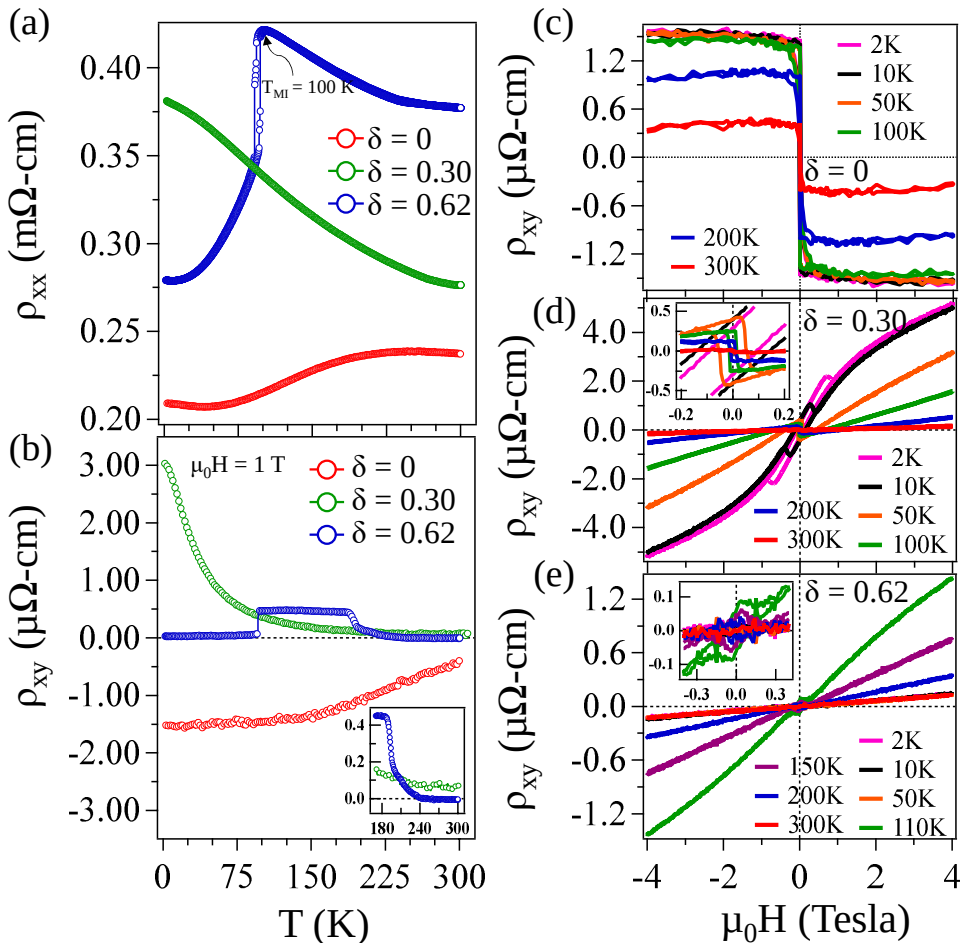

Figure 4.3: Temperature-dependent (a) longitudinal resistivity (ρ_{xx}) and (b) Hall resistivity (ρ_{xy}) plotted for δ=0, 0.30, and 0.62. Inset in (b) is the zoomed-in image taken to demonstrate the increase in total Hall resistivity of δ=0.62 below 230 K. Field-dependent Hall resistivity (ρ_{xy}) measured at various temperatures for δ=0 (c), δ=0.30 (d), and δ=0.62 (e) compounds. Inset in (d) and (e) are the zoomed-in images taken around zero field.

using both positive (+H) and negative (-H) fields to exclude the magnetoresistance contribution due to possible misalignment of the four-probe connection. The resultant Hall resistivity was calculated using the formula, $\frac{\rho_H(H,T)-\rho_H(-H,T)}{2}$. Thus, from Fig. 4.3(b), we can observe that the ρ_{xy} of the parent compound monotonically increases (negative value) with decreasing temperature which then saturates at low temperatures. This observation agrees with previous reports on this system [15]. ρ_{xy}(T) of the parent system bears a resemblance to the $M(T)$ data [see Fig. 4.2(a)]. On the other hand, the ρ_{xy} of δ=0.30 compound rapidly increases (positive) with decreasing temperature, possibly due to a rapid increase in the out-of-plane magnetization [see Fig. 4.5(d)]. Next, from the ρ_{xy} of δ=0.62, we can find significant Hall signal only within the temperature range of 100–230 K, which is consistent with the $M(T)$ data as shown in Fig. 4.2(c) where we notice one antiferromagnetic transition (AFM) at T_N=230 K and the other one (also AFM type) at T_t=100 K.

Field-dependent Hall resistivity [$\rho_{xy}(H)$] measured at various temperatures is plotted in Figs. 4.3(c), 4.3(d), and 4.3(e) from the δ=0, 0.30, and 0.62 compounds, respectively. From the parent compound, we observe a sudden jump in ρ_{xy} near the zero fields, which saturates with further increasing the field as shown in Fig. 4.3(c), which is a signature of the anomalous Hall effect (AHE). This observation is consistent with previous reports on similar systems [15, 16]. Also, in agreement with $\rho_{xy}(T)$ as shown in Fig. 4.3(b), the saturated $\rho_{xy}(H)$ value increases with decreasing temperature and becomes nearly constant below 100 K. On the other hand, with a Fe doping of δ=0.30, the AHE is significantly decreased, as we do not observe a sharp jump near the zero fields but only a gradual increase in ρ_{xy} with the field. Particularly at higher temperatures ($>$ 100 K), we observe a linear dependence of ρ_{xy} on the applied field due to the dominating normal Hall contribution. However, at lower temperatures ($<$ 100 K), we still find a non-linear and hysteretic $\rho_{xy}(H)$ behavior. Further increasing the Fe doping to δ=0.62, as shown in Fig. 4.3(e), the AHE signal is hardly visible at most of the measured temperatures except a small AHE is noticed at 110 and 200 K. Thus, the total Hall resistivity of δ=0.62 shown in Fig. 4.3(b) is mainly contributed by the normal Hall resistivity except for the temperature range of 100-230 K where a small AHE contribution also present.

Red-colored data in Fig. 4.4(a) depict the total Hall resistivity of δ=0.30 fitted using Eqn. 4.1 measured at various sample temperatures. Black-colored data in Fig. 4.4(a) are the fits using the Eqn. 4.1. We can notice that $\rho_{xy}(H)$ is not fitted well at lower fields because of the topological Hall contribution. Therefore, to extract the topological Hall contribution, one needs to subtract anomalous and normal Hall contributions from the total Hall resistivity such as $\rho^{T}_{xy}(H) = \rho_{xy}(H)$-[$\rho^{N}_{xy}(H) + \rho^{A}_{xy}(H)$]. Green-colored data in Fig. 4.4(a) depict the obtained topological Hall resistivity plotted as a function of field at various temperatures. From Fig. 4.4(a), we notice that the topological Hall effect is more significant at low temperatures with a maximum of $\rho^{T}_{xy} = 0.69$ $\mu\Omega$ cm for a critical field of 0.6 T at 2 K, which disappears at higher temperatures (>50 K).

$$\rho_H = \rho^N_H + \rho^A_H = R_0\mu_0 H + R_S\mu_0 M \tag{4.1}$$

Here, R_0 is the normal Hall coefficient and R_S is the anomalous Hall coefficient.

Next, in addition to $\rho_{xy}(H)$ of δ=0.30, $\rho_{xy}(H)$ of δ=0 and 0.62 were also fitted by the Eqn. 4.1 to estimate the values of normal (R_0) and anomalous (R_S) Hall coefficients. Fig. 4.4(b) shows temperature-dependent normal Hall coefficient. Since the normal Hall coefficient R_0 is related to carrier density (n) and charge (q) as $R_0 = \frac{1}{n|q|}$, we can obtain the carrier concentration as a function of temperature, shown in Fig. 4.4(c). From Fig. 4.4(c), we can notice that the carrier concentration of the parent system is almost constant with temperature. For δ=0.30, it hardly changes with temperature down to 50 K and with further decreasing the temperature the carrier concentration rapidly increases. On

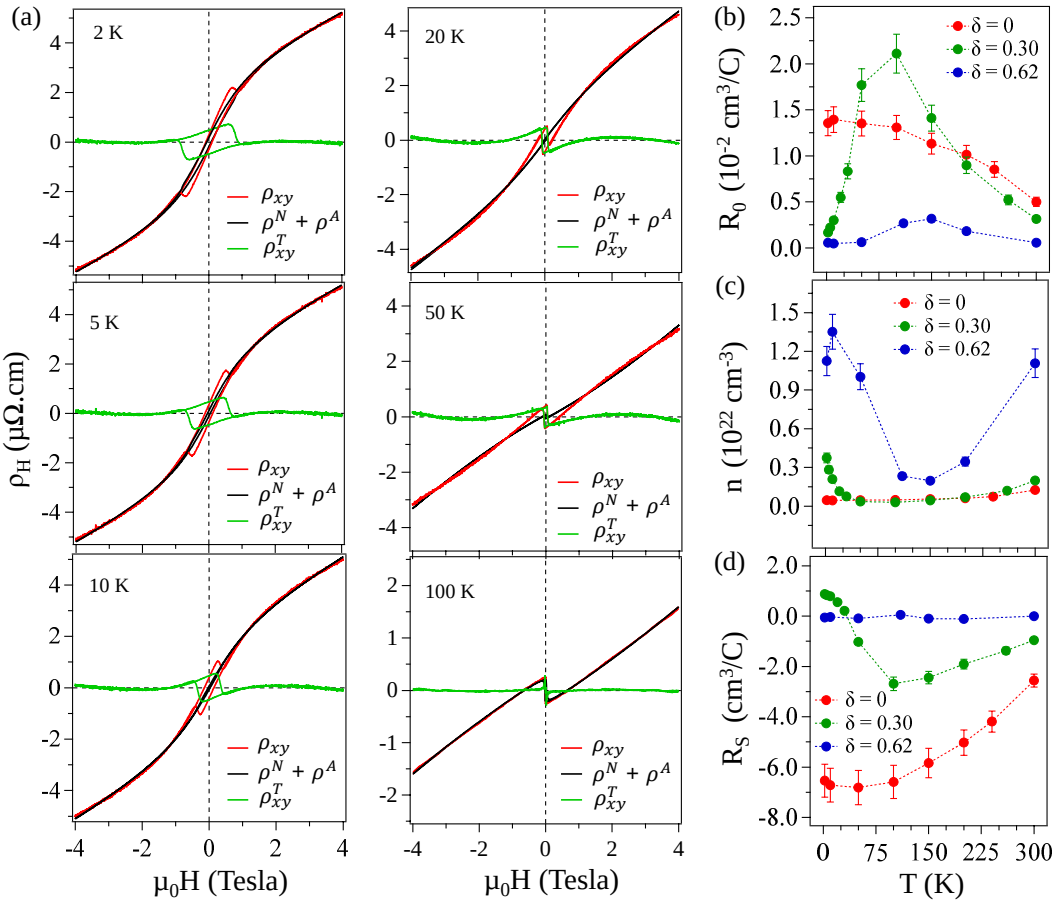

Figure 4.4: (a) Field-dependent in-plane Hall resistivity (ρ_{xy}) measured at different temperature of δ=0.30. The red curves are experimental data and the solid-black curves are the fits using the Eqn. 4.1 and green curves are the topological Hall resistivity (ρ^T_{xy}). (b) Normal Hall coefficient (R_0). (c) Carrier density plotted as a function of temperature. (d) Anomalous Hall coefficient (R_S) plotted as a function of temperature.

the other hand, the carrier concentration of δ=0.62 is nearly the same at both 2 and 300 K but it significantly decreases as the sample approaches 100 K. Such a change in carrier density is possibly related to the magnetic transition around this temperature. Further, the anomalous Hall effect is quantified by the anomalous Hall coefficient (R_S). From Fig. 4.4(d), we can find large R_S values for the parent system at 2 K, which decrease with increasing temperature, consistent with the total Hall resistivity [see Fig. 4.3(b)]. On the other hand, fluctuating R_S values are noticed in the δ=0.30 compound. To be precise, positive and negative R_S values are found below and above the sample temperature of 50 K, respectively. Such a crossover from positive to negative R_S values indicates the sign change in the anomalous Hall effect as observed in the inset of Fig. 4.3(d) [59]. Negligible R_S values found from the δ=0.62 suggest negligible AHE which is in agreement with Fig. 4.3(e). We further notice a change in the sign of AHE between the parent system ($-ve$) and the Fe doped system of δ=0.62 ($+ve$), possibly due to the change in carrier

concentration with Fe doping as a sign of the Hall conductivity or Berry curvature is sensitive to the chemical potential [49, 60]. The same can be valid for the δ=0.30 system as well, in which we observe a change in the sign of AHE below $(+ve)$ and above $(-ve)$ 50 K [see Figs. 4.4(c) and 4.4(d)].

4.4 Discussions

Overall, the electrical transport, magnetic, and magnetotransport properties of $Mn_{3.48}Ge$ are consistent with previous reports [47, 15, 16, 49, 46]. During this manuscript preparation, a report on $Mn_{2.34}Fe_{0.66}Ge$ has appeared in the literature [58], thoroughly discussing the magnetic and magnetotransport properties. Our magnetic and magnetotransport results on δ=0.62 compound agree with Ref. [58]. That means the antiferromagnetic transitions observed at 230 K and 100 K in our studied system are very close to the reported values of 240 K and 120 K, respectively. Further, the absence of in-plane anomalous Hall effect (ρ_{xy}) is consistent with the report. However, a small out-of-plane AHE (ρ_{zy}) is reported in Ref. [58] with a maximum of ρ_{zy}=0.7 $\mu\Omega$ cm at 130 K, which we could not study on our skinny samples. Nevertheless, the dominating normal Hall resistivity at all measured temperatures is in excellent agreement with Ref. [58]. In addition, the electrical transport and magnetic properties of our studied system $Mn_{2.69}Fe_{0.62}Ge$ are consistent with several other previous reports on $Mn_{3-\delta}Fe_{\delta}Ge$ ($\delta \geq 0.45$) [61–63]. Specifically, the metal-insulator transition observed at 100 K in our δ=0.62 system is in agrement with the previous report on $(Mn_{0.83}Fe_{0.2})_{3.25}Ge$ [63].

Next, the new results of this manuscript, not yet reported so far, are the electrical transport, magnetic, and Hall effect on $Mn_{2.97}Fe_{0.30}Ge$ compound. Interestingly, although both the parent and δ=0.62 compounds show an increase in longitudinal resistivity (ρ_{xx}) with temperature, at least in the low-temperature regime, $Mn_{2.97}Fe_{0.30}Ge$ does not display any metallic nature of the resistivity. Means the highest resistivity observed at 2 K gradually decreases with increasing temperature, like in magnetic semiconductors [64–66]. On the other hand, we could observe the topological Hall effect in δ=0.30 which was not found in the parent and δ=0.62 systems. There exist several mechanisms to understand the origin of the topological Hall effect, such as the Dzyaloshinskii-Moria (DM) interaction in noncentrosymmetric systems [44, 67, 68], uniaxial magnetocrystalline anisotropy in centrosymmetric systems [27, 69, 30], and chiral domain-wall-induced skyrmion lattice [70–73]. Furthermore, the recent theoretical and experimental studies suggest the stabilization of skyrmion lattice in centrosymmetric kagome systems [74, 75, 17] such as Gd_2PdSi_3 [45], $Gd_3Ru_4Al_{12}$ [76] due to geometrical magnetic frustration. Recently, we have also shown an enhancement of magnetocrystalline anisotropy in addition to the formation of the noncoplanar spin structure generating the topological Hall effect in $Mn_{3-\delta}Fe_{\delta}Sn$ [30]. The same could be true in the present case of δ=0.30 compound as

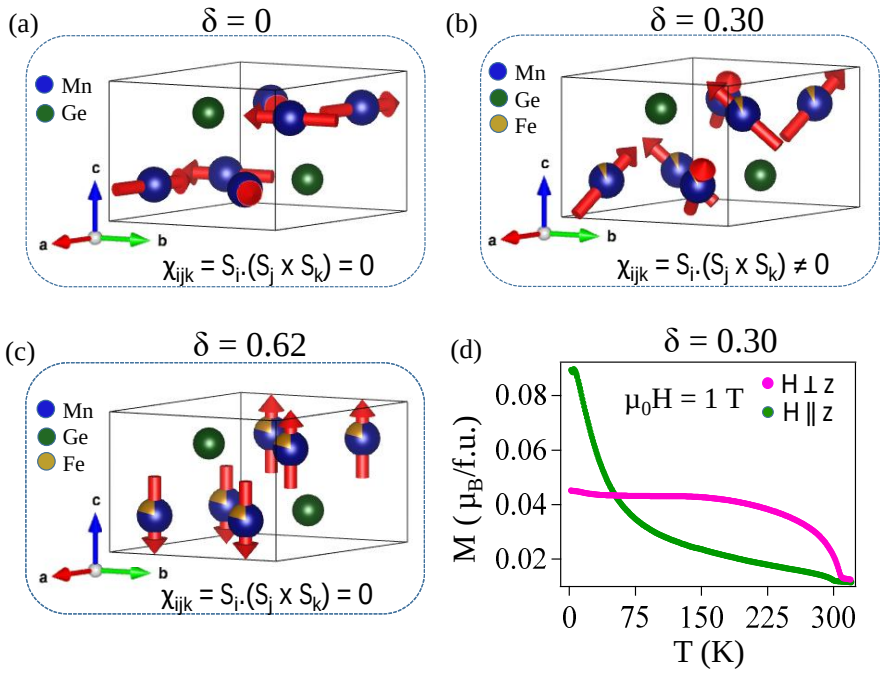

Figure 4.5: Schematic representation of the Mn magnetic moment arrangement in the parent (a), δ=0.30 (T < 50 K) (b), and δ=0.62 (T < 100 K) (c) compounds. (d) Magnetization plotted as a function of temperature measured at 1 T of applied field from δ=0.30 sample.

well.

Fig. 4.5 schematically demonstrates the magnetic structure observed in the studied compositions of δ=0, 0.30, and 0.62. Fig. 4.5(a) depicts the Mn_3Ge magnetic structure with an inverse-triangular arrangement of the Mn magnetic moments. Here, the Mn magnetic moments are in a noncollinear but coplanar antiferromagnetic order, leading to zero scalar spin chirality $\chi_{ijk} = S_i.(S_j \times S_k) = 0$. Thus, no topological Hall effect has been observed but only the anomalous Hall effect due to nonzero Berry curvature in the momentum space [46, 14, 16, 15]. With a Fe doping of δ=0.62, $Mn_{2.69}Fe_{0.62}Ge$ has a collinear out-of-plane AFM ordering as demonstrated in Ref. [58] by the neutron diffraction study as well in this study [see Fig. 4.2(f)], is schematically shown in Fig. 4.5(c). Since in this case also the scalar spin chirality is zero, no topological Hall effect is anticipated.

Fig. 4.5(b) schematically shows the noncoplanar arrangement of the Mn magnetic moments in $Mn_{2.97}Fe_{0.30}Ge$, where the magnetic moments align neither ferromagnetically nor antiferromagnetically in any particular direction under the external applied field. In this case, the scalar spin chirality will be nonzero, $\chi_{ijk} = S_i.(S_j \times S_k) \neq 0$. As a result, the topological Hall resistivity is warranted, as shown in Fig. 4.4(a). Further, to confirm that the system has a noncoplanar spin structure, we plotted $M(T)$ of $Mn_{2.97}Fe_{0.30}Ge$ under the applied field of 1 T in Fig. 4.5(d). From Fig. 4.5(d), we can notice that the in-plane magnetization gradually increases with decreasing temperature and nearly saturates below 150 K. On the other hand, the out-of-plane magnetization rapidly in-

creases with decreasing temperature and dominates the in-plane magnetization below 50 K. Such a crossover from dominating in-plane to out-of-plane magnetization indicates that the spins are canted towards out-of-plane directions, producing field-induced non-coplanar spin structure. This argument is further supported by Fig. 4.2(e), in which the in-plane magnetization dominates the out-of-plane magnetization at higher temperatures (T = 200 K). In contrast, the out-of-plane magnetization dominates the in-plane at 2 K, above 0.3 T of applied fields. Therefore, our results suggest that the noncoplanar spin structure stabilized by the strong magnetocrystalline anisotropy originates the topological Hall effect in $Mn_{2.97}Fe_{0.30}Ge$ [30].

4.5 Summary

We have systematically studied the electrical, magnetic, and magnetotransport properties of $Mn_{(3+x)-\delta}Fe_{\delta}Ge$ (δ=0, 0.30, and 0.62). We find that the electrical resistivity of the parent compound displays metallic behavior, while the system with δ=0.30 of Fe doping exhibits resistivity similar to a dilute magnetic semiconductor. With further Fe doping of δ=0.62, the system demonstrates a metal-insulator transition at 100 K. Fe doping increases ferromagnetism and magnetocrystalline anisotropy. It induces a spin-glass-like state at low temperatures. In addition, the spontaneous anomalous Hall effect observed in the parent system is significantly reduced with increasing Fe doping concentration. Importantly, the topological Hall effect observed in $Mn_{2.97}Fe_{0.30}Ge$ (δ=0.30), is not found from the parent system $Mn_{3.48}Ge$ or $Mn_{2.69}Fe_{0.62}Ge$ (δ=0.62).

References

[1] G. Xu, H. Weng, Z. Wang, X. Dai, Z. Fang, Chern Semimetal and the Quantized Anomalous Hall Effect in $HgCr_2Se_4$, Phys. Rev. Lett. 107 (2011) 186806.

[2] D. F. Liu, A. J. Liang, E. K. Liu, Q. N. Xu, Y. W. Li, C. Chen, D. Pei, W. J. Shi, S. K. Mo, P. Dudin, T. Kim, C. Cacho, G. Li, Y. Sun, L. X. Yang, Z. K. Liu, S. S. P. Parkin, C. Felser, Y. L. Chen, Magnetic Weyl semimetal phase in a Kagomé crystal, Science 365 (2019) 1282–1285.

[3] Z. Liu, M. Li, Q. Wang, G. Wang, C. Wen, K. Jiang, X. Lu, S. Yan, Y. Huang, D. Shen, J.-X. Yin, Z. Wang, Z. Yin, H. Lei, S. Wang, Orbital-selective Dirac fermions and extremely flat bands in frustrated kagome-lattice metal CoSn, Nat. Commun. 11 (2020).

[4] L. Ye, M. Kang, J. Liu, F. von Cube, C. R. Wicker, T. Suzuki, C. Jozwiak, A. Bostwick, E. Rotenberg, D. C. Bell, L. Fu, R. Comin, J. G. Checkelsky, Massive Dirac fermions in a ferromagnetic kagome metal, Nature 555 (2018) 638–642.

[5] H. Nakano, T. Sakai, Quantum Spin Liquid in the Kagome-Lattice Antiferromagnet and Related Systems, J Phys : Conf Ser 868 (2017) 012006.

[6] X. Wu, T. Schwemmer, T. Müller, A. Consiglio, G. Sangiovanni, D. Di Sante, Y. Iqbal, W. Hanke, A. P. Schnyder, M. M. Denner, M. H. Fischer, T. Neupert, R. Thomale, Nature of Unconventional Pairing in the Kagome Superconductors AV_3Sb_5 ($A = \mathrm{K}, \mathrm{Rb}, \mathrm{Cs}$), Phys. Rev. Lett. 127 (2021) 177001.

[7] E. Liu, Y. Sun, N. Kumar, L. Muechler, A. Sun, L. Jiao, S.-Y. Yang, D. Liu, A. Liang, Q. Xu, et al., Giant anomalous Hall effect in a ferromagnetic kagome-lattice semimetal, Nature physics 14 (2018) 1125–1131.

[8] X. Li, C. Collignon, L. Xu, H. Zuo, A. Cavanna, U. Gennser, D. Mailly, B. Fauqué, L. Balents, Z. Zhu, K. Behnia, Chiral domain walls of Mn_3Sn and their memory, Nat. Commun. 10 (2019) 3021.

[9] N. Kanazawa, Y. Onose, T. Arima, D. Okuyama, K. Ohoyama, S. Wakimoto, K. Kakurai, S. Ishiwata, Y. Tokura, Large Topological Hall Effect in a Short-Period Helimagnet MnGe, Phys. Rev. Lett. 106 (2011) 156603.

[10] S. Mühlbauer, B. Binz, F. Jonietz, C. Pfleiderer, A. Rosch, A. Neubauer, R. Georgii, P. Böni, Skyrmion Lattice in a Chiral Magnet, Science 323 (2009) 915–919.

[11] H. Zhang, H. Feng, X. Xu, W. Hao, Y. Du, Recent progress on 2d kagome magnets: Binary tmsnn (t= fe, co, mn), Advanced Quantum Technologies 4 (2021) 2100073.

[12] N. Chowdhury, K. I. A. Khan, H. Bangar, P. Gupta, R. S. Yadav, R. Agarwal, A. Kumar, P. K. Muduli, Kagome Magnets: The Emerging Materials for Spintronic Memories, Proceedings of the National Academy of Sciences, India Section A: Physical Sciences (2023).

[13] N. Morali, R. Batabyal, P. K. Nag, E. Liu, Q. Xu, Y. Sun, B. Yan, C. Felser, N. Avraham, H. Beidenkopf, Fermi-arc diversity on surface terminations of the magnetic Weyl semimetal $Co_3Sn_2S_2$, Science 365 (2019) 1286–1291.

[14] S. Nakatsuji, N. Kiyohara, T. Higo, Large anomalous Hall effect in a non-collinear antiferromagnet at room temperature, Nature 527 (2015) 212–215.

[15] A. K. Nayak, J. E. Fischer, Y. Sun, B. Yan, J. Karel, A. C. Komarek, C. Shekhar, N. Kumar, W. Schnelle, J. Kübler, et al., Large anomalous Hall effect driven by a

nonvanishing Berry curvature in the noncolinear antiferromagnet Mn_3Ge, Sci. Adv. 2 (2016) e1501870.

[16] N. Kiyohara, T. Tomita, S. Nakatsuji, Giant Anomalous Hall Effect in the Chiral Antiferromagnet Mn_3Ge, Phys. Rev. Applied 5 (2016) 064009.

[17] P. K. Rout, P. V. P. Madduri, S. K. Manna, A. K. Nayak, Field-induced topological Hall effect in the noncoplanar triangular antiferromagnetic geometry of Mn_3Sn, Phys. Rev. B 99 (2019) 094430.

[18] J. M. Taylor, A. Markou, E. Lesne, P. K. Sivakumar, C. Luo, F. Radu, P. Werner, C. Felser, S. S. P. Parkin, Anomalous and topological Hall effects in epitaxial thin films of the noncollinear antiferromagnet Mn_3Sn, Phys. Rev. B 101 (2020) 094404.

[19] H. Li, B. Ding, J. Chen, Z. Li, Z. Hou, E. Liu, H. Zhang, X. Xi, G. Wu, W. Wang, Large topological Hall effect in a geometrically frustrated kagome magnet Fe_3Sn_2, Appl. Phys. Lett. 114 (2019) 192408.

[20] Y. Shiomi, M. Mochizuki, Y. Kaneko, Y. Tokura, Hall Effect of Spin-Chirality Origin in a Triangular-Lattice Helimagnet $Fe_{1.3}Sb$, Phys. Rev. Lett. 108 (2012) 056601.

[21] K. S. Denisov, I. V. Rozhansky, N. S. Averkiev, E. Lähderanta, General theory of the topological Hall effect in systems with chiral spin textures, Phys. Rev. B 98 (2018) 195439.

[22] A. Neubauer, C. Pfleiderer, B. Binz, A. Rosch, R. Ritz, P. G. Niklowitz, P. Böni, Topological Hall Effect in the A Phase of MnSi, Phys. Rev. Lett. 102 (2009) 186602.

[23] N. Nagaosa, Y. Tokura, Topological properties and dynamics of magnetic skyrmions, Nat. Nanotechnol. 8 (2013) 899–911.

[24] X. Z. Yu, N. Kanazawa, Y. Onose, K. Kimoto, W. Z. Zhang, S. Ishiwata, Y. Matsui, Y. Tokura, Near room-temperature formation of a skyrmion crystal in thin-films of the helimagnet FeGe, Nat. Mater. 10 (2010) 106–109.

[25] S. X. Huang, C. L. Chien, Extended Skyrmion Phase in Epitaxial FeGe(111) Thin Films, Phys. Rev. Lett. 108 (2012) 267201.

[26] X. Z. Yu, Y. Onose, N. Kanazawa, J. H. Park, J. H. Han, Y. Matsui, N. Nagaosa, Y. Tokura, Real-space observation of a two-dimensional skyrmion crystal, Nature 465 (2010) 901–904.

[27] X. Z. Yu, Y. Tokunaga, Y. Kaneko, W. Z. Zhang, K. Kimoto, Y. Matsui, Y. Taguchi, Y. Tokura, Biskyrmion states and their current-driven motion in a layered manganite, Nat. Commun. 5 (2014).

[28] Z. Hou, W. Ren, B. Ding, G. Xu, Y. Wang, B. Yang, Q. Zhang, Y. Zhang, E. Liu, F. Xu, W. Wang, G. Wu, X. Zhang, B. Shen, Z. Zhang, Observation of Various and Spontaneous Magnetic Skyrmionic Bubbles at Room Temperature in a Frustrated Kagome Magnet with Uniaxial Magnetic Anisotropy, Adv. Mater. 30 (2018) 1706306.

[29] Q. Du, Z. Hu, M.-G. Han, F. Camino, Y. Zhu, C. Petrovic, Topological Hall Effect Anisotropy in Kagome Bilayer Metal Fe_3Sn_2, Phys. Rev. Lett. 129 (2022) 236601.

[30] A. Low, S. Ghosh, S. Changdar, S. Routh, S. Purwar, S. Thirupathaiah, Tuning of topological properties in the strongly correlated antiferromagnet Mn_3Sn via Fe doping, Phys. Rev. B 106 (2022) 144429.

[31] C. S. Spencer, J. Gayles, N. A. Porter, S. Sugimoto, Z. Aslam, C. J. Kinane, T. R. Charlton, F. Freimuth, S. Chadov, S. Langridge, J. Sinova, C. Felser, S. Blügel, Y. Mokrousov, C. H. Marrows, Helical magnetic structure and the anomalous and topological Hall effects in epitaxial B20 $Fe_{1-y}Co_yGe$ films, Phys. Rev. B 97 (2018) 214406.

[32] Y. Li, N. Kanazawa, X. Z. Yu, A. Tsukazaki, M. Kawasaki, M. Ichikawa, X. F. Jin, F. Kagawa, Y. Tokura, Robust Formation of Skyrmions and Topological Hall Effect Anomaly in Epitaxial Thin Films of MnSi, Phys. Rev. Lett. 110 (2013) 117202.

[33] C. Sürgers, G. Fischer, P. Winkel, H. v. Löhneysen, Large topological Hall effect in the non-collinear phase of an antiferromagnet, Nature Communications 5 (2014).

[34] B. G. Ueland, C. F. Miclea, Y. Kato, O. Ayala–Valenzuela, R. D. McDonald, R. Okazaki, P. H. Tobash, M. Torrez, F. Ronning, R. Movshovich, Z. Fisk, E. Bauer, I. Martin, J. Thompson, Controllable chirality-induced geometrical Hall effect in a frustrated highly correlated metal, Nat. Commun. 3 (2012).

[35] T. Taniguchi, K. Yamanaka, H. Sumioka, T. Yamazaki, Y. Tabata, S. Kawarazaki, Direct Observation of Chiral Susceptibility in the Canonical Spin Glass AuFe, Phys. Rev. Lett. 93 (2004) 246605.

[36] F. W. Fabris, P. Pureur, J. Schaf, V. N. Vieira, I. A. Campbell, Chiral anomalous Hall effect in reentrant AuFe alloys, Phys. Rev. B 74 (2006) 214201.

[37] Y. Machida, S. Nakatsuji, Y. Maeno, T. Tayama, T. Sakakibara, S. Onoda, Unconventional Anomalous Hall Effect Enhanced by a Noncoplanar Spin Texture in the Frustrated Kondo Lattice $Pr_2Ir_2O_7$, Phys. Rev. Lett. 98 (2007) 057203.

[38] H. Takatsu, S. Yonezawa, S. Fujimoto, Y. Maeno, Unconventional Anomalous Hall Effect in the Metallic Triangular-Lattice Magnet $PdCrO_2$, Phys. Rev. Lett. 105 (2010) 137201.

[39] L. M. Wang, Anomalous Hall Effect in $La_{0.7}Sr_{0.3}MnO_3/SrTiO_3$ Superlattices: Hopping Transport and a Probe of Dimensionality, Phys. Rev. Lett. 96 (2006) 077203.

[40] L. Vistoli, W. Wang, A. Sander, Q. Zhu, B. Casals, R. Cichelero, A. Barthélémy, S. Fusil, G. Herranz, S. Valencia, R. Abrudan, E. Weschke, K. Nakazawa, H. Kohno, J. Santamaria, W. Wu, V. Garcia, M. Bibes, Giant topological Hall effect in correlated oxide thin films, Nat. Phys. 15 (2018) 67–72.

[41] Y. Ohuchi, Y. Kozuka, M. Uchida, K. Ueno, A. Tsukazaki, M. Kawasaki, Topological Hall effect in thin films of the Heisenberg ferromagnet EuO, Phys. Rev. B 91 (2015) 245115.

[42] A. Soumyanarayanan, M. Raju, A. L. G. Oyarce, A. K. C. Tan, M.-Y. Im, A. P. Petrović, P. Ho, K. H. Khoo, M. Tran, C. K. Gan, F. Ernult, C. Panagopoulos, Tunable room-temperature magnetic skyrmions in Ir/Fe/Co/Pt multilayers, Nat. Mater. 16 (2017) 898–904.

[43] C. Liu, Y. Zang, W. Ruan, Y. Gong, K. He, X. Ma, Q.-K. Xue, Y. Wang, Dimensional Crossover-Induced Topological Hall Effect in a Magnetic Topological Insulator, Phys. Rev. Lett. 119 (2017) 176809.

[44] N. Kanazawa, M. Kubota, A. Tsukazaki, Y. Kozuka, K. S. Takahashi, M. Kawasaki, M. Ichikawa, F. Kagawa, Y. Tokura, Discretized topological Hall effect emerging from skyrmions in constricted geometry, Phys. Rev. B 91 (2015) 041122.

[45] T. Kurumaji, T. Nakajima, M. Hirschberger, A. Kikkawa, Y. Yamasaki, H. Sagayama, H. Nakao, Y. Taguchi, T. hisa Arima, Y. Tokura, Skyrmion lattice with a giant topological Hall effect in a frustrated triangular-lattice magnet, Science 365 (2019) 914–918.

[46] T. Chen, T. Tomita, S. Minami, M. Fu, T. Koretsune, M. Kitatani, I. Muhammad, D. Nishio-Hamane, R. Ishii, F. Ishii, et al., Anomalous transport due to Weyl fermions in the chiral antiferromagnets Mn_3X, X= Sn, Ge, Nature communications 12 (2021) 1–14.

[47] N. Yamada, H. Sakai, H. Mori, T. Ohoyama, Magnetic properties of ϵ-Mn_3Ge, Physica B+ C 149 (1988) 311–315.

[48] E. Arras, D. Caliste, T. Deutsch, F. Lançon, P. Pochet, Phase diagram, structure, and magnetic properties of the Ge-Mn system: A first-principles study, Phys. Rev. B 83 (2011) 174103.

[49] L. Xu, X. Li, X. Lu, C. Collignon, H. Fu, J. Koo, B. Fauqué, B. Yan, Z. Zhu, K. Behnia, Finite-temperature violation of the anomalous transverse Wiedemann-Franz law, Sci. Adv. 6 (2020) eaaz3522.

[50] C. Wuttke, F. Caglieris, S. Sykora, F. Scaravaggi, A. U. B. Wolter, K. Manna, V. Süss, C. Shekhar, C. Felser, B. Büchner, C. Hess, Berry curvature unravelled by the anomalous Nernst effect in Mn_3Ge, Phys. Rev. B 100 (2019) 085111.

[51] J. Dho, W. S. Kim, N. H. Hur, Reentrant Spin Glass Behavior in Cr-Doped Perovskite Manganite, Phys. Rev. Lett. 89 (2002) 027202.

[52] W. J. Feng, D. Li, W. J. Ren, Y. B. Li, W. F. Li, J. Li, Y. Q. Zhang, Z. D. Zhang, Glassy ferromagnetism in ni_3Sn-type $mn_{3.1}sn_{0.9}$, Phys. Rev. B 73 (2006) 205105.

[53] B. S. Wang, P. Tong, Y. P. Sun, X. B. Zhu, Z. R. Yang, W. H. Song, J. M. Dai, Observation of spin-glass behavior in antiperovskite compound SnCFe3, Appl. Phys. Lett. 97 (2010) 042508.

[54] P. Bag, P. R. Baral, R. Nath, Cluster spin-glass behavior and memory effect in $cr_{0.5}fe_{0.5}$Ga, Physical Review B 98 (2018) 144436.

[55] T. F. Duan, W. J. Ren, W. L. Liu, S. J. Li, W. Liu, Z. D. Zhang, Magnetic anisotropy of single-crystalline Mn3Sn in triangular and helix-phase states, Appl. Phys. Lett. 107 (2015) 082403.

[56] N. H. Sung, F. Ronning, J. D. Thompson, E. D. Bauer, Magnetic phase dependence of the anomalous Hall effect in Mn3Sn single crystals, Appl. Phys. Lett. 112 (2018) 132406.

[57] S. Tomiyoshi, Y. Yamaguchi, T. Nagamiya, Triangular spin configuration and weak ferromagnetism of Mn_3Ge, J. Magn. Magn. Mater. 31 (1983) 629–630.

[58] V. Rai, A. Stunault, W. Schmidt, S. Jana, J. Perßon, J.-R. Soh, T. Brückel, S. Nandi, Anomalous Hall effect and magnetic structure of the topological semimetal $(Mn_{0.78}Fe_{0.22})_3Ge$, Phys. Rev. B 107 (2023) 184413.

[59] H. Gu, J. Tian, C. Kang, L. Wang, R. Pang, M. Shen, K. Liu, L. She, Y. Song, X. Liu, W. Zhang, Sign change of anomalous Hall effect with temperature in $Cr_{2.63}V_{0.25}Te_4$ single crystal, Appl. Phys. Lett. 121 (2022) 191906.

[60] X. Wang, D. Pan, Q. Zeng, X. Chen, H. Wang, D. Zhao, Z. Xu, Q. Yang, J. Deng, T. Zhai, G. Wu, E. Liu, J. Zhao, Robust anomalous Hall effect and temperature-driven Lifshitz transition in Weyl semimetal Mn_3Ge, Nanoscale 13 (2021) 2601–2608.

[61] T. Hori, Y. Yamaguchi, Y. Nakagawa, Antiferromagnetic to ferromagnetic transition of hexagonal $(Mn_{1-x}Fe_x)_3Ge$, J. Magn. Magn. Mater. 104-107 (1992) 2045–2046.

[62] T. Hori, H. Niida, H. Kato, Y. Yamaguchi, Y. Nakagawa, Magnetic phase transition in $(Mn_{1-x}Fe_x)_{3+\delta}Ge$, Physica B: Condensed Matter 211 (1995) 93. Research in High Magnetic Fields.

[63] J. Du, D. Li, Y. B. Li, N. K. Sun, J. Li, Z. D. Zhang, Abnormal magnetoresistance in $\epsilon-(\mathrm{Mn}_{1-x}\mathrm{Fe}_x)_{3.25}\mathrm{Ge}$ antiferromagnets, Phys. Rev. B 76 (2007) 094401.

[64] T. Dietl, A ten-year perspective on dilute magnetic semiconductors and oxides, Nat. Mater. 9 (2010) 965.

[65] Z. Deng, C. Jin, Q. Liu, X. Wang, J. Zhu, S. Feng, L. Chen, R. Yu, C. Arguello, T. Goko, F. Ning, J. Zhang, Y. Wang, A. Aczel, T. Munsie, T. Williams, G. Luke, T. Kakeshita, S. Uchida, W. Higemoto, T. Ito, B. Gu, S. Maekawa, G. Morris, Y. Uemura, Li(Zn,Mn)As as a new generation ferromagnet based on a I–II–V semiconductor, Nat. Commun. 2 (2011) 422.

[66] S. Yu, G. Zhao, Y. Peng, X. Wang, Q. Liu, R. Yu, S. Zhang, J. Zhao, W. Li, Z. Deng, Y. J. Uemura, C. Jin, $(Ba,K)(Zn,Mn)_2Sb_2$: A New Type of Diluted Magnetic Semiconductor, Crystals 10 (2020) 690.

[67] J. Liu, L. Balents, Anomalous Hall Effect and Topological Defects in Antiferromagnetic Weyl Semimetals: Mn_3Sn/Ge, Phys. Rev. Lett. 119 (2017) 087202.

[68] A. S. Sukhanov, A. Heinemann, L. Kautzsch, J. D. Bocarsly, S. D. Wilson, C. Felser, D. S. Inosov, Robust metastable skyrmions with tunable size in the chiral magnet $FePtmo_3N$, Phys. Rev. B 102 (2020) 140409.

[69] M. Preißinger, K. Karube, D. Ehlers, B. Szigeti, H.-A. K. von Nidda, J. S. White, V. Ukleev, H. M. Rønnow, Y. Tokunaga, A. Kikkawa, Y. Tokura, Y. Taguchi, I. Kézsmárki, Vital role of magnetocrystalline anisotropy in cubic chiral skyrmion hosts, npj Quantum Materials 6 (2021).

[70] S. B. Gudnason, M. Nitta, Domain wall Skyrmions, Phys. Rev. D 89 (2014) 085022.

[71] R. Cheng, M. Li, A. Sapkota, A. Rai, A. Pokhrel, T. Mewes, C. Mewes, D. Xiao, M. De Graef, V. Sokalski, Magnetic domain wall skyrmions, Phys. Rev. B 99 (2019) 184412.

[72] T. Nagase, Y.-G. So, H. Yasui, T. Ishida, H. K. Yoshida, Y. Tanaka, K. Saitoh, N. Ikarashi, Y. Kawaguchi, M. Kuwahara, M. Nagao, Observation of domain wall bimerons in chiral magnets, Nat. Commun. 12 (2021).

[73] K. Yang, K. Nagase, Y. Hirayama, T. D. Mishima, M. B. Santos, H. Liu, Wigner solids of domain wall skyrmions, Nat. Commun. 12 (2021).

[74] T. Okubo, S. Chung, H. Kawamura, Multiple-q States and the Skyrmion Lattice of the Triangular-Lattice Heisenberg Antiferromagnet under Magnetic Fields, Phys. Rev. Lett. 108 (2012) 017206.

[75] S. Hayami, R. Ozawa, Y. Motome, Effective bilinear-biquadratic model for noncoplanar ordering in itinerant magnets, Phys. Rev. B 95 (2017) 224424.

[76] M. Hirschberger, T. Nakajima, S. Gao, L. Peng, A. Kikkawa, T. Kurumaji, M. Kriener, Y. Yamasaki, H. Sagayama, H. Nakao, K. Ohishi, K. Kakurai, Y. Taguchi, X. Yu, T. hisa Arima, Y. Tokura, Skyrmion phase and competing magnetic orders on a breathing kagomé lattice, Nat. Commun. 10 (2019).

Chapter 5

Temperature Dependent Intrinsic Anomalous Hall Conductivity Observed in Fe_3Ge, a Ferromagnetic Topological Metal

5.1 Introduction

The Hall effect, a cornerstone of solid-state physics, arises from Lorentz forces acting on charge carriers as they traverse in a conductor under perpendicular applied magnetic field [1, 2]. This fundamental phenomenon has found widespread utility in various technological applications, from precise magnetic field sensing to the characterization of materials' electronic properties [3]. The conventional Hall effect usually occurs in non-magnetic metals [2, 4]. In contrast, the magnetic materials exhibit an anomalous Hall effect (AHE), distinguished by a pronounced increase in Hall resistivity proportionate to the material's magnetization [4]. The AHE was initially attributed to two extrinsic scattering processes, namely the skew-scattering and the side-jump mechanisms [5, 6]. In 1954, Karplus and Luttinger (KL) proposed a different theory to understand the AHE by introducing a band structure-originated contribution to the AHE, an intrinsic contribution [7]. It was later understood that the intrinsic KL mechanism is directly related to the Berry phase effects on the occupied electronic Bloch states [8, 4]. Usually, the Berry phase in the momentum space is considered temperature-independent as the electronic band structure does not change much with temperature unless the system possesses temperature-dependent electronic, structural, or magnetic phase transitions. Therefore, not much information is available on the temperature-dependence of the intrinsic Hall contribution, except for one recent paper discussing the possibility of such effect [9].
In this read, the kagome lattice, consisting of two-dimensional corner-sharing triangles,

enables distinctive electronic behaviors such as van Hove singularities, Dirac-like dispersion, and flat bands [10–12]. Its unique structural geometry combined with topology and electronic correlations [11] provide a rich platform for exploring emergent quantum phenomena. The Hall effect in kagome systems is currently a hotbed of research activities. These materials exhibit large AHE [13, 14] and topological Hall effect (THE) [15], driving the exploration for novel electronic properties and functionalities in these systems. Among them, the Co-based ferromagnetic kagome material $Co_3Sn_2S_2$ stands out for its giant AHE [13, 16]. Interestingly, the Mn-based kagome compounds such as Mn_3X (X = Sn, Ge), despite being antiferromagnetic, demonstrate a large AHE, attributed to the intrinsic nonzero Berry curvature [14, 17, 18]. The ferromagnetic kagome system Fe_3Sn_2 exhibits both AHE and THE [19, 20, 15], while the ferromagnetic compound Fe_3Sn displays a substantial AHE, with contributions originated from both intrinsic and extrinsic sources [21].

On the other hand, the composition Fe_3Ge, similar to Fe_3Sn, has been reported to exhibit room-temperature ferromagnetism and large anomalous Hall effect (AHE) [22, 23]. Most importantly, unlike Fe_3Sn, Fe_3Ge shows the tuning of easy-magnetization axis from the out-of-plane to the in-plane below the spin-reorientation transition at around 380 K [22, 24, 25]. Such a spin-reorientation transition significantly changes the electronic band structure [26], providing an ideal platform to study the temperature effect on the intrinsic Hall conductivity. Therefore, we synthesized the single crystals of Fe_3Ge and thoroughly investigated its directional dependent magnetic and Hall effect properties. Magnetic measurements indicate that below T_{SR}, the Fe magnetic moments gradually cant from the z-direction towards the xy-plane as the temperature decreases. We observe that the Hall conductivity has both intrinsic and extrinsic contributions. Importantly, we demonstrate the temperature dependence of intrinsic Hall contribution due to tuning of the easy-magnetic axis from the out-of-plane to the in-plane with decreasing temperature. We further discuss the effect of electron-phonon scattering on the extrinsic Hall conductivity originating from the skew-scattering mechanism.

5.2 Methodology

5.2.1 Experimental details

Single crystals of Fe_3Ge were prepared by melt growth technique. In this method, high-purity iron (Alfa Aesar 99.999%) and germanium (Alfa Aesar 99.999%) powders were thoroughly ground in an argon-filled glove box to form a homogeneous mixture. The mixture was then transferred into an alumina crucible, which was subsequently sealed within a preheated quartz ampoule under a vacuum. The sealed ampoule was heated to 1120°C in a high-temperature box furnace and kept at that temperature for a day

for a thorough chemical reaction. Subsequently, the temperature was slowly reduced to 800°C at a controlled cooling rate of 2°/hour. After prolonged annealing for the next five days at 800°C, the sample was rapidly quenched in ice water to prevent the formation of low-temperature phases.

Phase purity and structural characterization were done using powder X-ray diffraction (XRD) with CuK_α radiation (9 kW) on a Rigaku X-ray diffractometer. Chemical composition was identified using energy-dispersive X-ray spectroscopy (EDS) measurements. The EDS data reveal that the exact chemical composition of the as-prepared samples is $Fe_{3.05}Ge_{0.95}$, which is very close to the nominal composition of Fe_3Ge (see Fig. 5.1(c)). Further, the EDS elemental mapping verifies the homogeneity and compositional uniformity of the single crystal studied single crystals (see Fig. 5.1(d)). Scanning electron microscope (SEM) image reveals no evidence of grain boundaries within the crystal, confirming the sample's single-crystalline nature (inset of Fig. 5.1(c)).

Electrical transport and magnetic properties were measured using a 9-Tesla physical property measurement system (PPMS, Dynacool, Quantum Design) over a broad temperature range between 2 and 380 K. High-temperature magnetic behavior was explored with a VSM-oven attached to the PPMS. Hall effect and transport measurements employed the standard four-probe method, with copper leads meticulously attached to the sample using H20E/1Oz silver epoxy for reliable contact. For convenience, the cartesian coordinates (x, y, z) are used instead of crystallographic axes (a, b, c) wherever required in this manuscript. We can identify the c-axis (z) and ab-plane (xy) using XRD measurements, but we were unable to differentiate between the a- and b-axes. Therefore, to streamline the manuscript, the longer side of the crystal's xy-plane (inset of Fig. 5.1(b)) is considered as the x-axis, and the shorter side as the y-axis.

5.2.2 First-principles Calculations

The electronic ground states of Fe_3Ge were calculated using density functional theory (DFT) within the Perdew-Burke-Ernzerhof (PBE) generalized gradient approximation (GGA), implemented in the Quantum Espresso (QE) simulation package [27]. The crystal structure was optimized with ultrasoft pseudo-potentials [28], using the force and energy convergence criteria of 10^{-4} $Ry/$Å and 10^{-5} Ry, respectively. An energy cutoff of 110 Ry and a charge density cutoff of 1320 Ry were applied for the plane-wave basis set. A $20 \times 20 \times 20$ k-point mesh was employed for Brillouin zone sampling. The Methfessel-Paxton (mp) smearing technique with a smearing parameter of $\sigma = 0.007$ Ry was utilized for the charge density evaluation. The spin-orbit coupling effect was incorporated using the fully relativistic pseudo-potentials. To explore the anomalous Hall conductivity (AHC), a tight-binding model was constructed using maximally localized Wannier functions (MLWFs) via the Wannier90 code [29]. The Berry curvature along high-symmetry

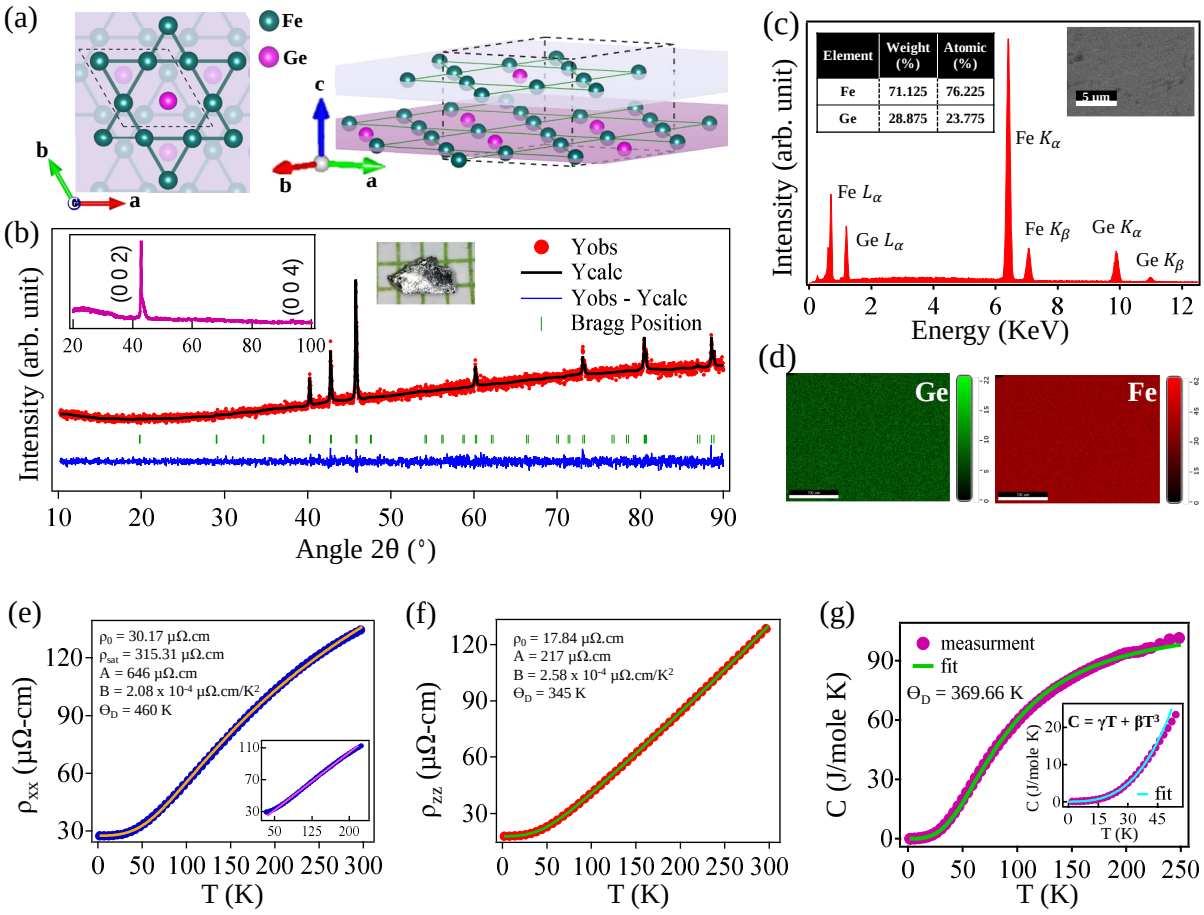

Figure 5.1: (a) Schematic crystal structure of the hexagonal unit cell and kagome lattice of Fe_3Ge. (b) Powder X-ray diffraction (XRD) pattern of the crushed single crystals of Fe_3Ge overlapped with the Rietveld refinement. Insets in (b) display a photographic image of the Fe_3Ge single crystal and XRD pattern taken on the Fe_3Ge single crystal. (c) EDS spectra of Fe_3Ge and inset shows the tabulated elemental ratios present in the system. (d) The elemental mapping of Fe and Ge in the studied single crystals. (e) and (f) depict the temperature dependent in-plane (ρ_{xx}) and out-of-plane (ρ_{zz}) electrical resistivity, respectively. The solid curves in (e) and (f) are fits using the Bloch-Wilson equation (see the text for more details). Inset in (e) shows the linear resistivity within the temperature range of 50-200 K. (g) Temperature-dependent specific heat. The solid line is a fit with the Debye model. The inset shows a zoomed-in image of the low-temperature region.

directions was computed using the Kubo formolism [30] as also implemented in Wannier90 code. The intrinsic AHC along the [001] and [010] directions were then obtained by integrating the z- and y-components of the Berry curvature over the entire Brillouin zone using the WannierTools code [31].

5.3 Result and Discussion

The left panel in Fig. 5.1(a) depicts the schematic view of the hexagonal crystal structure of Fe_3Ge and the right panel in Fig. 5.1(a) shows crystal structure projected onto *ab*-plane from which we can identify the kagome lattice plane formed by the Fe atoms with hexagons and triangles and Ge sitting in the center of the hexagon. The powder x-ray diffraction performed on the crushed single crystals of Fe_3Ge, as shown in Fig. 5.1(b), confirms the phase purity of the as-grown single crystals. The inset in Fig. 5.1(b) depicts XRD pattern taken on the Fe_3Ge single crystal with the (0 0 l) Bragg's plane, suggesting that the crystal growth axis is parallel to the *c*-axis. In-plane (ρ_{xx}) and out-of-plane (ρ_{zz}) longitudinal electrical resistivity were measured as a function of temperature as shown in Figs. 5.1(e) and 5.1(f), respectively, confirming the metallic nature of Fe_3Ge throughout the measured temperature range. The electrical resistivity data on our Fe_3Ge are consistent with previous reports [23, 25]. Further, ρ_{zz}(T) was fitted using the Bloch-Wilson equation (see Eq. 5.1) for n=3, which accounts for the phonon contribution to the resistivity in combination with T^2 term to account for the electron-electron scattering [32, 33]. On the other hand, for the best fitting of ρ_{xx}(T) data [see Fig. 5.1(e)], we need to add an extra term ρ_{sat} to Eq. 5.1 (see Eq. 5.2) as ρ_{xx}(T) tends to saturate at higher temperatures [34]. From these fittings, we obtained Debye temperature (Θ_D) of about 460 K from ρ_{xx} and 345 K from ρ_{zz} data. The average Debye temperature of 402 K is close to the Debye temperature (Θ_D =369 K) derived from the heat capacity measurements (see Fig. 5.1(g)).

$$\rho(T) = \rho_0 + A\left(\frac{T}{\Theta_D}\right)^3 \int_0^{\frac{\Theta_D}{T}} \frac{x^3}{(e^x-1)(1-e^{-x})}\,dx + BT^2 \tag{5.1}$$

$$\frac{1}{\rho_{tot}} = \frac{1}{\rho(T)} + \frac{1}{\rho_{sat}} \tag{5.2}$$

In Fig. 5.1(g), specific heat is plotted as a function of temperature for Fe_3Ge. The Debye model is used to fit the specific heat data using the Eq. 5.3. From the fitting we obtained a temperature of Θ_D =369 K.

$$C(T) = 9nR\left(\frac{T}{\Theta_D}\right)^3 \int_0^{\frac{\Theta_D}{T}} \frac{e^x x^4}{(e^x-1)^2}\,dx. \tag{5.3}$$

From the fitting, we obtained a value of $9nR = 311.80\,\mathrm{J\,mol^{-1}\,K^{-1}}$, which yields $3nR = 103.93\,\mathrm{J\,mol^{-1}\,K^{-1}}$. This is in good agreement with the expected Dulong–Petit limit of $3nR = 99.72\,\mathrm{J\,mol^{-1}\,K^{-1}}$, where $n = 4$ is the number of atoms per formula unit in Fe_3Ge, and $R = 8.31\,\mathrm{J\,mol^{-1}\,K^{-1}}$ is the universal gas constant. Further, specific heat at low temperatures can be expressed best by using the Eq. 5.4.

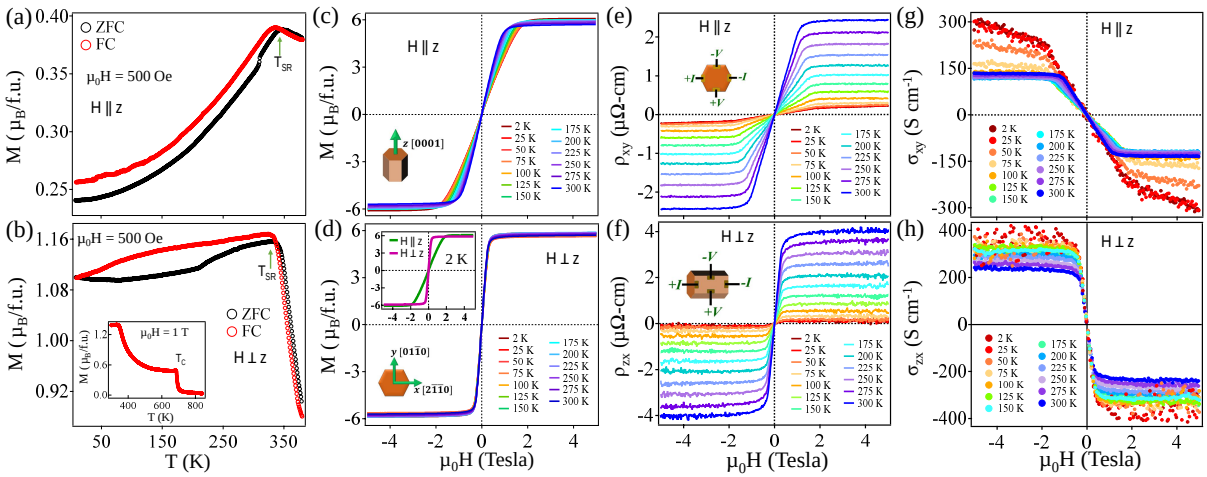

Figure 5.2: Temperature-dependent magnetization $[M(T)]$ of Fe_3Ge plotted for (a) $H \parallel z$ and (b) $H \perp z$ under an applied magnetic field of $H = 500$ Oe. Inset in (b) shows the $M(T)$ data at high temperatures. Magnetization isotherms $[M(H)]$ plotted for (c) $H \parallel z$ and (d) $H \perp z$ at various sample temperatures. In-plane (ρ_{xy}) and out-of-plane (ρ_{zx}) Hall resistivity plotted as a function of the field for (e) $H \parallel z$ and (f) $H \perp z$ at various sample temperatures. In-plane (σ_{xy}) and out-of-plane (σ_{zx}) Hall conductivity plotted as a function of the field for (g) $H \parallel z$ and (h) $H \perp z$ at various sample temperatures.

$$C = \gamma T + \beta T^3 \tag{5.4}$$

Here, γT represents the electronic contribution and βT^3 the phononic contribution to the specific heat. The obtained γ and β values are 2.98 mJ mol^{-1} K^{-2} and 0.18 mJ mol^{-1} K^{-4}, respectively.

To elucidate the magnetic properties of Fe_3Ge, we measured magnetization as a function of temperature $[M(T)]$ and field $[M(H)]$ as shown in Fig. 5.2 for both $H \parallel z$ and $H \perp z$. From the $M(T)$ data [see Figs. 5.2(a) and 5.2(b)], we find a spin-orientation transition at around T_{SR} =340 K below which the out-of-plane magnetization ($H \parallel z$) significantly reduces (35% from the maximum at 340 K) ingoing to low-temperature below T_{SR}. On the other hand, the in-plane magnetization ($H \perp z$) does not decrease much (5%) with decreasing temperature below T_{SR}. Further, we notice a ferromagnetic transition at a Curie temperature of T_C =680 K as demonstrated in the inset of Fig. 5.2(b). The magnetisation isotherms $M(H)$ for $H \parallel z$ and $H \perp z$ at different sample temperatures are shown in Figs. 5.2(c) and 5.2(d), respectively. The $M(H)$ data indicate that Fe_3Ge exhibits an in-plane ($H \perp z$) easy-axis of magnetization in its ground state, as evidenced by the inset shown in Fig. 5.2(d). Interestingly, the $M(H)$ of all temperatures for $H \perp z$ do not change significantly as the saturation magnetization remains almost constant across all measured temperatures. In contrast, for $H \parallel z$, the $M(H)$ curves progressively shift to higher saturation magnetization values as the temperature decreases. This observation

indicates that as the temperature decreases, the spins of Fe moments gradually reorient from the z-axis to the xy-plane, and eventually stabilize into an in-plane ferromagnetic configuration at low temperatures. This observation is consistent with the $M(T)$ data shown in Figs. 5.2(a) and 5.2(b). Earlier also, it was reported that the Fe magnetic moments in this material exhibit a gradual deviation from the z-axis towards the xy-plane below T_{SR} [22, 24, 23].

Next, the field-dependent Hall resistivity measured for in-plane (ρ_{xy}) and out-of-plane (ρ_{zx}) at various temperatures are presented in Figs. 5.2(e) and 5.2(f), respectively. A sharp increase in the Hall resistivity at low fields, followed by saturation at higher fields, confirms the presence of anomalous Hall effect (AHE) in Fe_3Ge [4, 25]. Figs. 5.2(g) and 5.2(h) depict the Hall conductivity derived from the Hall resistivity shown in Figs. 5.2(e) and 5.2(f), respectively, using the relation,

$$\sigma_{xy/zx} = \frac{-\rho_{xy/zx}}{\rho^2_{xy/zx} + \rho^2_{xx/zz}} \tag{5.5}$$

where $\rho_{xx/zz}$ is the longitudinal resistivity measured along the x/z direction of the crystal.

The total Hall resistivity of a ferromagnet can be written as

$$\rho_H = \rho^N_H + \rho^A_H = \mu_0 R_0 H + \mu_0 R_S M, \tag{5.6}$$

where R_0 and R_S are the normal and anomalous Hall coefficients [see Figs. 5.3 (a) and (b) for $R_0(T)$ and $R_S(T)$ plots, respectively] [35, 4]. Thus, the field-dependent Hall resistivity of $\rho_{xy}(H)$ and $\rho_{zx}(H)$ measured at various temperatures, as shown in Figs. 5.2(e) and 5.2(f), were fitted using the total resistivity equation and extracted the anomalous Hall resistivity ρ^A_{xy} and ρ^A_{zx} [see Fig. 5.3 (d)]. Finally, from the fits we converted $\rho_{xy}(H)$ and $\rho_{zx}(H)$ into the anomalous Hall conductivity σ^A_{xy} and σ^A_{zx}, and plotted as a function of temperature, as shown in Fig. 5.4(a).

A unified scaling relation between the anomalous Hall resistivity (ρ^A_H) and the longitudinal electrical resistivity (ρ) remains elusive. Different functional forms have been reported for ρ^A_H as a function of ρ, $\rho^A_H = f(\rho)$. Initially, Smit *et. al.* attributed the anomalous Hall effect to the extrinsic skew-scattering of electrons with magnetic impurities and proposed that $\rho^A_{sk} \propto \rho_{xx}$ [5]. On the other hand, Berger *et. al.* suggested that the extrinsic side-jump scattering of electrons with magnetic impurities could also contribute to the AHE such as $\rho^A_{sj} \propto \rho^2_{xx}$ [6]. In contrast, Karplus and Luttinger (KL) proposed an intrinsic contribution to the anomalous Hall effect, arising from the strong spin-orbit interactions combined with inter-band scattering, leading to $\rho^A_{int} \propto \rho^2_{xx}$ [7, 4]. The KL mechanism was recently revisited through the Berry phase mechanism, and it realized that the intrinsic

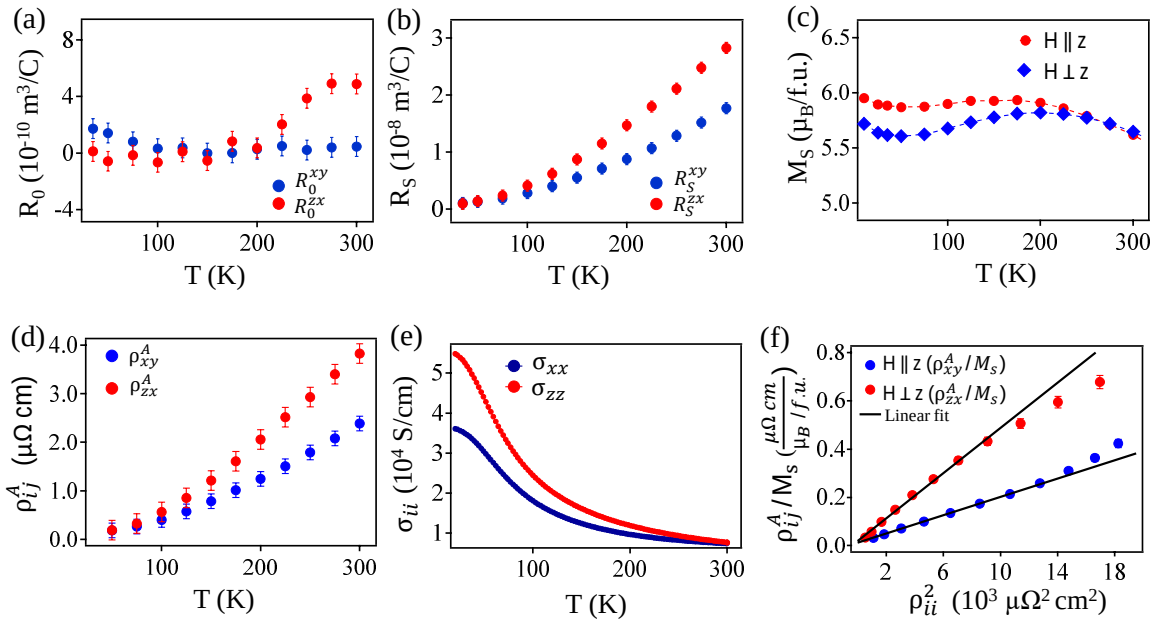

Figure 5.3: Panels (a) and (b) depict the temperature evolution of the normal Hall coefficient (R_0) and anomalous Hall coefficient (R_S), respectively. (c) Saturation magnetization (M_S) is plotted as a function of temperature. (d) and (e) Longitudinal electrical resistivity and conductivity are plotted as a function of temperature, respectively. (f) Plot of $\rho^A_{zx/xy}/M_s$ *vs.* $\rho^2_{zz/xx}$, with the solid line depicting a linear fit.

Hall effect is a dominant contributor to the anomalous Hall effect [4]. In this regard, the anomalous Hall conductivity can be expressed as some of all three contributions following Matthiessen's rule,

$$\sigma_{AH} = \sigma_{int} + \sigma_{sk} + \sigma_{sj}, \tag{5.7}$$

where σ_{int} is the intrinsic Hall contribution, σ_{sk} is the extrinsic skew-scattering contribution, and σ_{sj} is the extrinsic side-jump contribution.

Usually, intrinsic and extrinsic Hall contributions coexist, and distinguishing the intrinsic from the extrinsic contribution is a major experimental challenge. In this regard, Tian *et. al.* [36] proposed a novel scaling law (TYJ) for the anomalous Hall effect, which offered a more reliable and cohesive framework for comprehending the relation among various AHE contributions. The TYJ scaling law incorporates residual resistivity (ρ_{xx0}) as $\rho^A_{xy} = f(\rho_{xx0}, \rho_{xx})$. Thus, the empirical form of the TYJ model for AHE is given by,

$$\rho^A_{xy} = (\alpha\rho_{xx0} + \beta\rho^2_{xx0}) + b(T)\rho^2_{xx}, \tag{5.8}$$

$$-\sigma^A_{xy}(T) = (\alpha\sigma^{-1}_{xx0} + \beta\sigma^{-2}_{xx0})\sigma^2_{xx} + b(T), \tag{5.9}$$

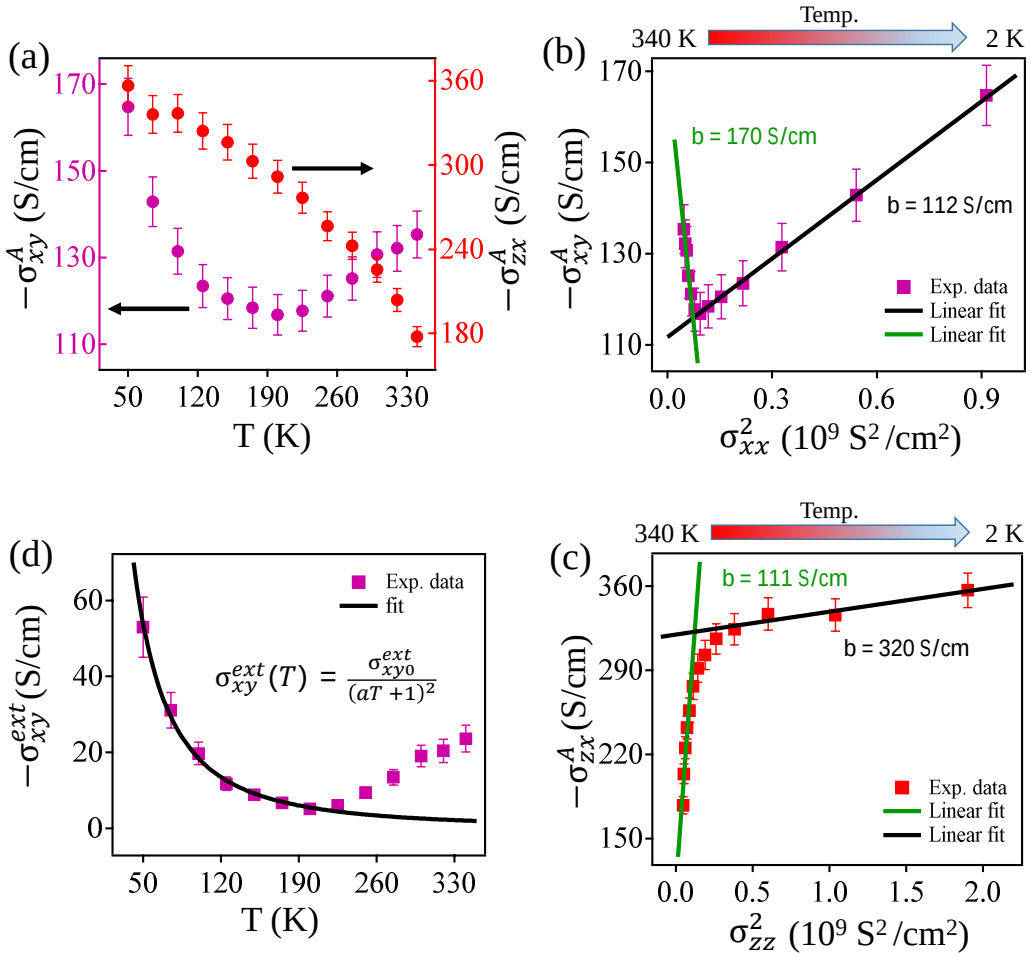

Figure 5.4: (a) σ^A_{xy} and σ^A_{zx} plotted as a function of temperature. (b) Plot of $-\sigma^A_{xy}$ *vs.* σ^2_{xx}. (c) Plot of $-\sigma^A_{zx}$ *vs.* σ^2_{zz}. The solid lines in (b) and (c) are the linear fits by the Eq. 5.10. (d) Temperature-dependent in-plane extrinsic AHC (σ^{ext}_{xy}).

$$-\sigma^A_{xy}(T) = \rho^{ext}_{xy0}\sigma^2_{xx}(T) + b(T), \tag{5.10}$$

where $\sigma_{xx0} = 1/\rho_{xx0}$ is the residual conductivity, α are β are constants, and $b(T)$ is temperature-dependent intrinsic Hall conductivity arising from the Berry curvature.

Fig. 5.4(b) depicts the plot of σ^A_{xy} *vs.* σ^2_{xx}, overlapped with fits (solid lines) using Eq. 5.10. From Fig. 5.4(b), it is evident that σ^A_{xy} shows differing linear dependencies on σ^2_{xx} in different temperature regions. As a result, we get the intrinsic Hall conductivity of $b = 170$ S/cm in the high-temperature region, which is 112 S/cm in the low-temperature region. Similarly, from the plot of σ^A_{zx} *vs.* σ^2_{zz} [see Fig. 5.4(c)] we observe $b = 111$ S/cm in the high-temperature region and 320 S/cm in the low-temperature region. These observations demonstrate the temperature dependence of intrinsic Hall contribution to the total Hall conductivity. This conclusion is further supported by the plot of $\rho^A_{xy/zx}/M_s$ *vs.* $\rho^2_{xx/zz}$ as depicted in Fig. 5.3(f), a deviation in the linear fit confirms the temperature-dependent intrinsic AHC, otherwise perfect linear behaviour is anticipated between ρ^A and ρ^2 for the

temperature independent intrinsic AHC [36, 37]. Importantly, in the high-temperature region, the in-plane intrinsic contribution dominates the out-of-plane. In contrast, the out-of-plane intrinsic contribution dominates the in-plane in the low-temperature region. Next, the extrinsic Hall conductivity can be isolated by subtracting the intrinsic contribution from the total Hall conductivity. Since the intrinsic Hall conductivity for σ_{xy} does not change much within the measured temperature range, the extrinsic contribution (σ_{xy}^{ext}) is obtained by subtracting the low-temperature intrinsic AHC of b =112 S/cm. The resultant σ_{xy}^{ext} is plotted as a function of temperature in Fig. 5.4(d), from which one can notice that with increasing temperature, its magnitude decreases significantly. Therefore, the sharp increase in total anomalous Hall conductivity below 200 K can be attributed to the extrinsic contribution. Note that the increase in AHE above 200 K is due to the high-temperature intrinsic AHC. In ferromagnetic metals, the value of $\frac{\epsilon_{SO}}{E_F}$ is of the order of $\sim 10^{-2}$ and $\frac{e^2}{ha'} \approx 7.97 \times 10^2$ S/cm for an average lattice constant of the studied system, $a' = (2a + c)/3 = 4.86$ Å [38, 39]. Thus, the extrinsic anomalous Hall conductivity due to the side-jump is given by $\sigma_{sj} \approxeq \frac{e^2}{ha'}(\frac{\epsilon_{SO}}{E_F}) \approx 7.97$ S/cm which is negligibly small. Therefore, the extrinsic skew-scattering mechanism dominates at low temperatures where the inelastic electron-electron scattering is minimal, and the sample's longitudinal conductivity is high [the clean limit regime] [40]. However, as the temperature increases, the probability of inelastic scattering increases because of the electron-phonon interactions, reducing the extrinsic skew-scattering contribution to the AHC [21].

Shitade *et. al.* had introduced a model that elucidates the impact of electron-phonon interactions on the skew-scattering contribution of the anomalous Hall conductivity [41]. Since in our studied system (Fe_3Ge) also we observe a strong electron-phonon interactions within the temperature range of 50 and 200 K [see Fig. 5.1(c)], using the inelastic scattering rate (γ) as implemented in Ref. [41], we could fit the extrinsic skew-scattering Hall conductivity by the equation

$$\sigma_{xy}^{ext} = \frac{\sigma_{xy0}^{ext}}{(\gamma/\gamma_0 + 1)^2} = \frac{\sigma_{xy0}^{ext}}{(aT + 1)^2} \tag{5.11}$$

as shown in Fig. 5.4(d). Here, $\gamma/\gamma_0 = aT$ for the electron-phonon scattering, and a is a constant. The same procedure cannot be applied for σ_{zx}^{A} data to extract the extrinsic Hall contribution as the intrinsic AHC values change significantly from the high-temperatures (111 S/cm) to the low-temperatures (320 S/cm).

To further understand the anomalous Hall conductivity in Fe_3Ge, we performed $ab-initio$ first-principles calculations as shown in Fig. 5.5. Since, experimentally, we notice that the magnetic easy-axis rotates from out-of-plane towards in-plane in-going from high-temperature to low-temperature, we performed the calculations by fixing the magnetic easy-axis at different angles (Θ) with respect to the crystallographic c-axis. $\Theta = 0^o$ means

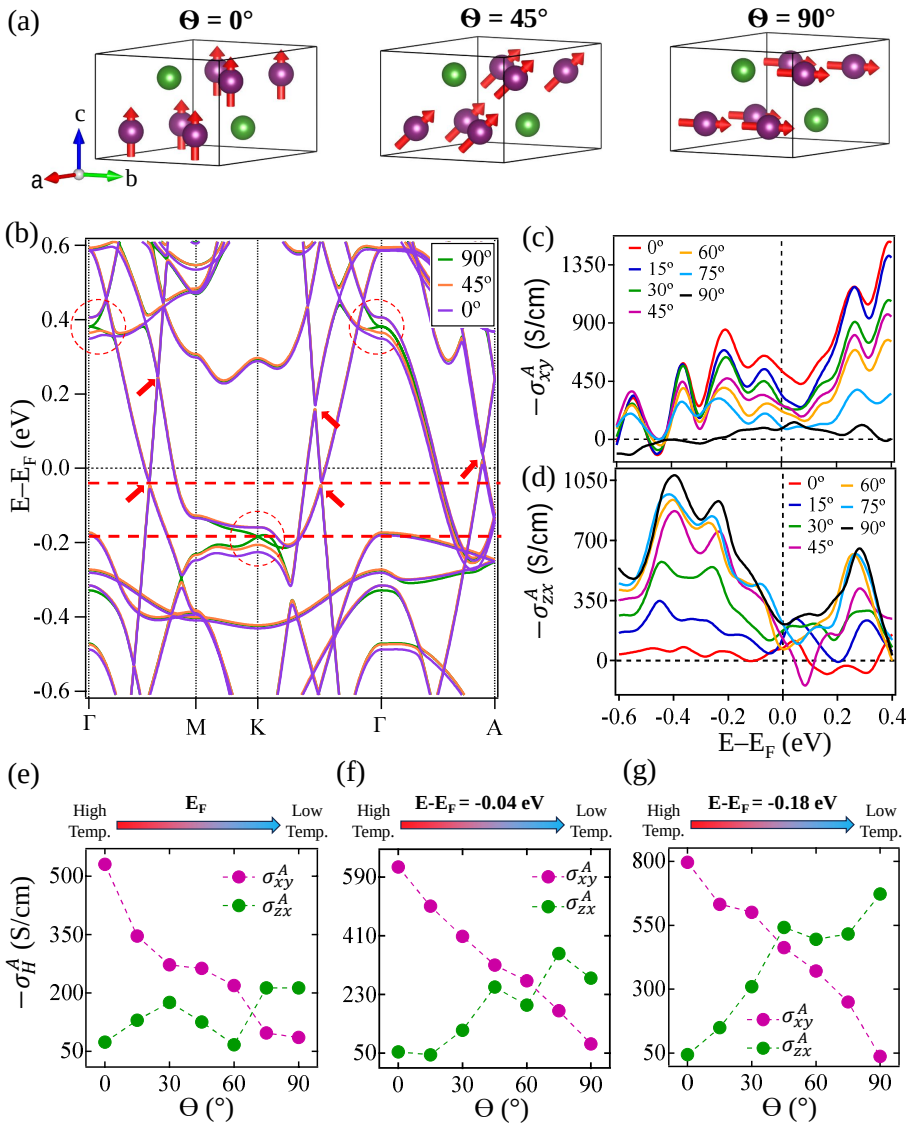

Figure 5.5: (a) Schematic representation of various spin configurations in Fe_3Ge. (b) Electronic band structure calculated using DFT for various spin configurations as depicted in (a) including the spin-orbit coupling effects. (c) In-plane (σ^A_{xy}) and (d) out-of-plane (σ^A_{zx}) intrinsic anomalous Hall conductivity, plotted as a function of binding energy, calculated for various spin configurations. (e)-(g) Intrinsic AHC plotted as a function of angle (Θ) at E_F, $E - E_F = -0.04$ eV (Weyl-node), and $E - E_F = -0.18$ eV (Dirac-node).

the magnetic easy-axis is parallel to the c-axis and 90^o means the magnetic easy-axis is perpendicular to the c-axis as demonstrated in the Fig. 5.5(a). Fig. 5.5(b) depicts the electronic band structure of Fe_3Ge calculated including the spin-orbit coupling effects for the magnetic configurations of $\Theta = 0^o$, 45^o, and 90^o. From Fig. 5.5(b), we can identify several Weyl points near the Fermi level that are gapped out due to spin-orbit coupling. In addition, we observe a couple of Dirac-like band crossings above and below the Fermi level at Γ and K high-symmetry points, respectively. Interestingly, the degeneracy of the Dirac point is intact for the $\Theta = 90^o$ magnetic configuration, i.e., the easy-magnetic axis is perpendicular to the c-axis. However, moving the easy-axis towards the c-axis,

the degeneracy of the Dirac points is lifted by opening a gap at the nodes. A maximum Dirac nodal gap is observed for the $\Theta = 0^o$ magnetic configuration.
Figs. 5.5(c) and 5.5(d) show the calculated anomalous Hall conductivity of in-plane (σ^A_{xy}) and out-of-plane (σ^A_{zx}), respectively, plotted as a function of binding energy for various spin configurations. σ^A_{xy} and σ^A_{zx} were calculated with the magnetization vector kept along the [0001] (z) and [01$\bar{1}$0](y) directions, respectively. Figs. 5.5(e)-5.5(g) show σ^A_{xy} and σ^A_{zx} plotted as a function spin-configuration angle at the Fermi level (E_F), the Weyl point (E_F-0.04 eV), and Dirac point (E_F-0.18 eV), respectively. From Figs. 5.5(e)-5.5(g), it is evident that the in-plane AHC (σ^A_{xy}) dominates the out-of-plane AHC (σ^A_{zx}) above T_{SR} ($\Theta = 0^o$). However, as the temperature decreases (Θ increases), the σ^A_{xy} (σ^A_{zx}) gradually decreases (increases). Though this behavior is similar at E_F, Weyl, and Dirac-point energy positions, σ^A_{zx} dominance over σ^A_{xy} at low temperatures is significantly higher at the Weyl and Dirac-points. Further, the dominance cross-over between σ^A_{xy} and σ^A_{zx} ingoing from T_{SR} to low-temperature is qualitatively in agreement with the experimental observations as demonstrated in Figs. 5.4(b) and 5.4(c).

The field-dependent Hall resistivity data presented in Fig. 5.2(e) and (f) were analyzed by fitting with Eq. 5.6, which accounts for the normal and anomalous Hall contributions. Examining the fitting data in depth revealed that the out-of-plane Hall resistivity (ρ_{zx}) is well described by Eq. 5.6, exhibiting excellent agreement with the fitted curve. Whereas, the in-plane Hall resistivity (ρ_{xy}) exhibited substantial deviations from the fitted curve, as shown in Fig. 5.6(a). These discrepancies suggest the presence of an additional contribution to the Hall signal, likely originating from a topological Hall effect (THE), which cannot be captured solely by the normal and anomalous Hall terms. Therefore, to accurately describe the in-plane Hall resistivity data, it is necessary to introduce an additional term in Eq. 5.6. Accordingly, the total Hall resistivity can be expressed as,

$$\rho_H = \rho^N_H + \rho^A_H + \rho^T_H \tag{5.12}$$

$$\rho^T_H = \rho_H - \rho^N_H - \rho^A_H, \tag{5.13}$$

where ρ^T_H is the topological Hall effect component to the Hall resistivity data. Now, we can extracted the topological Hall resistivity (ρ^T_{xy}) component using Eq.5.13 and plot it in Fig. 5.6 (b). A pronounced topological Hall effect is observed at room temperature (300 K), and the value of ρ^T_{xy} increases with the applied field, reaching a maximum ($\rho^{T_{max}}_{xy}$ = 0.4 $\mu\Omega.cm$) at 0.66 T, then subsequently decreases with further increase in field and eventually being completely suppressed at higher fields (see Fig. 5.6(b)). A similar trend is observed at other temperatures, however, the magnitude of $\rho^{T_{\max}}_{xy}$ systematically decreases with decreasing temperature and becomes nearly negligible at 2 K, as shown

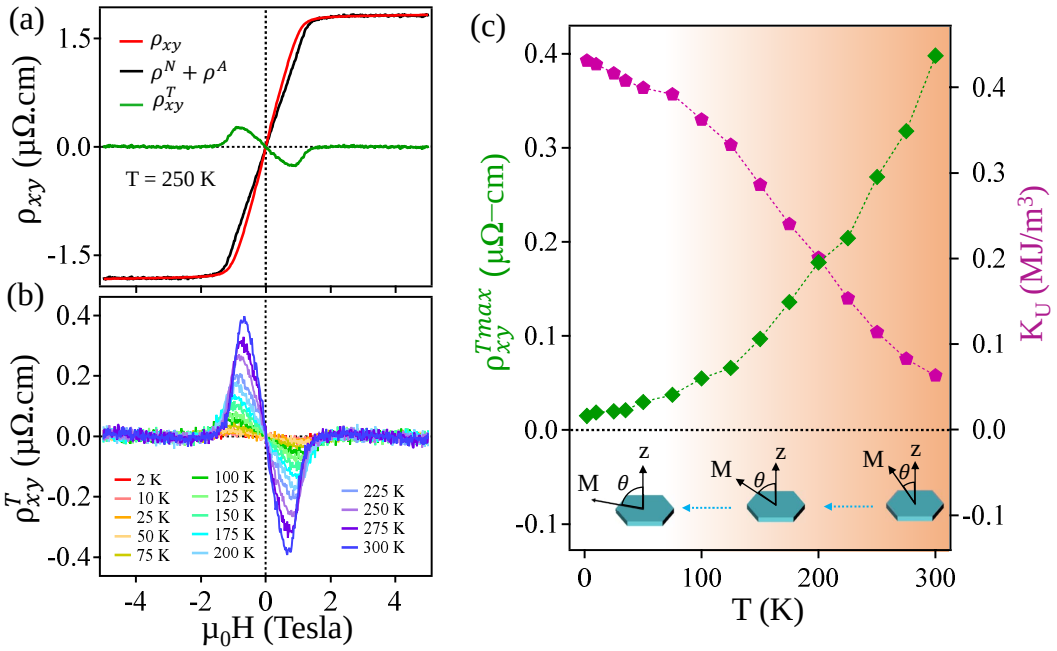

Figure 5.6: (a) Field-dependent Hall resistivity at 250 K fitted with Eq. 5.6 and extracted topological Hall resistivity. (b) The topological Hall resistivity (ρ^T_{xy}) is plotted as a function of magnetic field at various temperatures. (c) Temperature-dependent magnetocrystalline anisotropy energy density (right axis) and maximum value of topological Hall resistivity (left axis). The schematic illustrates the temperature-dependent variation in the angle between the magnetic easy axis and the z-direction of the crystal.

in Fig. 5.6(c).

The Topological Hall effect (THE) arises from noncoplanar spin structures, where the scalar spin chirality [$\chi_{ijk} = S_i.(S_j \times S_k)$] becomes nonzero. This nonzero scalar spin chirality leads to the formation of a real-space Berry curvature, thereby inducing THE [42, 43]. Non-coplanar spin textures in magnetic systems can emerge from a variety of intriguing origins, such as Dzyaloshinskii-Moriya interaction (DMI) in noncentrosymmetric systems, competition between uniaxial anisotropy and dipole-dipole interactions in centrosymmetric systems, and the emergence of skyrmion lattices induced by chiral domain walls [44–47]. In addition to these well-established mechanisms, recent theoretical and experimental studies have demonstrated that skyrmions can be stabilized in centrosymmetric materials [48, 49, 43], such as Gd_2PdSi_3 [50] and $Gd_3Ru_4Al_{12}$ [51], primarily due to magnetic frustration. Furthermore, recent investigations have shown that Fe doping in Mn_3Sn enhances magnetocrystalline anisotropy and induces a noncoplanar spin structure, leading to the emergence of a topological Hall effect (THE) at low temperatures [52]. Similarly, Fe_3Sn_2, another centrosymmetric system, exhibits THE and skyrmion bubbles, driven by the formation of a noncoplanar spin structure and large magnetocrystalline anisotropy [19].

To investigate the origin of the topological Hall effect (THE) in Fe_3Ge, we performed a

detailed analysis of its magnetocrystalline anisotropy, which plays a crucial role in stabilizing noncoplanar spin textures responsible for THE. The magnetocrystalline anisotropic energy density (K_U) is determined using the relation

$$K_U = \mu_0 \int_0^{M_s} [H_y^{eff}(M) - H_z^{eff}(M)]\, dM \tag{5.14}$$

where the effective magnetic field is corrected for the geometric demagnetization factor (N_d) using $H_{\text{eff}} = H - N_d M$. The demagnetization factors were calculated as $N_d = 0.64$ for fields applied along the z-axis and $N_d = 0.35$ for the y-axis. The magnetocrystalline anisotropic energy density (K_U) is estimated to be 0.43×10^6 J/m^3 at 2 K, with a subsequent decrease as the temperature increases, as shown in Fig. 5.6 (c).

It can be observed that the value of magnetocrystalline anisotropic energy density K_U increases monotonically as the temperature decreases. Concurrently, the Fe magnetic moments progressively reorient from the z-axis toward the xy-plane, as illustrated in Fig. 5.6 (c). Therefore, a canted ferromagnetic state is established below the temperature T_{SR}, leading to the formation of a non-coplanar spin structure, which is stabilized by the strong magnetocrystalline anisotropy. This nontrivial spin texture is the origin of the observed topological Hall effect (THE) in Fe_3Ge. At low temperatures, the easy axis aligns with the xy-plane, suggesting the disappearance of the canted spin structure, which accounts for the negligible topological Hall effect (THE) at 2 K.

The magnetic behavior and the topological Hall effect (THE) response observed in our system are similar to those in the ferromagnetic kagome material Fe_3Sn_2, where magnetic skyrmion bubbles have been reported [19, 15]. This suggests the possibility of observing room-temperature skyrmions in Fe_3Ge as well. However, more studies are required to explore this potential, which is beyond the scope of the current experimental investigation.

5.4 Conclusion

In conclusion, we conducted a comprehensive investigation on Fe_3Ge for its anomalous Hall effect behavior along the in-plane and out-of-plane directions. Our study reveals significant anisotropy in the anomalous Hall effect (AHE). Notably, the gradual spin reorientation from the out-of-plane to in-plane direction, from high-temperature to low-temperature in Fe_3Ge, provides a unique opportunity to study the temperature dependence on the intrinsic Hall conductivity experimentally. The theoretical predictions qualitatively support our experimental results. Furthermore, a topological Hall effect (THE) signal is observed along the in-plane direction, originating from the emergence of a non-coplanar spin structure stabilized by strong magnetocrystalline anisotropy below the spin reorientation temperature (T_{SR}).

References

[1] C. Kittel, Solid state physics, volume 3, Shell Development Company Emeryville, 1955.

[2] N. W. Ashcroft, N. D. Mermin, Solid State Physics, Cengage Learning, 1976.

[3] C. Chien, The Hall effect and its applications, Springer Science & Business Media, 2013.

[4] N. Nagaosa, J. Sinova, S. Onoda, A. H. MacDonald, N. P. Ong, Anomalous Hall effect, Rev. Mod. Phys. 82 (2010) 1539–1592.

[5] Smit, J, The spontaneous Hall effect in ferromagnetics I, Physica 21 (1955) 877–887.

[6] L. Berger, Side-jump mechanism for the Hall effect of ferromagnets, Physical Review B 2 (1970) 4559.

[7] R. Karplus, J. M. Luttinger, Hall Effect in Ferromagnetics, Physical Review 95 (1954) 1154–1160.

[8] T. Jungwirth, Q. Niu, A. H. MacDonald, Anomalous Hall Effect in Ferromagnetic Semiconductors, Phys. Rev. Lett. 88 (2002) 207208.

[9] L. Ye, Y. Tian, X. Jin, D. Xiao, Temperature dependence of the intrinsic anomalous Hall effect in nickel, Phys. Rev. B 85 (2012) 220403.

[10] M. Kang, L. Ye, S. Fang, J.-S. You, A. Levitan, M. Han, J. I. Facio, C. Jozwiak, A. Bostwick, E. Rotenberg, M. K. Chan, R. D. McDonald, D. Graf, K. Kaznatcheev, E. Vescovo, D. C. Bell, E. Kaxiras, J. van den Brink, M. Richter, M. Prasad Ghimire, J. G. Checkelsky, R. Comin, Dirac fermions and flat bands in the ideal kagome metal FeSn, Nature Materials 19 (2019) 163–169.

[11] J.-X. Yin, B. Lian, M. Z. Hasan, Topological kagome magnets and superconductors, Nature 612 (2022) 647–657.

[12] J. Sau, H. Banerjee, S. Saha, N. Kumar, M. Kumar, Exploring magnetic and topological complexity in $MgMn_6Sn_6$: from frustrated ground states to nontrivial Hall conductivity, 2024.

[13] N. Morali, R. Batabyal, P. K. Nag, E. Liu, Q. Xu, Y. Sun, B. Yan, C. Felser, N. Avraham, H. Beidenkopf, Fermi-arc diversity on surface terminations of the magnetic Weyl semimetal $Co_3Sn_2S_2$, Science 365 (2019) 1286–1291.

[14] S. Nakatsuji, N. Kiyohara, T. Higo, Large anomalous Hall effect in a non-collinear antiferromagnet at room temperature, Nature 527 (2015) 212–215.

[15] Q. Wang, Q. Yin, H. Lei, Giant topological Hall effect of ferromagnetic kagome metal Fe_3Sn_2, Chinese Physics B 29 (2020) 017101.

[16] Q. Wang, Y. Xu, R. Lou, Z. Liu, M. Li, Y. Huang, D. Shen, H. Weng, S. Wang, H. Lei, Large intrinsic anomalous Hall effect in half-metallic ferromagnet $Co_3Sn_2S_2$ with magnetic Weyl fermions, Nat. Commun. 9 (2018) 3681.

[17] A. K. Nayak, J. E. Fischer, Y. Sun, B. Yan, J. Karel, A. C. Komarek, C. Shekhar, N. Kumar, W. Schnelle, J. Kübler, et al., Large anomalous Hall effect driven by a nonvanishing Berry curvature in the noncolinear antiferromagnet Mn_3Ge, Science advances 2 (2016) e1501870.

[18] J. Kübler, C. Felser, Weyl fermions in antiferromagnetic Mn_3Sn and Mn_3Ge, EPL (Europhysics Letters) 120 (2018) 47002.

[19] Z. Hou, W. Ren, B. Ding, G. Xu, Y. Wang, B. Yang, Q. Zhang, Y. Zhang, E. Liu, F. Xu, W. Wang, G. Wu, X. Zhang, B. Shen, Z. Zhang, Observation of Various and Spontaneous Magnetic Skyrmionic Bubbles at Room Temperature in a Frustrated Kagome Magnet with Uniaxial Magnetic Anisotropy, Advanced Materials 29 (2017).

[20] L. Ye, M. K. Chan, R. D. McDonald, D. Graf, M. Kang, J. Liu, T. Suzuki, R. Comin, L. Fu, J. G. Checkelsky, de Haas-van Alphen effect of correlated Dirac states in kagome metal Fe_3Sn_2, Nat. Commun. 10 (2019) 4870.

[21] A. Low, S. Ghosh, S. Ghorai, S. Thirupathaiah, Effect of electron-phonon scattering on the anomalous Hall conductivity of Fe_3Sn: A kagome ferromagnetic metal, Phys. Rev. B 108 (2023) 094404.

[22] J. W. Drijver, S. G. Sinnema, F. Van Der Woude, Magnetic properties of hexagonal and cubic Fe_3Ge, Journal of Physics F Metal Physics 6 (1976) 2165–2177.

[23] Z. Li, Y. Wang, Z. Xia, Q. Zhang, Z. Li, E. Liu, Z. Liu, Anomalous Hall effect dominated by intrinsic mechanism in Fe3Ge with hexagonal DO19 Kagome lattice and cubic DO3 structure, Appl. Phys. Lett. 122 (2023).

[24] F. Albertini, D. Negri, L. Pareti, E. B. Watts, Z. Arnold, J. Kamarad, G. Calestani, A. Deriu, S. Besseghini, Magnetocrystalline anisotropy of Fe3Ge single crystal: Effect of pressure and Mn substitution for Fe, J Appl Phys 96 (2004) 2110–2114.

[25] Z. Zhang, M. Zhao, L. Ma, G. Li, C. Zhen, D. Zhao, D. Hou, Large topological Hall effect arising from spin reorientation in kagome magnet Fe_3Ge, 2024.

[26] R. Lou, L. Zhou, W. Song, A. Fedorov, Z. Tu, B. Jiang, Q. Wang, M. Li, Z. Liu, X. Chen, O. Rader, B. Büchner, Y. Sun, H. Weng, H. Lei, S. Wang, Orbital-selective effect of spin reorientation on the Dirac fermions in a non-charge-ordered kagome ferromagnet Fe_3Ge, Nat. Commun. 15 (2024) 9823.

[27] P. Giannozzi, S. Baroni, N. Bonini, M. Calandra, R. Car, C. Cavazzoni, D. Ceresoli, G. L. Chiarotti, M. Cococcioni, I. Dabo, A. Dal Corso, S. de Gironcoli, S. Fabris, G. Fratesi, R. Gebauer, U. Gerstmann, C. Gougoussis, A. Kokalj, M. Lazzeri, L. Martin-Samos, N. Marzari, F. Mauri, R. Mazzarello, S. Paolini, A. Pasquarello, L. Paulatto, C. Sbraccia, S. Scandolo, G. Sclauzero, A. P. Seitsonen, A. Smogunov, P. Umari, R. M. Wentzcovitch, QUANTUM ESPRESSO: a modular and open-source software project for quantum simulations of materials, Journal of Physics: Condensed Matter 21 (2009) 395502.

[28] D. Vanderbilt, Soft self-consistent pseudopotentials in a generalized eigenvalue formalism, Physical Review B 41 (1990) 7892–7895.

[29] A. A. Mostofi, J. R. Yates, G. Pizzi, Y.-S. Lee, I. Souza, D. Vanderbilt, N. Marzari, An updated version of wannier90: A tool for obtaining maximally-localised Wannier functions, Comput. Phys. Commun. 185 (2014) 2309–2310.

[30] D. J. Thouless, M. Kohmoto, M. P. Nightingale, M. den Nijs, Quantized Hall Conductance in a Two-Dimensional Periodic Potential, Physical Review Letters 49 (1982) 405–408.

[31] Q.-S. Wu, S. Zhang, H. Song, M. Troyer, A. Soluyanov, WannierTools: An open-source software package for novel topological materials, Computer Physics Communications 224 (2017).

[32] G. v. Minnigerode, Göran Grimvall, E. P. Wohlfahrt (Eds.): The Electron-Phonon Interaction in Metals, Vol. 16, aus: Selected Topics in Solid State Physics. North Holland Publishing Company, Amsterdam, New York, Oxford 1981. 304 Seiten, Dfl 125,—, Berichte der Bunsengesellschaft für physikalische Chemie 87 (1983) 453–454.

[33] S. Nandi, B. B. Maity, V. Sharma, R. Verma, V. Saini, B. Singh, D. Aoki, A. Thamizhavel, Magnetotransport and Fermi surface studies of a purported nodal line semimetal $ZrAs_2$, Phys. Rev. B 109 (2024) 075155.

[34] H. Wiesmann, M. Gurvitch, H. Lutz, A. Ghosh, B. Schwarz, M. Strongin, P. B. Allen, J. W. Halley, Simple Model for Characterizing the Electrical Resistivity in $A-15$ Superconductors, Phys. Rev. Lett. 38 (1977) 782–785.

[35] A. Neubauer, C. Pfleiderer, B. Binz, A. Rosch, R. Ritz, P. G. Niklowitz, P. Böni, Topological Hall Effect in the A Phase of MnSi, Phys. Rev. Lett. 102 (2009) 186602.

[36] Y. Tian, L. Ye, X. Jin, Proper Scaling of the Anomalous Hall Effect, Phys Rev Lett 103 (2009) 087206.

[37] M. Singh, J. Sau, B. Rai, A. Panda, M. Kumar, N. Kumar, Tuning intrinsic anomalous Hall effect from large to zero in two ferromagnetic states of $SmMn_2Ge_2$, Phys. Rev. Mater. 8 (2024) 084201.

[38] Q. Wang, S. Sun, X. Zhang, F. Pang, H. Lei, Anomalous Hall effect in a ferromagnetic Fe_3Sn_2 single crystal with a geometrically frustrated Fe bilayer kagome lattice, Phys Rev B 94 (2016) 075135.

[39] S. Roy, R. Singha, A. Ghosh, A. Pariari, P. Mandal, Anomalous Hall effect in the half-metallic Heusler compound Co_2TiX (X = Si, Ge), Phys. Rev. B 102 (2020) 085147.

[40] S. Onoda, N. Sugimoto, N. Nagaosa, Intrinsic Versus Extrinsic Anomalous Hall Effect in Ferromagnets, Phys. Rev. Lett. 97 (2006) 126602.

[41] A. Shitade, N. Nagaosa, Anomalous Hall Effect in Ferromagnetic Metals: Role of Phonons at Finite Temperature, Journal of the Physical Society of Japan 81 (2012) 083704.

[42] Y. Shiomi, M. Mochizuki, Y. Kaneko, Y. Tokura, Hall Effect of Spin-Chirality Origin in a Triangular-Lattice Helimagnet $Fe_{1.3}Sb$, Phys. Rev. Lett. 108 (2012) 056601.

[43] P. K. Rout, P. V. P. Madduri, S. K. Manna, A. K. Nayak, Field-induced topological Hall effect in the noncoplanar triangular antiferromagnetic geometry of Mn_3Sn, Phys. Rev. B 99 (2019) 094430.

[44] S. B. Gudnason, M. Nitta, Domain wall Skyrmions, Phys. Rev. D 89 (2014) 085022.

[45] R. Cheng, M. Li, A. Sapkota, A. Rai, A. Pokhrel, T. Mewes, C. Mewes, D. Xiao, M. De Graef, V. Sokalski, Magnetic domain wall skyrmions, Phys. Rev. B 99 (2019) 184412.

[46] T. Nagase, Y.-G. So, H. Yasui, T. Ishida, H. K. Yoshida, Y. Tanaka, K. Saitoh, N. Ikarashi, Y. Kawaguchi, M. Kuwahara, M. Nagao, Observation of domain wall bimerons in chiral magnets, Nat. Commun. 12 (2021).

[47] K. Yang, K. Nagase, Y. Hirayama, T. D. Mishima, M. B. Santos, H. Liu, Wigner solids of domain wall skyrmions, Nat. Commun. 12 (2021).

[48] T. Okubo, S. Chung, H. Kawamura, Multiple-q States and the Skyrmion Lattice of the Triangular-Lattice Heisenberg Antiferromagnet under Magnetic Fields, Phys. Rev. Lett. 108 (2012) 017206.

[49] S. Hayami, R. Ozawa, Y. Motome, Effective bilinear-biquadratic model for noncoplanar ordering in itinerant magnets, Phys. Rev. B 95 (2017) 224424.

[50] T. Kurumaji, T. Nakajima, M. Hirschberger, A. Kikkawa, Y. Yamasaki, H. Sagayama, H. Nakao, Y. Taguchi, T. hisa Arima, Y. Tokura, Skyrmion lattice with a giant topological Hall effect in a frustrated triangular-lattice magnet, Science 365 (2019) 914–918.

[51] M. Hirschberger, T. Nakajima, S. Gao, L. Peng, A. Kikkawa, T. Kurumaji, M. Kriener, Y. Yamasaki, H. Sagayama, H. Nakao, K. Ohishi, K. Kakurai, Y. Taguchi, X. Yu, T. hisa Arima, Y. Tokura, Skyrmion phase and competing magnetic orders on a breathing kagomé lattice, Nat. Commun. 10 (2019).

[52] A. Low, S. Ghosh, S. Changdar, S. Routh, S. Purwar, S. Thirupathaiah, Tuning of topological properties in the strongly correlated antiferromagnet Mn_3Sn via Fe doping, Phys. Rev. B 106 (2022) 144429.

Chapter 6

Extremely Large and Angle-Dependent Magnetoresistance Observed in Kagome Dirac Semimetal RFe_6Sn_6 (R=Ho, Dy)

6.1 Introduction

The kagome lattice, made up of geometrically frustrated corner-sharing triangles, has gained much attention recently due to their distinctive characteristics, including the van Hove singularities, flat bands, and Dirac points in the electronic band structure. Numerous kagome materials have been found to exhibit several interesting physical properties. For instance, the Co-based kagome system $Co_3Sn_2S_2$ shows giant anomalous Hall effect (AHE), Chiral anomaly, and Weyl fermions [1, 2]. Despite being an antiferromagnet, the Mn-based kagome system Mn_3X (X=Sn, Ge) shows surprisingly large anomalous Hall effect, anomalous Nernst effect (ANE), and Weyl fermions [3–8]. Whereas, the vanadium based kagome systems AV_3Sb_5 (A=K, Rs, Cs) show topological superconductivity [9, 10]. In this regard, the RM_6X_6 (R = rare earth, M = transition metals, X = Sn, Ge) family of kagome systems have become a hot research topic due to their intriguing combination of electronic and magnetic properties. Within the RM_6X_6 kagome family, researchers have so far focused on exploring the physical and magnetic properties of the manganese (Mn)-based RMn_6X_6 [11–14] and the vanadium (V)-based RV_6X_6 [15–18] subfamilies. However, the only experimental report available on the Fe-based YFe_6Sn_6 system discusses the magnetic and magnetotransport properties [19]. Particularly, a very low magnetoresistance (MR) was observed from YFe_6Sn_6 system, while a significant magnetoresistance was reported from the Mn-based RMn_6X_6 systems [20–23].
Magnetoresistance (MR) is the change in the longitudinal electrical resistivity under an

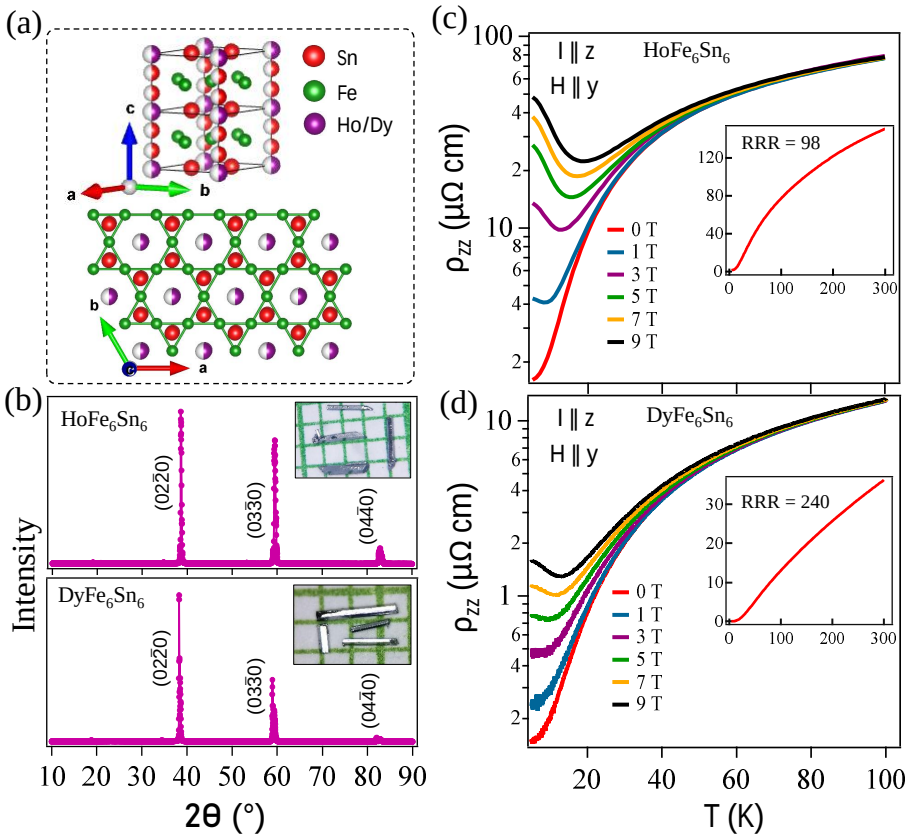

Figure 6.1: (a) Schematics of RFe_6Sn_6 crystal structure. (b) Powder X-ray diffraction patterns taken on the single crystal of $HoFe_6Sn_6$ and $DyFe_6Sn_6$. Insets in (b) show the photographic image of $HoFe_6Sn_6$ and $DyFe_6Sn_6$ single crystal. Temperature dependence of longitudinal resistivity (ρ_{zz}), measured at different transverse magnetic fields ($H \parallel y$) for $HoFe_6Sn_6$ (c) and $DyFe_6Sn_6$ (d). Inset of (c) and (d) show the temperature dependence of resistivity measured without magnetic field for $HoFe_6Sn_6$ and $DyFe_6Sn_6$, respectively.

external magnetic field (H), which is defined as $MR = [\rho(H) - \rho(0)]/\rho(0)$. Here, $\rho(H)$ and $\rho(0)$ are the resistivity measured with and without magnetic field, respectively. Extremely large MR in magnetic materials is a rare phenomena [24–26] but has potential technological applications in spintronics [27–29]. Therefore, searching for systems with extremely large magnetoresistance is a key research focus for physicists and materials scientists. Conventional non-magnetic metals generally display positive magnetoresistance (MR) [30, 31, 26], while ferromagnetic materials tend to exhibit negative MR [24, 31, 26]. In most of the bulk magnetic systems, the MR (%) values are relatively smaller and are typically below 5 % [24, 32, 31], while the giant magnetoresistance (GMR) is found in low dimensional systems such as in thin films or multilayered structures [33, 26]. Also, the colossal magnetoresistance (CMR) is mostly observed in the manganese-based perovskite oxides [27, 26]. On the other hand, the tunneling magnetoresistance (TMR) is observed in magnetic tunnel junctions (MTJs) produced by sandwiching a thin insulating barrier between two ferromagnetic layers [34]. Recently, an extremely large MR (XMR) of the

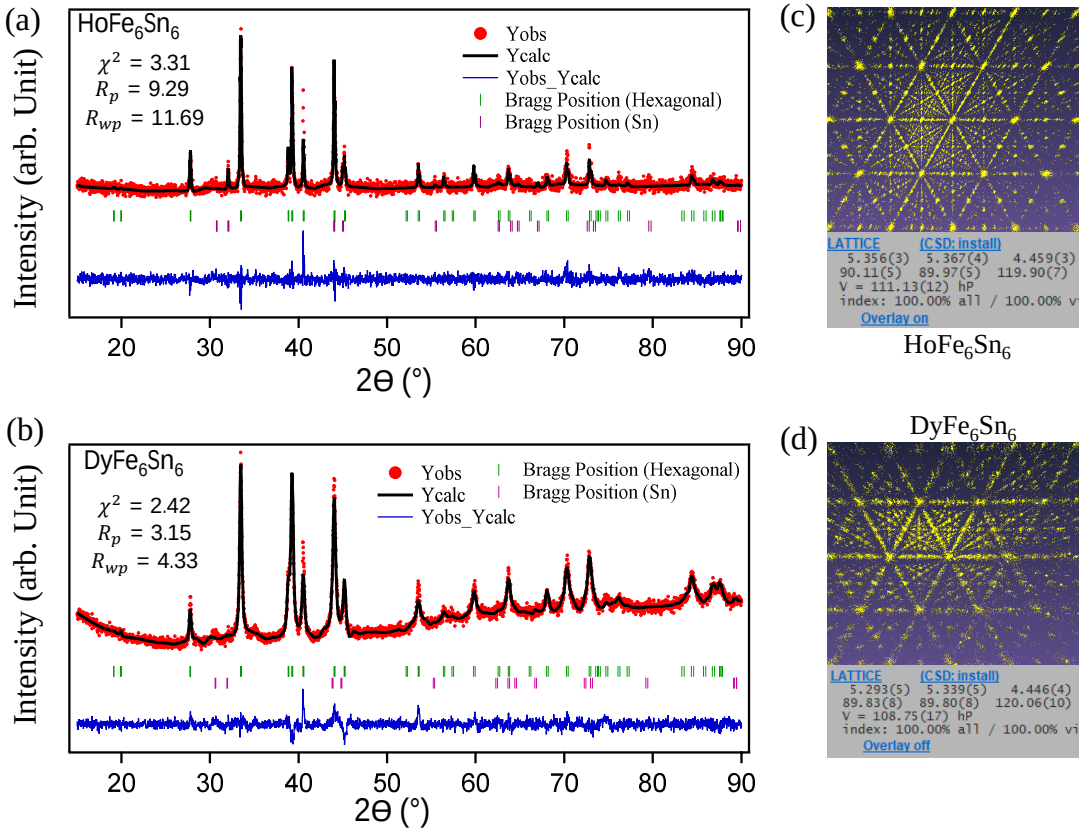

Figure 6.2: (a) Powder X-ray diffraction pattern of the crushed single crystals of $HoFe_6Sn_6$ (a) and $DyFe_6Sn_6$ (b), overlapped with Rietveld refinement. Since a large number of single crystals were crushed for powder XRD, some amount of Sn flux also got mixed with the powders, resulting in impurity peaks. Gnomonic projection of single crystal XRD (SCXRD) data shows a perfect hexagonal pattern of (c) $HoFe_6Sn_6$ and (d) $DyFe_6Sn_6$.

order of $10^3\% - 10^8\%$ has been found in many nonmagnetic materials [35–38], triggering a great deal of research interests on these systems. Astonishingly, even under super-high magnetic fields, the MR does not saturate in these systems [39, 36, 38, 40]. However, the XMR is not fully explored in kagome systems, and to the best of our knowledge, only $M_3In_2S_2$ (M = Ni, Co) kagome systems are recently found to show XMR [41, 42].

In this contribution, we systematically studied the magnetic and magnetotransport properties of the Fe-based RFe_6Sn_6 (R = Ho, Dy) kagome systems. RFe_6Sn_6 follows the YCo_6Sn_6-type hexagonal crystal structure of space group $P6/mmm$ with Fe forming the in-plane kagome lattice. The electrical resistivity data indicate a metallic nature throughout the measured temperature range. Magnetic measurements suggest an antiferromagnetic ordering around 570 K due to Fe sub-lattice and ferromagnetic behaviour at low temperatures due to the rare-earth-element (Ho and Dy) sub-lattice. Extremely large magnetoresistance (XMR) is observed at low temperatures with the maximum MR percentage reaching as high as 3×10^3 % for $HoFe_6Sn_6$ and 1×10^3 % for $DyFe_6Sn_6$ at 2 K under a 9 T of the magnetic field. Hall effect measurements suggest electron-hole

charge compensation, leading to the XMR at low temperatures. Further, the angle-dependent magnetoresistance (ADMR) measurements reveal very high anisotropic magnetoresistance for the fields applied in different crystallographic axes. Interestingly, the anisotropic magnetoresistance pattern significantly modifies when temperature is varied, which implies the temperature dependence of Fermi surface topology in these systems.

6.2 Experimental and Computational details

Single crystals of RFe_6Sn_6 (R = Ho, Dy) were grown with Sn as flux using the high temperature muffle-furnace. The starting elements of high purity R (Ho, Dy) ingot (99.9%, Alfa Aesar), Fe powder (99.99%, Stren Chemical), and Sn shorts (99.995%, Alfa Aesar) were mixed in the molar ratio of $1 : 6 : 30$. Next, an evacuated quartz ampoule was used to seal the alumina crucible containing the mixture. The ampoule was then heated to 1000^oC at a rate of $100^oC/hr$ and held there for 18 hours, and cooled the molten mixture down to 600^oC at a rate of $5^oC/hr$. After annealing for another five days at 600^oC, the ampoule was promptly transferred to a centrifuge to separate the as-grown single crystals from Sn-flux. In this approach, we obtained many hexagonal rod-shaped RFe_6Sn_6 (R = Ho, Dy) single crystals with a typical size of $(2 \times 0.3 \times 0.2)$ mm^3 as depicted in the inset of Fig. 6.1(b).

The phase purity and crystal structure of the as-grown single crystals were analyzed using the powder X-ray diffraction (XRD, 9 KW, Rigaku Smart Lab) and single crystal XRD (SXRD, SuperNova, Rigaku) techniques with Cu-K_α radiation ($\lambda = 1.5406$Å). The elemental composition of the as-grown single crystals were identified using energy-dispersive X-ray analysis (EDAX) coupled with scanning electron microscope (SEM, Quanta 250 FEG). The exact chemical composition were found to be the as-grown samples are found to be $Ho_{0.85}Fe_{6.12}Sn_{6.04}$ and $Dy_{1.16}Fe_{5.82}Sn_6$ using EDAX. For simplicity, we shall denote them by their nominal compositions of $HoFe_6Sn_6$ and $DyFe_6Sn_6$, wherever applicable. Electrical transport, Hall effect, and magnetic properties were conducted using a 9 Tesla physical property measurement system (PPMS, Dynacool, Quantum Design) within the temperature range of 2-300 K. High temperature magnetic measurements up to 750 K were carried out using the VSM-oven option in the PPMS. Electrical transport and Hall effect properties were measured using the four-probe technique. For this, silver epoxy (EPO-TEK H20E) was used to attach copper leads to the sample.

Density functional theory (DFT) calculations were conducted using the Quantum ESPRESSO package [43]. We employed ultrasoft pseudopotentials and Perdew-Burke-Ernzerhof (PBE) functional within the generalized gradient approximation (GGA) [44]. The kinetic energy cutoff for the wavefunction was at 140 Ry. To determine the equilibrium lattice parameters of $HoFe_6Sn_6$ and $DyFe_6Sn_6$, variable-cell relaxation calculations were executed with a k-grid of $6 \times 6 \times 4$. For the density of states (DOS) calculations, a denser $12 \times 12 \times 8$

k-grid was utilized. The convergence threshold for the self-consistent field was taken as 10^{-9} Ry.

6.3 Results and Discussions

Fig. 6.1(a) schematically shows the primitive unit cell of the hexagonal crystal structure of RFe$_6$Sn$_6$(top) and the crystal structure projected onto the ab-plane (bottom). From Fig. 6.1(a), we can see the ab-plane kogome lattice formed solely by the Fe-atoms. The XRD patterns obtained on the rod-shaped single crystals of RFe_6Sn_6 are shown in Fig. 6.1(b), displaying the (0 2 $\bar{2}$ 0) Bragg's reflections, implying that the c-axis is the crystal growth axis. We further measured powder XRD on the crushed single crystals of RFe_6Sn_6 and performed Rietveld refinement using the Fullprof software (see Fig.6.2 (a) and (b)). Rietveld refinement confirms that HoFe$_6$Sn$_6$ and DyFe$_6$Sn$_6$ crystallize into the hexagonal YCo_6Ge_6-type structure with a space group of $P6/mmm$ (191). The refined lattice parameters are $a = b$ =5.3542 (5) Å, c = 4.4493(4) Å, $\alpha = \beta = 90$, $\gamma = 120$ for HoFe$_6$Sn$_6$ and $a = b$ = 5.3549 (5) Å, c = 4.4518 (4) Å, $\alpha = \beta = 90$, $\gamma = 120$ for DyFe$_6$Sn$_6$. The hexagonal crystal structure is further confirmed by the single crystal XRD (SCXRD) (see Fig.6.2 (c) and (d)).

Figs. 6.1(c) and 6.1(d) exhibit temperature-dependent longitudinal electrical resistivity (ρ_{zz}) of HoFe$_6$Sn$_6$ and DyFe$_6$Sn$_6$, respectively, measured under various magnetic fields for $H \parallel y$ direction. Inset of Figs. 6.1(c) and 6.1(d) depict temperature-dependent longitudinal electrical resistivity with zero magnetic field from respective samples, demonstrating a metallic behaviour throughout the measured temperature range. The residual resistivity ratio [$RRR = \rho_{zz}(300K)/\rho_{zz}(2K)$] is about 98 for HoFe$_6Sn_6$ and 240 for DyFe$_6$Sn$_6$, suggesting good quality of the studied single crystals. As can be seen from Figs. 6.1(c) and 6.1(d), the low temperature resistivity [ρ_{zz} (T)] increases significantly with increasing field, demonstrating a significant magnetoresistance (MR) in the low temperature region.

Next, to explore the magnetic properties, temperature dependent magnetization [$M(T)$] and isothermal magnetization [$M(H)$] at different temperatures are performed for $H \parallel z$ and $H \parallel y$ directions . The top panels of Fig. 6.3 show the magnetization data of $HoFe_6Sn_6$, whereas the bottom panels show the magnetization data of DyFe$_6$Sn$_6$. From high temperature magnetisation data, we observe an antiferromagnetic transition at around 570 K for both HoFe$_6$Sn$_6$ and DyFe$_6$Sn$_6$ single crystals [see inset in Figs. 6.3(a) and 6.3(b)]. The magnetisation increases sharply at low temperatures, as seen in Fig. 6.3(a) and Fig. 6.3(b), suggesting a ferromagnetic type ordering at low temperatures. Using the first derivative of temperature-dependent magnetization data (not shown here), we identified the ferromagnetic ordering temperature of $T_C \approx 5.1$ K from $HoFe_6Sn_6$ and 8.5 K from DyFe$_6$Sn$_6$.

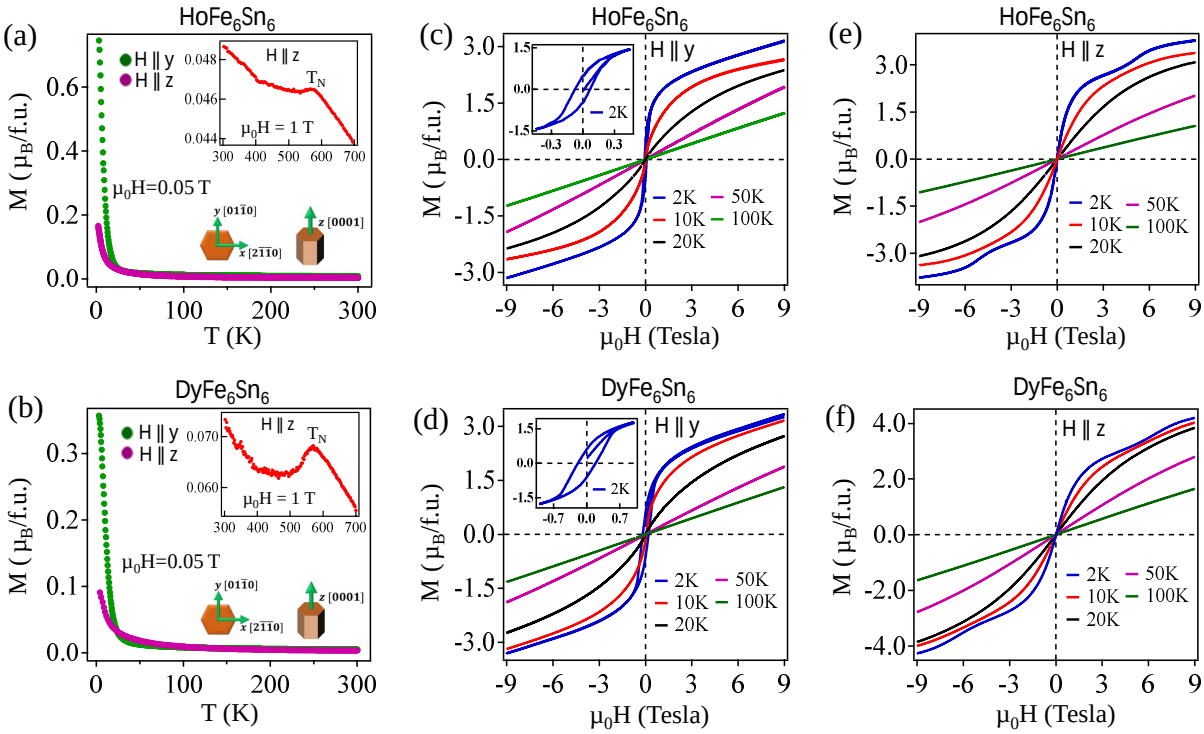

Figure 6.3: Temperature dependent magnetization $[M(T)]$, measured for both $H \parallel z$ and $H \parallel y$ on the single crystals of (a) $HoFe_6Sn_6$ and (b) $DyFe_6Sn_6$. The inset of (a) and (b) shows the high temperature $M(T)$ data of $HoFe_6Sn_6$ and $DyFe_6Sn_6$, respectively. (c) and (d) show the magnetization isotherms $[M(H)]$ measured at different temperatures for $H \parallel y$ from $HoFe_6Sn_6$ and $DyFe_6Sn_6$, respectively. The inset of (c) and (d) shows the zoomed-in $M(H)$ at 2 K of $HoFe_6Sn_6$ and $DyFe_6Sn_6$, respectively. Similarly, (e) and (f) show $M(H)$ data, measured at different temperatures for $H \parallel z$ from $HoFe_6Sn_6$ and $DyFe_6Sn_6$, respectively.

Figs. 6.3(c) and 6.3(d) show the isothermal magnetization $[M(H)]$, measured at various temperatures for $H \parallel y$ from $HoFe_6Sn_6$ and $DyFe_6Sn_6$ single crystals, respectively. The $M(H)$ curves at 2 K and 10 K exhibit a rapid increase in the low-field region, followed by a slower increase in the high-field region, without reaching saturation up to an applied field of 9 T. In agreement to the magnetization data which suggest ferromagnetic nature at low temperatures, we observe magnetic hysteresis for both systems when measured at 2 K [see the inset in Figs. 6.3(c) and 6.3(d)]. Thus, $HoFe_6Sn_6$ and $DyFe_6Sn_6$ show ferrimagnetic nature at low temperatures. However, $M(H)$ shows linear behaviour above 50 K due to melting of FM state and leaving behind the antiferromagnetic state alone. Figs. 6.3(e) and 6.3(f) show $M(H)$ data measured at various temperatures for $H \parallel z$ on $HoFe_6Sn_6$ and $DyFe_6Sn_6$ single crystals, respectively. Interestingly, the $M(H)$ data measured at 2 K shows a *kink* at around 5 Tesla for both systems which indicates a field-induced metamagnetic state for $H \parallel z$. However, the metamagnetic state disappears above 10 K. Such a low-temperature metamagentic state was observed earlier in DyV_6Sn_6 due to field induced spin-canting [45]. Further, in contrast to the M(H) data measured

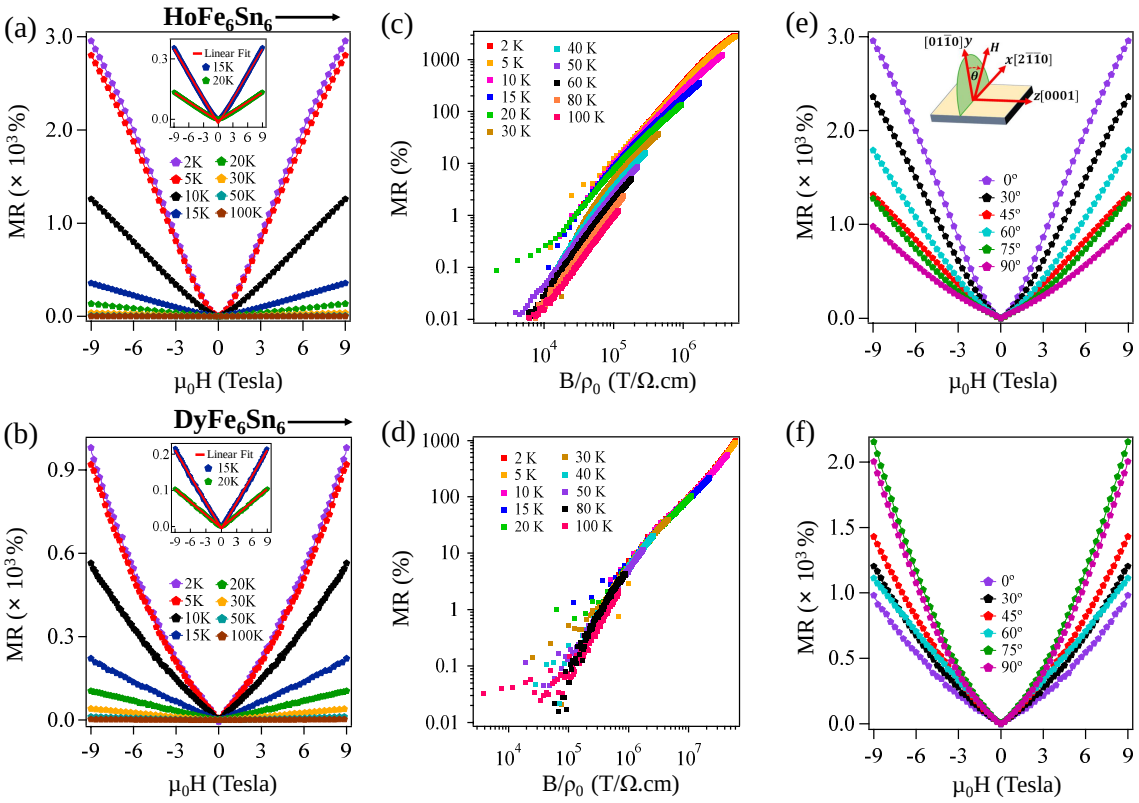

Figure 6.4: Magnetoresistance (MR) as a function of magnetic field is plotted for different temperatures from (a) $HoFe_6Sn_6$ and (b) $DyFe_6Sn_6$. The insets of (a) and (b) show MR data taken 15 and 20 K MR overlapped with liner fit from $HoFe_6Sn_6$ and $DyFe_6Sn_6$, respectively. Scaling analysis of MR data using Kohler's rule for various temperatures from (c) $HoFe_6Sn_6$ and (d) $DyFe_6Sn_6$. MR as a function of field is measured at different field angles (θ) when rotated in the xy-plane from (e) $HoFe_6Sn_6$ and (f) $DyFe_6Sn_6$. The inset in (e) illustrates measurement geometry.

for $H \parallel y$, magnetic hysteresis is not found from both $HoFe_6Sn_6$ and $DyFe_6Sn_6$ for $H \parallel z$. Nevertheless, similar to $H \parallel y$, the systems become completely antiferromagnetic above 50 K for $H \parallel z$ as well.

Earlier, in the case of Fe-based RFe_6Ge_6 and RFe_6Sn_6 (R = rare earth) series of intermetallic compounds an independent magnetic behaviour of the rare-earth (R) and Fe sublattices was identified [46–48]. In RFe_6Sn_6, while the Fe sublattice shows an antiferromagnetic ordering below the Néel temperature of $T_N \approx 560$ K, the rare-earth sublattice orders ferromagnetically at significantly lower temperatures. For R = Gd - Er, the ferromagnetic ordering temperature of rare-earth sublattice ranges from 3 K for $ErFe_6Ge_6$ to 45 K for $GdFe_6Sn_6$, without affecting the Fe sublattice AFM ordering temperature. Our experimental findings also reveal a similar magnetic ordering pattern for the $HoFe_6Sn_6$ and $DyFe_6Sn_6$ exhibiting an antiferromagnetic ordering at around 570 K whereas a ferromagnetic ordering is found at 5.1 K for $HoFe_6Sn_6$ and 8.5 K for $DyFe_6Sn_6$. These observations are in well agreement with previous reports on similar systems [46–48]. Further, the estimated magnetic moment per Ho in $HoFe_6Sn_6$ is about 3.78 μ_B for

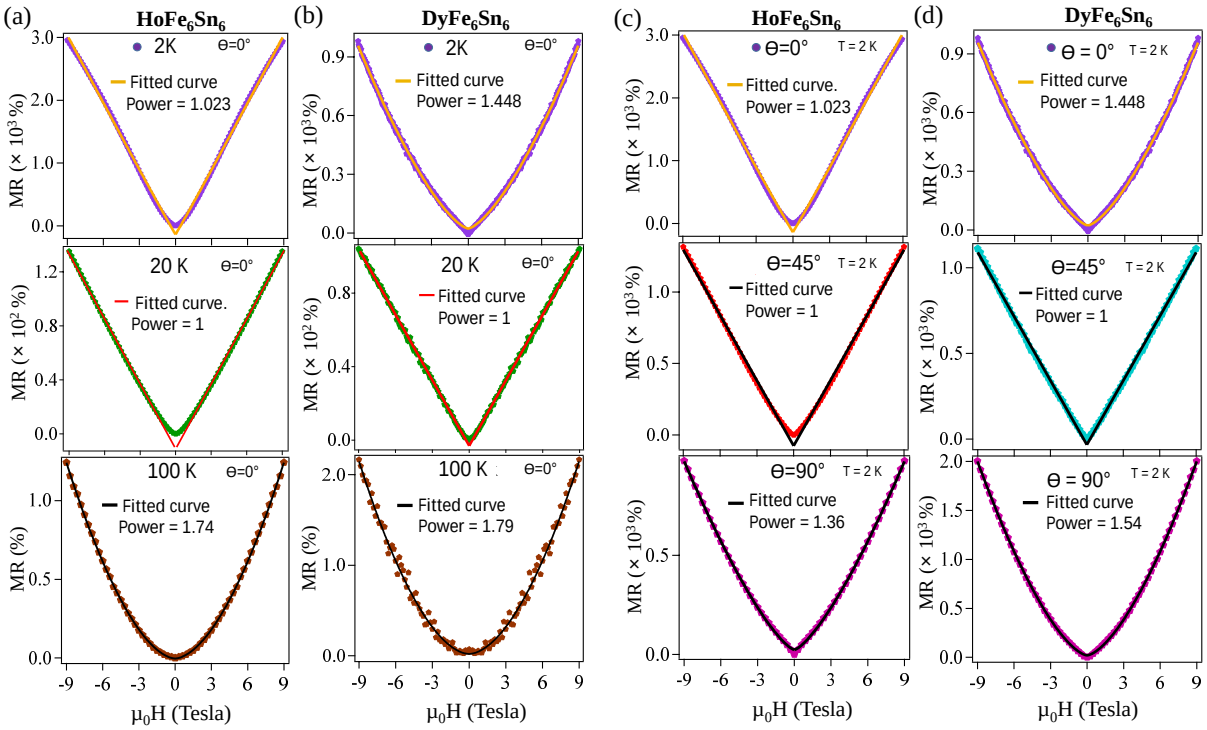

Figure 6.5: Field-dependent magnetoresistance (MR) curves fitted using a power-law relation (MR $\propto B^m$) for (a) $HoFe_6Sn_6$ and (b) $DyFe_6Sn_6$ at various temperatures with the magnetic field aligned along $\theta = 0°$, and for (c) $HoFe_6Sn_6$ and (d) $DyFe_6Sn_6$ at different field angles measured at a fixed temperature of 2 K.

$H \parallel z$ and 3.11 μ_B for $H \parallel y$. These values are substantially lower than the magnetic moments of free Ho^{3+} (10.0 μ_B) ion. The same has been noticed from $DyFe_6Sn_6$, that the magnetic moment per Dy is about 4.20 μ_B for H $\parallel z$ and 3.34 μ_B for $H \parallel y$, which is also substantially lower than the magnetic moment of free Dy^{3+} (10.6 μ_B) ion. This observation clearly confirms that the magnetic moment of the measured systems is not fully polarised even at an external magnetic field of 9 T, resulting into the coexistence of both FM and AFM states in $Ho(Dy)Fe_6Sn_6$ single crystals at low temperatures.
Next, coming to the important observations of this study, Figs. 6.4(a) and 6.4(b) depict the transverse magnetoresistance (MR), i.e., the resistance measured under transverse electric and magnetic fields, at different sample temperatures for $HoFe_6Sn_6$ and $DyFe_6Sn_6$, respectively. Here, we measure MR with the current applied along z-axis and field applied along y-axis. We calculate MR using the relation

$$MR(\%) = [\rho_{zz}(T, \mu_0 H) - \rho_{zz}(T, 0)]/\rho_{zz}(T, 0) \times 100\%$$

. In both systems, a positive non-saturating magnetoresistance was observed at all measured temperatures with the field applied up to 9 T. At 2 K and 9 T, MR reaches a maximum value of $3 \times 10^3\%$ for $HoFe_6Sn_6$ and $1 \times 10^3\%$ for $DyFe_6Sn_6$. The value of MR decreases rapidly with increasing temperature and reaches 1% for $HoFe_6Sn_6$ and 2%

for $DyFe_6Sn_6$ at 100 K and 9 T. This is surprising as the magnetic bulk intermetallic systems usually do not show large MR. Also, let us emphasize here that this is first study showing such as extremely large magnetoresistance (XPR) from the magnetic Fe-based kagome systems. The only other studies showing XMR are on the $M_3In_2S_2$ (M = Ni, Co) kagome systems [41, 42].

To understand the nature magnetoresistance, we fitted the field dependent MR with equation, MR $\propto B^m$ [see Fig.6.5 (a) and (b)] [49]. From the fittings, we estimate $m \simeq 1.02$ for $HoFe_6Sn_6$ and 1.45 for $DyFe_6Sn_6$ at 2 K. At, 15 and 20 K, the MR follows linear field dependence (m =1) for both crystals as shown in the inset of Figs. 6.4(a) and 6.4(b). At 100 K, we estimated $m \simeq 1.74$ for $HoFe_6Sn_6$ and 1.79 for $DyFe_6Sn_6$ [see Fig.6.5 (a) and (b)]. Conventional MR generally changes quadratically with field, but in our case we find that the MR dependence on field changes with temperature. To further confirm this phenomenon, we performed scaling analysis using the Kohler's rule and plotted the MR curves as a function of B/ρ_0 (Kohler's plot) measured at different temperatures as shown in Figs. 6.4(c) and 6.4(d). From the Kohler's plots it is evident that the MR curves do not collapse onto a single universal curve for all measured temperatures, indicating the break down of Kohler's rule. The violation of Kohler's rule suggests a single scattering mechanism is not applicable to explain the MR in the studied systems. Therefore, different temperature regions have distinct scattering mechanism [50, 51, 41]. Further, we measured the field-dependent MR at 2 K by applying the magnetic field along different crystallographic axis while fixing the current direction. The inset of Fig. 6.4(e) schematically shows the angle-dependent MR (ADMR) configuration, with the current along the z [0001] axis and the magnetic field direction varies in the xy-plane. As can be seen from Fig. 6.4(e), in $HoFe_6Sn_6$, the MR gradually decreases from 3×10^3 % to 1×10^3 % as the angle θ increases from 0° to 90°. Conversely, the MR in $DyFe_6Sn_6$ increases from 1×10^3 % to 2×10^3 % as we increase θ from 0° to 90° and reaching maximum 2.2×10^3 at $\theta = 75°$ [Fig. 6.4(f)]. Thus, we can see that the MR is highly crystallographic axis dependent. To further investigate the directional dependent MR, we fit the data using a power law function (MR $\propto B^m$) at different angles as shown in the Fig.6.5 (c) and (d). From the fittings, we estimate $m \simeq 1.02$, 1 and 1.36 at the angles 0°, 45° and 90° for $HoFe_6Sn_6$ and 1.45, 1, and, 1.54 at the angles 0°, 60° and 90° for $DyFe_6Sn_6$, respectively. We find linear MR at 15 and 20 K for both the $HoFe_6Sn_6$and $DyFe_6Sn_6$ systems at an angle of 0°.

For more insights on the angle-dependent magnetoresistance (ADMR), we measured MR at different temperatures under a fixed magnetic field of 9 T and by rotating the field direction with respect to the crystal axis as shown in Figs. 6.6(a) and 6.6(b) for $HoFe_6Sn_6$ and $DyFe_6Sn_6$, respectively. For a given field and temperature the ADMR is calculated using the formula, $ADMR(\%) = \frac{\rho_{zz}(\theta)-\rho_{zz}(\theta_{min})}{\rho_{zz}(\theta_{min})}\times100\%$. θ_{min} is about 86° for $HoFe_6Sn_6$, whereas θ_{min} is about 196° for $DyFe_6Sn_6$. In Fig. 6.6(a), the ADMR measured at 2 K

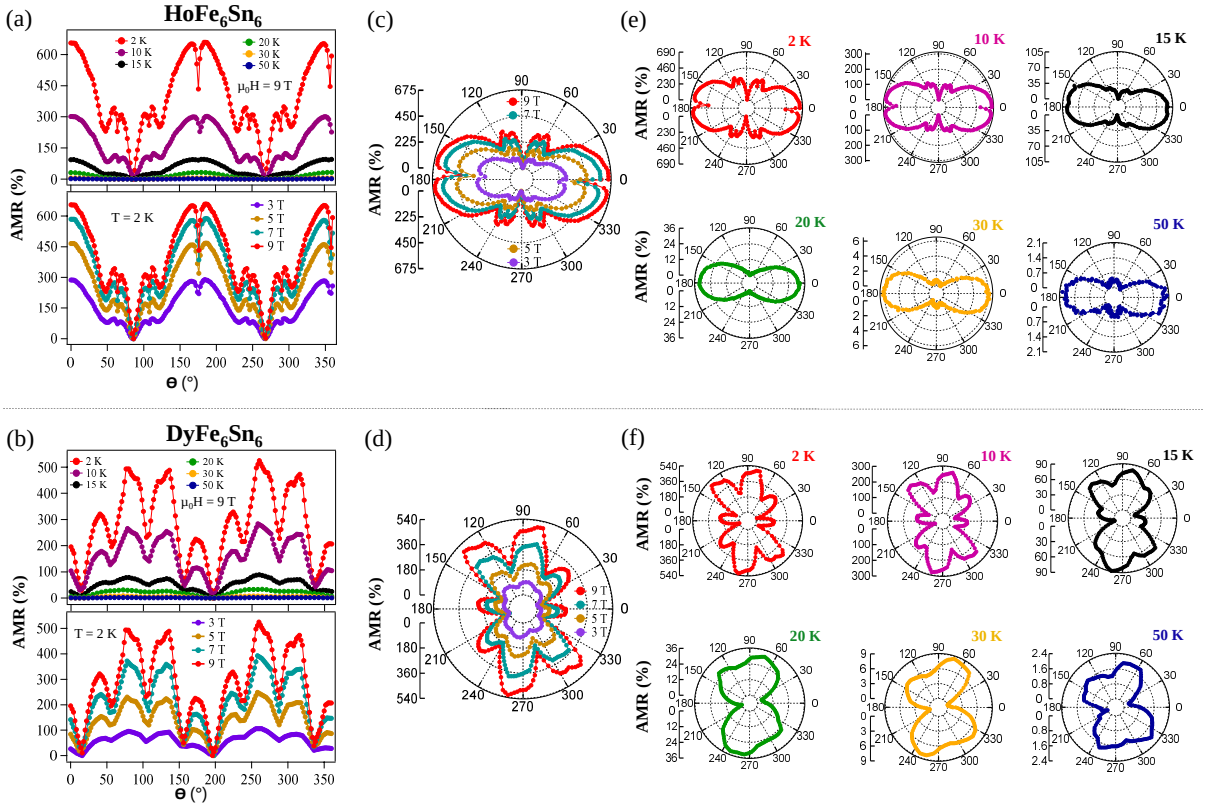

Figure 6.6: Angular-dependent magnetoresistance (ADMR) measured for (a) $HoFe_6Sn_6$ and (b) $DyFe_6Sn_6$ by varying the temperature at a fixed magnetic field of 9 T (top panels) and by varying the magnetic fields at a fixed temperature of 2 K (bottom panels). Current flows along the z-axis and the field is rotated within the xy-plane as depicted in the inset of Fig. 6.4(e). Polar plot of ADMR measured at 2 K by varying the field for (c) $HoFe_6Sn_6$ and (d) $DyFe_6Sn_6$. Polar plot of ADMR measured at 9 T by varying the temperature for (e) $HoFe_6Sn_6$ and (f) $DyFe_6Sn_6$.

shows a total of 12 local maxima and 12 local minima, resulting in a total of 12 lobes for $HoFe_6Sn_6$. This pattern remains unchanged up to 10 K. However, as the temperature increases further the ADMR pattern evolves by decreasing the number of lobes. Similarly, in Fig. 6.6(b), the ADMR at 2 K for $DyFe_6Sn_6$ displays 8 local maxima and 8 local minima, forming the ADMR pattern with 8 lobes. As the temperature increases, the number of lobes decreases similar to $HoFe_6Sn_6$. From Figs. 6.6(a) and 6.6(b), it is evident that the MR is highly sensitive to field angle, indicating the presence of strong anisotropic MR in these systems.

For a better visualization, we plotted the ADMR in polar graphs as depicted in Figs. 6.6(c)-6.6(f). Figs. 6.6(c) and 6.6(d) show the polar-plot of ADMR measured at 2 K under different magnetic fields for $HoFe_6Sn_6$ and $DyFe_6Sn_6$, respectively. Figs. 6.6(e) and 6.6(f) show the polar-plot of ADMR measured under an applied field of 9 T at various sample temperatures for $HoFe_6Sn_6$ and $DyFe_6Sn_6$, respectively. Further, from Fig. 6.6(c), we can see a butterfly-like ADMR pattern for $HoFe_6Sn_6$ at 2 K and the pattern remains

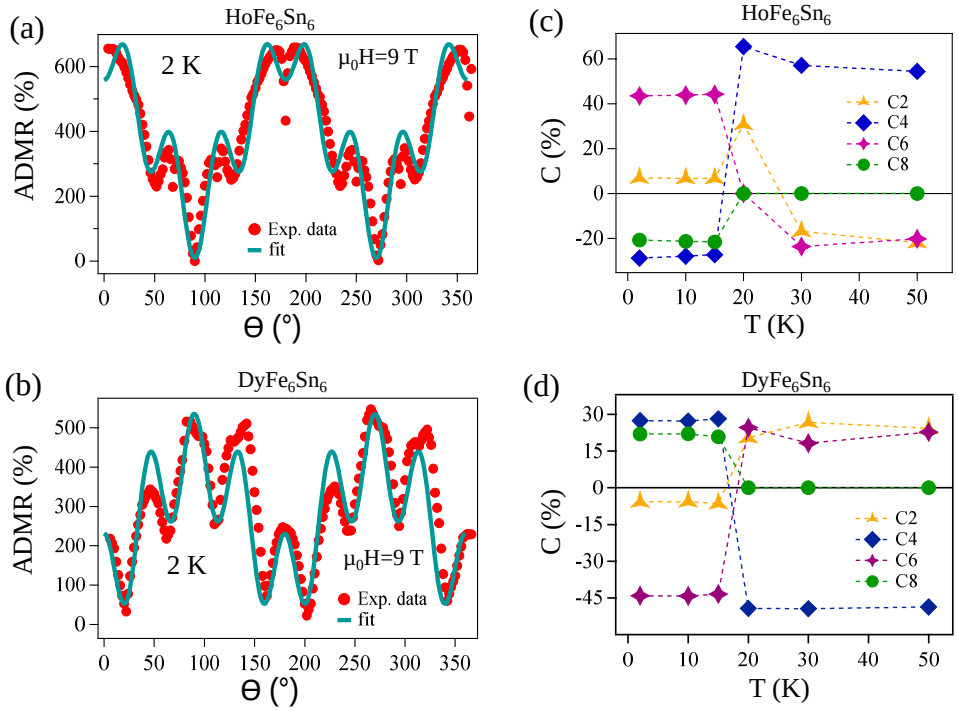

Figure 6.7: ADMR measured for (a) $HoFe_6Sn_6$ and (b) $DyFe_6Sn_6$ at 2 K and 9 T. The solid curves are fits of ADMR using the Eq. 6.1 (see the text for more details). The normalized relative amplitudes (absolute values) C_2 (two-fold), C_4 (four-fold), C_6 (six-fold), and C_8 (eight-fold) components of the ADMR as a function of temperature are shown for (c) $HoFe_6Sn_6$ and (d) $DyFe_6Sn_6$. In (c) and (d), $|C_{2n}| = C_{2n}/\sum_{n=1}^{4} C_{2n}$.

almost constant, though the value of MR% decreases with decreasing field. Similarly, ADMR pattern of $DyFe_6Sn_6$ [see Fig. 6.6(d)] also looks butterfly-like but rotated by 90°. On the other hand, from Figs. 6.6(e) and 6.6(f), one can clearly see that the polar-plot of ADMR changes significantly with temperature. Importantly, the evolution of ADMR with temperature is different between $HoFe_6Sn_6$ and $DyFe_6Sn_6$. For instance, in the case of $HoFe_6Sn_6$ [see Fig. 6.6(e)], the butterfly-like pattern with 12 lobes are visible at 2 and 10 K. As the temperature rises, the ADMR pattern changes from a butterfly-like to a dumbbell-like at 20 K, with only two lobes visible. Further increasing the temperature, at 30 and 50 K, an additional two lobes have reemerged at 90° and 180°. In the case of $DyFe_6Sn_6$ [see Fig. 6.6(f)], the butterfly pattern, with eight lobes, is visible up to 15 K. Between 20 and 50 K, only four lobes are visible.

Next, Figs. 6.7(a) and 6.7(b) depict the ADMR measured at 2 K under the magnetic field of 9 T for $HoFe_6Sn_6$ and $DyFe_6Sn_6$, respectively. The ADMR data is fitted by Eq. 6.1 having contribution up to 8-fold symmetry. Although the fitting is not perfect, but the Eq. 6.1 can reasonably reproduce the experimental data. The fittings for higher temperature ADMR data are shown in Figs.6.8 (a) and (b). The normalized relative amplitudes C_2 (two-fold), C_4 (four-fold), C_6 (six-fold), and C_8 (eight-fold) of ADMR are plotted as a function of temperature in Figs. 6.7(c) and 6.7(d) for $HoFe_6Sn_6$ and

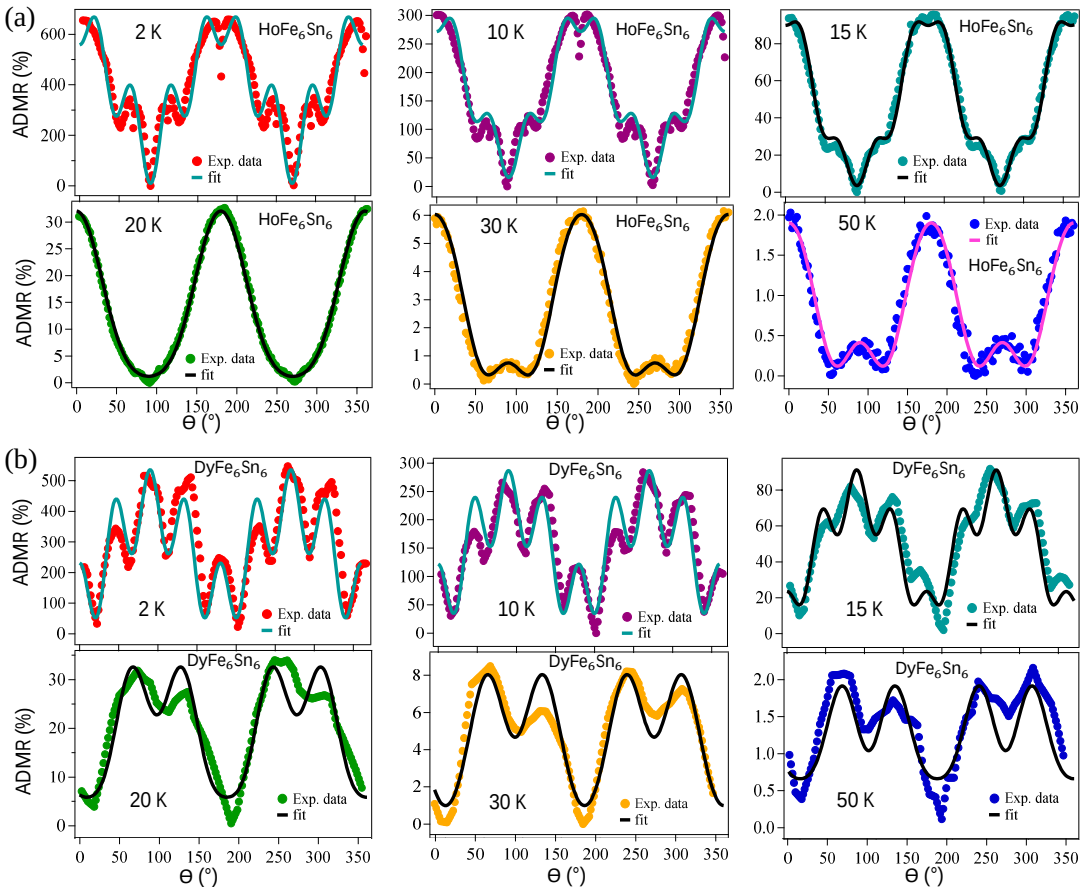

Figure 6.8: Angle-dependent magnetoresistance (ADMR) measured at various temperatures under the magnetic field of 9 T for (a) $HoFe_6Sn_6$ and (b) $DyFe_6Sn_6$. Solid lines represent fits to the experimental data using Eq.6.1.

$DyFe_6Sn_6$, respectively. From the temperature dependent relative amplitudes, we can notice that all symmetry components contribute to the ADMR up to 20 K. However, from 20 K, the eight-fold symmetry contribution to ADMR is totally suppressed.

$$ADMR = C_0 + C_2\ Cos^2\theta + C_4\ Cos^4\theta + C_6\ Cos^6\theta + C_8\ Cos^8\theta \tag{6.1}$$

where C_0 is a constant, $C_2\ Cos^2\theta$, $C_4\ Cos^4\theta$, $C_6\ Cos^6\theta$, and $C_8\ Cos^8\theta$ account for the two, four, six, and eight fold components, respectively. The constants C_2, C_4, C_6, and C_8 are the amplitudes.

Several mechanisms exist in the literature explaining the manyfold symmetric ADMR, such as (i) magnetocrystalline anisotropy [52–54], (ii) spin scattering near the antiphase boundaries (APBs) [55–57], (iii) exchange bias [58], (iv) relaxation time anisotropy [59, 42], (v) symmetry of the lattice [60, 42], and (vi) density of states modulation near the Fermi level [59, 61]. As can be seen from Figs. 6.6(c) and 6.6(d), the ADMR is insensitive to the applied field. Therefore, the observed ADMR in $HoFe_6Sn_6$ and $DyFe_6Sn_6$ may not be originated from the magnetism. Further, the mean free path of the charge carriers calculated from Hall effect measurement data (shown later) at 2 K is about 25.20 μm

for $HoFe_6Sn_6$ and 15.96 μm for $DyFe_6Sn_6$, which are much higher than the distance of $Fe-Fe$ (2.67 Å), $Ho-Ho$ (5.35 Å), or $Dy-Dy$ (5.35 Å) magnetic moments. Therefore, we can neglect the spin-charge scattering in these systems, allowing us to safely exclude the influence of magnetism on the observed ADMR as discussed in the points (i)-(iv). The other possibilities of ADMR are the crystal symmetry or the band structure near the Fermi level. As discussed above, the studied systems shows 2-, 4-, 6-, and 8-fold symmetry in the ADMR at low temperature (< 20 K) and at higher temperatures the 8-fold component completely gets suppressed leaving only the 2-, 4-, and 6-fold symmetries. Particularly, the 2-fold symmetry contribution is very small at low temperatures, and thus the total ADMR is dominated by the higher-fold symmetries. At higher temperatures, except the 8-fold symmetry component, the other symmetries significantly contribute to the total ADMR. Since the field is applied always perpendicular to the z-axis and is rotated within the xy-plane, the 6-fold symmetry contribution could be originated from the DOS modulation near the Fermi level and from the hexagonal crystal symmetry. On the other hand, the 2-fold and 4-fold symmetry contributions to the ADMR might have originated from the DOS modulation near the Fermi level [59, 61, 42]. This is because, in the momentum space, the charge carriers orbit around the Fermi surface cross-sections that are perpendicular to the magnetic field (B) direction [62]. As a result, the anisotropic shape of the Fermi surface leads to variation in the cyclotron mass and velocity, following the relation $\upsilon_k = \frac{1}{\hbar}\nabla_k \varepsilon_k$. This variation in the cyclotron mass and velocity, has an effect on how easily the charge carrier trajectories bend under the magnetic field, influence the value of MR [63, 62].

To better understand band structure contribution to the anisotropic MR in these systems, we performed the density functional theory (DFT) calculations. Performing DFT calculations on Ho(Dy)Fe_6Sn_6 (YCo_6Ge_6-type structure) system is quite challenging due to its disordered nature. As illustrated in Fig. 6.9(a), the YCo_6Ge_6-type structure can be viewed as a combination of two $HfFe_6Ge_6$-type unit cells where one of them is translated by $c/2$ [64, 19]. To address the challenges associated with the disordered and partially occupied YCo_6Ge_6-type structure, we used the ordered $HfFe_6Ge_6$-type structure for the DFT calculations. This approach aligns well with previous studies on the related systems [19, 65]. Although the $HfFe_6Ge_6$-type and YCo_6Ge_6-type structures share the same space group (P6/mmm, 191), they differ in their atomic arrangement. Our DFT calculations suggest that in the ground state the Fe magnetic moments align antiferromagnetically, while the Ho(Dy) magnetic moments align ferromagnetically within the ab-plane as shown in Fig. 6.9(b). This prediction is inline with our magnetization measurements which suggest that the easy magnetization axis lies on the ab-plane [see Fig. 6.3].

Figs. 6.9(c) and 6.9(d) show the electronic band structure plotted for $HoFe_6Sn_6$ and $DyFe_6Sn_6$, respectively, without considering the spin-orbit coupling (SOC). The band dispersions of both systems qualitatively look similar. Both band structures exhibit

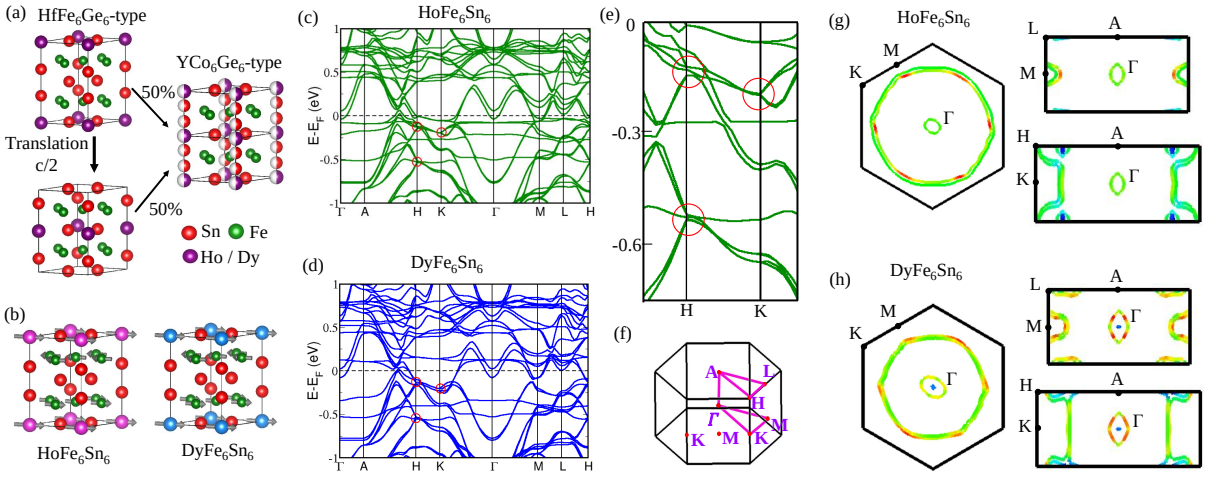

Figure 6.9: (a) Schematic demonstration of two $HfFe_6Ge_6$-type crystal structures forming one partially filled YCo_6Ge_6. (b) Ground state magnetic structure of $HoFe_6Sn_6$ and $DyFe_6Sn_6$, derived from the DFT calculations. (c) and (d) Electronic band structures of $HoFe_6Sn_6$ and $DyFe_6Sn_6$, respectively, calculated without including spin-orbit coupling (SOC). (e) Zoomed-in image of the (c) highlighting the Dirac-like band dispersions near the Fermi level. (f) Hexagonal Brillouin zone with high symmetry points located. (g) and (h) In-plane and out-of-plane Fermi contours of $HoFe_6Sn_6$ and $DyFe_6Sn_6$, respectively, calculated without including SOC.

several parabolic bands crossing the Fermi level, confirming the metallic nature of the studied systems. Interestingly, we notice several non-dispersive flat bands near the Fermi level mostly contributed by the Ho(Dy) $4f$ orbitals [see Fig.6.10] [15, 66, 67]. Further, from a zoomed-in band structure shown in Fig. 6.9(e), we observe several Dirac-like band crossings in the vicinity of the Fermi level marked by red-circles. These band crossings are mainly originating from the Fe $3d$ orbitals. Next, Figs. 6.9(g) and 6.9(h) show the Fermi maps of $HoFe_6Sn_6$ and $DyFe_6Sn_6$, respectively, from the in-plane and out-of-plane momentum space. From the in-plane (ΓKM) Fermi map, we mainly observe one small and two large Fermi sheets around Γ point. On comparing the Fermi sheets with the electronic band dispersions shown in Fig. 6.9(e), we can conclude that the two large Fermi contours are of hole-type and the smaller one is of electron-type. Similarly, from the Fermi map taken in the ΓMLA plane, we could observe two small electron-like highly dispersive out-of-plane Fermi sheets along the $M-L$ direction and another electron-type Fermi sheet dispersing along the $\Gamma - A$ direction. In addition, from the Fermi map taken in the ΓKHA plane, we could observe two out-of-plane highly dispersive large electron-type Fermi sheets along the $K - H$ direction and two hole-like in-plane Fermi sheets along the $H - A$ direction. Since the applied field is perpendicular to the $z(k_z)$-axis, the Fermi sheets lying in the ΓKHA and ΓMLA planes contribute to the magnetoresistance. And can be seen from Figs. 6.9(g) and 6.9(h), the Fermi sheets in these planes show 2- and 4-fold (nearly) symmetries. On rotating the magnetic field axis in the xy-plane, we

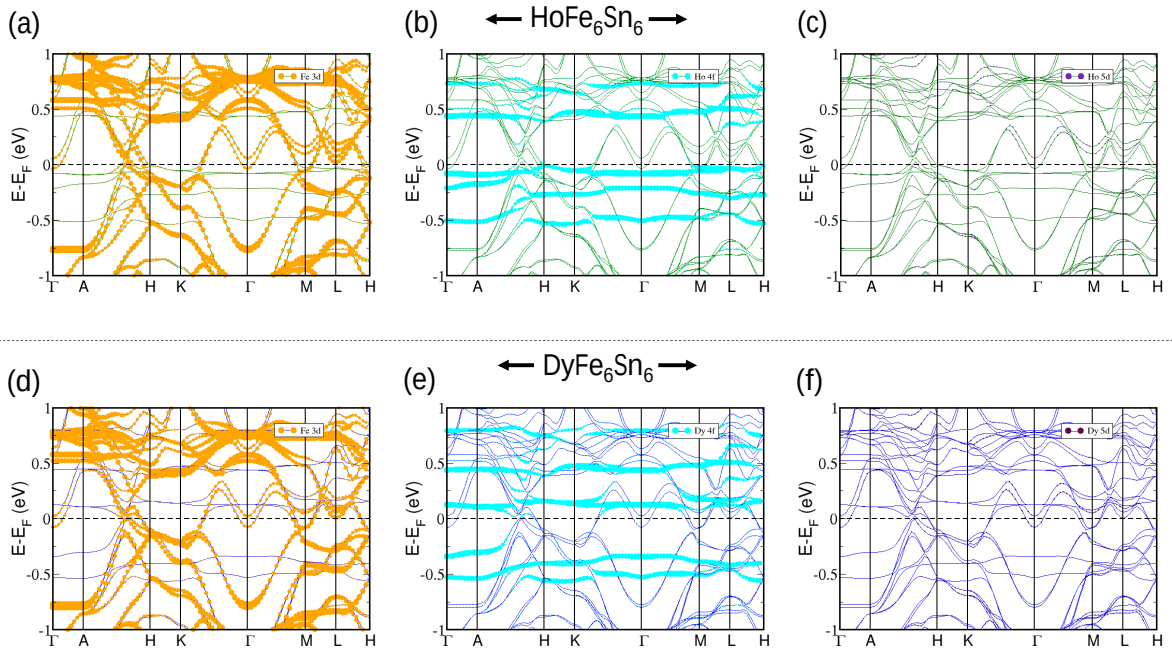

Figure 6.10: Band structure of $HoFe_6Sn_6$ for (a) Fe $3d$, (b) Ho $4f$, and (c) Ho $5d$ orbitals. Band structure of $DyFe_6Sn_6$ for (d) Fe $3d$, (e) Dy $4f$, and (f) Dy 5d orbitals.

could get the 6-fold modulation of the Fermi sheets of the ΓKHA and ΓMLA planes. We note that the band structures presented here are calculated without spin-orbit coupling. Spin-orbit coupling calculations are very challenging and lead to convergence issues due to the presence of $4f$ states.

Next, as the Hall effect is sensitive to the topological band structure, we performed Hall effect measurements for both $HoFe_6Sn_6$ and $DyFe_6Sn_6$ systems. The field-dependent Hall resistivity (ρ_{zx}) measured at different temperatures is shown in Figs. 6.11(a) and 6.11(b) for $HoFe_6Sn_6$ and $DyFe_6Sn_6$, respectively. Here, ρ_{zx} corresponds to the current applied along the z-direction, field applied along the y-direction, and the Hall voltage was measured along the x-direction. From Fig. 6.11(a), it is clear that the Hall resistivity is not linear with magnetic filed, suggesting more than one-type of charge carriers dominating the magnetotransport. Importantly, the slope of ρ_{zx} $vs.$ H curve is positive below 30 K and negative for 50 and 100 K. We could not measure the Hall effect above 100 K due to high noise to signal ratio. Similar behaviour was also observed from $DyFe_6Sn_6$ as shown in Fig. 6.11(b). Figs. 6.11(c) and 6.11(d) show the Hall conductivity (σ_{zx}) calculated from the Hall resistivity (ρ_{zx}) and longitudinal resistivity (ρ_{zz}) data using the equation,

$$\sigma_{zx} = -\frac{\rho_{zx}}{\rho_{zz}^2 + \rho_{zx}^2} \tag{6.2}$$

Following the semiclassical two band model, we fitted the Hall conductivity σ_{zx} using the equation,

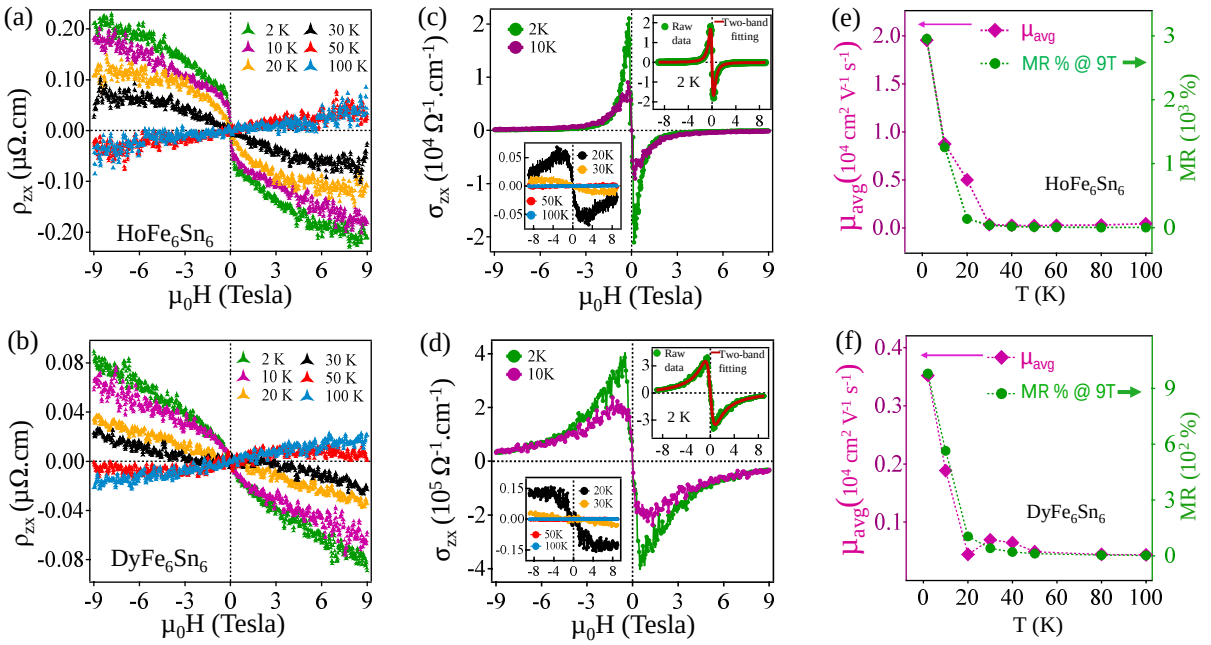

Figure 6.11: Field-dependent Hall resistivity (ρ_{zx}) measured at various temperatures for (a) $HoFe_6Sn_6$ and (b) $DyFe_6Sn_6$. Hall conductivity (σ_{zx}) derived from Hall resistivity (ρ_{zx}) at 2 K and 10 K of (c) $HoFe_6Sn_6$ and (d) $DyFe_6Sn_6$. Bottom left inset of (c) and (d) are the Hall conductivity (σ_{zx}) derived at 20 and 30 K. Top right inset of (c) and (d) show two-band model fitting of σ_{zx} at 2 K. Mean carrier mobility (left axis), $\bar{\mu} = \sqrt{\mu_h \mu_e}$ and MR(%) at 9 T (right axis) are plotted as a function of temperature for (e) $HoFe_6Sn_6$ and (f) $DyFe_6Sn_6$.

$$\sigma_{zx} = \left[\frac{n_h \mu_h^2}{1 + (\mu_h B)^2} - \frac{n_e \mu_e^2}{1 + (\mu_e B)^2} \right] eB \tag{6.3}$$

where $n_h(n_e)$ and $\mu_h(\mu_e)$ are hole (electron) density and mobility, respectively. The two-band fitting of σ_{zx} at 2 K are shown in the top right inset of Fig. 6.11(c) and Fig. 6.11(d) for $HoFe_6Sn_6$ and $DyFe_6Sn_6$, respectively. From the Hall conductivity fitting of $HoFe_6Sn_6$ at 2 K, the hole and electron density are found to be $n_h = 0.64 \times 10^{19}\ cm^{-3}$ and $n_e = 0.69 \times 10^{19}\ cm^{-3}$. The ratio of hole and electron density $n_h/n_e = 0.93$, which is close to 1 for a perfect electron-hole compensation. Also, the hole and electron mobility are found to be $\mu_h = 1.05 \times 10^4\ cm^2\ V^{-1}\ s^{-1}$ and $\mu_e = 3.62 \times 10^4\ cm^2\ V^{-1}\ s^{-1}$, respectively, for $HoFe_6Sn_6$. The mean mobility is estimated to be $\bar{\mu} = 1.5 \times 10^4\ cm^2\ V^{-1}\ s^{-1}$, using the relation $\bar{\mu} = \sqrt{\mu_h \mu_e}$ [35] . The mean mobility in this system is high and comparable to the numerous other systems showing XMR [68, 36, 69, 70, 26].

Further, in Fig. 6.11(e) we can notice that the mean carrier mobility rapidly decreases with increasing temperature between 2 and 100 K. Additionally, we also notice that the MR% value drops between 2 and 100 K in a similar fashion of the mean mobility [see Fig. 6.11(e)]. This observation suggests that the carrier mobility has a significant influence on the observed XMR and ADMR [see Fig. 6.7]. According to the earlier reports, XMR

behaviour in $\alpha - WP_2$ strongly depends on the high carrier mobility rather than electron-hole compensation, which is consistent with our observation in $HoFe_6Sn_6$ [71]. Note that the band dispersions near the Fermi level controls the carrier mobility, and thus it is the electronic band structure playing the dominant role of ADMR in these systems. Further, $DyFe_6Sn_6$ also exhibits similar behaviour of carrier mobility to that of $HoFe_6Sn_6$. In $DyFe_6Sn_6$ at 2 K, the hole and electron density are found to be $n_h = 3.95 \times 10^{20}\ cm^{-3}$ and $n_e = 3.77 \times 10^{20}\ cm^{-3}$, respectively. The ratio of hole and electron density is $n_h/n_e = 1.05$. The hole and electron mobility are found to be $\mu_h = 0.10 \times 10^4\ cm^2\ V^{-1}\ s^{-1}$ and $\mu_e = 1.18 \times 10^4\ cm^2\ V^{-1}\ s^{-1}$, yielding the mean mobility of $\bar{\mu} = 0.35 \times 10^4\ cm^2\ V^{-1}\ s^{-1}$.

6.4 Summary

In conclusion, we systematically studied the magnetic and magnetotransport properties on the high-quality single crystals of the Fe-based RFe_6Sn_6 (R = Ho, Dy) kagome systems. Extremely large magnetoresistance (XMR) is observed at low temperatures reaching the maximum MR percentage as high as 3×10^3 % for $HoFe_6Sn_6$ and 1×10^3 % for $DyFe_6Sn_6$ at 2 K under 9 T of applied magnetic field. Hall effect measurements demonstrate the electron-hole charge compensation and high-carrier mobility, leading to extremely large magnetoresistance at low temperatures. Further, the angle-dependent magnetoresistance (ADMR) data reveal high anisotropy in the magnetoresistance. Importantly, the magnetoresistance anisotropic pattern changes significantly with temperature, implies the temperature dependence of the Fermi surface topology in these systems.

References

[1] N. Morali, R. Batabyal, P. K. Nag, E. Liu, Q. Xu, Y. Sun, B. Yan, C. Felser, N. Avraham, H. Beidenkopf, Fermi-arc diversity on surface terminations of the magnetic Weyl semimetal $Co_3Sn_2S_2$, Science 365 (2019) 1286–1291.

[2] Q. Wang, Y. Xu, R. Lou, Z. Liu, M. Li, Y. Huang, D. Shen, H. Weng, S. Wang, H. Lei, Large intrinsic anomalous Hall effect in half-metallic ferromagnet $Co_3Sn_2S_2$ with magnetic Weyl fermions, Nat. Commun. 9 (2018).

[3] S. Nakatsuji, N. Kiyohara, T. Higo, Large anomalous Hall effect in a non-collinear antiferromagnet at room temperature, Nature 527 (2015) 212–215.

[4] A. K. Nayak, J. E. Fischer, Y. Sun, B. Yan, J. Karel, A. C. Komarek, C. Shekhar, N. Kumar, W. Schnelle, J. Kübler, et al., Large anomalous Hall effect driven by a

nonvanishing Berry curvature in the noncolinear antiferromagnet Mn_3Ge, Sci. Adv. 2 (2016) e1501870.

[5] J. Kübler, C. Felser, Weyl fermions in antiferromagnetic Mn_3Sn and Mn_3Ge, EPL (Europhysics Letters) 120 (2018) 47002.

[6] A. Low, S. Ghosh, S. Changdar, S. Routh, S. Purwar, S. Thirupathaiah, Tuning of topological properties in the strongly correlated antiferromagnet Mn_3Sn via Fe doping, Phys. Rev. B 106 (2022) 144429.

[7] S. Changdar, S. Ghosh, A. Bose, I. Kar, A. Low, P. L. Fèvre, F. Bertran, A. Narayan, S. Thirupathaiah, Weak electronic correlations observed in magnetic Weyl Semimetal Mn_3Ge, J. Phys. Condens. Matter 36 (2023) 125502.

[8] S. Ghosh, A. Low, S. Ghorai, K. Mandal, S. Thirupathaiah, Tuning of electrical, magnetic, and topological properties of magnetic Weyl semimetal $Mn_{3+x}Ge$ by Fe doping, J. Phys. Condens. Matter 35 (2023) 485701.

[9] Y.-X. Jiang, J.-X. Yin, M. M. Denner, N. Shumiya, B. R. Ortiz, G. Xu, Z. Guguchia, J. He, S. Hossain, X. Liu, J. Ruff, L. Kautzsch, S. S. Zhang, G. Chang, I. Belopolski, Q. Zhang, T. A. Cochran, D. Multer, M. Litskevich, Z.-J. Cheng, X. P. Yang, Z. Wang, R. Thomale, T. Neupert, S. D. Wilson, M. Z. Hasan, Unconventional chiral charge order in kagome superconductor KV_3Sb_5, Nat. Mater. 20 (2021) 1353–1357.

[10] Y. Hu, X. Wu, B. R. Ortiz, S. Ju, X. Han, J. Z, MA, N. C. Plumb, M. Radovic, R. Thomale, S. D. Wilson, A. P. Schnyder, M. Shi, Rich nature of Van Hove singularities in Kagome superconductor CsV_3Sb_5, Nat. Commun. 13 (2022).

[11] W. Ma, X. Xu, J.-X. Yin, H. Yang, H. Zhou, Z.-J. Cheng, Y. Huang, Z. Qu, F. Wang, M. Z. Hasan, S. Jia, Rare Earth Engineering in $R\mathrm{Mn_6Sn_6}$ (R = Gd−Tm, Lu) Topological Kagome Magnets, Phys. Rev. Lett. 126 (2021) 246602.

[12] G. Dhakal, F. Cheenicode Kabeer, A. K. Pathak, F. Kabir, N. Poudel, R. Filippone, J. Casey, A. Pradhan Sakhya, S. Regmi, C. Sims, K. Dimitri, P. Manfrinetti, K. Gofryk, P. M. Oppeneer, M. Neupane, Anisotropically large anomalous and topological Hall effect in a kagome magnet, Phys. Rev. B 104 (2021) L161115.

[13] L. Gao, S. Shen, Q. Wang, W. Shi, Y. Zhao, C. Li, W. Cao, C. Pei, J.-Y. Ge, G. Li, J. Li, Y. Chen, S. Yan, Y. Qi, Anomalous Hall effect in ferrimagnetic metal RMn_6Sn_6 (R = Tb, Dy, Ho) with clean Mn kagome lattice, Appl. Phys. Lett. 119 (2021).

[14] H. Zhou, M. Shi, Y. Huang, W. Ma, X. Xu, J. Wang, S. Jia, Metamagnetic transition and anomalous Hall effect in Mn-based kagomé magnets $R\mathrm{Mn_6Ge_6}(R = \mathrm{Tb{-}Lu})$, Phys. Rev. Mater. 7 (2023) 024404.

[15] S. Peng, Y. Han, G. Pokharel, J. Shen, Z. Li, M. Hashimoto, D. Lu, B. R. Ortiz, Y. Luo, H. Li, M. Guo, B. Wang, S. Cui, Z. Sun, Z. Qiao, S. D. Wilson, J. He, Realizing Kagome Band Structure in Two-Dimensional Kagome Surface States of $R\mathrm{V_6Sn_6}$ ($R = \mathrm{Gd}$, Ho), Phys. Rev. Lett. 127 (2021) 266401.

[16] X. Zhang, Z. Liu, Q. Cui, Q. Guo, N. Wang, L. Shi, H. Zhang, W. Wang, X. Dong, J. Sun, Z. Dun, J. Cheng, Electronic and magnetic properties of intermetallic kagome magnets $R\mathrm{V_6Sn_6}(R = \mathrm{Tb{-}Tm})$, Phys. Rev. Mater. 6 (2022) 105001.

[17] J. Lee, E. Mun, Anisotropic magnetic property of single crystals $R\mathrm{V_6Sn_6}$ ($R = \mathrm{Y, Gd{-}Tm, Lu}$), Phys. Rev. Mater. 6 (2022) 083401.

[18] H. W. S. Arachchige, W. R. Meier, M. Marshall, T. Matsuoka, R. Xue, M. A. McGuire, R. P. Hermann, H. Cao, D. Mandrus, Charge Density Wave in Kagome Lattice Intermetallic $\mathrm{ScV_6Sn_6}$, Phys. Rev. Lett. 129 (2022) 216402.

[19] Y. Liu, M. Lyu, J. Liu, S. Zhang, J. Yang, Z. Du, B. Wang, H. Wei, E. Liu, Structural Determination, Unstable Antiferromagnetism and Transport Properties of Fe-Kagome $Y_{0.5}Fe_3Sn_3$ Single Crystals, Chinese Phys. Lett. 40 (2023) 047102.

[20] C. Q. Xu, T. W. Heitmann, H. Zhang, X. Xu, X. Ke, Magnetic phase transition, magnetoresistance, and anomalous Hall effect in Ga-substituted $\mathrm{YMn_6Sn_6}$ with a ferromagnetic kagome lattice, Phys. Rev. B 104 (2021) 024413.

[21] F. Kabir, R. Filippone, G. Dhakal, Y. Lee, N. Poudel, J. Casey, A. P. Sakhya, S. Regmi, R. Smith, P. Manfrinetti, L. Ke, K. Gofryk, M. Neupane, A. K. Pathak, Unusual magnetic and transport properties in $\mathrm{homn_6sn_6}$ kagome magnet, Phys. Rev. Mater. 6 (2022) 064404.

[22] C. Liu, H. Zhang, Z. Li, Y. Yan, Y. Zhang, Z. Hou, X. Fu, Nontrivial spin textures induced remarkable topological Hall effect and extraordinary magnetoresistance in kagome magnet $TmMn_6Sn_6$, Surfaces and Interfaces 39 (2023) 102866.

[23] A. Low, T. K. Bhowmik, S. Ghosh, S. Thirupathaiah, Anisotropic nonsaturating magnetoresistance observed in $\mathrm{HoMn_6Ge_6}$: A kagome Dirac semimetal, Phys. Rev. B 109 (2024) 195104.

[24] C. W. Heaps, The Magnetoresistance of Nickel in Large Fields, Physical Review 55 (1939) 1069–1071.

[25] S. S. P. Parkin, N. More, K. P. Roche, Oscillations in exchange coupling and magnetoresistance in metallic superlattice structures: Co/Ru, Co/Cr, and Fe/Cr, Phys. Rev. Lett. 64 (1990) 2304–2307.

[26] R. Niu, W. Zhu, Materials and possible mechanisms of extremely large magnetoresistance: a review, J. Phys. Condens. Matter 34 (2021) 113001.

[27] A. P. Ramirez, Colossal magnetoresistance, J. Phys. Condens. Matter 9 (1997) 8171–8199.

[28] S. Yang, J. Zhang, Current progress of magnetoresistance sensors, Chemosensors 9 (2021) 211.

[29] O. Vitayaya, P. Z. Z. Nehan, D. R. Munazat, M. T. E. Manawan, B. Kurniawan, Magnetoresistance (MR) properties of magnetic materials, RSC Advances 14 (2024) 18617–18645.

[30] A. B. Pippard, Magnetoresistance in metals, volume 2, Cambridge university press, 1989.

[31] S. Blundell, Magnetism in condensed matter, OUP Oxford, 2001.

[32] J. Nickel, Magnetoresistance overview, Hewlett-Packard Laboratories, Technical Publications Department Palo Alto ..., 1995.

[33] E. Tsymbal, D. Pettifor, Perspectives of giant magnetoresistance, 2001.

[34] J. Inoue, S. Maekawa, Theory of tunneling magnetoresistance in granular magnetic films, Phys. Rev. B 53 (1996) R11927–R11929.

[35] M. N. Ali, J. Xiong, S. Flynn, J. Tao, Q. Gibson, L. M. Schoop, T. Liang, N. Haldolaarachchige, M. Hirschberger, N. P. Ong, R. J. Cava, Large, non-saturating magnetoresistance in WTe_2, Nature 514 (2014) 205–208.

[36] F. Han, J. Xu, A. S. Botana, Z. L. Xiao, Y. L. Wang, W. G. Yang, D. Y. Chung, M. G. Kanatzidis, M. R. Norman, G. W. Crabtree, W. K. Kwok, Separation of electron and hole dynamics in the semimetal LaSb, Phys. Rev. B 96 (2017) 125112.

[37] W. Gao, N. Hao, F.-W. Zheng, W. Ning, M. Wu, X. Zhu, G. Zheng, J. Zhang, J. Lu, H. Zhang, C. Xi, J. Yang, H. Du, P. Zhang, Y. Zhang, M. Tian, Extremely Large Magnetoresistance in a Topological Semimetal Candidate Pyrite $PtBi_2$, Phys. Rev. Lett. 118 (2017) 256601.

[38] K. Okawa, M. Kanou, H. Namiki, T. Sasagawa, Extremely large magnetoresistance induced by hidden three-dimensional Dirac bands in nonmagnetic semimetal InBi, Phys. Rev. Mater. 2 (2018) 124201.

[39] C. Shekhar, A. K. Nayak, Y. Sun, M. Schmidt, M. Nicklas, I. Leermakers, U. Zeitler, Y. Skourski, J. Wosnitza, Z. Liu, Y. Chen, W. Schnelle, H. Borrmann, Y. Grin, C. Felser, B. Yan, Extremely large magnetoresistance and ultrahigh mobility in the topological Weyl semimetal candidate NbP, Nat. Phys. 11 (2015) 645–649.

[40] R. Mondal, S. Sasmal, R. Kulkarni, A. Maurya, A. Nakamura, D. Aoki, H. Harima, A. Thamizhavel, Extremely large magnetoresistance, anisotropic Hall effect, and Fermi surface topology in single-crystalline WSi_2, Phys. Rev. B 102 (2020) 115158.

[41] Y. Zhang, Z. Li, K.-W. Chen, L. Li, C. Uher, Extremely large magnetoresistance and quantum oscillations in semimetal $Ni_3In_2S_2$, Mater. Today Phys. 40 (2024) 101318.

[42] S. Lv, H. Guo, Q. Qi, Y. Li, G. Hu, Q. Zheng, R. Wang, N. Si, K. Zhu, Z. Zhao, Y. Han, W. Yu, G. Xian, L. Huang, L. Bao, X. Lin, J. Pan, S. Du, J. He, H. Yang, H. Gao, Field-Induced Butterfly-Like anisotropic magnetoresistance in a Kagome semimetal $Co_3In_2S_2$, Adv. Funct. Mater. (2024).

[43] P. Giannozzi, S. Baroni, N. Bonini, M. Calandra, R. Car, C. Cavazzoni, D. Ceresoli, G. L. Chiarotti, M. Cococcioni, I. Dabo, A. D. Corso, S. De Gironcoli, S. Fabris, G. Fratesi, R. Gebauer, U. Gerstmann, C. Gougoussis, A. Kokalj, M. Lazzeri, L. Martin-Samos, N. Marzari, F. Mauri, R. Mazzarello, S. Paolini, A. Pasquarello, L. Paulatto, C. Sbraccia, S. Scandolo, G. Sclauzero, A. P. Seitsonen, A. Smogunov, P. Umari, R. M. Wentzcovitch, QUANTUM ESPRESSO: a modular and open-source software project for quantum simulations of materials, J. Phys. Condens. Matter 21 (2009) 395502.

[44] J. P. Perdew, K. Burke, M. Ernzerhof, Generalized Gradient Approximation Made Simple [Phys. Rev. Lett. 77, 3865 (1996)], Phys. Rev. Lett. 78 (1997) 1396–1396.

[45] X.-Y. Zeng, H. Wang, X.-Y. Wang, J.-F. Lin, J. Gong, X.-P. Ma, K. Han, Y.-T. Wang, Z.-Y. Dai, T.-L. Xia, Magnetic and magnetotransport properties in the vanadium-based kagome metals DyV_6Sn_6 and HoV_6Sn_6, Phys. Rev. B 109 (2024) 104412.

[46] J. M. Cadogan, D. H. Ryan, Independent magnetic ordering of the rare-earth (R) and Fe sublattices in the RFe_6Ge_6 and RFe_6Sn_6 series, J. Alloy. Compd. 326 (2001) 166–173.

[47] J. M. Cadogan, Suharyana, D. H. Ryan, O. Može, W. Kockelmann, Neutron diffraction and Mossbauer study of the magnetic structure of $HoFe_6Sn_6$, IEEE Transactions on Magnetics 37 (2001) 2606–2608.

[48] J. M. Cadogan, O. Može, D. H. Ryan, Suharyana, M. Hofmann, Magnetic ordering in $DyFe_6Sn_6$, Physica B 385-386 (2006) 317–319.

[49] R. Singha, A. Pariari, B. Satpati, P. Mandal, Magnetotransport properties and evidence of a topological insulating state in LaSbTe, Phys. Rev. B 96 (2017) 245138.

[50] A. Narayanan, M. D. Watson, S. F. Blake, N. Bruyant, L. Drigo, Y. L. Chen, D. Prabhakaran, B. Yan, C. Felser, T. Kong, P. C. Canfield, A. I. Coldea, Linear Magnetoresistance Caused by Mobility Fluctuations in n-Doped Cd_3As_2, Phys. Rev. Lett. 114 (2015) 117201.

[51] W. L. Zhu, Y. Cao, P. J. Guo, X. Li, Y. J. Chen, L. J. Zhu, J. B. He, Y. F. Huang, Q. X. Dong, Y. Y. Wang, R. Q. Zhai, Y. B. Ou, G. Q. Zhu, H. Y. Lu, G. Li, G. F. Chen, M. H. Pan, Linear magnetoresistance induced by mobility fluctuations in iodine-intercalated tungsten ditelluride, Phys. Rev. B 105 (2022) 125116.

[52] C. Jin, P. Li, W. B. Mi, H. L. Bai, Magnetocrystalline anisotropy-dependent six-fold symmetric anisotropic magnetoresistance in epitaxial $Co_xFe_{3-x}O_4$ films, Europhys. Lett. 100 (2012) 27006.

[53] Y. Miao, D. Yang, L. Jia, X. Li, S. Yang, C. Gao, D. Xue, Magnetocrystalline anisotropy correlated negative anisotropic magnetoresistance in epitaxial $Fe_{30}Co_{70}$ thin films, Appl. Phys. Lett. 118 (2021).

[54] J. Zhang, X. Chen, M. Wang, Q. Zhang, W. Shi, X. Zhan, M. Zhao, Z. Li, J. Zheng, H. Zhang, F. Han, H. Yang, T. Zhu, B. Liu, F. Hu, B. Shen, Y. Chen, Y. Zhang, Y. Chen, W. Zhao, J. Sun, Proximity-Induced Fully Ferromagnetic Order with Eightfold Magnetic Anisotropy in Heavy Transition Metal Oxide $CaRuO_3$, Adv. Funct. Mater. 33 (2023).

[55] R. Ramos, S. K. Arora, I. V. Shvets, Anomalous anisotropic magnetoresistance in epitaxial Fe_3O_4 thin films on MgO(001), Phys. Rev. B 78 (2008) 214402.

[56] P. Li, E. Y. Jiang, H. L. Bai, Fourfold symmetric anisotropic magnetoresistance based on magnetocrystalline anisotropy and antiphase boundaries in reactive sputtered epitaxial Fe_3O_4 films, Appl. Phys. Lett. 96 (2010).

[57] P. Li, C. Jin, E. Y. Jiang, H. L. Bai, Origin of the twofold and fourfold symmetric anisotropic magnetoresistance in epitaxial Fe_3O_4 films, J Appl Phys 108 (2010).

[58] Z. Li, W. Mi, X. Wang, X. Zhang, Interfacial Exchange Coupling Induced Anomalous Anisotropic Magnetoresistance in Epitaxial Fe_4N/CoN Bilayers, ACS Appl. Mater. Interfaces 7 (2015) 3840. PMID: 25643137.

[59] Y. Dai, Y. W. Zhao, L. Ma, M. Tang, X. P. Qiu, Y. Liu, Z. Yuan, S. M. Zhou, Fourfold Anisotropic Magnetoresistance of $L1_0$ FePt Due to Relaxation Time Anisotropy, Phys. Rev. Lett. 128 (2022) 247202.

[60] C. Hu, J. Zhu, G. Chen, J. Li, Y. Wu, Direct comparison of anisotropic magnetoresistance and planar Hall effect in epitaxial Fe_3O_4 thin films, Phys. Lett. A 376 (2012) 3317–3321.

[61] J. Chen, H. Li, T. Guo, P. Chen, D. Zheng, G. Yu, Y.-C. Lau, X. Xi, W. Wang, Anomalous anisotropic magnetoresistance in the topological semimetal HoPtBi, NPG Asia Mater. 15 (2023).

[62] J. Wang, H. Yang, L. Ding, W. You, C. Xi, J. Cheng, Z. Shi, C. Cao, Y. Luo, Z. Zhu, J. Dai, M. Tian, Y. Li, Angle-dependent magnetoresistance and its implications for Lifshitz transition in W_2As_3, npj Qantum Materials 4 (2019).

[63] S. Zhang, Q. Wu, Y. Liu, O. V. Yazyev, Magnetoresistance from Fermi surface topology, Phys. Rev. B 99 (2019) 035142.

[64] A. Weiland, L. J. Eddy, G. T. McCandless, H. Hodovanets, J. Paglione, J. Y. Chan, Refine intervention: Characterizing disordered $Yb_{0.5}Co_3Ge_3$, Cryst. Growth Des. 20 (2020) 6715–6721.

[65] X. Huang, Z. Cui, C. Huang, M. Huo, H. Liu, J. Li, F. Liang, L. Chen, H. Sun, B. Shen, Y. Zhang, M. Wang, Anisotropic magnetism and electronic properties of the kagome metal SmV_6Sn_6, Phys. Rev. Mater. 7 (2023) 054403.

[66] K. Guo, J. Ye, S. Guan, S. Jia, Triangular Kondo lattice in YbV_6Sn_6 and its quantum critical behavior in a magnetic field, Phys. Rev. B 107 (2023) 205151.

[67] X. Xu, J. Yin, Z. Qu, S. Jia, Quantum interactions in topological R166 kagome magnet, Rep. Prog. Phys. 86 (2023) 114502.

[68] G. Zheng, J. Lu, X. Zhu, W. Ning, Y. Han, H. Zhang, J. Zhang, C. Xi, J. Yang, H. Du, K. Yang, Y. Zhang, M. Tian, Transport evidence for the three-dimensional Dirac semimetal phase in $ZrTe_5$, Phys. Rev. B 93 (2016) 115414.

[69] Q.-H. Yu, Y.-Y. Wang, R. Lou, P.-J. Guo, S. Xu, K. Liu, S. Wang, T.-L. Xia, Magnetoresistance and Shubnikov-de Haas oscillation in YSb, EPL (Europhysics Letters) 119 (2017) 17002.

[70] Q. Wang, P.-J. Guo, S. Sun, C. Li, K. Liu, Z.-Y. Lu, H. Lei, Extremely large magnetoresistance and high-density Dirac-like fermions in ZrB_2, Phys Rev B 97 (2018) 205105.

[71] Y.-Y. Lv, X. Li, J. Zhang, B. Pang, S.-S. Chen, L. Cao, B.-B. Zhang, D. Lin, Y. B. Chen, S.-H. Yao, J. Zhou, S.-T. Zhang, M.-H. Lu, M. Tian, Y.-F. Chen, Mobility-controlled extremely large magnetoresistance in perfect electron-hole compensated $\alpha - WP_2$ crystals, Phys. Rev. B 97 (2018) 245151.

Chapter 7

Conclusions

This thesis comprises four research projects conducted during my Ph.D. The main findings emerging from these studies are summarized below.

In the first project, we have grown $Mn_{2.94}Ge$ (Ge-rich) single crystals to study the electrical transport, magnetic, and magnetotransport properties. Importantly, we show that the magnetic and magnetotransport properties of $Mn_{2.94}Ge$ are different from $Mn_{3+\delta}Ge$ (Mn-rich), particularly at low temperatures. We identify that the magnetic and Hall properties of $Mn_{2.94}Ge$ are qualitatively similar to those of Mn_3Sn. Consistent with the magnetic properties, the Hall effect study shows unusual behavior around the spin-reorientation transition. This observation contrasts the previous studies on $Mn_{3+\delta}Ge$ as no such spin-reorientation transition is observed. Further, by comparing the results of $Mn_{2.94}Ge$ and $Mn_{3.20}Ge$ from this study with those of previous reports on $Mn_{3+\delta}Ge$ we propose that the Mn concentration plays a crucial role in shaping the magnetic and Hall properties of Mn_3Ge.

In the second project, we have systematically studied the electrical, magnetic, and magnetotransport properties of $Mn_{(3+x)-\delta}Fe_\delta Ge$ (δ=0, 0.30, and 0.62). We find that the electrical resistivity of the parent compound displays metallic behavior, while the system with δ=0.30 of Fe doping exhibits resistivity similar to a dilute magnetic semiconductor. With further Fe doping of δ=0.62, the system demonstrates a metal-insulator transition at 100 K. Fe doping increases ferromagnetism and magnetocrystalline anisotropy. It induces a spin-glass-like state at low temperatures. In addition, the spontaneous anomalous Hall effect observed in the parent system is significantly reduced with increasing Fe doping concentration. Importantly, the topological Hall effect observed in $Mn_{2.97}Fe_{0.30}Ge$ (δ=0.30), is not found from the parent system $Mn_{3.48}Ge$ or $Mn_{2.69}Fe_{0.62}Ge$ (δ=0.62).

In the third project, we conducted a comprehensive investigation on Fe_3Ge for its anomalous Hall effect behavior along the in-plane and out-of-plane directions. Our study re-

veals significant anisotropy in the anomalous Hall effect (AHE). Notably, the gradual spin reorientation from the out-of-plane to in-plane direction, from high-temperature to low-temperature in Fe_3Ge, provides a unique opportunity to study the temperature dependence on the intrinsic Hall conductivity experimentally. The theoretical predictions qualitatively support our experimental results. Furthermore, a topological Hall effect (THE) signal is observed along the in-plane direction, originating from the emergence of a noncoplanar spin structure stabilized by strong magnetocrystalline anisotropy below the spin reorientation temperature (T_{SR}).

In the fourth project, we systematically studied the magnetic and magnetotransport properties on the high-quality single crystals of the Fe-based RFe_6Sn_6 (R = Ho, Dy) kagome systems. Extremely large magnetoresistance (XMR) is observed at low temperatures, reaching the maximum MR percentage as high as 3×10^3 % for $HoFe_6Sn_6$ and 1×10^3 % for $DyFe_6Sn_6$ at 2 K under 9 T of applied magnetic field. Hall effect measurements demonstrate the electron-hole charge compensation and high carrier mobility, leading to extremely large magnetoresistance at low temperatures. Further, the angle-dependent magnetoresistance (ADMR) data reveal high anisotropy in the magnetoresistance. Importantly, the magnetoresistance anisotropic pattern changes significantly with temperature, implies the temperature dependence of the Fermi surface topology in these systems.

Future Prospects

In the Ge-rich $Mn_{2.94}Ge$ compound, a gradual spin-reorientation transition is observed around 100 K. Although neutron diffraction studies exist for Mn-excess compositions, similar investigations for Ge-rich variants are still lacking. A detailed neutron diffraction study would be critical to uncover the ground-state spin configuration and the underlying mechanism driving the spin reorientation. In the Fe-doped system, $Mn_{(3+x)-\delta}Fe_\delta Ge$, a pronounced topological Hall effect appears below 50 K, indicating the possible emergence of nontrivial spin textures such as skyrmions. Lorentz transmission electron microscopy (LTEM) could provide direct real-space imaging to confirm their presence and strengthen the understanding of topological magnetic phases in this material. For Fe_3Ge, temperature-dependent reorientation of Fe spins from out-of-plane (above T_{SR}) to in-plane significantly alters the band structure, leading to a temperature-dependent intrinsic anomalous Hall effect driven by Berry curvature evolution. Temperature-dependent neutron diffraction measurements would help quantify the spin canting angle and elucidate the coupling between spin texture and electronic topology. In RFe_6Sn_6, the strong temperature dependence of angle-dependent magnetoresistance (ADMR) suggests modulation of the Fermi surface with temperature. Angle-resolved photoemission spectroscopy (ARPES) would be a valuable technique to directly visualize these changes, offering in-

sights into temperature-induced electronic structure evolution. In general, these findings open up several avenues for future research. Advanced characterization tools such as neutron diffraction, LTEM, and ARPES will be essential to unravel the microscopic magnetic and electronic structures and their interplay in these complex systems.

List of Publications

Publications related to this thesis

1. **Susanta Ghosh**, Achintya Low, Soumya Ghorai, Kalyan Mandal, and Setti Thirupathaiah, "Tuning of electrical, magnetic, and topological properties of magnetic Weyl semimetal $Mn_{3+x}Ge$ by Fe doping", Journal of Physics: Condensed Matter 35 (2023) 485701.

2. **Susanta Ghosh**, Achintya Low, Susmita Changdar, Shubham Purwar and Setti Thirupathaiah, "Unusual multiple magnetic transitions and anomalous Hall effect observed in antiferromagnetic Weyl semimetal, $Mn_{2.94}Ge$ (Ge-rich)," Journal of Physics: Condens. Matter 36 (2024) 215705.

3. **Susanta Ghosh***, Achintya Low*, Nayana Devaraj, Susmita Changdar, Awadhesh Narayan, and S. Thirupathaiah, "Extremely large and angle-dependent magnetoresistance observed in kagome Dirac semimetal RFe_6Sn_6 (R=Ho, Dy)" (Under Review). (*equal contribution).

4. **Susanta Ghosh**, Tushar Kanti Bhowmik, Achintya Low, and S. Thirupathaiah, "Temperature dependent intrinsic anomalous hall conductivity observed in Fe_3Ge, a ferromagnetic topological metal." (Under Review).

Other publicatins

1. Susmita Changdar*, **Susanta Ghosh***, Anumita Bose, Indrani Kar, Achintya Low, Patrick Le Fèvre, François Bertran, Awadhesh Narayan and Setti Thirupathaiah, "Weak electronic correlations observed in magnetic Weyl Semimetal Mn_3Ge" Journal of Physics: Condensed Matter 36 (2024) 125502. (*equal contribution)

2. Achintya Low, **Susanta Ghosh**, Susmita Changdar, Sayan Routh, Shubham Purwar, and S. Thirupathaiah. "Tuning of topological properties in the strongly correlated antiferromagnet Mn_3Sn via Fe doping." Physical Review B 106, 144429 (2022).

3. Susmita Changdar, **Susanta Ghosh**, Kritika Vijay, Indrani Kar, Sayan Routh, P.K. Maheshwari, Soumya Ghorai, Soma Banik, and S. Thirupathaiah, "Nonmagnetic Sn doping effect on the electronic and magnetic properties of antiferromagnetic topological insulator $MnBi_2Te_4$" Physica B: Condensed Matter 657 (2023) 414799.

4. Achintya Low, **Susanta Ghosh**, Soumya Ghorai, and S. Thirupathaiah, "Effect of Electron-Phonon Scattering on the Anomalous Hall Conductivity of Fe_3Sn, a Kagome Ferromagnetic Metal " Physical Review B 108, 094404 (2023).

5. Shubham Purwar, Susmita Changdar, **Susanta Ghosh**, Tushar Kanti Bhowmik, and S. Thirupathaiah, Intricate magnetic interactions and topological Hall effect observed in itinerant room-temperature layered ferromagnet $Cr_{0.83}Te$, Acta Materialia 271, 119898 (2024).

6. Achintya Low, Tushar Kanti Bhowmik, **Susanta Ghosh**, and S. Thirupathaiah. "Anisotropic nonsaturating magnetoresistance observed in $HoMn_6Ge_6$: A kagome Dirac semimetal." Physical Review B 109, 195104 (2024).